

CARRIER TRANSPORT IN NANOSTRUCTURES:
PROBING PHONONS AND ELECTRONS

A Dissertation

Presented to the Faculty of the Graduate School

of Cornell University

In Partial Fulfillment of the Requirements for the Degree of

Doctor of Philosophy

by

Obafemi Oluwaseun Otelaja

February 2016

© 2016 Obafemi Oluwaseun Otelaja

CARRIER TRANSPORT IN NANOSTRUCTURES:
PROBING PHONONS AND ELECTRONS

Obafemi Oluwaseun Otelaja, Ph.D.

Cornell University 2016

Spectrally resolved phonon transport is important for understanding nanoscale heat flow, which have implications for the realization of efficient thermoelectric and microelectronic cooling devices, for the realization of efficient cryogenic particle detectors, and for the realization of robust implementations of quantum computers.

This thesis describes the development and utilization of a microscale phonon spectrometer. Aluminum superconducting tunnel junctions (STJ) are utilized for the emission and detection of non-thermal phonons with frequencies ranging from ~ 100 to ~ 870 GHz in silicon nanostructures. The energy resolution of the spectrometer is ~ 60 - 80 μeV , corresponding to a frequency resolution of ~ 15 - 20 GHz, which is about 20 times better than the energy resolution of conventional thermal transport measurements that rely on a Planck distribution of phonons. The spectrometer is utilized to probe surface scattering and phonon backscattering in silicon.

To probe surface scattering, silicon nanosheets were fabricated, their surface roughness (~ 1 nm) was determined using atomic-force microscopy, and their phonon scattering rates were measured. Our results indicate that the well-known Ziman theory, which takes into account the roughness of the surface, underestimates the probability for totally diffusive scattering in nanostructures. To probe phonon backscattering, phonon ‘enhancers’ (~ 90 μm deep) were etched around the STJ detectors, and the

measured backscattered phonon signal increases with the number of enhancers. Using a geometric analysis of the phonon pathways, we show that the mechanism of the backscattered phonon enhancement is due to confinement of the ballistic phonon. These results have implications for ballistic phonon transport, phonon-mediated detection, and thermal transport studies, and highlight the important effects of phonon scattering from surfaces and interfaces in nanoscale geometrical designs.

Finally, a facile room-temperature method, comprising ammonium sulfide treatment and electrophoretic deposition, was developed for assembling colloidal copper sulfide (Cu_{2-x}S) nanoparticles into highly electrically conducting films. Electronic properties of the treated films are characterized with a combination of Hall Effect measurements, field-effect transistor measurements, temperature-dependent conductivity measurements, and capacitance-voltage measurements, revealing their highly-doped p-type semiconducting nature. In addition to being important for solution-processed electronics, the periodicity introduced by nanoparticles and their arrays presents a model system for probing phonon transport in complex interfaces.

BIOGRAPHICAL SKETCH

Obafemi Otelaja is a native of Ilishan-Remo in Ogun State, Nigeria. He completed his Bachelors of Science degree in Electrical and Computer Engineering at Howard University, after transferring from the Obafemi Awolowo University (formerly University of Ife), Ile-Ife, Nigeria. After undergraduate summer research stints at Corning Incorporated, Brookhaven National Laboratory, and Merck Research Laboratories, he enrolled in the PhD program in the School of Electrical and Computer Engineering at Cornell University where he conducted research in the area of nanoscale phonon transport and electron transport in nanoparticle films.

To whom there is neither variableness nor shadow of turning

And

To my family

ACKNOWLEDGMENTS

I would like to thank my research advisor, Prof. Richard Robinson, for the opportunity to work in his group and for providing the resources that supported me and my work throughout my graduate studies. Rich's guidance and patience played a major role in the completion of this thesis. I thank Prof. Michael Spencer, for serving as my committee member and for providing advice and support throughout my program. I am very grateful for his willingness to listen and discuss science and career related matters at any given time. I am also thankful to Prof. Bruce van Dover for willing to serve on my graduate committee. I have learnt much from taking his class, using his equipment, skimming his old research notes and equipment manuals, and discussing freshly taken data and equipment issues with him.

I like to thank Prof. Shefford Baker for allowing me access to his lab and facilities. I am indebted to Prof. Hakim Weatherspoon for his encouragement and mentoring throughout my graduate studies. I also like to thank my undergraduate Professors (Dr. James Mitchell, Dr. Gary Harris, Dr. Mihai Dimian, Dr. Charles Kim, and Dr. Tepper Gill) and summer research supervisors (Dr. Boh Ruffin (Corning) and Dr. Ron Pindak (BNL)) for their mentoring and encouragement to pursue graduate studies. I am grateful to the staff of the CNF, CCMR, and LASSP for their training and maintenance efforts on world class research facilities. Notably I am grateful to Eric Smith (LASSP), Derek Stewart, Rob Ilic, Daron Westly, Meredith Metzler, Don Tennant, Jon Shu, Steve Kriske, Mick Thomas, Paul Bishop, and Phillip Carubia.

The work in this thesis was supported in part by the National Science Foundation under Agreement Nos. DMR-1149036 and CBET-1066406, and in part by the Cornell Center for Materials Research (CCMR) with funding from the Materials Research Science and Engineering Center program of the National Science Foundation

(cooperative agreement DMR 1120296). Parts of this thesis were partially funded through support of the Energy Materials Center at Cornell (EMC2), an Energy Frontier Research Center funded by the U.S. Department of Energy, Office of Science, Office of Basic Energy Science under Award Number DE-SC0001086. The work in this thesis was also supported in part by Award No. KUS-C1-018-02, made by King Abdullah University of Science and Technology (KAUST). Fabrication and simulations for this work were performed in part at the Cornell Nanoscale Facility, a member of the National Nanotechnology Infrastructure Network, which is supported by the National Science Foundation (Grant ECS-0335765).

I will also like to thank all the members of the Robinson Group, old and new that I have interacted with over the years. On the phonon project I am grateful to have worked with Jared Hertzberg, Naoki Yoshida, Mahmut Aksit, Jesseon Chang, and Alex Lin. I am particularly indebted to Jared for being an excellent teacher and mentor, and for always patiently trying to find answers to my numerous questions. Mahmut performed all the Monte Carlo simulations reported in this thesis. I am also grateful to Haitao Zhang, Don-Hyung Ha, and Louis Solomon who have been great lab mates and good friends outside the lab. I am grateful to the excellent undergraduate students I have interacted with over the years: Lianne Moreau, Tiffany Ly, Victoria Savikhin, and Ha Kim.

Outside the Robinson Group, I am indebted to several graduate students and researchers with whom our interactions and friendships have been immensely valuable to my work: Kwame Amponsah, Michael Mak, Debo Olaosebikan, Weimin Chan, Kiran Matthews, Changju Lee, David Korda, Dickson Kirui, Kevin Whitham, David Agyeman-Budu, Laura Hockaday, Alex Melnick, and Shankar Radhakrishnan. Outside the lab I am indebted to Lateef Yusuf, Korede Akinlabi-Oladimeji, Segun Ogunnaike, Supo Johnson, and Ayomide Atewologun for always being there to listen and encourage

and for being great friends.

I am grateful to my parents for providing a solid educational foundation throughout my formative years and for their endless encouragement in this journey. To my siblings and their families, especially the Iyanoyes, I am forever grateful for all the love and support. To the Okeowo family, I am very grateful for the love, understanding and support throughout the years.

I am extremely grateful to my wife, Modupe—a jewel of inestimable value—for her love, patience, and understanding throughout this journey. Without her constant love and support, this thesis would not have been completed. Thank you.

TABLE OF CONTENTS

ACKNOWLEDGMENTS	vii
TABLE OF CONTENTS	x
LIST OF FIGURES.....	xiv
LIST OF TABLES	xvi
1 INTRODUCTION	1
1.1. Motivation	1
1.2. Phonons as Heat Carriers.....	7
1.3. Comparing Thermal Conductance and Phonon Spectroscopy	8
1.4. Superconducting Tunnel Junctions	10
1.5. Other Spectroscopic Phonon Detection Methods	15
1.6. Electron Transport in Nanoparticle Films	17
1.7. Hopping Conduction Mechanism	18
1.8. Thesis Outline	20
2 DESIGN AND OPERATION OF A MICROFABRICATED PHONON SPECTROMETER UTILIZING SUPERCONDUCTING TUNNEL JUNCTIONS AS PHONON TRANSDUCERS	21
2.1. Abstract	21
2.1.1. Importance of Nanoscale Phonon Spectroscopy	22
2.1.2. Spectrometer Design.....	24
2.2. Principles of Operation.....	28
2.2.1. Phonon Emission with STJ.....	28
2.2.2. Modeling the Phonon Emission Spectrum	30
2.2.3. Phonon Detection with STJ	36
2.2.4. Modeling the Detector Behavior.....	37
2.2.5. Estimation of the Detector Efficiency	39
2.3. Fabrication Techniques and Challenges.....	42

2.4.	Instrumentation, Measurement, and Characterization of Spectrometer	47
2.4.1.	Low Temperature Apparatus	47
2.4.2.	DC Characterization of STJ Emitters and Detectors	49
2.4.3.	Josephson Current Suppression	51
2.4.4.	Modulated Phonon Transport Measurements	55
2.5.	Results of Phonon Spectroscopy Measurements	60
2.5.1.	Energy Resolution and Sensitivity	60
2.5.2.	Ballistic Phonon Propagation	62
2.5.3.	A Numerical Example of Phonon Emission Rate	66
2.6.	Conclusion	67
3	DIRECT MEASUREMENTS OF SURFACE SCATTERING IN Si	
	NANOSHEETS: IMPLICATIONS FOR CASIMIR-LIMIT PREDICTED BY	
	ZIMAN-THEORY	69
3.1.	Abstract.....	69
3.2.	Surface Scattering	70
3.2.1.	Need for Frequency Resolved Measurements of Surface Scattering.....	70
3.2.2.	Casimir-Ziman Model.....	70
3.3.	Experiment.....	73
3.4.	Results	84
3.5.	Conclusions on Surface Scattering Studies	103
4	ENHANCEMENT OF PHONON BACKSCATTERING DUE TO	
	CONFINEMENT OF BALLISTIC PHONON PATHWAYS IN SILICON AS	
	PROBED WITH A MICROFABRICATED PHONON SPECTROMETER	106
4.1.	Abstract.....	106
4.2.	Introduction.....	107
4.3.	Phonon Backscattering and Phonon Enhancers.....	108
4.4.	Backscattered Phonon Enhancement Results	112
4.5.	Geometric Analysis of Phonon Backscattering	117
4.6.	Conclusion	122

5	HIGHLY CONDUCTIVE Cu_{2-x}S NANOPARTICLE FILMS THROUGH ROOM TEMPERATURE PROCESSING AND AN ORDER OF MAGNITUDE ENHANCEMENT OF CONDUCTIVITY VIA ELECTROPHORETIC DEPOSITION.....	123
5.1.	Abstract.....	123
5.2.	Overview of Solution-Processed Electronic Fabrication	124
5.3.	Experimental Section	126
5.3.1.	Overview of Experimental Procedures	126
5.3.2.	Optimal Nanoparticle Film Deposition Conditions	128
5.4.	Results and Discussion.....	130
5.4.1.	Structural Characterization.....	130
5.4.2.	Composition Studies with XPS	133
5.4.3.	Electronic Characterization	135
5.4.3.1.	Hall Measurements	135
5.4.3.2.	Temperature-Dependent Conductivity Measurements	140
5.4.3.3.	Effect of Porosity on Conductivity	142
5.4.3.4.	Hopping Conduction Mechanism	144
5.4.3.5.	Thermal Stability and Light Sensitivity	145
5.4.3.6.	Field-Effect Transistor (FET)- Geometry Measurements.....	146
5.4.3.7.	Capacitance–Voltage Measurements.....	149
5.5.	Conclusion	151
6	CONCLUSION AND OUTLOOK.....	152
6.1.	Summary of Thesis	152
6.2.	Additional Phonon Transport Studies	155
6.2.1.	Phonon Transport in Silicon Oxide Films.....	155
6.2.2.	Temperature Dependence of Phonon Transmission	160
6.2.3.	Modulation Frequency Dependence of Phonon Transmission.....	161
6.3.	Future Work.....	162

APPENDIX A: SUPPLEMENTARY INFORMATION FOR CHAPTER 3	164
APPENDIX B: SUPPLEMENTARY INFORMATION FOR CHAPTER 4	188
APPENDIX C: SUPPLEMENTARY INFORMATION FOR CHAPTER 5	191
APPENDIX D: ADDITIONAL EXPERIMENTAL DETAILS AND TECHNIQUES	209
BIBLIOGRAPHY	227

LIST OF FIGURES

Figure 1.1: Near-exponential increase of CPU power density in recent decades.	3
Figure 1.2: Effect of size on the thermoelectric figure of merit.	6
Figure 1.3: Schematic illustrating modulation technique.	9
Figure 1.4: Phonon spectroscopy versus thermal conductance.	10
Figure 1.5: Density of state diagram for three typical voltages and resulting I-V characteristics of a superconducting tunnel junction.	14
Figure 1.6: A Transmission electron micrograph and schematic illustration showing morphology of nanocrystal arrays.	18
Figure 1.7: A cartoon depicting Variable-Range Hopping.	19
Figure 2.1: (a) False-colored SEM micrograph of completed phonon spectrometer... (b) Optical microscope image of 4.5 square mm device comprising six spectrometers.	25 26
Figure 2.2: Phonon emission principles and emission spectrum.	29
Figure 2.3: Spectrometer fabrication.	43
Figure 2.4: (a) Plot of exposure parameter with the area specific resistance (b) Plots showing the effect of oxygen doping on Aluminum films.	46 46
Figure 2.5: Sample stage and mounting on fridge.	48
Figure 2.6: Plots of dc I-V Characterization.	50
Figure 2.7: Plots of Josephson current suppression and subgap thermometry.	53
Figure 2.8: Phonon transport measurements.	56
Figure 2.9: Detector noise spectrum.	62
Figure 2.10: Results of ballistic phonon propagation.	63
Figure 2.11: Comparison of the modulated detector response scaled by detector efficiency factor Eff (scatter plots and left axis) with the unscaled detector response	66
Figure 3.1: Design of Spectrometer to Probe Phonon Transmission through Silicon Nanosheet Arrays.	75
Figure 3.2: Phonon Spectrometer Operating Principles.	77
Figure 3.3: Phonon Transmission Spectra through Nanosheet Arrays.	86
Figure 3.4: 2D Phonon Focusing Factor Map of Angles Relative to Si [110] Direction	89
Figure 3.5: Measured Phonon Transmission Signals through Un-etched (bulk) Si Mesa and Comparison to Simulated Transmission Factors.	90
Figure 3.6: Measured Phonon Transmission Signals through Si Nanosheet Arrays: Comparison to Modeled Transmission Factors.	98
Figure 3.7: Estimated Transmission Through Si Nanosheet, as a Function of Nanosheet Length, for Phonon Distribution Peaked at 400 GHz.	101
Figure 4.1: Experimental geometry for backscattering measurements.	111
Figure 4.2: Measured phonon backscattering with and without enhancers.	114
Figure 4.3: Plot of relative intensity of oxygen resonance peaks of backscattered signals with and without enhancers.	116
Figure 4.4: Analysis of enhanced phonon backscattering mechanism.	117
Figure 5.1: (a) Schematic depiction of experimental plan to study electronic transport	

in EPD and spin-cast copper sulfide films. (b) TEM of starting copper sulfide nanoparticles with average particle size of 5 nm. (c) AFM height image.....	130
Figure 5.2: Structural characterization with XRD and TEM.....	132
Figure 5.3: Compositional studies of copper sulfide nanoparticle films with XPS...	134
Figure 5.4: Hall Effect measurements for two spin-cast films on glass substrates....	136
Figure 5.5: Temperature-dependent electrical conductivity measurements.....	141
Figure 5.6: FET measurements of EPD and spin-cast films.....	148
Figure 5.7: Capacitance-Voltage studies.....	150
Figure 6.1: Optical microscope image of a phonon spectrometer fabricated on silicon oxide films for phonon transport experiments via reflection.....	156
Figure 6.2: Phonon transport in silicon oxide membranes.....	157
Figure 6.3: SEM of a fully suspended silicon oxide membrane with STJs and trench.	159
Figure 6.4: Temperature-dependent phonon transmission measurements.....	160
Figure 6.5: Effect of modulation frequency on detected phonon signal	161
Figure 6.6: SEM images of (a) straight nanosheets, (b) nanosheets with cavities, and (c) bent nanosheets on silicon mesas.....	162

LIST OF TABLES

Table 1.1: T_c and superconducting energy gap for some metals.....	11
Table 1.2: Comparison of STJ technique and prominent TDTR method	16
Table 3.1: Geometry of phonon spectrometers and measured silicon nanosheets.	76
Table 3.2: Electronic characterization of the phonon spectrometers for silicon nanosheet measurements.	80
Table 5.1: Hall Effect measurements on spin-cast nanoparticle-based films.	137
Table 5.2: Linear fits of conductivity to Mott variable-range hopping equation.	145

CHAPTER 1

1 INTRODUCTION

1.1. Motivation

As modern devices are continuously being scaled down to nanoscale dimensions, the effect of the low-dimensionality on the fundamental energy carriers is yet to be fully unraveled. This thesis is concerned with the fundamental understanding of the transport of two of such carriers in two nanoscale systems — phonons in silicon nanostructures and electrons in copper sulfide nanoparticle films.

The atoms and bonds that make up materials could be modeled as masses connected by springs. At zero temperature, the masses and springs are still; however, they vibrate at finite temperatures. These lattice vibrations results in mechanical waves propagating in the crystal. The quantized lattice vibrations are called phonons, and they carry discrete packets of energy. The quantum mechanical nature of phonons accords them a wave-particle duality nature, which is observed in other quantized particles such as electrons and photons. From the aforementioned facts about phonons, they are the fundamental particle responsible for sound and heat, and some researchers have described a ‘phononic spectrum’ to illustrate that phonons give rise to sound and heat.[1] A significant difference, however, is that while sound consists of low frequency vibrations (~KHz regime), heat is comprised of high frequency phonons (>100 GHz to THz regime). [1, 2] Due to their high frequency nature, nanoscale structures are often needed to engineer and control heat flow. This thesis is concerned with probing acoustic phonons and elucidating their importance to nanoscale heat transport.

Why is a fundamental understanding of the dynamics phonons at the nanoscale important? Since all materials and devices are made up of atoms and bonds, phonons are intrinsic to all condensed matter devices. An understanding of phonon propagation provides insight that enable better control and engineering of heat flow at the nanoscale, which in turn have ramifications for the realization of efficient thermoelectric and microelectronic cooling devices. In addition, the ability to engineer phonons at the nanoscale also has implications for the realization of robust cryogenic particle detectors, and for understanding sources of decoherence of qubits in quantum computing systems. In general, nanoscale phonon studies are important for all phonon-mediated detection systems.

The ability to understand and resolve some of the fundamental questions about the dynamics of phonons at the nanoscale will have implications for several of the phonon engineering applications highlighted above. How does surface scattering affect nanoscale phonon propagation? What are the effects of phonon backscattering and interfacial scattering on phonon propagation? Can phonon interference effects be exploited for nanoscale heat manipulation? Resolving some of these questions is the aim of this thesis. While the plausible applications of phonon engineering are extensive, [1, 3, 4] the importance of understanding nanoscale heat transport as it relates to (i) microelectronic cooling, (ii) cryogenic particle detection, (iii) quantum bits, and (iv) thermoelectric devices will be highlighted as follows:

(i) Microelectronics and localized hot spots

As the active devices in microelectronic circuits are continually getting smaller and operating at faster speeds, localized hot spots around the active regions become a major

limiting factor for optimum device performance. As of 2010, the power density of the central processing unit (CPU) of computers by most of the major semiconductor manufacturers was approaching $\sim 100 \text{ W/cm}^2$ as depicted in Figure 1.1. [5] This is a significant amount of heat dissipation, which is better understood when compared to the power density of a nuclear reactor ($\sim 100 \text{ W/cm}^2$) and the Sun's surface ($\sim 6000 \text{ W/cm}^2$).[5]

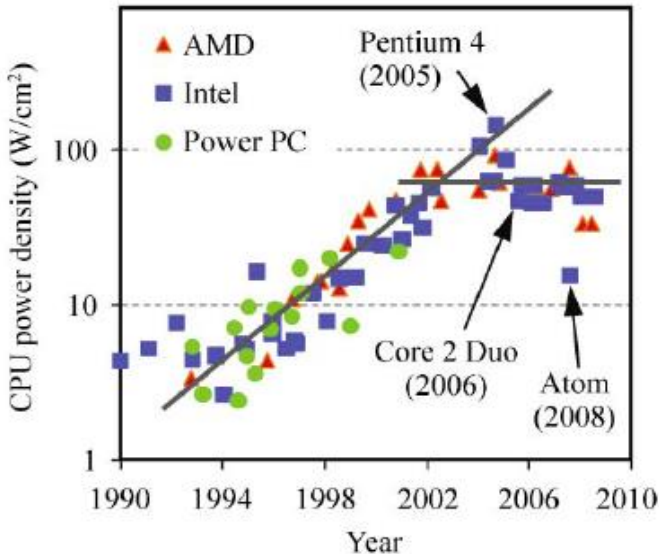


Figure 1.1: Near-exponential increase of CPU power density in recent decades. Power density has flattened with the introduction of multi-core CPUs (solid lines show approximate trends); by comparison, the power density on the surface of the sun is approximately 6000 W/cm^2). Adapted from [5]

Research efforts have focused on methods to realize materials with enhanced thermal conductivity for passive cooling of microelectronics. [5-7] Therefore, understanding

nanoscale phonon transport could lead to engineering materials to have enhanced phonon conduction.

(ii) Cryogenic particle detectors based on phonon-mediated detection

In the field of high energy particle detection, cryogenic temperatures are employed for low $k_B T$ operation in order to realize superior energy resolution.[8] Some of the typically used detectors include superconducting bolometers, superconducting transition-edge sensors, microwave kinetic inductance detectors (MKID) and superconducting tunnel junctions. [9-12] These detectors are mostly used as phonon sensors in cryogenic dark matter searches and neutrino detection. When high energy particles are incident on a substrate containing an array of particle sensors, the particle substrate interaction produces ionizations and phonons which can be collected and measured as signatures of the particular incident particle.[13, 14] The sensitivity and fidelity of such detection systems depends on the directionality of phonon propagation in the substrates with respect to the phonon sensors; hence, a thorough understanding of phonon propagation and backscattering in substrates is important.

(iii) Qubit decoherence due to phonons

The difference between classical computers and proposed quantum computers is that while the former computes based on two classical states (0 and 1), computation in the latter involves two quantum mechanical states or qubits ($|0\rangle$ and $|1\rangle$) as well as a superposition of these states. Several implementations of qubits include Josephson junction qubits (charge, phase and flux qubits), electron qubits (spin or charge qubits),

or photon-based qubits. [15, 16] A major challenge for the development of quantum computers is qubit decoherence (loss of time memory of a qubit state) due to interactions with the environment, in particular phonons. Acoustic phonon radiation in substrates have been shown to be sources of decoherence in both superconducting qubits[17] and spin qubits.[18] For instance, Mozysky et al showed that Ge is a less preferable material than Si for quantum computing applications because of the stronger coupling of the localized spins in Ge to phonons.[18] Hence, an understanding of nanoscale phonon dynamics in substrates would guide material selection for robust quantum computers.

(iv) Thermoelectrics for waste heat recovery

Roughly 60% of the total energy input in automobiles is lost as waste heat, and only about 21% is used to drive the car.[19] This energy lost as heat could be harnessed. Thermoelectric devices — devices that convert heat into electricity — could be utilized to harness waste heat for useful energy; however, they are not efficient enough to be commercially viable. Hicks and Dresselhaus showed that the thermoelectric figure of merit, $ZT = (S^2\sigma/\kappa) T$ (S is the Seebeck coefficient, σ is the electronic conductivity, and κ is the thermal conductivity), of a thermoelectric material could be enhanced by preparing the material in the form of a multilayered superlattice.[20] This layered approach was proposed to enable the reduction of the phonon thermal conductivity due to interfacial scattering, without affecting the 2D-confined electrons. Khitun and Balandin[21] also showed by computation that in $\text{Si}_{1-x}\text{Ge}_x$ quantum wires, the thermoelectric figure of merit could be enhanced due to spatial confinement of acoustic

phonons and increased phonon relaxation rates. These results evince that the behavior of phonons in low-dimensional structures are markedly different from the bulk, as illustrated in Figure 1.2.

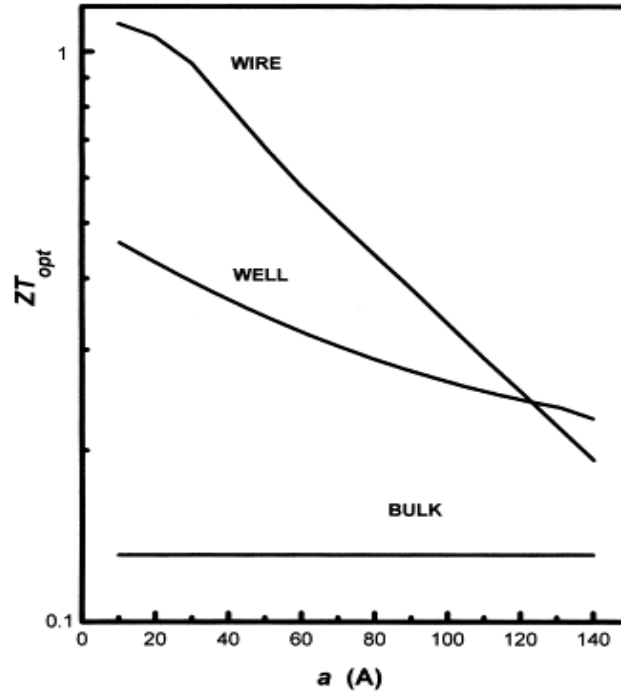


Figure 1.2: Effect of size on the thermoelectric figure of merit. Calculated thermoelectric figures of merit of the $\text{Si}_{0.9}\text{Ge}_{0.1}$ quantum well and quantum wire as the functions of thickness and radius a , correspondingly. Results are shown for room temperature. Adapted from [21].

Experimental works on thermal transport in confined nanostructures, such as single carbon nanotubes [22] and silicon nanowires, [23, 24] followed the theoretical works and later provided an insight to the importance of phonon scattering due to modified phonon dispersion relations and interfacial effects such as acoustic mismatch,

defects and dislocations, and surface roughness. [4, 25] Several experimental techniques have been developed to probe nanoscale heat transport [26-30]; however, these studies treat phonons as thermal equilibrium quantities such as heat capacity and thermal conductance, rather than specifically probing the vibrational quanta. As a result, questions on the fundamental understanding of nanoscale heat transport due to scattering of phonons at surfaces and interfaces, and due to interference of phonons remain unresolved. To this end, a more precise experimental probe to spectrally resolve acoustic phonon transmission and scattering in nanostructures is needed.

1.2. Phonons as Heat Carriers

Phonons are quantized lattice vibrations, which are analogous to photons (quantized electromagnetic waves), and allow a particle description of lattice vibrations. The energy of an elastic mode of angular frequency ω , occupied by n phonons is given by: [31]

$$\epsilon = \left(n + \frac{1}{2}\right) \hbar\omega \quad (1.1)$$

where $\frac{1}{2} \hbar\omega$ is the zero point energy of the mode. The average phonon number in a given mode in thermal equilibrium is given by the Bose-Einstein statistics:[31]

$$\langle n \rangle = \frac{1}{\exp\left(\frac{\hbar\omega}{k_B T}\right) - 1} \quad (1.2)$$

The higher the temperature, the larger the vibration of the lattice atoms and the larger the phonon number $\langle n \rangle$. At low temperatures, acoustic phonons rather than optical

phonons play the important role. This equilibrium description of phonons, also called a Planck distribution, is the foundation of thermal conductance measurements.

1.3. Comparing Thermal Conductance and Phonon Spectroscopy

In thermal conductance measurements, phonons are measured as heat flow between two thermal reservoirs. [26-30] This implies phonons of a broad range of frequencies are emitted and characterized, and often, it is assumed the thermal energy is carried by phonons at the peak of the Planck distribution (the dominant phonon approximation: $\nu_{dom} = 4.25(k_B/h)T = (90 \text{ GHzK}^{-1})T$).

However, the ultimate goal of phonon spectroscopy is to emit and detect non-equilibrium phonons, whose energy can be tuned irrespective of temperature. In particular, this thesis is focused on phonon spectroscopy utilizing superconducting tunnel junctions (STJ) as the phonon transducers. Non-equilibrium phonon emission and detection with STJ was first demonstrated over 40 years ago by Eisenmenger and others [32-34]. While these previous spectroscopic phonon studies were performed on bulk-sized samples, this thesis extends this spectroscopic phonon technique to the micro/nanoscale for the first time, offering sub-micron spatial resolution. In fact, our initial work on non-equilibrium phonon generation and detection in microstructure devices was the first adaptation of the STJ phonon spectroscopy at the microscale.[35]

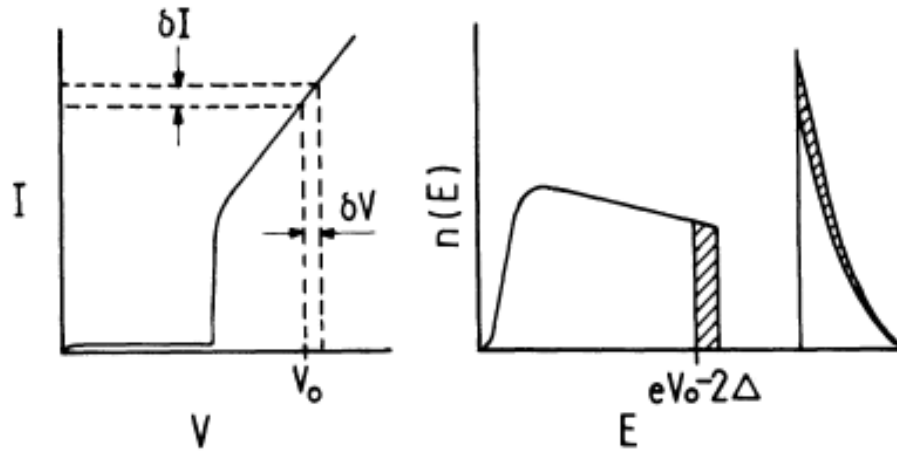


Figure 1.3: Schematic illustrating modulation technique. The change of the emitted “bremsstrahlung spectrum on a small voltage change is quasi monochromatic. Adapted from [34].

As shown in Figure 1.3, the relaxation phonon emission spectrum of an STJ has a sharp discontinuity that is voltage dependent. This voltage dependence allows for a modulation technique in which a thin slice of the entire phonon spectrum could be isolated. This modulation technique allows for spectral resolution of phonons unlike the techniques based on Planck distribution. In Figure 1.4, the advantage of phonon spectroscopy over thermal conductance is depicted by estimating and plotting the modulated STJ power per unit frequency and a Planck distribution peak power per unit frequency (both peaked at 300 GHz). This plot shows that phonon spectroscopy is in theory able to realize ~ 20 times better frequency resolution.

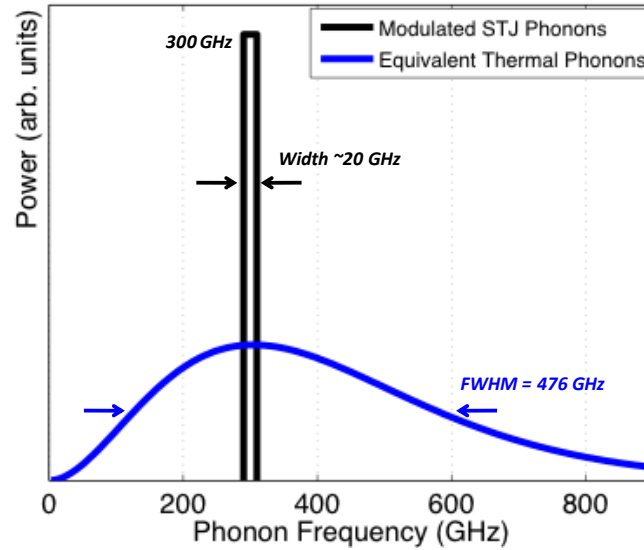


Figure 1.4: Phonon spectroscopy versus thermal conductance. An illustration comparing the frequency resolution of thermal equilibrium phonon probes (thermal conductance measurements) and a non-equilibrium phonon probe (modulated STJ). Both plots are peaked at ~ 300 GHz and have approximately equal areas under their entire emission spectrum.

1.4. Superconducting Tunnel Junctions

Superconducting tunnel junctions (STJ) are essentially the primary active device in the majority of this thesis. While the operating principle of the STJ as phonon transducers as it relates to a microfabricated spectrometer will be discussed in Chapter 2, the theoretical background to understand superconductivity, tunneling, phonon emission and detection will be addressed here.

The theoretical foundation that explains the characteristics of STJs is based on the BCS theory of superconductivity described by Bardeen, Cooper and Schrieffer in

1957.[36] Below a critical temperature, T_c , the ground state of a superconducting metal is for electrons to form Cooper pairs.[37] Any unpaired electrons are excitations from this ground state (or quasiparticles), and these excitations may occur due to thermal lattice vibrations or due to the incidence of photons. The binding energy of the paired electron is described in BCS theory by a temperature dependent gap parameter, which is related to the critical temperature T_c by:[38, 39]

$$2\Delta(0) = 3.52k_B T_c \quad (1.3)$$

The actual values of the material dependent critical temperature are determined from tunneling and electromagnetic absorption experiments. Table 1.1 shows the critical temperature and superconducting gaps for some relevant materials.

Table 1.1: T_c and superconducting energy gap for some metals. [38]

Material	T_c (K)	$2\Delta(0)$ (meV)
Al	1.175	0.34
Nb	9.25	3.05
Pb	7.196	2.73
Sn	3.722	1.15

The consequence of the superconducting gap for excitations is a gap in the quasiparticle density of states in a superconductor when compared to a normal metal. In the superconducting state, the density of states is given by: [38]

$$N_s(E) = \frac{N_n(0)E}{\sqrt{(E^2 - \Delta^2)}} \quad (1.4)$$

$N_n(0)$ is the normal density of states at the Fermi energy, and there are no excitation states in the range $0 \leq E \leq \Delta$. Since quasiparticles are fermions (while the Cooper pairs are Bosons), the number of thermal quasiparticles at any given temperature could be obtained by integrating the product of the Fermi distribution and $N_s(E)$ over all energy range as follows:

$$N_{QP} = \int_0^\infty \frac{N_s(E)E}{1 + \exp\left(\frac{E}{k_B T}\right)} dE \approx N_n(0) \sqrt{2\pi k_B T \Delta} \exp\left(-\frac{\Delta}{k_B T}\right) \quad (1.5)$$

Hence, the number of thermal quasiparticles at a finite temperature has an exponential dependence on temperature. When a photon or phonon is incident on a superconductor, Cooper pairs are broken and the resulting increase in quasiparticle density is a direct probe of the photons or phonons (we are concerned with only phonons in this thesis).

Josephson junctions[40] comprise a weak link of non-superconducting material sandwiched between two superconducting metals. The non-superconducting material could be either an insulating layer or a normal metal, forming Superconductor-Insulator-Superconductor (SIS) or Superconductor-Normal-Metal-Superconductor (SNS) junctions respectively. STJs are S-I-S Josephson junctions, and both Cooper pairs and quasiparticles can tunnel through the barrier. The current-voltage relationship describing the behavior the tunneling of Cooper pairs (Josephson current) is given in the Josephson relations:

$$I = I_c \sin \phi, \quad (1.6)$$

where I is the current across the junction, I_c is the critical current density and ϕ is the

phase difference of the paired electron wave function across the junctions. [38]

The time evolution of the phase difference is given as

$$\frac{\partial\phi}{\partial t} = \frac{2e}{\hbar}V, \quad (1.7)$$

The critical current density is the maximum zero-voltage current density, and it is given by Ambegaokar and Baratoff expression: [41]

$$I_c = \frac{\pi}{4} \frac{2\Delta(T)}{eR_n} \tanh \frac{\Delta(T)}{2k_B T}, \quad (1.8)$$

where Δ is the superconducting band gap, R_n is the tunnel resistance when the junction is biased above its energy gap. Since it is the increase in quasiparticle currents that represents the incidence of phonons, the Josephson current must be suppressed for phonon detection with STJs. To achieve this suppression, a DC SQUID (Superconducting quantum interference device) is formed with two parallel junctions (with currents I_1 and I_2 flowing through each) and a magnetic flux is applied across the junction. The critical current is periodic with respect to the magnetic flux:[38, 39]

$$I_c(\Phi) = \sqrt{(I_1 - I_2)^2 + 4I_1I_2 \cos^2\left(\frac{\pi\Phi}{\Phi_0}\right)} \quad (1.9)$$

Φ is the total flux through the junction, and $\Phi_0 = \hbar/2e$ is the magnetic flux quantum (2.07×10^{-15} Wb). When the junctions are identical equation (1.9) reduces to

$$I_c(\Phi) = 2I_0 \left| \cos\left(\frac{\pi\Phi}{\Phi_0}\right) \right| \quad (1.10)$$

It is therefore important to fabricate junctions with identical areas for full Josephson current suppression.

The tunneling of quasiparticles (quasiparticle current) across the junction constitutes the desirable signal of the STJ for phonon transduction. In Figure 1.5, the

density of states diagram illustrates three different regions of the I-V curve.

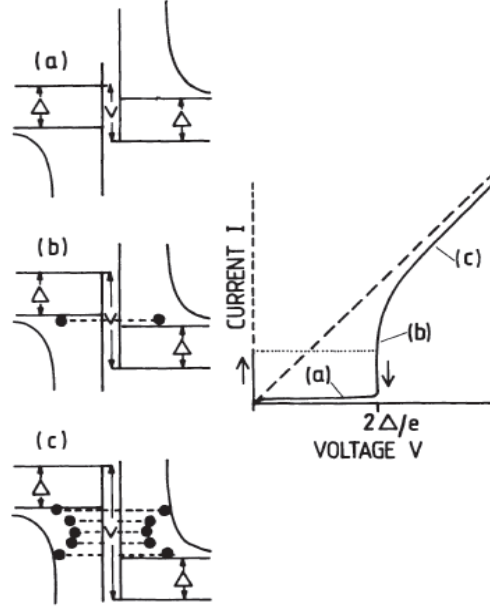


Figure 1.5: Density of state diagram for three typical voltages and resulting I-V characteristics of a superconducting tunnel junction. [34]

In region (a), the applied voltage is below the superconducting gap and no tunneling occurs at zero temperature. In region (b) the density of states is large on both sides of the junction, resulting in a steep rise in current. In region (c), the tunnel states increases linearly with applied voltage asymptoting towards a normal metal I-V characteristic. The tunneling current between two superconductors is obtained by considering the density of occupied and unoccupied states on either side: [38]

$$\begin{aligned}
 I_{ss} &= \frac{1}{eR_n} \int_{-\infty}^{\infty} N_{s1}(E' - eV) N_{s2}(E') [f(E' - eV) - f(E')] dE' \\
 &= \frac{1}{eR_n} \int_{-\infty}^{\infty} \frac{|E' - eV|}{\sqrt{(E' - eV)^2 - \Delta_1^2}} \frac{|E'|}{\sqrt{E'^2 - \Delta_2^2}} [f(E' - eV) - f(E')] dE' \quad (1.11)
 \end{aligned}$$

At finite temperature, the subgap current (i.e region (a) in Figure 1.5) is non-zero due to the presence of thermally excited quasiparticles. For STJs with identical superconductors, (such as Al-Al_xO_y-Al) and at sufficiently low temperature ($T \ll \Delta/k_B$), equation (1.11) is approximated by: [38]

$$I_{SS} = \frac{2}{eR_n} \exp\left(-\frac{\Delta}{k_B T}\right) \sqrt{\frac{2\Delta}{eV+2\Delta}} (eV + \Delta) \left(\sinh \frac{eV}{2k_B T}\right) K_0\left(\frac{eV}{2k_B T}\right) \quad (1.12)$$

where K_0 is the zeroth-order modified Bessel function. Equation (1.12) is utilized to calculate all quasiparticle densities in subsequent chapters. In Chapter 2, phonon emission and detection with STJ will be discussed.

1.5. Other Spectroscopic Phonon Detection Methods

Having discussed the basic physics of the active device in this thesis (the STJ), it is worth pointing out that there are several techniques for probing nanoscale heat transport in addition to STJ-based phonon spectroscopy. These include thermal conductivity measurements (discussed above), heat pulse measurements, scanning thermal microscopy, and time-domain thermoreflectance (TDTR). The phonon sources are either coherent or incoherent. Excellent literature reviews on phonon spectroscopy methods and nanoscale heat transport exist, [4, 42, 43] but it is important to highlight the distinguishing characteristics of STJ-phonon spectroscopy with these methods. In heat pulse measurement, the detectors are bolometric; hence, they absorb all incident phonons with no frequency selectivity as with the STJs. Scanning thermal microscopy requires specialized tips that measure the temperature of a surface; however, the temperature and spatial resolution are dependent on the size of the tip, size and shape of

the substrate features, and heat transfer between the tip and the substrate.[42] In the past decade, TDTR has gained broad appeal as a measurement technique of choice for nanoscale thermal transport.[42] It is therefore a worthy exercise to contrast TDTR and the tool of the trade in this thesis. We make such comparisons in Table 1.2.

Table 1.2: Comparison of STJ technique and prominent TDTR method

	Phonon Spectroscopy with STJ	Time-Domain Thermoreflectance
Phonon Emission	Decay of excited quasiparticle states	100 fs laser pulse causes thermoelastic expansion of metal (typically Al) film attached to sample
Polarizations generated	All polarizations (mostly transverse due to higher density of states)	Phonons originate as a pressure pulse in the Al film, so they are only longitudinal waves; other polarizations may be possible by applying laser pulse to specific metal film lattices or patterns
Detection	Excitation of quasiparticles in detector. Has a high-pass cutoff.	Stress or strain in Al film attached to surface changes the metal film's reflectivity due to changes in the electron gas.
Ease of use	Scalable method that requires attaching STJ to sample. Requires cryogenic methods and low noise electronics	Easy to use. Room temperature. Simple metal film deposition onto sample. Requires optics and lasers expertise.
Transport path geometry	Transmission typical; any geometry that can be microfabricated and for which the generator and detector can be attached at necessary places. Direct reflection to same spot	Reflection is most convenient because generation and detection can be focused at same spot through one set of optics. Transmission can be achieved but the optical alignment is challenging.

	not possible to measure.	
Spatial resolution	Limited mainly by fabrication methods. STJ generators of ~100 nm size and detector 'fingers' of < 50 nm size are feasible; careful control of geometry needed so that quasiparticle diffusion does not overwhelm these	Limited by laser spot size. 1 micron minimum possible; ~10 micron definitely demonstrated in literature (smaller may also be demonstrated in literature?)
Cost	~\$50,000	~\$160,000

Compiled by J.B Hertzberg

1.6. Electron Transport in Nanoparticle Films

In general, the study of collective excitations such as phonons is lagging behind studies of electrons, particularly in systems with complex interfaces (e.g. nanocrystal solids.) In nanoparticle films or nanocrystal arrays, periodicity arises from both the atomic lattice of individual particles as well as the arrays of particles stabilized by surfactant ligands as shown in Figure 1.6.[44-48] Nanocrystal arrays are solids with complex interfaces, and our understanding of phonon transport is lacking. However, in order to probe phonon transport in nanoparticle films, the films must be properly assembled and their electronic properties should be well characterized. To this end, using copper sulfide as a model system, a room-temperature solution-processed film assembly method was developed. Solution-processing of electronic and optoelectronic materials

has generated tremendous interest due to the low-cost and applicability of these materials for such applications as flexible and large area electronic devices. While several strategies for assembling electrically conducting nanoparticle-based films have been undertaken, the conductivities of such films are orders of magnitude less than their bulk counterparts, and often require high temperature processing. The work in this section of the thesis develops strategies for assembling electrically conductive nanoparticle films, as well as their electronic and structural characterization, with a forward-looking expectation that such films will be ideal for understanding phonon transport across complex interfaces with the microscale spectrometer.

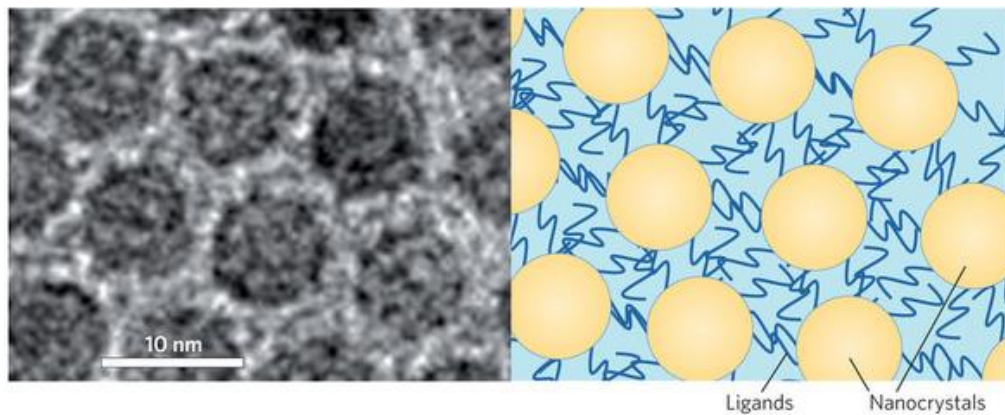


Figure 1.6: A Transmission electron micrograph and schematic illustration showing morphology of nanocrystal arrays. [44]

1.7. Hopping Conduction Mechanism

Charge transport mechanism in nanoparticle assemblies in the non-metallic regime show deviations from Arrhenius behavior. The observed conductivity versus temperature relationship is: [46, 48]

$$\sigma \approx \exp \left[- \left(\frac{T_0}{T} \right)^\nu \right] \quad (1.13)$$

where T_0 is a constant, and ν ranges from 0 to 1. $\nu = 1$ represents Arrhenius behavior, while fractional values of ν are indicative of variable-range hopping (VRH). This hopping-type conduction is a consequence of localized electronic states in the nanocrystals as compared to a band-like conduction in typical solids. As depicted in Figure 1.7, charge carriers from one localized site can generate current by acquiring thermal energy and hop to another site.[48, 49] The balance between nearest-neighbor hopping and hopping to sites with lower activation barriers, results in the fractional value of ν . $\nu = \frac{1}{2}$ typically describes Efros-Shklovskii VRH [50], while $\nu = 1/4$ describes Mott-VRH.[51]

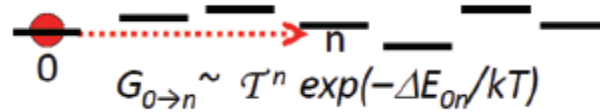


Figure 1.7: A cartoon depicting Variable-Range Hopping (in VRH, the conductance to a more distant state is favored because of the smaller activation energy).[49]

1.8.Thesis Outline

In Chapter 1, an overview of the main ingredients in this thesis (phonon transport in nanostructures, superconducting tunnel junctions, and electron transport in nanoparticles) is presented for a holistic understanding of subsequent chapters. The need for the development of spectroscopic techniques for understanding nanoscale phonon transport is established. To this end, this thesis (in Chapter 2) is focused on the development of a microscale phonon spectrometer utilizing STJs. The fabrication, operating principle, and characterization of the spectrometer are presented. Subsequent sections of this thesis focus on the utilization of the spectrometer to probe some of the important and unresolved questions on nanoscale phonon transport (surface scattering and phonon backscattering). Chapter 3 focuses on the utilization of the microscale spectrometer to directly probe surface scattering rates in monolithically integrated silicon nanosheets. In Chapter 4, an experiment that elucidates on the enhancement mechanisms of phonon backscattering is presented. In chapter 5, a study of assembly techniques and electronic transport in nanocrystal arrays, with the goal that the periodicity arising from the individual particles as well as their arrays could in the future be exploited for preliminary spectroscopic phonon studies of foreign materials. In Chapter 6, preliminary experiments demonstrating phonon interference in silicon oxide films and temperature dependent phonon spectroscopy, as well as proposed future experiments are discussed.

CHAPTER 2

2 DESIGN AND OPERATION OF A MICROFABRICATED PHONON SPECTROMETER UTILIZING SUPERCONDUCTING TUNNEL JUNCTIONS AS PHONON TRANSDUCERS[♦]

2.1. Abstract

In order to fully understand nanoscale heat transport it is necessary to spectrally characterize phonon transmission in nanostructures. Towards this goal we have developed a microfabricated phonon spectrometer. We utilize microfabricated superconducting tunnel junction-based (STJ) phonon transducers for the emission and detection of tunable, non-thermal, and spectrally resolved acoustic phonons, with frequencies ranging from ~ 100 to ~ 870 GHz, in silicon microstructures. We show that phonon spectroscopy with STJs offers a spectral resolution of ~ 15 - 20 GHz, which is ~ 20 times better than thermal conductance measurements, for probing nanoscale phonon transport. The STJs are Al-Al_xO_y-Al tunnel junctions and phonon emission and detection occurs via quasiparticle excitation and decay transitions that occur in the superconducting films. We elaborate on the design geometry and constraints of the spectrometer, the fabrication techniques, and the low-noise instrumentation that are essential for successful application of this technique for nanoscale phonon studies. We discuss the spectral distribution of phonons emitted by an STJ emitter and the efficiency

[♦] The content of this chapter was originally published as: O.O. Otelaja, J.B. Hertzberg, M. Aksit, and R.D. Robinson, "Design and Operation of a Microfabricated Phonon Spectrometer Utilizing Superconducting Tunnel Junctions as Phonon Transducers," *New J. Physics*, vol. 15, p. 43018, 2013. Reprinted with permission from the Institute of Physics.

of their detection by an STJ detector. We demonstrate that the phonons propagate ballistically through a silicon microstructure, and that submicron spatial resolution is realizable in a design such as ours. Spectrally resolved measurements of phonon transport in nanoscale structures and nanomaterials will further the engineering and exploitation of phonons, and thus have important ramifications for nanoscale thermal transport as well as the burgeoning field of nanophononics.

2.1.1. Importance of Nanoscale Phonon Spectroscopy

One of the grand challenges of nanoscience is to develop experimental tools to understand the fundamental science of heat flow at the nanoscale [52, 53]. In insulators and dielectrics, acoustic phonons are the dominant heat carriers [54], [4]. In nanostructures, as the sample's dimension or surface morphology becomes comparable to phonon characteristic lengths — wavelength, mean free path, and coherence length — the interactions of phonons with these structural features lead to regimes of phonon propagation in which the effect of confinement, scattering, and/or interference of phonons dominates heat transport [27], [2]. To probe these nanoscale effects on phonon transport, one needs a measurement technique that can precisely distinguish wavelength (or frequency) and position of the phonon modes. Previous studies have investigated the effects of nanoscale geometries on thermal transport using Joule-heated metal films on suspended structures [26], [30], [29], [24], [23], but because a thermal conductance measurement employs a broad spectral distribution of phonons, the frequency dependence of the phonon transport in such measurements is difficult to distinguish. Therefore, there is a strong need for a nanoscale technique that will spectroscopically

measure phonon transport at hypersonic (>1 GHz) frequencies — particularly at frequencies above 100 GHz which are most relevant to heat flow [55]. Such a technique will be apt for the development of the burgeoning field of nanophononics [3].

An ability to fully understand the propagation of phonons will inform the engineering and exploitation of nanostructures and nanomaterials. For instance, through careful phonon engineering the realization of more efficient thermoelectric materials and microelectronic coolers will be feasible [6, 24, 56]. Such phonon engineering strategies have been recently demonstrated with silicon phononic crystal structures, which displayed a reduction in phonon thermal conductivity in comparison to bulk crystals [28] [57]; however, the exact mechanism and frequency dependence of this reduction is not completely understood because diagnostic tools for nanoscale phonon spectroscopy were not available.

In this work we describe a new tool for nanoscale phonon spectroscopy using microfabricated superconducting tunnel junctions (STJs) – we detail its design and principle of operation, the fabrication techniques and challenges, the instrumentation and measurement procedures, and the results of selected phonon transport measurements. Phonon spectroscopy with STJs uses a narrow, non-thermal, and tunable frequency distribution of acoustic phonons to probe the phonon transport through nanostructures. STJ-based phonon spectroscopy has previously been performed extensively in macroscale samples by only a few research groups. [32, 33] [43, 58] However, with the development in recent years of advanced micro/nanofabrication techniques, the phonon spectrometer can now be fabricated at the microscale and offer exceptional spatial resolution. The microfabricated phonon

spectrometer has the advantage of probing nanoscale effects such as phonon confinement [54], end-coupling diffraction [59], and surface scattering [60], with submicron spatial resolution. We have recently demonstrated a prototype microfabricated spectrometer for emission and detection of non-equilibrium phonons with frequencies ranging from 0 to ~200 GHz [35], and have now tuned the phonon source (emitter) to emit phonons with frequency ranging from 0 to ~870 GHz. The spectrometer comprises a pair of aluminum-aluminum oxide-aluminum ($\text{Al-Al}_x\text{O}_y\text{-Al}$) superconducting tunnel junctions serving as phonon emitter and phonon detector on opposite sides of a silicon microstructure. The spectrometer measures the rate of phonons that propagate ballistically through the microstructure. Here we discuss in full detail the design, fabrication steps, required characterization, electronics, and measurement techniques involved in successfully realizing phonon spectroscopy with microscale STJ phonon transducers.

2.1.2. Spectrometer Design

The device design for each spectrometer consists of two STJ phonon transducers — one emitter and one detector — attached on opposite sides of a mesa that is monolithically etched on a silicon substrate (Figure 2.1a). The mesas, which are ~0.8 μm high and have widths ranging from 7 to 15 μm , allow for the isolation of a ballistic path for phonon propagation. The devices are fabricated on a 525 μm thick silicon (100) wafer and the mesa sidewalls are on the Si (111) plane. (Because the mean free path of phonons at our experimental temperature and frequencies is $\gg 1$ mm [61], the detected phonons will also include phonons that backscatter from the bottom of the substrate.)

The ballistic path along the $\langle 110 \rangle$ direction between emitter and detector may be blocked by etching a trench into the mesa in order to determine this contribution of backscattered phonons [35]. This phonon transport measurement platform also enables the monolithic integration of nanostructures into the mesa. Microfabrication methods make the experiments very scalable – spectrometers are fabricated in lots of 100 on 100 mm Si wafers. Each 4.5 mm square chip contains up to 6 spectrometers, as shown in Figure 2.1b.

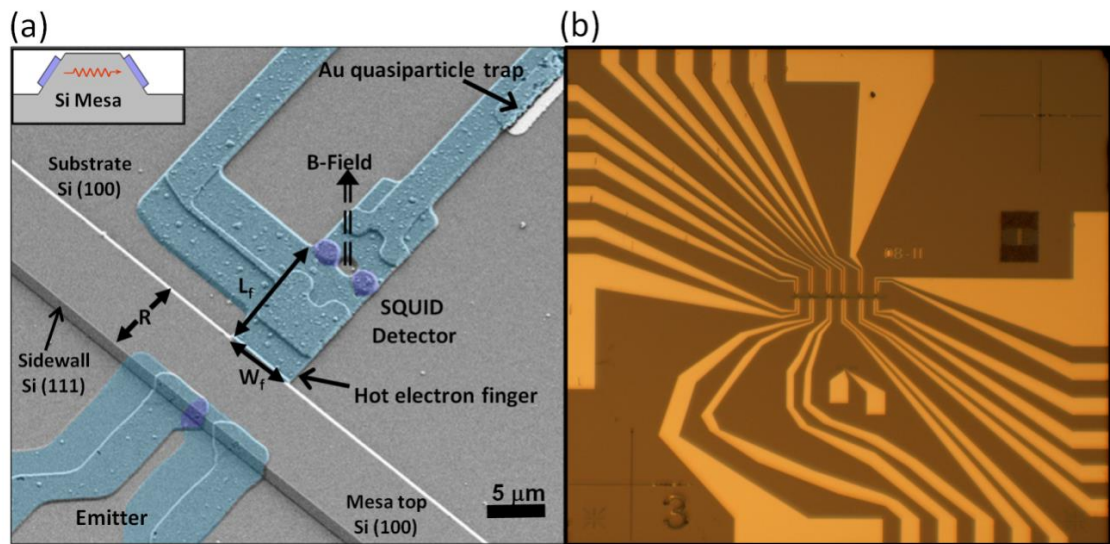


Figure 2.1: (a) False-colored SEM micrograph of completed phonon spectrometer. The STJ emitter is fabricated with the tunnel junction lying mostly on the sidewall of the $0.8 \mu\text{m}$ high mesa structure. The width of the mesa, $R = 7, 10$ or $15 \mu\text{m}$. The mesa structure isolates a ballistic path for phonon transport between emitter and detector. The detector is fabricated in double-junction SQUID geometry with a hot electron finger for the collection of ballistically propagating phonons. Finger widths, W_f , were varied ($1.5, 2, 3$ or $6 \mu\text{m}$) to observe the effects of geometry on phonon transmission. Magnetic field

~ 1 G is applied perpendicular to the SQUID detector for Josephson current suppression. $0.5 \mu\text{m}$ thick silver film is deposited on the backside of the $500 \mu\text{m}$ thick silicon substrate to reduce phonon backscattering from the bottom of the substrate. (inset is a schematic of the side view of a silicon mesa with phonon transducers). (b) Optical microscope image of 4.5 square mm device comprising six spectrometers.

The phonon emitter is a single Al-Al_xO_y-Al tunnel junction with the majority of the junction area lying on the sidewall of the mesa. The aluminum films are designed to be thin enough (<100 nm) to ensure that the decay length of the phonons is greater than the film thickness in order to minimize phonon reabsorption (emitted phonons breaking quasiparticles within the emitter film) [62]. As will be described, we isolate narrow bands of phonon energy by modulation of the emitter voltage. Emitter junction resistance should therefore be made low enough to maximize the amount of current (and therefore phonon signal) flowing at a given modulation amplitude, while the resistance must also be large enough to inhibit overinjection of electrons through the tunnel barrier into the Al film. Such overinjection may locally suppress the superconducting gap and thereby degrade energy resolution [63]. Residual inhomogeneities in the gap are inherent in the film and may be assessed from an I-V curve of the junction. Typically we use emitters having junction resistances from ~ 800 to $\sim 5000 \Omega$, and we observe an inhomogeneity of about ~ 60 to $\sim 80 \mu\text{eV}$ (~ 15 to ~ 20 GHz) which represents the upper limit of our energy resolution.

The detector is designed to have a double-junction (SQUID geometry) with a ‘hot electron finger’ extending onto the mesa sidewall to capture the incident phonons.

The actual detector junctions lie on the (100) plane of the silicon substrate. The SQUID geometry enables the suppression of Josephson current via the application of a magnetic field. With the Josephson current suppressed, we can readily distinguish an incident phonon flux as an increase in the ‘subgap’ tunnel current due to the incident phonons breaking Cooper pairs in the Al. Incident phonons of energy $\geq 2\Delta_d$ break Cooper pairs in the aluminum film of the detector finger, and the excited quasiparticles diffuse to the junctions and tunnel through the oxide barrier. Some of the detectors have quasiparticle traps made from thin Au films. These traps are designed to ensure that excess quasiparticle energies do not reach the junction, and they also prevent back tunneling of quasiparticles [64]. When we change the length of the detector fingers, L_f , from 10 μm to 20 μm (Figure 2.1a), we found no discernible difference in the detected phonon transmission signal levels. We conclude from this that the quasiparticle diffusion length is much longer than the finger length, a conclusion that agrees with diffusion lengths reported in the literature [65]. The tunnel junction therefore faithfully measures the rate of phonon arrival at the tip of the finger several microns distant. Forming the double-junctions on the flat Si (100) plane reduces their asymmetry, therefore facilitating Josephson-current suppression, simplifies fabrication, and offers great flexibility in spatial resolution to be achieved merely by changing the width and position of the finger [35].

2.2. Principles of Operation

2.2.1. Phonon Emission with STJ

Phonon emission in STJs occurs via the excitation and decay of quasiparticles (single electrons) in superconducting films. As depicted in Figure 2.2a,b, when the emitter STJ is biased above the superconducting gap ($2\Delta_e$) such that $V_e \geq 2\Delta_e/e$ ($V_e = I_e R_n$, where I_e , V_e , and R_n are the current through, voltage across, and normal state tunneling resistance of the emitter junction respectively), the Cooper pairs (paired electrons) in the first aluminum film break apart and quasiparticles tunnel through the oxide barrier into excited energy states ranging from Δ_e to $eV_e - \Delta_e$ (all energies referenced to the Fermi level in the aluminum film at the opposing side of the junction) [32, 33]. The Al emitters in our experiments have $2\Delta_e$ of ~ 400 μeV at a temperature of ~ 0.3 K. These excited quasiparticles rapidly decay towards the edge of the superconducting gap, emitting phonons as they decay. Due to the singularity in the density of states at the gap edge, this ‘relaxation’ process typically requires only one or two decay steps before the quasiparticle energy is reduced to Δ_e . This process thus emits a broad distribution of phonons of energies ranging from 0 to $eV_e - 2\Delta_e$. The phonons are incoherent and to a first approximation will have both random polarization and random direction due to elastic scattering of the tunneled electrons within the Al film. The shape of this ‘relaxation’ phonon distribution includes a sharp cutoff at energy $eV_e - 2\Delta_e$, thus allowing a small modulation of V_e to isolate a narrow portion of the spectrum that is sharply peaked at energy $eV_e - 2\Delta_e$.

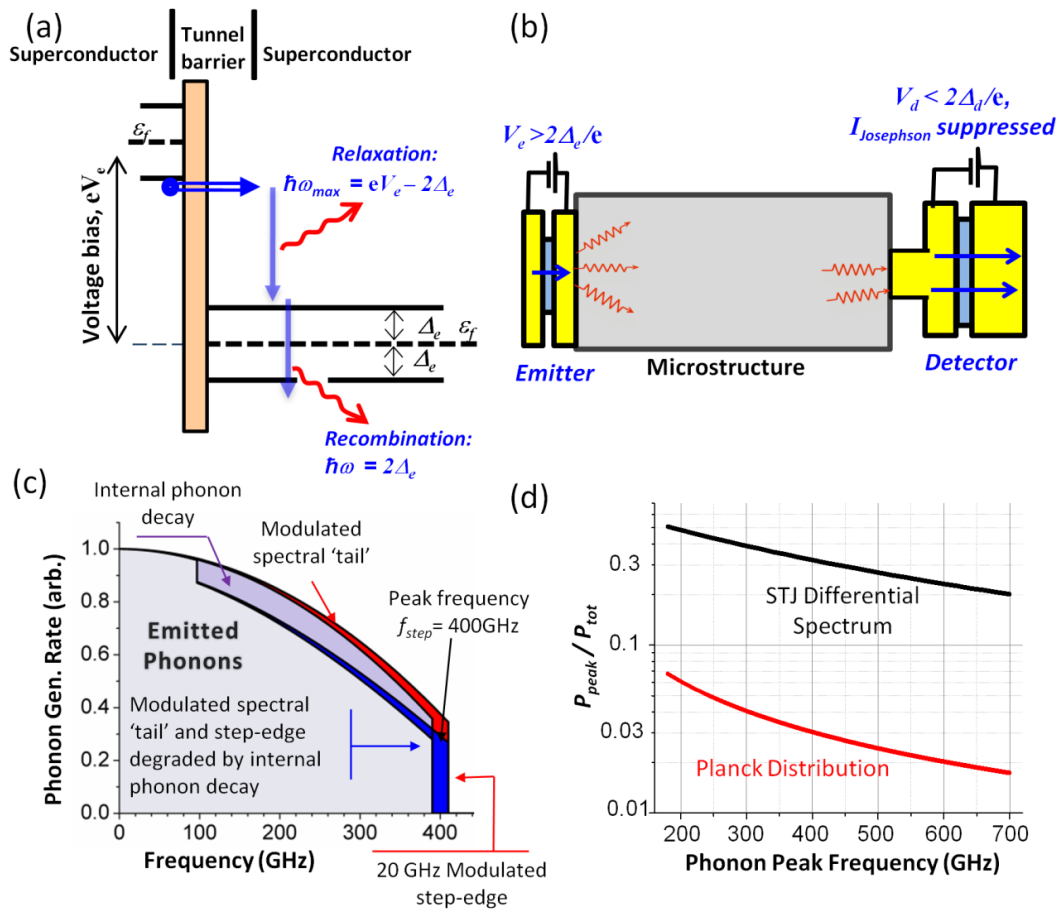


Figure 2.2: Phonon emission principles and emission spectrum. (a) Energy diagram illustrating phonon emission with superconducting tunnel junctions. (b) Schematic diagram of the microfabricated phonon spectrometer. The diagram shows the emitter STJ on the left is biased above its superconducting gap ($2\Delta_e$) leading to phonon emission into the microstructure. The STJ detector on the right, which is biased below its superconducting gap and has its Josephson current suppressed, detects incident phonons with energy greater than $2\Delta_d$. The detector will capture incident phonons within the solid angle subtended by the detector finger with respect to the emitter. (c) Calculation of approximate phonon spectrum due to first-step relaxation of tunneled electrons, for a typical Al emitter STJ biased at ~ 2.1 mV to produce peak frequency

$(eV_e - 2\Delta_e)/h = 400$ GHz and peak width $\delta\omega/2\pi = 20$ GHz. Differential portion of the spectrum produced by modulation is shaded red. Following phonon attenuation within the Al, remaining differential spectrum is shaded in dark blue (partially obscuring red-shaded area). (d) Calculation of P_{peak}/P_{tot} for phonon spectrum emitted by quasiparticle relaxation in typical STJ emitter, found by integrating spectrum from part (c) and adding contributions of 2nd-step quasiparticle relaxation, quasiparticle recombination, and phonon reabsorption/reemission. For comparison, we calculate also P_{peak}/P_{tot} of Planck distribution for a slice of width $\delta\omega/2\pi = 20$ GHz around the dominant phonon frequency.

Subsequent recombination of the quasiparticles into Cooper pairs lead to the emission of recombination phonons of energy $2\Delta_e$. The average relaxation τ_{rel} and recombination τ_{rec} times are on the order of ~ 1 ns and 30 μ s respectively [66]. When the STJ emitters are attached to one end of a microstructure, relaxation and recombination phonons — both longitudinal and transverse polarizations — are emitted and ballistically propagate through the microstructure; however, only the relaxation phonons are controlled by modulation techniques for spectroscopic studies.

2.2.2. Modeling the Phonon Emission Spectrum

When considering spectral precision of a phonon source, a convenient figure of merit is the ratio P_{peak}/P_{tot} of phonon power near the peak of the distribution, to the total power

in the measurement. For instance, a thermal conductance measurement at temperature T employs a Planck's distribution of phonon modes, having power spectral density $P(\omega)d\omega \sim \frac{\hbar\omega^3 d\omega}{2\pi^2 v^3} / (e^{\hbar\omega/k_B T} - 1)$, where ω is the angular frequency of the phonon and v is the phonon speed. This distribution is peaked at the so-called 'dominant phonon frequency' $\omega_{dom} = 2.78k_B T/\hbar$, but the distribution is quite broad and therefore a slice of spectrum within $\delta\omega$ around the peak contains only a small fraction of the total power. For instance, if we wish to interrogate a spectral feature at 400 GHz with 20 GHz precision, a Planck distribution at $T = 6.9$ K offers $\omega_{dom}/2\pi = 400$ GHz but contains only 3% of its power within +/-10 GHz of this peak.

To model the phonon emission profile of the modulated STJ phonon spectrum and to estimate P_{peak}/P_{tot} of this distribution, we must carefully consider the non-equilibrium electron-phonon interactions within the superconducting film in the emitter STJ. These include phonon attenuation due to Cooper-pair breakage [62, 66, 67] and acoustic-mismatch transmission across the Al/Si boundary [68] as well as quasiparticle diffusion and reemission of absorbed phonons. The total emitted phonon power resulting from the quasiparticle relaxation process will comprise the phonons emitted in first-step relaxation, plus any emitted in second-step relaxation, minus the fraction reabsorbed by Cooper pair breakage within the aluminum, plus the power that is reemitted following this reabsorption processes.

For voltages V_e not greatly exceeding $2\Delta_e$, nearly all injected quasiparticles decay to energy Δ_e , so that first-step relaxation dominates, the entire modulated spectral power falls at frequency $(eV_e - 2\Delta_e)/\hbar$, and if we neglect the effect of reabsorption

then $\frac{P_{peak}}{P_{tot}} \cong 1$ [33]. For higher bias voltages, a fraction of the quasiparticles will relax first to intermediate energies before undergoing secondary relaxation to the band edge energy Δ_e . The precise distribution of generated phonon energies may be found by convolution integral of the quasiparticle injection rates, densities of states and decay rates [66, 69]. For simplicity, we will assume that the phonon density of states in the Al follows a Debye model, and adopt an approximate model of phonon production rate, presented by Eisenmenger et al., based on the spectrum of phonons emitted by first-step relaxation of electrons injected across a normal-state tunnel junction of resistance R_n at $T = 0$ [66, 70].

$$\dot{N}_e(\omega)d\omega = \frac{3}{e^2 R_n} \left(1 - \left(\frac{\hbar\omega}{eV_e} \right)^2 \right) d\omega \quad (2.1)$$

This rate of phonon production per unit bandwidth $\dot{N}_e(\omega)$ is shown in figure 2c, and extends from $\omega = 0$ to a sharp cutoff at $\omega = (eV_e - 2\Delta_e)/\hbar$. This is a good approximation for voltages $eV_e \gg 2\Delta_e$ [66, 70]. It is evident from the shape of this distribution that a portion of the differential phonon power is produced at the peak $\hbar\omega = (eV_e - 2\Delta_e)$ while the remainder is produced at energies broadly distributed over the range 0 to $eV_e - 2\Delta_e$. The power spectral density $P(\omega)d\omega$ may be found from equation (2.1) as $P(\omega)d\omega = \hbar\omega\dot{N}_e(\omega)d\omega$. Second-step relaxation may add up to 25% additional phonon power, mostly at frequencies well below the cutoff at $(eV_e - 2\Delta_e)/\hbar$ [66].

We must also consider reabsorption and reemission of phonon energy. Attenuation of the phonon population within the superconductor will occur as phonons of energy $\hbar\omega > 2\Delta_e$ break Cooper pairs, creating fresh quasiparticles. The probability

that a phonon will survive traveling a distance r within the aluminum is $e^{-r/\Lambda_{ph}}$, the mean absorption length of $\Lambda_{ph}(\omega)$ being dependent on phonon energy $\hbar\omega$ and band gap energy Δ_e [66]. If we treat the phonons as point-particles traveling ballistically within the Al, then the probability of a phonon generated at a distance z from the Al/Si interface and traveling at an angle θ to the normal, to escape into the Si before reabsorption is [66, 71]

$$e^{-z/(\Lambda_{ph}\cos\theta)}T_{AlSi}(\theta). \quad (2.2)$$

Here $T_{AlSi}(\theta)$ is an acoustic-mismatch transmission factor for wave transmission from Al into Si. The films of some of our emitter STJs have lower and upper layer thicknesses of ~ 20 nm and ~ 79 nm respectively on the mesa sidewall (as determined by profilometry measurement and adjusted for sidewall angle). For simplicity, we treat all phonons as being generated within the lower layer at a spatially uniform rate. We assume the phonons' velocities are distributed uniformly in all directions, and that those entering the top layer may reflect from the Al/vacuum boundary, reenter the lower layer, and reach the Al/Si boundary. For phonons to emerge and travel directly across the mesa towards the detector (an angle ~ 35.3 degrees to the sidewall normal), we estimate the refraction angle within the Al using Snell's law, assuming average wave speeds $\overline{v_{Al}} = 4.4 \times 10^3$ in Al and $\overline{v_{Si}} = 6.6 \times 10^3$ m/s in Si, to be $\theta \sim 22.7^\circ$. From reported values of the acoustic impedances of Al and Si, we estimate T_{AlSi} to be > 0.9 for such an angle and to be frequency-independent [2, 66]. Kaplan et al. have calculated values for phonon decay time in Al as a function of phonon energy $\hbar\omega$ and bandgap energy Δ_e [62]. We multiply these by $\overline{v_{Al}}$ to find $\Lambda_{ph}(100 \text{ GHz}) \cong 1.04 \mu\text{m}$,

$\Lambda_{ph}(400 \text{ GHz}) \cong 0.38 \text{ } \mu\text{m}$ and $\Lambda_{ph}(700 \text{ GHz}) \cong 0.22 \text{ } \mu\text{m}$. While these values are greater than some reported experimental values of Λ_{ph} in Al at energy $\hbar\omega = 2\Delta_e$, they are comparable to measured values of normal-state acoustic attenuation corrected to the [66-68, 71-73] superconducting state. Averaging equation (2.2) over our full Al layer thicknesses, we estimate that in the direction pointing out towards the detector, ~90% of phonons at $\omega/2\pi = 100 \text{ GHz}$ will escape into the Si, ~78% at $\omega/2\pi = 400 \text{ GHz}$ and ~68% at $\omega/2\pi = 700 \text{ GHz}$. We use these attenuation factors to modify the spectrum in equation (2.1), as shown in Figure 2.2c.

To find the total rate of absorbed phonons, we must average equation (2.2) over all depths and angles. At large values of θ we note that $T_{AlSi}(\theta)$ will be $\ll 1$, regardless of phonon frequency, and for angles above about 45 degrees, $T_{AlSi}(\theta)$ will be zero due to total internal reflection within the Al [66, 68]. Transmission coefficients $\langle T_{AlSi} \rangle$ averaged over all angles and phonon polarizations have been calculated by Kaplan, from which we estimate $\langle T_{AlSi} \rangle \sim 0.44$ assuming the three phonon polarizations to be equally populated [68]. Thus at any frequency $\omega > 2\Delta_e/\hbar$, at least 56% of all phonons produced are liable to be reabsorbed within the Al. We can approximate the additional frequency-dependency by multiplying this $\langle T_{AlSi} \rangle$ by the average of equation (2.2) over the full Al layer thickness and all angles less than the critical angle. Therefore among all phonons at all angles we estimate that ~61% are reabsorbed at $\omega/2\pi = 100 \text{ GHz}$, ~67% at $\omega/2\pi = 400 \text{ GHz}$, and ~71% at $\omega/2\pi = 700 \text{ GHz}$. For each bias voltage V_e , we apply these proportions to the spectrum of equation (2.1) and integrate to find the total reabsorbed power.

By conservation of energy, all of this reabsorbed power must be reemitted. The

quasiparticles created in the reabsorption subsequently relax and recombine to emit additional phonons of lower frequency than the ones initially absorbed. We estimate based on typical decay times and on the geometry of our STJ on the mesa sidewall that the quasiparticles do not travel far prior to reemission, so that about 80% of the power is reemitted at the same or nearby location as the original tunneling injection in the Al film on the mesa sidewall.

Taking together first-step relaxation, second-step relaxation (constituting up to ~25% of the total relaxation phonon power), attenuation, and reabsorbed/reemitted power, we find that for typical V_e values of up to a few mV, the total modulated power P_{tot} emitted from the emitter STJ is roughly proportional to the modulated emitter current δI_e . The power emitted due to recombination on the other hand (Figure 2.2a) should remain fixed as V_e is varied, and for large V_e we take this to be a negligibly small fraction of the total power. Therefore the total emitted differential phonon rate is $\sim \delta I_e/e$.

To find P_{peak}/P_{tot} at a given peak frequency ω_{peak} , we take $P(\omega_{peak})\delta\omega$ from equation (2.1), for a given peak width $\delta\omega$ (e.g. $\delta\omega/2\pi = 20\text{GHz}$), attenuate this quantity according to equation (2.2) as described above, and divide by the total power P_{tot} found as described above at $V_e = (\hbar\omega_{peak} + 2\Delta_e)/e$. The result of this calculation for our typical emitter film thicknesses appears in Figure 2.2d. For a peak width $\delta\omega/2\pi = 20$ GHz, at a peak frequency of $\omega/2\pi = 100$ GHz, P_{peak}/P_{tot} is ~50%. This diminishes to ~32% at peak $\omega/2\pi = 400$ GHz, and further at higher peak frequencies. As shown in Figure 2.2d, the values of P_{peak}/P_{tot} from the STJ-emitted

phonon spectrum compare very favorably to a Planck distribution, exceeding it by more than an order of magnitude for $\omega/2\pi > 300$ GHz. This analysis demonstrates that aluminum STJs made of films a few tens of nm thick will emit narrow spectral distributions of acoustic phonons into Si at frequencies up to several hundred GHz.

Phonon emission from aluminum STJs has been reported elsewhere at frequencies up to ~ 2 THz, but P_{peak}/P_{tot} is likely to be very small at such a peak frequency even if the films are made very thin [74]. The wavelength in Al at 700 GHz is ~ 6 nm while the granularity in the Al film and the roughness at the Al/Si interface are most likely a few nm; hence, for $\omega/2\pi$ above ~ 700 GHz, we expect to see the spectrum further modified by the effects of elastic scattering of phonons within the Al film [71], inelastic phonon scattering at the Al/Si boundary [75] and modification of phonon spectra due to excess injected quasiparticle population in the Al film [63]. All such effects are liable to become more severe as V_e and ω are increased.

2.2.3. Phonon Detection with STJ

The phonons incident on the detector are registered as an increase in the tunnel current through the detector junctions. The STJ detector is biased below its superconducting gap with voltage $V_d < 2\Delta_d/e$ (Figure 2.2b). Phonons incident on the detector finger with energy greater than or equal to $2\Delta_d$ will break Cooper pairs in the detector films, and the quasiparticles will diffuse until a portion reaches the detector junction and tunnel through. The STJ detectors are made from aluminum films with superconducting gap $2\Delta_d \sim 360$ μeV (corresponding to ~ 90 GHz), and in essence these detectors act as high

pass filters of acoustic phonons with cut-off frequency ~ 90 GHz. A lock-in detector selects only the modulated portion δI_d of the detector current, corresponding to the modulated emitter phonons that strike the detector. The phonon spectrum therefore comprises phonons of frequencies between ~ 90 GHz and $(eV_e - 2\Delta_e)/h$, with a sharp peak at frequency $(eV_e - 2\Delta_e)/h$. Because the modulated emitter phonon power is proportional to δI_e , the measured differential transfer function $\delta I_d/\delta I_e$ tells us the fraction of this spectrum that is transmitted from emitter through the sample to the detector.

2.2.4. Modeling the Detector Behavior

We may use quasiparticle-phonon interactions to model and quantify the phonon detector behavior. For a differential rate $\dot{n}_{ph,d}$ of phonons of frequency ω striking the detector finger, we expect the average differential rate of phonon-induced quasiparticle generation $\dot{n}_{QP,ph}$ to be

$$\begin{aligned}
 \dot{n}_{QP,ph} &= 0 && \text{for } \hbar\omega < 2\Delta_d \\
 \dot{n}_{QP,ph} &= T_{SiAl} \cdot \alpha_{abs}(\omega) \cdot 2\dot{n}_{ph,d}(\omega) && \text{for } 2\Delta_d \leq \hbar\omega < 4\Delta_d \\
 \dot{n}_{QP,ph} &= T_{SiAl} \cdot \alpha_{abs}(\omega) \cdot 2 \left(\frac{\hbar\omega}{2\Delta_d} - 1 \right) \dot{n}_{ph,d}(\omega) && \text{for } \hbar\omega \geq 4\Delta_d
 \end{aligned} \tag{2.3}$$

In equations (2.3), T_{SiAl} is the acoustic transmission factor for phonons transiting from Si into Al, which we estimate from acoustic impedances to be >0.9 over all incidence angles. [68] The fraction of phonons $\alpha_{abs}(\omega)$ absorbed in the finger will be approximately $\alpha_{abs}(\omega) = 1 - e^{-2d/\Lambda_{ph}(\omega)}$. In our detector fingers, the thickness d in

the direction of phonon incidence is 140 to 205 nm, thus we expect $\alpha_{abs}(\omega)$ to equal at least 0.2 for $\omega/2\pi = 100$ GHz, and at least 0.8 for $\omega/2\pi = 700$ GHz. In our devices, the diminishing fraction P_{peak}/P_{tot} as peak frequency is increased (Figure 2.2d) motivates us to treat α_{abs} as independent of peak frequency and having value $\alpha_{abs} \sim 0.25$. In the signal of a typical spectrometer transmitting through bulk Si, we see a modulated signal that is consistent with this assumption and with the detector response behavior of equations (2.3).

To find $\dot{n}_{QP,ph}$ and thereby the phonon arrival rate $\dot{n}_{ph,d}$ from the measured differential detector tunnel current δI_d , we must account for quasiparticle loss processes in the detector. The primary loss process comprises diffusion of the quasiparticles into the attached wiring leads, followed by recombination into Cooper pairs [66, 76, 77]. Using conventional theories of tunneling rate and quasiparticle recombination, we may express a nondimensional efficiency factor $\{\text{Eff}\} = \delta I / e\dot{n}_{QP,ph}$ for each detector [66, 75, 77]:

$$\{\text{Eff}\} = \sqrt{\frac{\tau_{rec}}{D}} \cdot \frac{1.15}{2e^2 R_n N_0 W_{tr} d_{tr}} \quad (2.4)$$

where R_n is the normal-state tunneling resistance of the junction, N_0 is the normal density of states at the Fermi level ($1.75 \times 10^{10} \cdot \mu\text{m}^{-3} \text{eV}^{-1}$ in Al) [66], and W_{tr} and d_{tr} are respectively the average total width and thickness of the wiring trace connected to the detector STJ. The factor $D \cong 20 \text{ cm}^2/\text{s}$ is the diffusion constant for quasiparticles in Al, and $\tau_{rec} \sim 30 \mu\text{s}$ is the average quasiparticle recombination time in Al at a temperature of 0.3 K [66, 78, 79] [65, 76]. In our detectors $\{\text{Eff}\}$ is typically ~ 0.1 .

2.2.5. Estimation of the Detector Efficiency

The measured differential tunnel current δI in our detector will be proportional to the change in nearby quasiparticle density N_{QP} [66, 75, 77]

$$\delta I = \frac{1}{2eR_n} \frac{\delta N_{QP}}{N_0} \frac{eV + \Delta_d}{\sqrt{(eV + \Delta_d)^2 - \Delta_d^2}} \quad (2.5)$$

where R_n is the normal-state tunneling resistance of the junction, N_0 is the normal density of states at the Fermi level ($1.75 \times 10^{10} \cdot \mu\text{m}^{-3} eV^{-1}$ in Al), and the last factor reduces to 1.15 at our detector bias voltage $V = \Delta_d/e$ [66]. Equation (2.3) presents the differential rate of quasiparticle generation $\dot{n}_{QP,ph}$ as a function of differential rate $\dot{n}_{ph,d}$ of phonons incident on the detector. From this $\dot{n}_{QP,ph}$, we can determine the differential change in quasiparticle density δN_{QP} by the steady-state assumption that the rate of quasiparticles generated must balance all quasiparticle loss rates. The primary loss process comprises diffusion of the quasiparticles into the attached wiring leads, followed by recombination into Cooper pairs [76]. We will assume that the tunneling itself does not contribute significantly to quasiparticle loss. For quasiparticles diffusing into a volume vol , the recombination loss rate is [66, 77]

$$\dot{n}_{QP,rec} = -\delta N_{QP} \cdot vol / \tau_{rec} . \quad (2.6)$$

The recombination time τ_{rec} is strongly sensitive to the total quasiparticle density $N_{QP} = N_{QP,th} + N_{QP,DC} + \delta N_{QP}$, where $N_{QP,th}$ is the thermally-activated quasiparticle density, $N_{QP,DC}$ is the quasiparticle density due to the full rate of incident phonons and δN_{QP} is due to modulated incident phonons. However, as long as $N_{QP,DC} +$

$\delta N_{QP} \ll N_{QP,th}$, we may treat τ_{rec} as constant [80]. At a temperature of 0.3K, τ_{rec} is roughly 30 μs [66, 78, 79]. To check the dependence of detector response on N_{QP} , we repeated one of our spectral measurements at a temperature of 0.36 K, at which I_d was 3 times its value at 0.3K. We found that the detector response was degraded by only $\sim 10\%$ compared to the 0.3 K measurements. Thus, we expect that restricting I_d to only 1.5 times its unperturbed (thermal) value should maintain the condition $N_{QP,DC} + \delta N_{QP} \ll N_{QP,th}$, and therefore maintain a consistent detector sensitivity. We note that the $\sim 10\%$ reduction upon raising the temperature to 0.36K is less than what would be predicted by the theory of Rothwarf and Taylor [80], suggesting that in our devices τ_{rec} is less temperature-dependent than this theory. One possible explanation is that magnetic flux trapped in the Al detector film contributes to the quasiparticle recombination rate in our detectors [77]. In some cases, cycling our devices above T_c resulted in variations of a few percent in the measured phonon transmission signal, which is consistent with the presence of detector efficiency variations due to trapped flux.

In considering $\dot{n}_{QP,rec}$, the volume vol primarily comprises the wiring trace attached to the finger, so we have $vol \cong W_{tr} \cdot d_{tr} \cdot \sqrt{D \cdot \tau_{rec}}$, where W_{tr} and d_{tr} are respectively the average total width and thickness of the trace, which in our devices are respectively 3.2 μm and 530 to 580 nm, and $\sqrt{D \cdot \tau_{rec}}$ is the diffusion length of the quasiparticles. For diffusion constant $D = 20 \text{ cm}^2/\text{s}$, this length is $\sim 250 \mu\text{m}$ [65, 76]. Thus the recombination rate found from equation (2.6) is $\dot{n}_{QP,rec} = -\delta N_{QP} \cdot W_{tr} \cdot d_{tr} \cdot \sqrt{D/\tau_{rec}}$. In steady-state we take the total rate of change of quasiparticle density to be

zero, thus $\dot{n}_{QP,ph} + \dot{n}_{QP,rec} = 0$, and we find

$$\delta N_{QP} = \dot{n}_{QP,ph} \cdot \sqrt{\frac{\tau_{rec}}{D}} \cdot \frac{1}{(W_{tr} \cdot d_{tr})} \quad (2.7)$$

Thus the tunnel current may be related to the rate of quasiparticle generation by incident phonons found from equation (2.3:

$$\delta I = \sqrt{\frac{\tau_{rec}}{D}} \cdot \frac{1.15}{2eR_n N_0 W_{tr} d_{tr}} \cdot \dot{n}_{QP,ph} \quad (2.8)$$

From equation (2.8) we may define the nondimensional efficiency factor {Eff} for each detector as the ratio of measurable current δI to charge production rate $e\dot{n}_{QP,ph}$:

$$\{\text{Eff}\} = \sqrt{\frac{\tau_{rec}}{D}} \cdot \frac{1.15}{2e^2 R_n N_0 W_{tr} d_{tr}} \quad (2.9)$$

We note that the relatively large magnitude of quasiparticle diffusion length $\sqrt{D \cdot \tau_{rec}}$ (of order 100 μm) means that phonons reflected from the bottom of the Si chip and striking the wiring leads very far from the junction or the mesa may generate quasiparticles that register as a tunneling current at the detector STJ, therefore contributing to the measured backscatter signal level. It is interesting to think about whether we could reduce or eliminate the measured background level (which represents a source of experimental uncertainty) by redesign of the detector or wiring traces. However, we note from equations (2.5) to (2.9) that changes in the wiring trace dimensions may not achieve this goal: if we reduce the width W_{tr} of the wiring traces in order to diminish the intercepted phonon flux, we also reduce the volume *vol*

occupied by the quasiparticles and thereby increase the tunneling efficiency {Eff} for both the quasiparticles formed in the finger and those formed in the leads.

2.3. Fabrication Techniques and Challenges

Figure 2.3a illustrates the step-by-step fabrication of the mesas and transducers. The mesas are formed by a shallow depth anisotropic etching of silicon using KOH (50% KOH, 48 °C, 4 min.) with a low-stress silicon nitride etch mask. We found that standard RCA cleaning of the wafers prior to etching is crucial to obtaining smooth surfaces. The smoothness of the (100) and (111) planes is necessary to enable deposition of continuous Al films, and to minimize phonon scattering from rough surfaces. Simultaneous magnetic stirring and ultrasonication during the KOH etch helps to improve the smoothness of the etched surfaces. The trenches are simultaneously formed, where needed, on the mesas. Neither hydrochloric acid nor surfactants was added.

We fabricate the emitter tunnel junctions on the sidewall of the mesa using double-angle evaporation as shown in Figure 2.3b. A bilayer of S1818 photoresist (Rohm and Haas Inc.) and LOR lift-off resist (Microchem Inc.) is spun onto the fabricated mesas and the emitter geometry, wiring trace and bond pads are photolithographically patterned into the resist. The depth of field of our photolithography tool ($\pm 2.42 \mu\text{m}$) limits the range of mesa heights and resists thickness used to form the junctions.

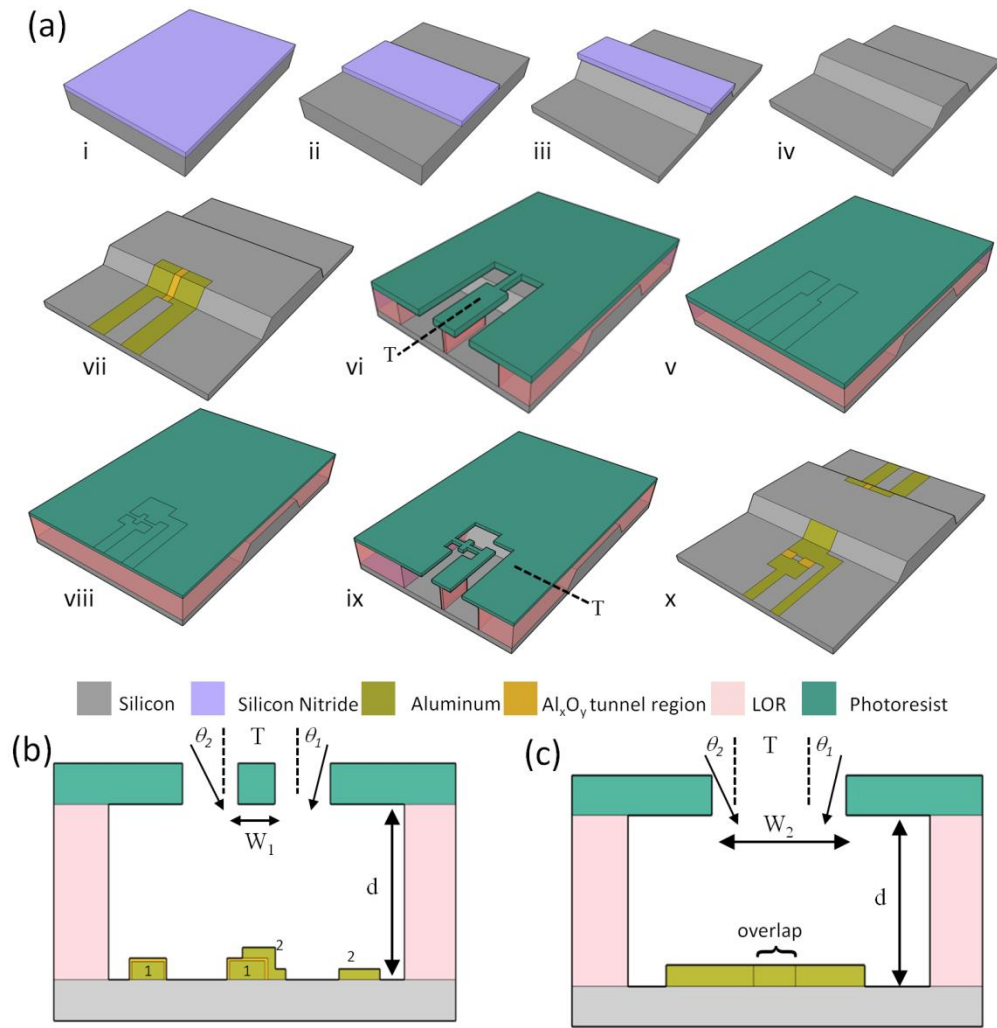


Figure 2.3: Spectrometer fabrication. (a) Schematic of fabrication steps for STJ phonon transducers and mesas (steps i-x). (i) Low stress silicon nitride (~ 80 nm) grown on a silicon substrate (ii) Silicon nitride etched with CHF_3/O_2 to define mesa (iii) Anisotropic etching in KOH masked by Si_xN_y (iv) Nitride etched in BOE (v) Bilayer of LOR and photoresist spun on mesas and emitter pattern and wiring trace is exposed on the top resist layer (vi) Exposed pattern developed, forming resist bridge across mesa sidewall (vii) Double angle evaporation and oxidation of aluminum followed by lift-off. Tilt axis (T) is indicated (viii) Bilayer of LOR and photoresist is re-spun and detector is patterned

(ix) Detector pattern is developed forming Dolan bridges. Tilt axis (T) is indicated (x) Double angle evaporation and oxidation of detector film shown after lift-off. (b) Schematic diagram of double-angle evaporation. T indicates the tilt axis pointing into the page. θ_1 and θ_2 are the first and second deposition angles forming aluminum films numbered 1 and 2. First film is oxidized (orange colored region) before the second evaporation. The junction overlap width = $d \cdot (\tan\theta_1 + \tan\theta_2) - W_1$. (c) Schematic of overlapping films of the wiring traces with overlap width = $W_2 - d \cdot (\tan\theta_1 + \tan\theta_2)$. W_2 should be made wide enough to ensure overlap.

The patterned resist is developed in AZ MIF 300 (AZ Electronic Materials) for ~60 seconds until a “Dolan Photoresist Bridge” is formed with sufficient undercut (Figure 2.3a and 2.3b) [81]. The surfaces must be cleaned with Argon or oxygen plasma prior to evaporation to prevent poor aluminum film adhesion and aging of the tunnel junctions formed [82],[83].

As shown in Figure 2.3a, arrays of detector and emitter STJs are patterned and deposited. The film thicknesses in the emitter are made only a few tens of nm (lower layer is ~20 nm thick and upper layer is ~38 to 80 nm thick on the mesa sidewall), to enable phonons to escape into the Si without reabsorption, whereas the detector film thicknesses are made several hundred nm thick to maximize the absorption of incident phonons. We utilize a two-step electron-beam angle evaporation interspersed with a static oxidation procedure to form the aluminum tunnel junctions. The overlap area of the tunnel junctions is dependent on the angles at which the evaporation is done (Figure 2.3b). Assuming that the height of the bridge or thickness of the LOR layer is d μm and

the width of the bridge is W_1 μm , the overlap width is $d \cdot (\tan\theta_1 + \tan\theta_2) - W_1$, where θ_1 and θ_2 are the two deposition angles measured from the normal to the substrate surface (Figure 2.3b). The width of the wiring traces, W_2 , should be made wide enough that the double angle evaporation forms a single overlapping metal trace (Figure 2.3c). We found that the best quality films were obtained at evaporation rates $\sim 4.5 - 5$ $\text{\AA}/\text{s}$. The films were evaporated at base pressures ranging from 2×10^{-7} Torr to 1.2×10^{-6} Torr. The base pressures were sometimes lowered further by the initial evaporation of 50-100 nm Al in the chamber. The evaporated aluminum acts as a getter for particles in the chamber. The tunnel barrier is formed by static oxidation in between the two Al deposition steps, with an exposure parameter defined as $\text{exposure} (\text{Pa} - \text{secs}) = \text{pressure} (\text{Pascal}) \times \text{time}(\text{seconds})$ [84]. The emitter tunnel barrier was grown in 3 Torr of oxygen for 60 minutes resulting in emitter resistances ~ 1.5 k Ω . The detector tunnel barrier was grown at 300 mTorr for ~ 70 minutes resulting in resistances of ~ 200 Ω . Figure 2.4a shows the exposure parameter plotted against the area-specific resistances of the tunnel junctions. This guide can be used to estimate the exposure parameters that will produce emitters or detectors with desired junction resistances. The plot was fitted to a power law ($f(x) = x^{0.59}$) with an adjusted- R^2 value of 0.997. The area of each junction was calculated from scanning electron micrograph (SEM) inspection and can be estimated prior to fabrication based on the overlap area calculations discussed above. The post-evaporation processing includes metal lift-off, dicing of the wafer into 4.5 sq. mm chips, and the evaporation of ~ 500 nm thick silver on the backside. Silver has been shown to be a good absorber of phonons [61]; hence, the addition of silver reduces the backscattered signals from the bottom of the chip. The

junctions are very sensitive to static discharge, and therefore, proper grounding is essential at all times.

The base pressure at which the Al films are deposited is important as it may affect their room-temperature resistivity, which in turn affects their critical temperature T_c and superconducting gap. Such variations in the superconducting gaps of aluminum films with respect to their room-temperature resistivity have been reported to be due to oxygen doping [85], [86]. In Figure 2.4b, we show the dependence of the room-temperature resistivity of thin aluminum films of identical dimensions on increased oxygen partial pressure during evaporation.

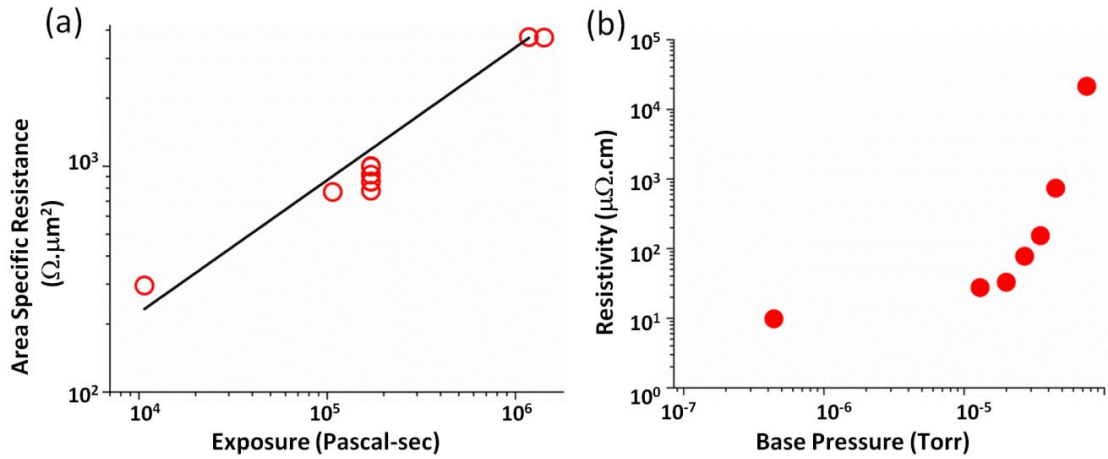


Figure 2.4: (a) Plot of exposure parameter with the area specific resistance of 11 different tunnel junctions fabricated with 5 different exposure parameters. Power law fit ($f(x) = x^{0.59}$, $\text{adj-R}^2 = 0.997$). (b) Plots showing the effect of oxygen doping on Aluminum films. We measured the room temperature resistivity of aluminum evaporated in varying oxygen pressures starting with a film deposited at base pressure of 4.4×10^{-7} Torr (No oxygen).

The dimensions of the films were patterned by photolithography and the first film was evaporated at a base pressure of 0.44 μTorr . By increasing the base pressure due to the continuous flow of oxygen into the chamber, we show that the resistivity of the films varies with base pressure. The typical transition temperature, T_c , for films evaporated at base pressures of 27 μTorr and 35 μTorr was measured to be 1.75 K and 1.89 K respectively (increased T_c compared to a pure Al film with $T_c \sim 1.12$ K).

2.4. Instrumentation, Measurement, and Characterization of Spectrometer

2.4.1. Low Temperature Apparatus

The apparatus for the low temperature phonon transport experiments includes a He-3-cryostat with a custom designed sample stage immersed in a liquid helium Dewar. The fridge wiring consists of twisted pair lines with room temperature pi-filters (Tusonix 4701 EMI) enclosed in brass block Faraday cage, allowing up to ~ 90 dB attenuation at frequencies > 100 MHz. The cold stage filters are ‘tapeworm’ type low-pass filters [64], but the extent of cold stage filtering is limited by the space in our vacuum can. The fridge is cooled down to a base temperature of 0.3 K and the sample is held in vacuum. The thermometer at the He-3 stage is a CernoxTM RTD (Lakeshore Cryotronics) and a silicon diode thermometer (DT-470-SD-12A, Lakeshore Cryotronics) monitors temperature at the 1 K-pot. Attempts are made to minimize the coupling of noise from the thermometry wiring into the measurement wiring. Metal film resistors are used in all bias networks, as this type of resistor is known to exhibit superior temperature

stability and reduced $1/f$ noise. As shown in Figure 2.5a, the chips containing the spectrometers are wire-bonded onto the gold plated copper sample stage. The backside of the chips must be properly anchored to the sample stage by thermalizing with Apiezon N grease or silver paint. A 5000 turn superconducting magnetic coil is attached to the top of the sample box for Josephson current suppression as shown in Figure 2.5b, c, and d. Once the fridge is immersed in the helium Dewar, we ensure proper grounding of the fridge and equipment rack. We place rubber pads underneath the wheels of the Dewar to reduce mechanical vibration.

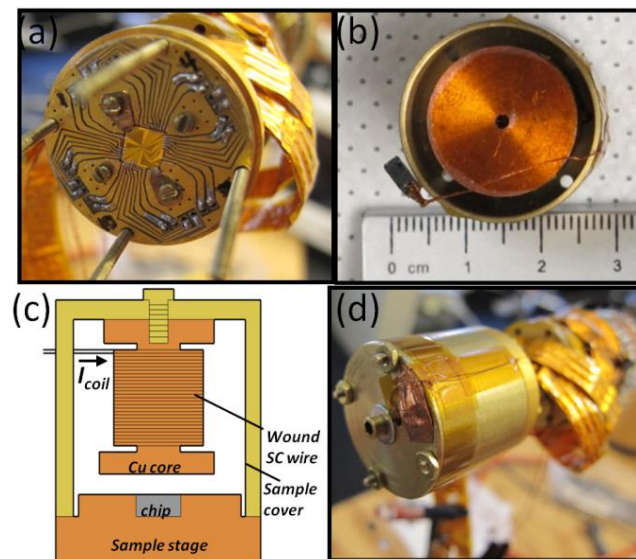


Figure 2.5: Sample stage and mounting on fridge. (a) Photograph of 4.5 sq. mm chip wire-bonded unto a gold plated sample stage of our He-3 cryostat. (b) Interior photograph of the sample box cover showing magnetic coil (~5000 turns of superconducting wire wound around a copper core). (c) Schematic of the coil assembly.

Coil allows for the application of magnetic field perpendicular to the chip in order to suppress the Josephson current in the detector. Up to ~ 2.5 Gauss of magnetic field may be applied by passing current through the coil. (d) Sample cover mounted on the sample stage prior to cool down.

2.4.2. DC Characterization of STJ Emitters and Detectors

The DC characteristics of emitter and detector tunnel junctions are determined from current-biased current-voltage (I-V) measurements at ~ 0.3 K. Figure 2.6a shows how we estimate the superconducting gap from the I-V behavior. From the I-V curves we also calculate the normal state resistance, R_n , of the junctions. In Figure 2.6b, we show the current-biased I-V curves in the subgap regime for four SQUID detectors with the current normalized by their normal state resistances for comparison. The red plot shows significant rounding-off which is due to poor filtering on that particular signal line, allowing stray voltage noise to add a random perturbation to the junction voltage.

In Figure 2.6c, we show the resistance-normalized I-V curves for four emitters with normal state resistance values of 212Ω , 935Ω , 2250Ω and 5559Ω . This plot illustrates several possible problems in emitter performance. In the 212Ω emitter (red plot), we observe ‘back bending’ of the gap rise step at $V_e = 2\Delta_e/e$. This is a signature of quasiparticle overinjection, which appears consistently in emitter STJs of $R_n < 700 \Omega$, leading to local suppression of the superconducting gap Δ_e and poor phonon energy resolution. In the 2250Ω junction (magenta plot), the I-V curve shows a signature of being partially shorted (this could occur either at their formation or during processing)

which will add an uncontrolled thermal phonon population to the junction's emission. The black and blue curves indicate a limitation on emitter energy resolution. For an ideal STJ, the 'gap rise' step at $V = 2\Delta/e$ should be infinitely sharp, but in practice, we observe a breadth of $\sim 60\text{-}80 \mu\text{V}$ (~ 15 to 20 GHz). This behavior most likely indicates that the superconductor's gap Δ_e varies within the junction by $\sim 60\text{-}80 \mu\text{eV}$ (corresponding to a ~ 15 to 20 GHz imprecision in emitted phonon frequency).

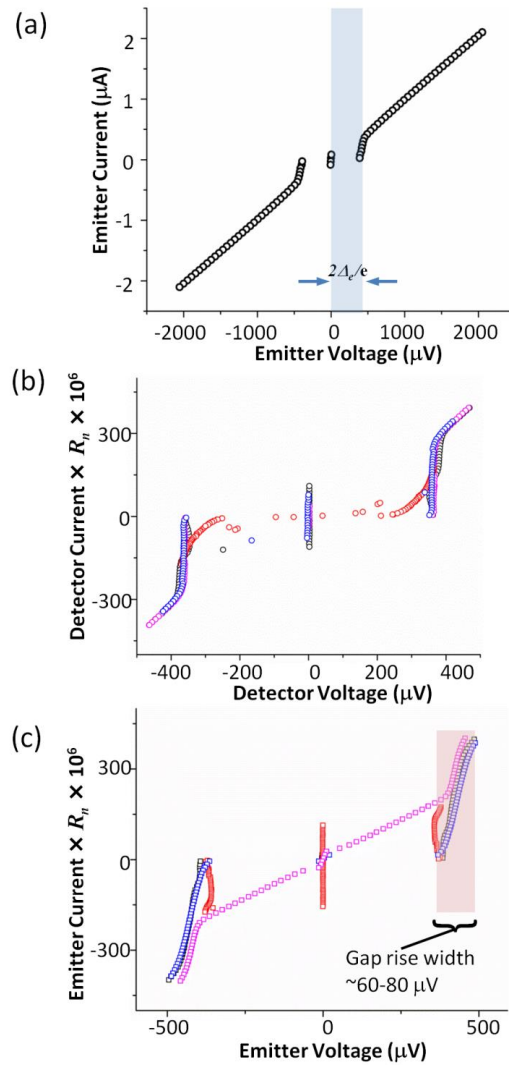


Figure 2.6: Plots of dc I-V Characterization. (a) Typical current biased I-V measurement

of an emitter. The band gap of the junction $2\Delta_e$ is $\sim 400 \mu\text{eV}$. (b) $I \times R_n - V$ curves of four detectors taken without Josephson current suppression and focusing on the subgap regime. All the detectors are SQUIDs. Detector resistances range from 167Ω (black), 213Ω (magenta), 849Ω (red), to 817Ω (blue). Poorly filtered lines lead to rounding-off of gap rise as shown in the red plot. (c) $I \times R_n - V$ curves of four emitters focusing on the subgap region. Emitter resistances range from 935Ω (black), 2250Ω (magenta), 212Ω (red), to 5556Ω (blue). The plot illustrates how to identify common emitter problems: Magenta-colored plot shows a partly shorted device. The red plot exhibits severe ‘back bending’ of the gap rise due to overinjection and local suppression of superconducting gap, commonly seen in the case of low emitter resistance. The gap-rise width (black and blue plots) indicates inhomogeneity in superconducting gap $2\Delta_e$, which limits the energy resolution for phonon spectroscopy.

2.4.3. Josephson Current Suppression

Josephson current (or supercurrent) in the detector must be suppressed, so that the detector may be voltage-biased and its quasiparticle tunneling current clearly distinguished. To do so, we apply a magnetic field perpendicular to the SQUID loop, using a small superconducting coil mounted as close as possible to the top of the chip to minimize vibration-coupled flux noise. For our coil geometry (Figure 2.5c), we calculate (using Biot-Savart law) the axial magnetic field to be 1.27 Gauss/mA . The heat load resulting from typical coil current is $\leq 2 \mu\text{W}$. The maximum supercurrent in the SQUID detector junction, assuming perfect symmetry, is given as $I_c(\Phi) =$

$2I_c(0) \left| \cos\left(\frac{\pi\Phi}{\Phi_0}\right) \right|$, where Φ_0 , Φ , and $I_c(0)$ are the flux quantum (2.07×10^{-15} Wb), applied flux, and critical current at zero magnetic field respectively [39]. By applying a magnetic flux proportional to $\frac{n\Phi_0}{2}$, where n is an odd integer, the supercurrent should be fully suppressed. We typically employ the minimum effective flux (equivalent to $n = 1$), in order to minimize flux trapping. In practice, we find that the supercurrent is not always fully suppressed, probably due to asymmetry between the two junctions. Figure 2.7a illustrates our technique for determining the detector bias point for phonon transport studies. The detector voltage is swept in the subgap regime between ~ -300 to ~ 300 μV . At each voltage step, the coil current is swept from 0 to 2 mA and the tunnel current is measured at each step. In the 3D plot in Figure 2.7a, the current measured per the detector bias voltage and per coil current is shown. We set the voltage bias point of the detector to $\sim \Delta_d/e$ (~ 180 μV) and coil current to ~ 1 mA, where the minimum critical current is obtained. The measured zero-voltage and zero B-field supercurrent for the detector ($R_n = 116$ Ω) in Figure 2.7a is ~ 1.2 μA (z-axis) and is closely predicted by the Ambegaokar-Baratoff expression for $T \sim 0$ K, $I_{c0} = \frac{\pi\Delta}{2eR_n}$ [39]. By applying a magnetic field ~ 1 Gauss at the bias point, the supercurrent is suppressed to ~ 1 nA.

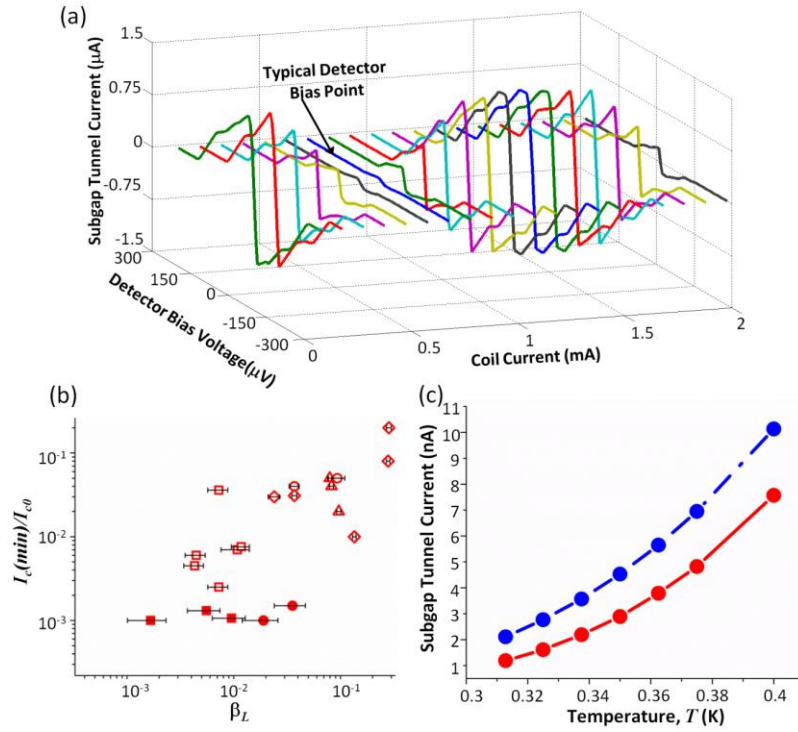


Figure 2.7: Plots of Josephson current suppression and subgap thermometry. (a) Detector Josephson current suppression. The subgap tunnel current (before Josephson current suppression) is measured at each coil current from 0-2 mA as the bias voltage is swept from 300 μV to 300 μV . For operation in spectrometer, the detector is typically biased in the subgap region ($\sim 180 \mu\text{V}$) and at external magnetic field ~ 1 Gauss (1.27 Gauss/mA) were the critical current is mostly suppressed. The plot also shows the periodic nature of the critical current with applied magnetic field. (b) Plot of $\beta_L (\frac{2LI_{c0}}{\Phi_0})$ versus the ratio of the minimum suppressed critical current to the calculated critical current ($I_c(min)/I_{c0}$) at $T=310$ mK for several SQUID designs. Junctions formed on flat surface are represented by solid symbols, while the open symbols represent junctions formed on the sidewall; Loop areas vary from $\leq 2 \mu\text{m}^2$ (squares), to $\sim 10 \mu\text{m}^2$ (circles), to $\sim 120 \mu\text{m}^2$ (triangles), and to $\sim 180 \mu\text{m}^2$ (diamond). (c) Temperature

dependent subgap tunnel current (after Josephson current suppression) measured at $V_d = \Delta_d/e$ (180 μV) as function of temperature (red plot) and estimated tunnel current based on BCS prediction (blue plot).

The extent to which the supercurrent in the SQUID detectors may be suppressed is dependent on two geometric properties: self-induced flux and junction symmetry. The self-induced flux is proportional to the self-inductance, L , of the SQUID loop, which we estimate based on the inductance of a rectangular loop [87]. The more closely identical the two junctions are, the more closely the current flowing through them may be made to cancel. In Figure 2.7b, we plot the ratio of the minimum obtainable critical current to the maximum zero voltage critical current ($I_c(\text{min})/I_{c0}$) versus the parameter $\beta_L = \frac{2LI_c}{\Phi_0}$, the ratio of self-induced flux to the flux quantum. Each symbol in Figure 2.7b represents a unique SQUID design based on the location of the junction and the loop area: Junctions formed on flat surface are represented by solid symbols, while the open symbols represent junctions formed on the sidewall; Loop areas vary from $\leq 2 \mu\text{m}^2$ (squares), to $\sim 10 \mu\text{m}^2$ (circles), to $\sim 120 \mu\text{m}^2$ (triangles), and to $\sim 180 \mu\text{m}^2$ (diamond). Smaller loop areas and larger junction resistances lead to smaller values of β_L and in general to better supercurrent suppression; however, for the SQUID detectors formed on the sidewall, we observe a large variation in suppression for devices with similar β_L . This is likely due to junction asymmetry. For devices formed on the flat (100) surface, supercurrent suppression is more consistent and exceeds ~ 3 orders of magnitude for $\beta_L < 2 \cdot 10^{-3}$, indicating more symmetric junction formation. We also note a tradeoff in detector design: while Josephson critical current scales inversely with

normal-state tunnel resistance $I_{c0} = \frac{\pi\Delta}{2eR_n}$, detector efficiency (equation (2.4)) also scales inversely with R_n . In practice we find that a loop area of $\sim 2 \mu\text{m}^2$ and detector resistance $R_n \sim 200$ to 300Ω enable both suppression of I_c to levels smaller than thermal quasiparticle tunneling current, as well as detector efficiencies of ~ 0.1 that permit readily measurable spectrometer signals.

With the supercurrent suppressed, we measured the subgap tunnel current due to thermally excited quasiparticles at detector voltage $V_d = \Delta_d/e$ and at different temperatures (~ 0.3 to 0.4 K) as shown in Figure 2.7c (red plot). We compare the results to the BCS approximation of the subgap tunnel current for an S-I-S junction (blue plot).[38] The measurement shows exponential dependence of subgap current on temperature, as predicted by BCS theory. The deviation between the data and prediction may be due to our inability to fully suppress the supercurrent and to possible inaccuracies of our cold stage thermometer at temperatures below ~ 0.34 K.

2.4.4. Modulated Phonon Transport Measurements

The schematic of our phonon transport experiments is shown in Figure 2.8a. For phonon emission ($V_e \geq 2\Delta_e/e$), the emitter is current biased by applying a DC voltage, $V_b = \frac{V_e}{R_n} R_b$ through bias resistor $R_n \sim 500 \text{ k}\Omega$, where $V_e (= I_e R_n)$ is the voltage across the emitter junction and R_n is the normal state resistance of the emitter junction.

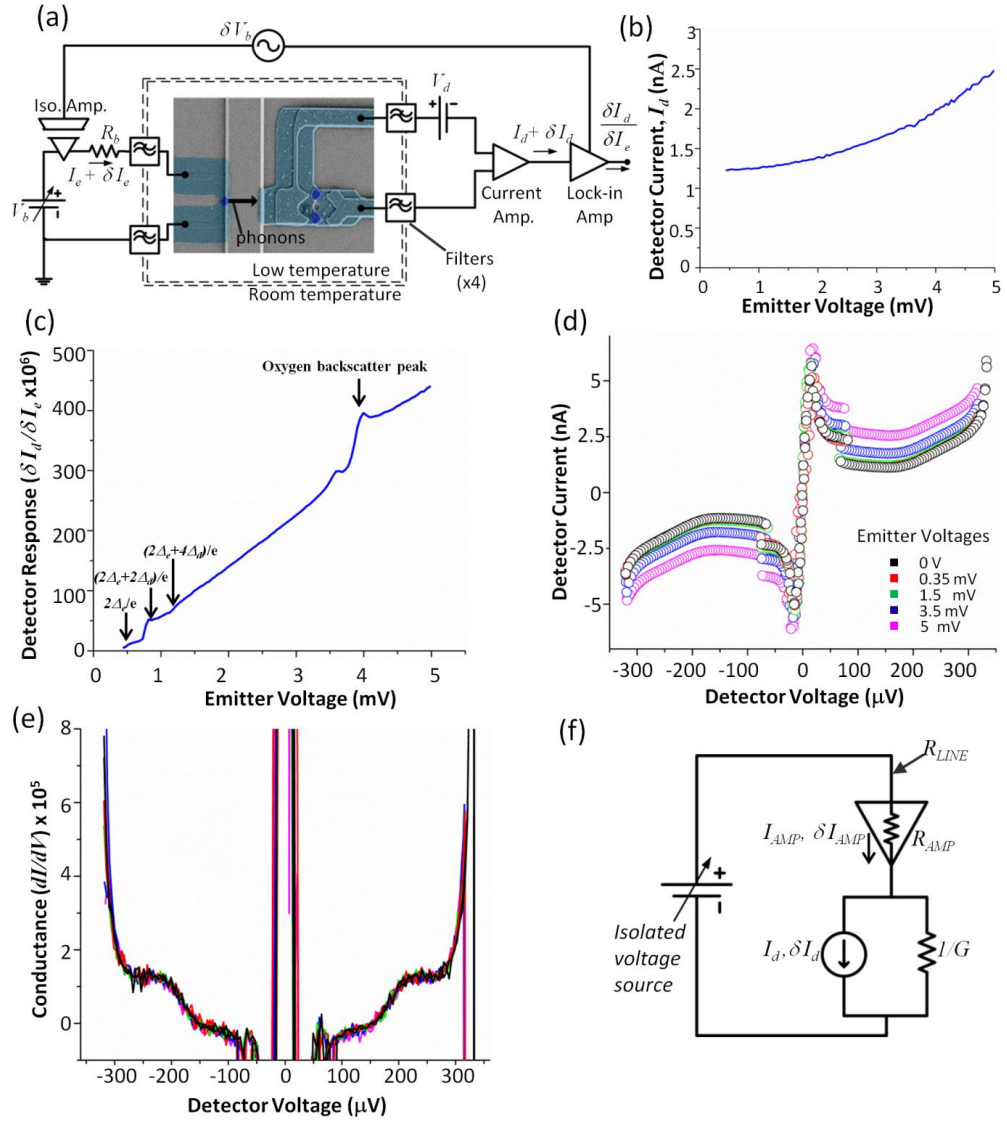


Figure 2.8: Phonon transport measurements. (a) Schematic of phonon spectroscopy measurements. (b) Steady state detector current, I_d . (c) Differential transfer function $\delta I_d / \delta I_e$, representing the fraction of emitted phonon flux that reaches the detector. The emitter tunnel junction turns on above $V_e = 2\Delta_e$ and emits detectable relaxation phonons only above $V_e = (2\Delta_e + 2\Delta_d)/e$. For $V_e = (2\Delta_e + 4\Delta_d)/e$, the emitted relaxation phonons may break multiple cooper pairs in the detector. The peak at ~ 4 mV represents resonant backscattering of oxygen impurities in the Si, typically seen at \sim

870 GHz [88]. (d) Voltage-biased detector I-V curves with varying emitter voltages and partially-suppressed Josephson current. (e) Differential conductance calculated from the I-V measurements in figure 8d (colors are same as in 8d). (f) Equivalent circuit model of detector as a current source. The DC current I_d and modulated current δI_d follow the incident flux of phonons.

All the device wiring comprises filtered twisted-pair lines, and shielded coaxial cables are used for all connections. The DC current through the emitter junction is stepped from $I_e = \sim 0.35$ to $2 \mu\text{A}$, which corresponds to emitter voltages $V_e = \sim 0.35$ to 2 mV for a junction resistance of $R_n = 1 \text{ k}\Omega$. In addition to the DC current applied to the junction, an AC modulation current $\delta I_e \sim 20 \text{ nA}_{\text{RMS}}$ is applied by adding an AC modulation δV_b to the DC level V_b through a unity-gain isolation amplifier (Burr Brown ISO124P) and $100\times$ voltage divider; the output is independent of frequency between 4 and 1000 Hz and exhibits noise of $\sim 10^{-6} \text{ V}/\sqrt{\text{Hz}}$. The typical modulation frequencies for our measurements range between 7 - 11 Hz.

For phonon detection, the detector is voltage biased in the subgap regime ($V_d \sim \Delta_d/e$) with the Josephson current suppressed. The detector signal comprises a steady state plus a modulated component, as indicated in Figure 2.8a. The steady state DC detector current $I_d = \sim 1$ to 2.5 nA for emitter voltages $V_e = 0.35$ to 5 mV as shown in Figure 2.8b. For DC detector tunnel currents I_d up to 1.5 times the unperturbed (thermal) level of the steady state detector current, we treat τ_{rec} as being constant and therefore equation (2.4) as being valid and {Eff} being fixed [77, 80]. We checked this assumption by raising the device temperature until I_d rose by a factor of 3, and observed

very small change in the differential transfer function $\delta I_d/\delta I_e$. Thus for $I_d < 1.5$ times its thermal level, we can safely assume that the detector response remains linear with incident phonon flux. (We note that for $I_d > 1.5$ times its thermal level, the detector response may be nonlinear with the incident phonon flux.) In our devices τ_{rec} may be limited by magnetic flux trapped in the Al detector film as well as by quasiparticle population.[77]

The modulated AC detector current (also differential response or differential transfer function) of our detector (Figure 2.8c), which represents the modulated portion of the incident phonons, is isolated via a low-noise current pre-amplifier (DL 1211) and a lock-in amplifier (SRS 830) over a range from 0 to ~ 1 pA_{RMS}. As shown in Figure 2.8c, the emitter tunnel junction turns on at emitter voltage above $V_e = 2\Delta_e/e$: the step in detector response at $V_e = (2\Delta_e + 2\Delta_d)/e$ occurs because the emitted relaxation phonons (peak energy = $eV_e - 2\Delta_e$) above this voltage are energetic enough to break Cooper pairs in the detector (gap energy $2\Delta_d$, i.e. ~ 90 GHz). When $V_e = (2\Delta_e + 4\Delta_d)/e$, we observe a further change in detected signal level, as the emitted relaxation phonons acquire enough energy to break multiple cooper pairs in the detector (See also equation (2.3)). We have also considered the effect of microwave Josephson radiation on the detector signal [89]. In one spectrometer, we biased the emitter at $V_e = 0$ and modulated the Josephson branch of the emitter I-V curve. We observed zero detector response. We conclude that our measurement is not influenced by Josephson radiation or inductive coupling of the emitter Josephson current into the detector.

The peak frequency of the emitted relaxation phonon distribution is related to the emitter bias voltage as $(eV_e - 2\Delta_e)/h$. The feature in Figure 2.8c at $V_e \sim 4$ mV is

believed to be due to backscattering by oxygen impurities in the silicon. This peak was observed at ~ 870 GHz in past studies of STJ phonon spectroscopy [88],[90]. While this behavior confirms that our aluminum STJ-based spectrometer emits a strong and tunable signal well above 800 GHz, we note that at such high frequencies (Figure 2.2d), we estimate only $\sim 20\%$ of the total phonon power to be at the peak frequency of $(eV_e - 2\Delta_e)/h$.

In Figure 2.8d, we present voltage-biased I-V curves of a detector recorded while varying the emitter voltage from 0 to ~ 5 mV. (We note that in this detector we were unable to suppress Josephson current below ~ 5 nA.) For emitter voltage $V_e = 0$ V, the subgap current at detector voltage $V_d = \Delta_d/e$ (180 μ V) is exactly the same as that shown in Figure 2.7c at a temperature of ~ 313 mK. As a larger and larger phonon flux is transmitted to the detector, the total quasiparticle density in the detector increases well beyond the thermal level, and the detector current rises. In Figure 2.8e, we calculate the differential conductance (dI/dV) from the subgap I-V measurements of Figure 2.8d. The conductance of the detector remains essentially the same as emitter voltage is varied. At the typical bias point of $V_d = \Delta_d/e$, conductance G remains fixed at $\sim 5 \times 10^{-6} / \Omega$. The only difference is in the total current level.

These measurements motivate a simplified equivalent circuit model for our STJ phonon detector, shown in Figure 2.8f. The phonon detector is modeled as a current source in parallel with a resistance $1/G$. The DC current I_d and modulated current δI_d follow the incident flux of phonons. The detector is in series with the current amplifier (input impedance R_{AMP} and current through I_{AMP}) and line resistance R_{LINE} . The bias point on the detector is maintained by an isolated voltage source (Stanford Research

SIM928, output through a 10^5 voltage divider) across the entire network. Typical values for R_{LINE} and R_{AMP} are $\sim 70 \Omega$ and $2 \text{ k}\Omega$ respectively (R_{AMP} is the manufacturer's specification). This model, and the measurements of Figures 2.8d and 2.8e, makes clear that the STJ maintains a steady bias throughout our measurement range—even if I_d rises by 1 nA, the bias across the STJ will change by only a few μV . Similarly, the current through the amplifier, accurately registers the modulated current δI_d through the detector. Modulated amplifier current δI_{AMP} equals $\delta I_d / (1 + G \cdot (R_{LINE} + R_{AMP}))$, which is only $\sim 1\%$ different than δI_d for typical values of R_{LINE} , R_{AMP} and G .

2.5. Results of Phonon Spectroscopy Measurements

2.5.1. Energy Resolution and Sensitivity

The energy resolution of our measurement is limited by noise, by the band gap inhomogeneity of the emitter STJ, and by the modulation amplitude. Voltage noise across the emitter STJ adds random fluctuations to bias voltage V_e , while inhomogeneity in the emitter gap Δ_e likewise reduces precision of phonon energies. In practice, we assess these effects based on the width of the gap rise in the emitter I-V curve (Figure 2.6c), typically $\sim 60\text{-}80 \mu\text{eV}$. The modulation current δI_e applied to the emitter may also reduce energy resolution by adding a voltage oscillation of peak amplitude $2\sqrt{2}R_n\delta I_e$ to the emitter voltage $V_e = I_e R_n$. For typical emitter junction resistance $R_n \sim 800 \Omega$ and $\delta I_e \sim 20 \text{ nA}_{\text{RMS}}$, this modulation envelope is only $\sim 40 \mu\text{eV}$, and therefore the bandgap inhomogeneity imposes the limit on energy resolution: $\sim 60\text{-}80 \mu\text{eV}$ —corresponding to a frequency resolution $\sim 15\text{-}20 \text{ GHz}$.

The sensitivity of the measurement is limited by detector noise, which may comprise electrical pick up noise, vibrational pickup in wiring and amplifier noise, as well as fundamental contributions such as Johnson noise in wiring and shot noise in the tunnel junction. Figure 2.9 shows a typical noise spectrum of the detector, exhibiting peaks in the spectrum at 60 Hz and its multiples due to power-line noise pickup, as well as an unexplained resonance at ~ 600 Hz. Wiring and apparatus to minimize noise are discussed in the section on instrumentation. Based on detector noise spectra such as Figure 2.9, we typically choose modulation frequencies between 3 and 12 Hz, adding line-frequency notch filters and low-pass filters at the input of the preamplifier and lock-in amplifier to avoid amplifier overload. The lowest noise level obtained at modulation frequency of 11 Hz was $\sim 60 fA/\sqrt{Hz}$. We note that a tunnel junction passing a DC current of 1 nA should exhibit a shot noise of $\sim 18 fA/\sqrt{Hz}$ (assuming a Fano factor of 1), so our experimental noise is not far above the shot noise level. To reduce uncertainty in a spectral measurement, we typically repeat it 25 times and average the results. Considering the typical detector efficiencies $\{\text{Eff}\} \sim 0.1$ (equation (2.4)) as well as acoustic-transmission and absorption factors T_{SiAl} and α_{abs} (see equation (2.3)), we estimate the noise equivalent power (NEP) for phonon detection to be $\sim 10^{-15} W/\sqrt{Hz}$, or $\sim 2 \times 10^7$ phonons of energy $\sim 2 \Delta_d$ per second per \sqrt{Hz} . A comparative analysis of similar low temperature thermal detectors found similar sensitivities.[91]

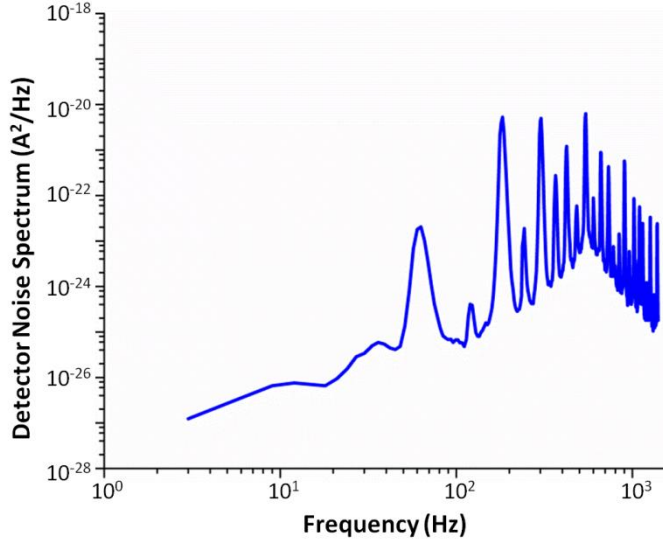


Figure 2.9: Detector noise spectrum. Modulation frequency for transport measurements range from 3 -12 Hz.

2.5.2. Ballistic Phonon Propagation

The ballistic nature of phonon transport is evidenced by comparing the differential detector response ($\delta I_d/\delta I_e$) of spectrometers with varying mesa widths, detector finger widths, blocked ballistic path, and offset line-of-sight between emitters and detectors (Figure 2.10a-d). To enable measurements made with different detectors to be compared equivalently, we divide each measured value of $\delta I_d/\delta I_e$ by {Eff} for that detector to obtain the phonon transmission signal. Following equations (2.3) and (2.4), we expect the resulting scaled value to equal $T_{SiAl} \cdot \alpha_{abs} \cdot \frac{2e\delta\dot{n}_{ph,d}}{\delta I_e}$ for $2\Delta_d \leq \hbar\omega < 4\Delta_d$, and $T_{SiAl} \cdot \alpha_{abs} \cdot \frac{2e\delta\dot{n}_{ph,d}}{\delta I_e} \cdot (\hbar\omega/2\Delta_d - 1)$ for $\hbar\omega \geq 4\Delta_d$. Since T_{SiAl} and α_{abs} are expected to be roughly the same from one detector to another, we do not rescale the

data for these factors. We note that the quasiparticle diffusion length $\sqrt{D \cdot \tau_{rec}}$ is of order $100 \mu\text{m}$, so that phonons reflected from the bottom of the Si chip and striking the wiring leads far from the junction or the mesa may also contribute to a measured 'background' signal level that is also subject to the same efficiency $\{\text{Eff}\}$ as the signal resulting from phonons striking the detector finger [75].

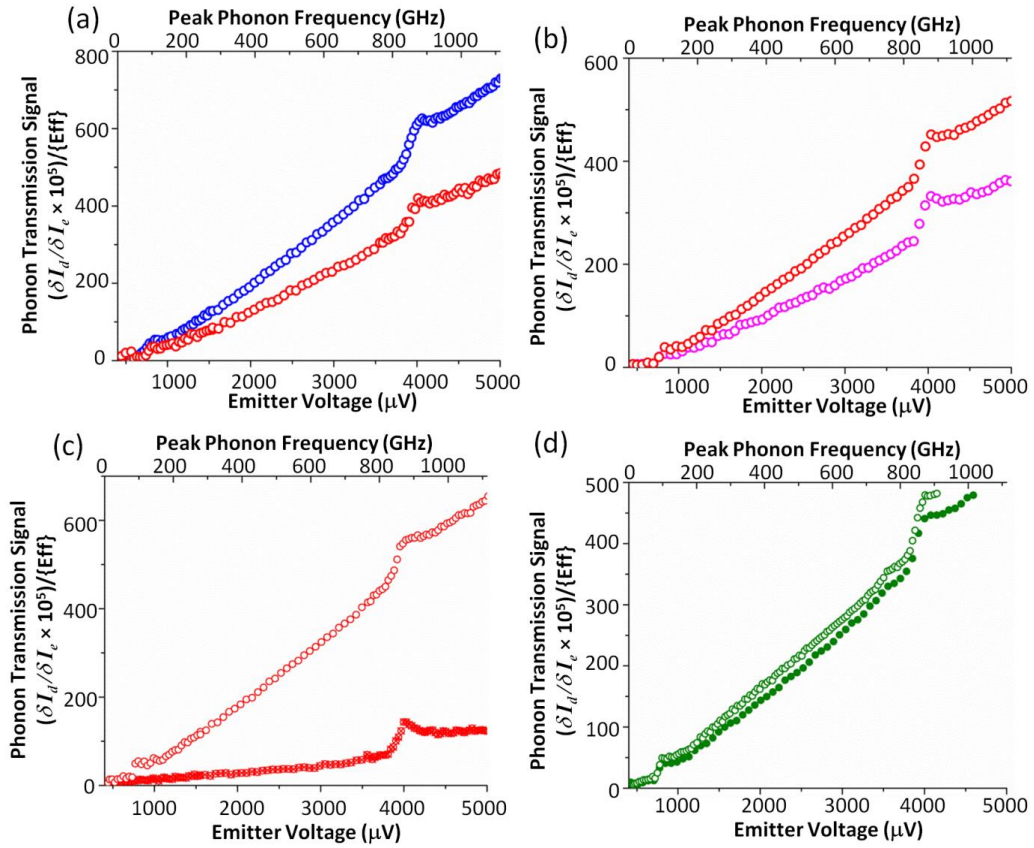


Figure 2.10: Results of ballistic phonon propagation. (a) Ballistic phonon transport measurements on different mesa widths. Detector signal level decreases as mesa width increases from $7 \mu\text{m}$ (blue) to $10 \mu\text{m}$ (red). The detector finger width is $6 \mu\text{m}$ in all cases. (b) Ballistic phonon transmission with varying detector finger widths. Detector signal collected by the $6 \mu\text{m}$ detector finger (red) is higher compared to the $3 \mu\text{m}$ detector

finger (magenta). Mesa width is 10 μm in both cases. (c) Plots comparing phonon transmission through a mesa with (hatched red circle) and without (open red circle) a trench etched into the mesa. The trench blocks the line of sight between the emitter and detector. Mesa width is 10 μm and detector finger is 6 μm wide in both cases. (d) Ballistic phonon transport measurement with varying angle between emitter and detector. In the solid green circle plot, the emitter and detector have a straight line of sight, but in the open green circle plot the emitter and detector are offset by ~ 50 degrees. The mesa width is 7 μm and detector finger width is 3 μm in both cases. (Plots in Figure 2.10 are not restricted to the region where the detector response is linear with incident phonon flux, i.e. for portions of the plot $I_d > 1.5$ times its thermal level.)

The rate of ballistic phonons striking the detector finger, as measured by the differential detector response, is proportional to

$$\frac{\delta I_e}{e} \int dA_e \int \frac{d\Omega_d}{\pi} T_{ALSi} \cdot \cos \theta \cdot T_{SiAl} \cdot A_{foc}(\theta, \phi), \quad (2.10)$$

where A_e is the fraction of emitter STJ visible from the detector, $\cos \theta$ is a Lambert law phonon emission distribution, $A_{foc}(\theta, \phi)$ is the phonon focusing factor, T_{ALSi} and T_{SiAl} are acoustic transmission factors described previously, and $d\Omega_d$ is the solid angle subtended by the detector with respect to the emitter STJ [66], [92], [93], [94], [95]. Figure 2.10a shows the phonon transmission signal between emitter and detector formed on different widths of mesas (7 μm (blue) and 10 μm (red)) with 6 μm detector finger widths. As the mesa width increases from 7 to 10 μm , the solid angle Ω_d subtended by the detector with respect to the emitter decreases; hence, the

differential detector signal decreases as expected. We further verified the ballistic phonon transmission by varying the width, W_f , of the detector fingers. For a 10 μm mesa, we show the phonon transmission signal for a 6 μm wide (red plot) and a 3 μm wide (magenta plot) detector finger (Figure 2.10b). The wider finger will subtend a larger solid angle; hence, the detector signal is larger as expected for the 6 μm wide detector finger shown in Figure 2.10b. In Figure 2.10c, we blocked the ballistic path between the emitter and detector by etching a trench into the mesa. The mesa width and detector finger widths are 10 μm and 6 μm respectively for both the bulk (open circle) and trench (hatched circle). The latter measurement reveals a significant portion of the transmitted phonon signals that are due to backscattering from the bottom of the chip ('background signal'). The difference between the trench transmission and the transmission through the mesa represents the dynamic range of our measurements. In Figure 2.10d, we compare the phonon transmission signals for emitters and detectors that have a straight line-of-sight along the mesa width (along the $\langle 110 \rangle$ crystal direction, solid green plot), with emitter and detectors offset with line-of-sight offset by $\sim 50^\circ$ (near to the $\langle 100 \rangle$ crystal direction, open green plot). A slightly higher detector signal level is observed for the offset geometry. For this geometry, the ballistic signal is affected by phonon focusing—the attenuation or enhancement of phonon propagation in preferred direction in an anisotropic crystal such as silicon [94]. In silicon crystals, the phonon focusing factor is ~ 2 times higher in the $\langle 100 \rangle$ direction than in the $\langle 110 \rangle$ direction.[95] These measurements evince the sensitivity of our phonon spectrometer to submicron variations in device geometry. We point out, however, that the measured differential response of the detector must be scaled by the efficiency factor $\{\text{Eff}\}$ in order

to compare measurements from different detectors. In Figure 2.11, we replot the results in Figure 2.10a (phonon transmission through different mesa widths) with the unscaled detector response $\delta I_d/\delta I_e$, and we show that with typical detector efficiency factors $\{\text{Eff}\} \sim 0.1$, there is an order of magnitude difference between the scaled and unscaled signals.

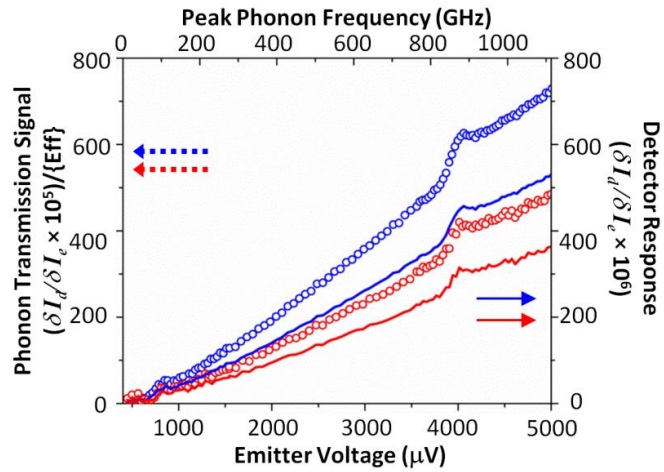


Figure 2.11: Comparison of the modulated detector response scaled by detector efficiency factor $\{\text{Eff}\}$ (scatter plots and left axis) with the unscaled detector response (line plots and right axis) for plots in figure 10a. The measured detector response must be scaled by the efficiency factor in order to ascertain the phonon transmission signal. (Plots in figure 11 are not restricted to the region where the detector response is linear with incident phonon flux, i.e. for portions of the plot $I_d > 1.5$ times its thermal level.)

2.5.3. A Numerical Example of Phonon Emission Rate

As a numerical example, a typical aluminum STJ having normal-state tunnel resistance $R_n = 1000 \Omega$ and biased at ~ 2.1 mV to produce a peak at 400 GHz, with a ± 10 GHz

modulation, will produce ~ 4 nW of total phonon power and about ~ 0.4 nW of modulated phonon power. Because of the geometry of our spectrometer, only about 0.1% of this modulated power, or ~ 0.4 pW, will participate in the measurement. Of this about $\sim 32\%$, i.e. roughly 5×10^8 phonons/sec, will be carried by the peak phonons in the 20 GHz band around 400 GHz; the remainder of the power (roughly 1 to 3×10^9 phonons/sec) is carried by phonons of energy lower than the peak. In contrast, a thermal source peaked at 400 GHz and emitting the same experimental power (~ 0.4 nW) will emit a similar fraction (0.4 pW) in the proper direction to participate in the experiment, but only $\sim 3\%$ of this, or roughly 5×10^7 phonons/sec, will be carried by phonons within ± 10 GHz of the peak. Of the remaining power, roughly half will be carried by phonons of frequency > 410 GHz and half by phonons of frequency < 390 GHz.

2.6. Conclusion

We have designed and microfabricated a phonon spectrometer utilizing superconducting tunnel junction transducers for the emission and detection of hypersonic (100 to ~ 870 GHz) acoustic phonons in silicon microstructures. We model the phonon emission profile of the modulated STJ phonon spectrum considering the electron-phonon interactions within the superconductor films of the emitter STJ, and we also model the phonon detector behavior by considering quasiparticle-phonon interactions. Our energy resolution of ~ 60 - 80 μ eV, corresponding to a frequency resolution of ~ 15 - 20 GHz, is about 20 times better than the energy resolution obtainable from conventional thermal transport measurements, which rely on a Planck distribution of phonons. We have demonstrated that with a phonon detection noise equivalent

power, NEP, of $10^{-15} W/\sqrt{Hz}$, the sensitivity of our STJ phonon detectors is comparable to similar low temperature thermal detectors that are available. The design of our spectrometer—comprising a silicon mesa with STJs on the sides—serves as a good platform for phonon transport studies. The ballistic phonon transmission through the mesa alone can be distinguished from backscattering from the substrate by subtracting the mesa-with-trench phonon transmission signal from the mesa-without-trench signal – a method which eliminates the need for more complicated suspended structures as is typical for thermal conductance measurements. The silicon mesa platform is adaptable to studies of phonon transmission through nanostructures or nanomaterials by etching or depositing these into the ballistic path defined by the mesa. Finally, we have evinced spectrally resolved ballistic phonon transport in microstructures with submicron spatial resolution. Our STJ-based spectrometer provides a state-of-the-art tool for examining nanoscale effects on phonon transport.

CHAPTER 3

3 DIRECT MEASUREMENTS OF SURFACE SCATTERING IN Si NANOSHEETS: IMPLICATIONS FOR CASIMIR-LIMIT PREDICTED BY ZIMAN-THEORY♦

3.1. Abstract

Thermal transport in nanostructures is strongly affected by phonon-surface interactions, which are expected to depend on the phonon's wavelength and the surface roughness. Here we fabricate silicon nanosheets, measure their surface roughness (~1 nm) using atomic-force microscopy (AFM), and assess the phonon scattering rate in the sheets with a novel technique: a microscale phonon spectrometer. The spectrometer employs superconducting tunnel junctions (STJs) to produce and detect controllable non-thermal distributions of phonons from ~90 to ~870 GHz. This technique offers spectral resolution nearly 10 times better than a thermal conductance measurement. We compare measured phonon transmission rates to rates predicted by a Monte Carlo model of phonon trajectories, assuming that these trajectories are dominated by phonon-surface interactions and using the Ziman theory to predict phonon-surface scattering rates based on surface topology. Whereas this model predicts a diffuse surface scattering probability of less than 40%, our measurements are consistent with a 100%

♦ The content of this chapter was originally published as: J.B. Hertzberg*, M. Aksit*, O.O. Otelaja*, D.S. Stewart, and R.D. Robinson, "Direct Measurement of Surface Scattering in Si Nanosheets: Implications for Casimir-Limit Predicted by Ziman Theory," *Nano Lett.*, vol. 14, p. 403-415, 2014. (* These authors contributed equally to this work). Reprinted with permission from the American Chemical Society.

probability. Our nanosheets therefore exhibit the so-called ‘Casimir limit’ at a much lower frequency than expected if the phonon scattering rates follow the Ziman theory for a 1 nm surface roughness. Such a result holds implications for thermal management in nanoscale electronics and the design of nanostructured thermoelectrics.

3.2. Surface Scattering

3.2.1. Need for Frequency Resolved Measurements of Surface Scattering

Developing experimental tools to understand heat flow at nanoscale dimensions is a grand challenge of nanoscience.[24, 29, 30, 57, 96-99] While recent works have demonstrated the ability to accurately predict thermal conductivity in bulk materials;[100-102] phonons – the primary heat carrier in dielectrics – are expected to behave differently in nano-dimensional channels and structures.[54, 96, 99, 103-105] Our lack of experimental diagnostics in this area has created bottlenecks to understanding the basic physics of phonons. Unresolved questions include frequency-dependent phonon dynamics and transport through nanostructures, the effects of acoustic confinement on transport, and the frequency-dependence of phonons scattered by boundaries.

3.2.2. Casimir-Ziman Model

The limit on thermal conductivity through finite-sized channels has been historically described by the “Casimir limit.” In the classical kinetic model, thermal conductivity can be expressed as $\kappa_{ph} = \frac{1}{3} v_{ph} C_V \Lambda$, where v_{ph} is the group velocity of

the phonons, C_V is the specific heat, and Λ is the phonon mean free path.[2] In the boundary-scattering regime, in which phonon-surface scattering dominates all other phonon scattering mechanisms, the mean free path Λ will equal the surface-scattering mean free path l_{eff} . In the limit of extremely roughened surfaces the phonons will scatter diffusively from the walls and l_{eff} reduces to the ‘Casimir limit’ mean free path l_0 , which is a function of both the height and width of the channel.[106] For over seventy years, efforts to include the effects of surface roughness on both electronic and thermal transport have focused primarily on the concept of a specularity parameter, p , first introduced by Fuchs in 1938 in modeling electrical transport in thin films.[107] In the Boltzmann transport equation, p is employed as a phenomenological parameter to set boundary conditions on the solutions at the channel surfaces. A value $p = 0$ corresponds to a surface that diffusively scatters the phonons 100% of the time, while $p = 1$ corresponds to a perfectly specular surface (see also Supplementary Discussion 1).[29, 60, 108] Borrowing from diffraction theory, Ziman offered a physical basis for the specularity by expressing it as a function of the phonon wavelength λ and a surface roughness or ‘asperity parameter’ η , defined as the standard deviation of the local surface amplitude. In Ziman’s theory, the mean free path l_{eff} of a phonon of wavelength λ in a channel of characteristic dimension l_0 and roughness η may be described: [29, 60, 109-111]

$$p(\lambda) = e^{-\left(\frac{4\pi\eta}{\lambda}\right)^2} \quad (3.1)$$

$$l_{eff} = l_0 \frac{1+p(\lambda)}{1-p(\lambda)} \quad (3.2)$$

While the Ziman specularly parameter has been widely used to explain experimental measurements of phonon boundary scattering, the results are often contradictory or inconclusive. The mean free paths of acoustic phonons in ultra-thin silicon membranes measured with optical pump probe techniques[112] and the thermal conductance of silicon nanowires in the mesoscopic size limit[29] have been shown to match the Ziman expression. However, in cases where the model has been applied to thermal conductance measurements of suspended membranes[113] and nanocrystalline silicon[114], as well as radiative ballistic phonon transport in suspended membranes[115, 116], the Ziman expression alone does not explain the experimental values for mean free paths or specularly parameters. In addition, models that fit the specularly parameter to the measured thermal conductivity of Si nanowires often appear to require diffusive scattering beyond the Casimir limit[117, 118], or else permit multiple specularly values to fit the same data set.[2, 119] It remains unclear whether such disparities stem from unexplored experimental factors, or from limitations of the Ziman model. In particular, correlating thermal transport measurements to measured surface roughness at the nanoscale has not been widely attempted. To our knowledge, only one such study appears in the recent literature, employing single crystalline Si nanowires and a limited TEM projection method to assess surface roughness.[99] The remaining open questions motivate a more direct method for examining the validity of the model.

Existing experimental studies of the Casimir-Ziman theory rely on measurements of thermal conductivity κ_{ph} to probe the wavelength dependence of l_{eff} . [4, 29, 98, 120] Thermal phonons comprise a Planck distribution of frequencies.

In the Debye model, at low temperatures phonons in the interval $d\omega$ around frequency ω contribute to the specific heat C_V and thereby to κ_{ph} a fraction proportional to $e^{\frac{\hbar\omega}{k_B T}} \cdot \left(\frac{\hbar\omega}{k_B T}\right)^4 d\omega / \left(e^{\frac{\hbar\omega}{k_B T}} - 1\right)^2$. This distribution is peaked at the so-called 'dominant phonon frequency' $\omega_{dom} = 3.83k_B T/\hbar$ but is quite broad, and this naturally limits the spectral precision in assessing l_{eff} . [29, 120] [61] For instance, to measure scattering by phonons in the interval 390-410 GHz, we may measure κ_{ph} at $T = 5.0$ K, where $\omega_{dom} = 2\pi \cdot 400$ GHz. However, the phonons in the 20 GHz interval around the peak contribute only 3.6% of κ_{ph} . The measured value of l_{eff} will thus represent a much larger range of phonon frequencies.

Some recent studies have attempted to address this spectral imprecision by varying heating areas in order to distinguish different mean-free-path regimes. [105, 121, 122] A technique using a narrow distribution of phonons, on the other hand, would allow more precise assessment of the Casimir limit. Such narrow-band phonon sources are realizable using superlattice structures optically-pumped to produce acoustic emission [123], but can require complicated engineering, especially to couple the phonons into a nanostructure such as a nanowire or nanosheet.

3.3. Experiment

In this work, we utilize an alternative narrow-band phonon probe that is compact, simply fabricated, scalable, and excellently suited to studying scattering behavior in nanostructures: a microscale phonon spectrometer employing thin-film aluminum superconducting tunnel junctions (STJs) as phonon source and detector

(Figure 3.1a, 3.1b). Rather than measuring thermal conductance, this device measures the phonon power transmitted through nanostructures as a function of phonon frequency. It employs a non-thermal distribution of phonons, in which a large fraction of the phonon power lies in a band ~ 20 GHz around the peak.[124] For peak frequencies of several hundred GHz, the ratio of peak power to total power (P_{peak}/P_{tot}) exceeds 30%, thus enabling a spectral precision nearly 10 times that of a thermal measurement. We apply this technique to observe phonon transmission through arrays of silicon nanosheets (Figure 3.1b-d and Table 3.1), and compare our results to theory by incorporating careful measurements of the nanosheet surface roughness (Figure. 3.1e). Nanostructured silicon is of interest because of silicon's critical importance to semiconductor technology and its potential application as an efficient thermoelectric[96, 125], and nanosheet geometries have also received interest for thermoelectric applications.[114, 126, 127] Our precise measurement of surface roughness combined with precise control of phonon frequency allows for a unique characterization of the contributions of phonon surface scattering to the total phonon transmission, and this, in turn, has implications for predictions made by the Casimir-Ziman theory.

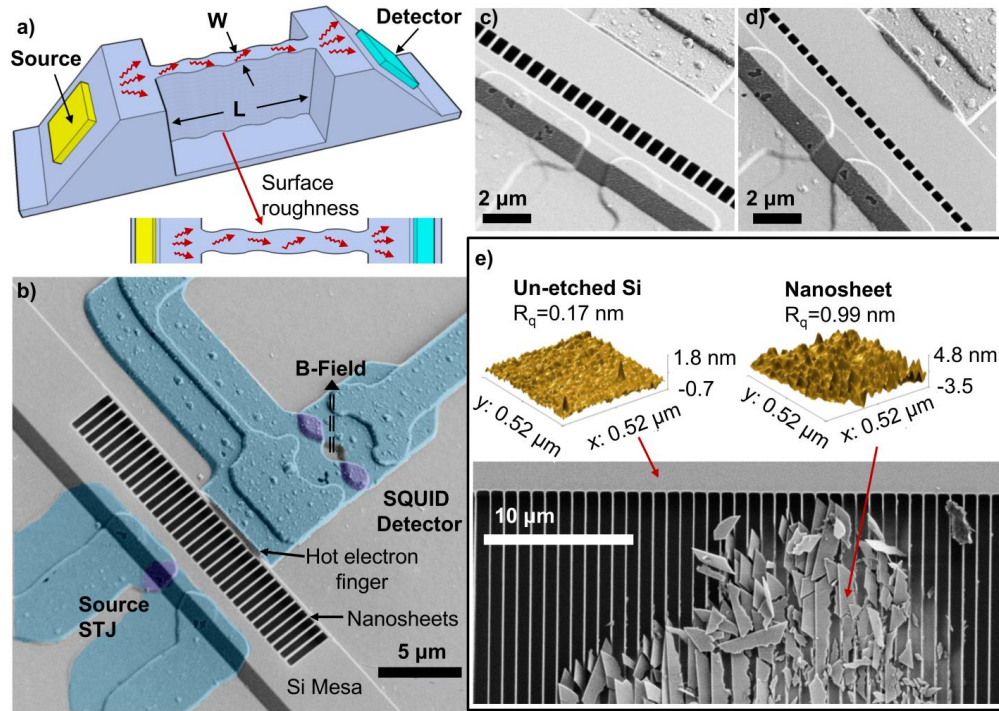


Figure 3.1: Design of Spectrometer to Probe Phonon Transmission through Silicon Nanosheet Arrays. a) Schematic of phonon transmission measurement geometry. Source transducer emits phonons of known frequency, which travel ballistically in line-of-sight through bulk silicon crystal, enter the nanosheet, scatter at the nanosheet surfaces, emerge from far end and are collected by a detector. b) False-colored SEM image of spectrometer containing nanosheet array type C (3.9 μm long nanosheets, see Table 1). Nanosheets are embedded into 0.8 μm high by 7 μm wide silicon mesa, formed on top of a 525 μm thick Si chip. The full set of measured nanosheets (see Table 1) has dimensions ranging from 0.2 to 3.9 μm long, 0.12 to 0.38 μm wide and 0.6 to 0.8 μm high. Source STJ comprises two Al layers of thickness 20 nm and 79 nm on side-wall of silicon mesa. Detector comprises a 'hot electron finger' in contact with opposite side-wall of the mesa, which intercepts the phonon flux, and a double-junction STJ to register the resulting tunnel current. c) SEM image of a spectrometer with 1 μm

long nanosheets (similar to type B, see Table 1). d) SEM image of spectrometer with nanosheet array type A (0.4 μm long nanosheets, see Table 1). e) (top) Atomic-force microscope measurement of surface roughness of typical un-etched Si wafer surface (top left), and Si nanosheet sidewall surface (top right) for comparison. Vertical scales are -0.7 to 1.8 nm (top left) and -3.5 to 4.8 nm (top right). Standard deviation R_q of surface amplitude is equivalent to roughness η . (bottom) SEM image of etched nanosheets showing method for breaking nanosheets to permit AFM measurements of their surface roughness.

Table 3.1: Geometry of phonon spectrometers and measured silicon nanosheets. Each lettered spectrometer comprises an STJ phonon source, nanosheet array, and STJ phonon detector fabricated on a 7 μm wide by 0.8 μm high mesa. All dimensions are in μm . Calculated specularly assumes roughness $\eta = 1$ nm.

Nano-sheet type	Array Pitch (μm)	Sheet Length, L (μm)	Sheet Width, W (μm)	Sheet Height (μm)	Source STJ Width (μm)	Detector Finger Width (μm)	Detector Finger Height (μm)	Simulated Nanosheet Transmission Factors		Measured phonon transmission signal $\delta I_d / \delta I_s$, peak frequency 400 GHz ($\times 10^4$)
								$[\Gamma_{los}(s \rightarrow ns \rightarrow d) + \Gamma_{sc}(s \rightarrow ns \rightarrow d) + \Gamma_{los}(s \rightarrow d)] \times 10^3$		
								Using specularity = 0	Using specularity found from Eq. (1) for $\eta_0 = 1$ nm, $f_{\text{peak}} = 400$ GHz and $P_{\text{peak}}/P_{\text{tot}} = 0.32$	
A	0.60	0.40	0.15	0.75	2.11	5.38	0.80	3.67	6.44	4.02 +/- 0.27
B	0.60	1.01	0.15	0.80	2.17	5.53	0.80	1.77	4.89	2.08 +/- 0.27
C	0.60	3.94	0.14	0.80	1.68	6.12	0.80	0.29	1.95	0.28 +/- 0.13
D	0.30	0.21	0.13	0.60	2.35	6.22	0.55	7.25	10.02	10.8 +/- 0.3
E	0.30	0.59	0.12	0.65	2.08	6.27	0.54	4.14	7.14	6.41 +/- 0.31
F	0.30	0.99	0.13	0.65	2.08	6.28	0.53	3.45	6.41	3.16 +/- 0.26
G	0.30	2.99	0.13	0.70	2.15	1.79	0.47	0.61	1.85	1.02 +/- 0.32
H	0.65	0.57	0.33	0.70	1.46	2.75	0.80	5.53	8.34	9.36 +/- 0.60
I	0.65	0.94	0.34	0.70	1.37	5.84	0.80	6.96	13.52	8.70 +/- 0.60
J	0.65	3.94	0.38	0.80	1.93	1.88	0.53	1.12	4.64	1.70 +/- 0.14

Our measurement and principles of operation are illustrated in Figures 3.1a, 3.1b, 3.2a, and 3.2b. A non-thermal phonon flux emerging ballistically from an STJ source transducer enters the nanosheet; the portion emerging at the far end is collected by the detector. We isolate narrow portions of phonon spectrum by modulating the source STJ's current (I_s) at a frequency of a few Hz and monitoring the resulting modulations in the detector current I_d . The measured differential transfer function $\delta I_d / \delta I_s$ tells us the fraction of the phonon power within the chosen spectrum that is transmitted to the detector.[33, 35, 66, 124]

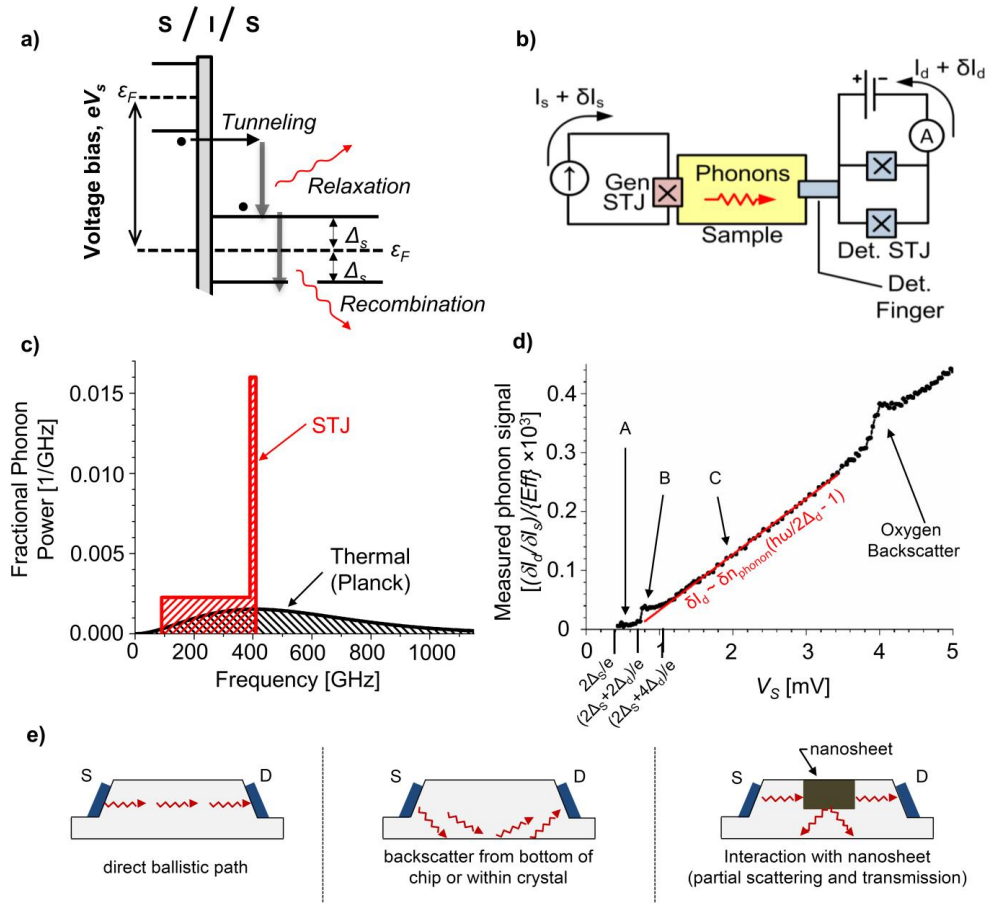


Figure 3.2: Phonon Spectrometer Operating Principles. a) Band diagram of quasiparticle tunneling and phonon decay processes in source STJ of superconducting

gap Δ_s , biased at voltage $V_s \geq 2\Delta_s/e$. Electrons tunnel from superconducting (S) layer through insulating (I) barrier, entering excited states in second superconducting (S) layer. As they decay (relax) from these states towards the edge of superconducting gap, they emit acoustic phonons. The resulting distribution of phonons exhibits a sharp step-edge at energy $eV_s - 2\Delta_s$. Further decay into the Cooper-paired state (recombination) emits additional phonons of energy $\sim 2\Delta_s$. **b)** Schematic of device operation and wiring. Bias current I_s holds source STJ at fixed voltage V_s while source modulation δI_s selects differential portion of emitted spectrum. Resulting modulation δI_d in detector current indicates differential phonon power transmitted through the sample. **c)** Spectral density of differential phonon power, estimated for source STJ of figure 1b, biased at ~ 2.1 mV. Modulation δI_s produces differential spectrum with peak frequency $(eV_s - 2\Delta_s)/h = 400$ GHz and width $\delta\omega/2\pi = 20$ GHz. For comparison, we have also included the power spectral density of thermal phonons, $\sim \frac{\hbar\omega^3 d\omega}{2\pi^2} / (e^{\hbar\omega/k_B T} - 1)$, which at temperature 6.8 K exhibits peak power at $\omega = 2\pi \cdot 400$ GHz. Each spectrum is normalized so that total detectable power (power carried by phonon frequencies $\omega/2\pi > 90$ GHz) is unity. **d)** Phonon transmission through bulk silicon, typical measurement. Differential transfer function $\delta I_d/\delta I_s$ indicates fraction of phonon power emitted from the source that arrives at the detector. Phonon emission & detection regimes A, B, C correspond to the three regimes of equation (3). Feature at $V_s \sim 4$ mV indicates ~ 870 GHz resonant backscatter from oxygen impurities in silicon substrate.[88] **e)** Phonon pathways between STJ source (S) and detector (D). Acoustic energy can either travel ballistically unimpeded in line-of-sight from source to detector

(rates $\dot{n}_{los}(s \rightarrow d)$ and $\dot{n}_{los}(s \rightarrow ns \rightarrow d)$), scatter from bottom of silicon chip or from scattering centers within the chip (\dot{n}_{bs}), or partially scatter within nanosheets placed between source and detector ($\dot{n}_{sc}(s \rightarrow ns \rightarrow d)$).

To produce narrow-band phonons, we exploit emission processes in superconducting tunnel junctions (STJs) at a temperature $T \cong 0.3$ K.[32, 33, 35, 43, 66, 69, 124] Our phonon source comprises an aluminum STJ having superconducting gap $2\Delta_s \cong 400 \mu\text{eV}$, biased at a voltage $V_s > 2\Delta_s/e$ to break the electrons out of the paired state into quasiparticle excited states, and drive them across the tunnel barrier (Figure 3.2a). The tunneled electrons relax to lower energies by emission of acoustic phonons in a broad non-thermal energy distribution with a sharp cutoff at energy $eV_s - 2\Delta_s$ (relaxation phonons in Figure. 3.2a).[66, 69, 90] The phonons are incoherent and to a first approximation will have both random polarization and random direction due to elastic scattering of the tunneled electrons within the Al film.[66] Further decay by recombination into Cooper pairs releases additional phonons of fixed energy $\sim 2\Delta_s$, which at bias voltages $V_s \gg 4\Delta_s/e$ contribute a small additional emitted power (recombination phonons in Figure 3.2a).[66] For a STJ of normal-state tunnel resistance R_n (Table 3.2 and Figure A1), the small AC modulation δI_s adds a modulation $\delta V_s = \delta I_s R_n$ to voltage V_s . The resulting modulation $2V_s \delta I_s$ in the power emitted by the STJ comprises a differential distribution of phonons that is sharply peaked at the spectral cutoff energy $\hbar\omega_{peak} = eV_s - 2\Delta_s$, as illustrated in Figure 3.2c.[33, 35, 66, 69] Taking the total differential phonon power $P_{tot} \approx 2V_s \delta I_s$ to be the integral $\int \hbar\omega \dot{n}_{ph,s}(\omega) d\omega$ of

power across the phonon distribution, a spectrum having $P_{peak} = P_{tot}$ would comprise phonons of frequency ω_{peak} emitted at rate $\dot{n}_{ph,s} = 2\delta I_s/e$ (Figure A2).[124]

Table 3.2: Electronic characterization of the phonon spectrometers for silicon nanosheet measurements. Each lettered spectrometer comprises an STJ phonon source, nanosheets, and an STJ phonon detector. Letters (Nanosheet Type) correspond to same devices as listed in Table 3.1.

Nanosheet Type	Source STJ R_n (Ω)	Det. STJ R_n (Ω)	$2\Delta_s$ (μeV)	$2\Delta_d$ (μeV)	Source IV Step Width (μeV)	Modul. Amp δV_s ($\mu\text{V rms}$)	Maximum Detector Linearity Range (GHz)	Det. Noise (fA/VHz)	Estimated Detector Efficiency $\{Eff\}$
A	700	128	414	363	76	7.37	643	110	0.11
B	733	123	418	356	81	7.37	696	140	0.11
C	935	167	419	367	58	9.82	491	90	0.08
D	762	116	415	353	71	9.84	619	55	0.12
E	786	113	411	353	71	9.87	696	118	0.12
F	790	115	409	365	72	9.06	649	130	0.12
G	726	117	405	351	66	10.32	698	80	0.12
H	1148	197	400	365	68	9.39	687	70	0.07
I	1221	211	403	368	70	8.80	687	120	0.07
J	895	138	394	367	54	8.00	693	60	0.10

Phonons are detected using a second STJ. The detector is formed in a double-junction (SQUID) configuration so that its Josephson current may be suppressed by an applied magnetic field, and is biased at voltage $\sim 180 \mu\text{V}$, allowing precise measurement of its quasiparticle tunnel currents. A ‘finger’ of superconducting Al serves to collect phonons from a well-defined region, and the total detector current I_d rises in response to total incident phonon flux (Figure 3.2b and Figure A3). The modulated detector current δI_d resulting from the differential portion of incident phonons is distinguished using a lock-in amplifier.[124] Since the detector STJ is sensitive only to phonons of energy greater than the gap value $2\Delta_d/h \approx 90 \text{ GHz}$, the measured phonon population

comprises phonons of frequencies between ~ 90 GHz and $(eV_s - 2\Delta_s)/h$, with a sharp peak at frequency $(eV_s - 2\Delta_s)/h$. In practice, this spectrometer allows us to probe our nanosheets quasi-monochromatically over a range of frequencies from ~ 100 to ~ 870 GHz (wavelengths ~ 60 to ~ 7 nm in Si).[124] In addition to studies of nanosheet surface scattering, this range should allow these spectrometers to probe a wide variety of effects in silicon. For instance, ~ 800 GHz phonons in Si have been reported to exhibit dispersion-related effects on the anisotropy of propagation.[92] The energy resolution of our measurement is ~ 60 - 80 μeV (~ 15 to 20 GHz). Sensitivity is limited by detector noise level, the lowest achieved being ~ 60 fA/ $\sqrt{\text{Hz}}$ at a modulation frequency of 11 Hz (Table 3.2). The corresponding noise equivalent power, NEP, for phonon detection is $\sim 10^{-15}$ W/ $\sqrt{\text{Hz}}$, or $\sim 2 \times 10^7$ phonons of energy $\sim 2\Delta_d$ per second per $\sqrt{\text{Hz}}$.[124]

The detector's response to incident phonons may be modeled by considering quasiparticle-phonon interactions.[124] If phonons of frequency ω strike the finger at a differential rate $\dot{n}_{ph,d}$, then the average differential rate of quasiparticle production $\dot{n}_{QP,ph}$ within the detector film should be

$$\begin{aligned}
 \dot{n}_{QP,ph} &= 0 && \text{for } \hbar\omega < 2\Delta_d \\
 \dot{n}_{QP,ph} &= T_{SiAl} \cdot \alpha_{abs}(\omega) \cdot 2\dot{n}_{ph,d}(\omega) && \text{for } 2\Delta_d \leq \hbar\omega < 4\Delta_d \\
 \dot{n}_{QP,ph} &= T_{SiAl} \cdot \alpha_{abs}(\omega) \cdot 2 \left(\frac{\hbar\omega}{2\Delta_d} - 1 \right) \dot{n}_{ph,d}(\omega) && \text{for } \hbar\omega \geq 4\Delta_d
 \end{aligned} \quad (3.3)$$

In equations (3.3), factor T_{SiAl} is the acoustic transmission factor for phonons transiting from Si into Al. For incidence angles not far from normal, this factor should be >0.9 .[68] The fraction of phonons $\alpha_{abs}(\omega)$ absorbed in the detector finger will

depend on the frequency-dependent phonon absorption lengths in Al, and is of order 0.5 for these phonon frequencies and the thickness of our detector film.[62, 124] To calculate the total differential rate $\langle \dot{n}_{QP,ph} \rangle$ of quasiparticles produced by incident phonons, equation (3.3) must be integrated across the differential spectrum of incident phonons. (In Supplementary Figure A2 we explore integrating across emitter spectra of the type depicted in Figure 3.2c.) The measurable differential detector tunnel current δI_d is then related to quasiparticle production rate via $\delta I_d = e \cdot \{Eff\} \cdot \langle \dot{n}_{QP,ph} \rangle$, where $\{Eff\}$ is a non-dimensional efficiency factor that accounts for the rate of tunnel current compared to other quasiparticle loss processes in the aluminum.[124] In practice, the measured $\delta I_d / \delta I_s$, plotted as a ‘spectrum’ against phonon peak frequency, follows closely the three regimes represented in equations (3.3). This is illustrated in Figure 3.2d, where the regimes are indicated by letters A, B, C.

To enable consistent comparisons among different detectors’ signals, we scale each measured differential transfer function $\delta I_d / \delta I_s$ by the value of $\{Eff\}$ for that detector.[124] We calculate $\{Eff\}$ for each detector using conventional theories of tunneling rate and quasiparticle recombination. This efficiency factor is inversely proportional to the detector’s tunnel-barrier resistance, which may be measured to allow calculation of $\{Eff\}$, resulting in typical values of ~ 0.1 (Table 3.2).[124] For moderate increases in total detector current I_d , this efficiency remains constant and therefore detector response remains linear and equation (3.3) remains valid.[124] In Table 3.2, we report for each spectrometer the corresponding maximum phonon peak frequency, designated ‘Maximum detector linearity range’. Reported phonon transmission signals are restricted to this range.

The spectrometers are fabricated using photolithography, wet chemical etch and thin-film deposition.[35] We first form $0.8\ \mu\text{m}$ high silicon ‘mesas’ on top of a $525\ \mu\text{m}$ thick Si chip (Figure. A4). The top surface of the mesa is a [100] plane of the Si crystal. For phonon scattering studies, we embed nanosheet arrays of desired geometry into the bulk silicon of the mesa. The entrance to each array is positioned $1.9\ \mu\text{m}$ from the side-wall holding the STJ phonon source. The transmission through an array of identical nanosheets is larger and more easily measured than through a single sheet. We define the structures using electron-beam lithography and selectively etch them into the silicon using a non-scalloping DRIE plasma etch technique (Figure 3.1b,c,d , Table 3.1, Supplementary Methods 1 and Supplementary Figures A5 and A6).

Our nanosheets have height 0.6 to $0.8\ \mu\text{m}$ and width $0.12\ \mu\text{m}$ to $0.38\ \mu\text{m}$ (Table 3.1). The nanosheets are anchored to the substrate, so that their bottom end offers an avenue for phonons to escape, while their top surface is smooth polished Si and therefore likely to reflect specularly. The plasma-etched side-walls, however, constitute the great majority of surface area and therefore we expect the roughness of these walls to dominate the phonon scattering in the channel. The Casimir-limit mean free path l_0 should therefore be similar to the sheet width. At room temperature, such dimensions are comparable to published estimates of 250 - $300\ \text{nm}$ for the mean free path of phonon thermal transport in silicon.[2, 128] At temperatures below $1\ \text{Kelvin}$, however, phonon-phonon scattering is negligible.[92, 108, 129] Spontaneous decay of acoustic phonons, while possible even at very low temperatures, should also be negligible for frequencies below $1\ \text{THz}$, as shown previously by researchers.[130] Surface scattering should therefore dominate. We performed atomic force microscope (AFM) measurements of

etched nanosheet sidewall surfaces (Figure 3.1e and Figure. A5). AFM offers a highly accurate two-dimensional measurement, in contrast to the line-edge roughness found by methods such as TEM.[98, 131] The measurement region, several phonon wavelengths in extent, exhibits an approximately Gaussian distribution of heights. The roughness η is given by the RMS deviation of ~ 1 nm from the mean amplitude.

3.4. Results

A total of ten different silicon-nanosheet arrays were measured (Table 3.1). All of these arrays were embedded into $7 \mu\text{m}$ wide silicon mesas. In Figure 3.3a we present transmission measurements through four arrays of similar cross-section dimensions but differing sheet lengths. Transmission through an un-etched (bulk) Si mesa is also presented for comparison. (In these data, the contribution of substrate backscatter has been subtracted from the signal, as described below in equation (3.4). (See Figure A7 for comparison with a spectrometer in which a trench blocks the line-of-sight phonon transmission). These four measured spectra (along with six additional spectra, Figure A8) exhibit two significant behaviors: 1) Signals show a sharp decrease as the length of the channel is increased. 2) The transmission as a function of phonon peak frequency is very similar to that seen in bulk silicon. Introducing nanosheets into the phonons' path sharply reduces the transmission, but appears to do so independent of frequency. We explore the frequency dependence more closely by trying to quantify the shape of the transmission spectra curves. In Figure 3.3b, we apply linear fits in the frequency regimes $\sim 160\text{-}300$ GHz (colored lines) and ≥ 300 GHz (black lines) (See also Supplementary Table A1). In the bulk Si measurement (Figure 3.3b, light blue), both

frequency ranges fit well to a single straight line – consistent with the STJ detector’s dependence on incident phonon energy (Eq. (3.3)). Ballistic transmission of phonons through bulk Si is frequency-independent, and various spectrometers measuring through bulk Si present a similar spectral shape (Figure 3.2d). A subtly different behavior emerges, however, when measuring transmission through nanosheets. For phonon peak frequencies above 300 GHz, the signal values clearly lie on a straight line, but below this frequency they fit best to a different line of distinctly higher slope. (Such behavior cannot be readily explained by phenomena within the source and detector STJs. In Figure A2, we show that in principle, frequency-dependent phonon absorption in the detector would raise, not lower, the slope as phonon peak frequency rises.) We can infer from this behavior that phonon transmission through these nanosheets exhibits frequency-dependence only below ~ 300 GHz. At higher frequencies, the strict similarity to the bulk behavior suggests the onset of totally diffusive phonon scattering — the Casimir limit.

The combination of these trends – weak frequency dependence but strong dependence on path length – is consistent with a specularity $p \ll 1$ and short mean free path (l_{eff}) for phonon scattering (equation (3.2)). The Ziman expression, however, does not predict a low specularity throughout this frequency regime: Taking the experimentally-determined roughness $\eta = 1$ nm, and averaging $p(\lambda)$ over a phonon spectral distribution with peak frequency at 400 GHz and $P_{peak}/P_{tot} = 0.32$,^[124] the mean specularity is $p = 0.68$, indicating that the phonons should reflect specularly 68% of the time from this surface.

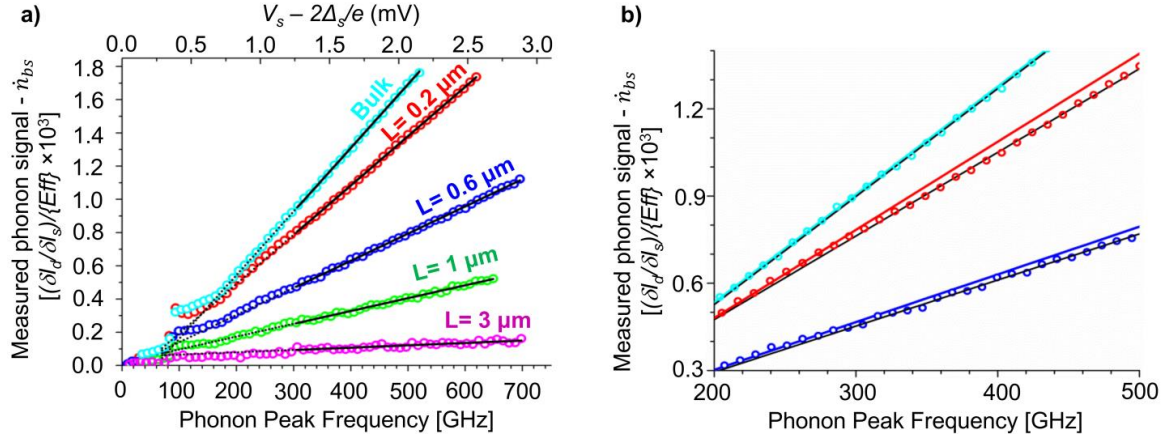


Figure 3.3: Phonon Transmission Spectra through Nanosheet Arrays. a) Measured transmission signal $(\delta I_d/\delta I_s)/\{Eff\}$ vs. phonon peak frequency for nanosheet arrays D, E, F, G (see Table 3.1) and representative bulk Si sample, after subtraction of measured \dot{n}_{bs} spectral levels. Comparison to the bulk signal indicates that frequency-dependence of the phonon transmission through nanosheets is small throughout the measured spectral range, and negligible above ~ 300 - 400 GHz. The linear fits to each signal are computed for the data above 300 GHz. b) Linear fits to the bulk spectrum and two of the nanosheet spectra in a) for regions above and below 300 GHz: The black lines are linear fits for signals ≥ 300 GHz while the colored lines are linear fits for signal between ~ 160 - 300 GHz.

To more quantitatively predict the signal levels at frequencies above and below the Casimir limit, we must consider the different components of phonon flux arriving at the detector. Below 1 THz, scattering lengths for phonon-phonon and isotope scattering in Si should be much longer than the length of our nanosheets, even exceeding the $500 \mu\text{m}$ thickness of our sample chip.[92, 108] The rate $\dot{n}_{ph,d}$ of phonons striking the

detector therefore comprises four possible components, where s (source), d (detector) and ns (nanosheets) indicate the phonon pathways: (Figure 3.2e and Supplementary Discussion A2 and A3.)

$$\begin{aligned}
& \dot{n}_{los}(s \rightarrow d) \text{(line-of-sight through bulk Si, frequency-independent)} & (3.4) \\
& \dot{n}_{bs} \text{(back-scattering from substrate, possibly frequency-dependent)} \\
& \dot{n}_{los}(s \rightarrow ns \rightarrow d) \text{(line-of-sight transit through nanosheets, frequency-independent)} \\
& \dot{n}_{sc}(s \rightarrow ns \rightarrow d) \text{(scattering \& reflection through nanosheets, frequency-dependent)}
\end{aligned}$$

As the quasiparticle diffusion length in aluminum at 0.3 K is of order 100 μm [75], the measured signal level \dot{n}_{bs} may include the contribution of phonons that strike the wiring leads far from the junction or the mesa.

In the simplest case, transmission through bulk silicon with no nanosheets, the detected phonon rate should be $\dot{n}_{ph,d} = \dot{n}_{bs} + \dot{n}_{los}(s \rightarrow d)$. By defining a line-of-sight ballistic transmission factor $\Gamma_{los}(s \rightarrow d)$ (having value between 0 and 1), and taking the phonons to be emitted at a single frequency (i.e. assuming for simplicity that $P_{peak} = P_{tot}$), we may express $\dot{n}_{los}(s \rightarrow d)$ as $\dot{n}_{los}(s \rightarrow d) = (2\delta I_s/e) \cdot \Gamma_{los}(s \rightarrow d)$. This bulk transmission factor may be found simply geometrically:

$$\Gamma_{los}(s \rightarrow d) = \int dA_s \int \frac{d\Omega_d}{2\pi} T_{AlSi} \cdot 2 \cdot \cos \psi \cdot T_{SiAl} \cdot A_{foc}(\theta, \phi) \quad (3.5)$$

Here A_s is the fraction of the source STJ visible from the detector (i.e., if only 30% of the source STJ lies on the sidewall facing the detector, then we expect only 30%

of the phonons produced by δI_s to participate in the measurement). The factor $2 \cdot \cos \psi$ introduces a ‘Lambert law’ distribution to the intensity of emitted phonons where ψ is the angle relative to the surface normal of the source STJ sidewall.[63, 75] T_{AlSi} and T_{SiAl} are acoustic transmission factors of order 1, while integration over $d\Omega_d$ and dA_s covers all solid angles subtended by the detector with respect to all visible elements of the source STJ.[35, 66, 92-95] (We note that by properly defining dA_s and $d\Omega_d$, equation (3.5) may also be re-stated to express the fraction of phonons transiting from source to detector via specular reflection at the mesa top surface.) The factor $A_{foc}(\theta, \phi)$ is a ‘phonon focusing’ factor indicating how much the elastic anisotropy in the crystal enhances ($A_{foc} > 1$) or reduces ($A_{foc} < 1$) the phonon intensity along the particular crystal direction (θ, ϕ) . [94] We find this factor by a Monte Carlo simulation algorithm – a random k -vector direction and polarization is assigned to a phonon, and the Christoffel equation is solved for cubic symmetry and the known elastic constants of Si, to find the resulting group velocity (See Supplementary Methods A2, Supplementary Discussion A4 and Supplementary Table A2). [94, 132] Repetition over all k -vector orientations reveals that the phonon flux concentrates along preferred directions. Figure 3.4 shows a map of phonon focusing factors $A_{foc}(\theta, \phi)$ centered on the (110) crystallographic direction of Si (See Supplementary Figure A9 for a similar calculation in the (100) direction, and comparison to literature data). In our measurements, A_{foc} ranges from 0 to 25 within the integrand of equation (3.5).

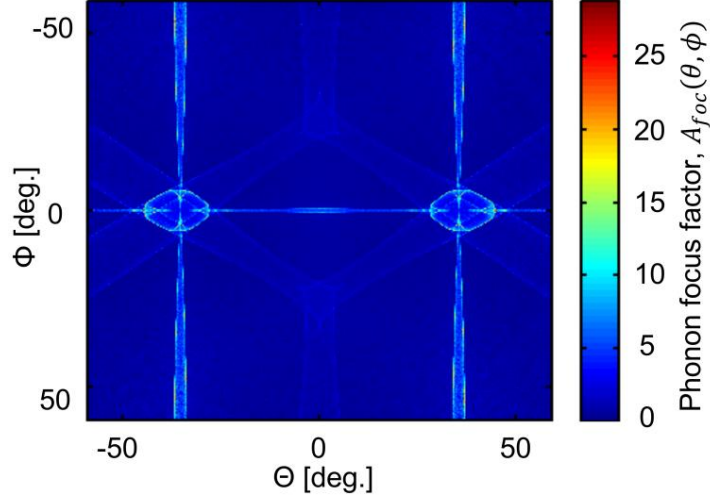


Figure 3.4: 2D Phonon Focusing Factor Map of Angles Relative to Si [110] Direction Generated by Monte Carlo Algorithm. Focusing factors $A_{foc}(\theta, \phi)$ are presented for angles ϕ and θ ranging from -59° to 59° with average angular resolution of $\sim 0.12^\circ$. Angle $(\theta, \phi) = (0^\circ, 0^\circ)$ is [110] direction, angle $(\theta, \phi) = (45^\circ, 0^\circ)$ is [100] direction and angle $(\theta, \phi) = (0^\circ, -90^\circ)$ is [001] direction. In the Monte Carlo simulations, approximately equal numbers of phonons are assigned to slow transverse, fast transverse and longitudinal polarizations. (Plot was prepared by M.Aksit)

If we experimentally vary $\Gamma_{los}(s \rightarrow d)$ while keeping all other parameters constant, we expect a linear correspondence between the measured signal and the value of $\Gamma_{los}(s \rightarrow d)$. In Figure 3.5 we present such a measurement. We designed and constructed ten spectrometers transmitting through bulk Si mesas of widths 7, 10 or 15 μm and employing detector fingers of width 3 and 6 μm , so that a large range of transmission factors were represented. All devices were fabricated at the same time on a single silicon wafer, so that all parameters except for $\Gamma_{los}(s \rightarrow d)$ were held as constant as possible for all ten of the devices. The spectrometer dimensions were

verified by inspection in an SEM, to a precision of ~ 30 nm (Figure 3.1c, 3.1d and Figure A4). We mounted the chips similarly so that substrate back-scattering levels \dot{n}_{bs} should also be consistent among all the measurements. We made twelve separate transmission measurements through these devices. Because detector STJ tunnel resistance could not be reproduced precisely from one device to another, we were careful to divide each signal level by the value of $\{Eff\}$ for that particular detector [75, 88] (see also Table A3). According to equations (3.3) and (3.4), the measured detector tunnel currents δI_d should therefore all be proportional to $\dot{n}_{ph,d} = \dot{n}_{bs} + (2\delta I_s/e) \cdot \Gamma_{los}(s \rightarrow d)$.

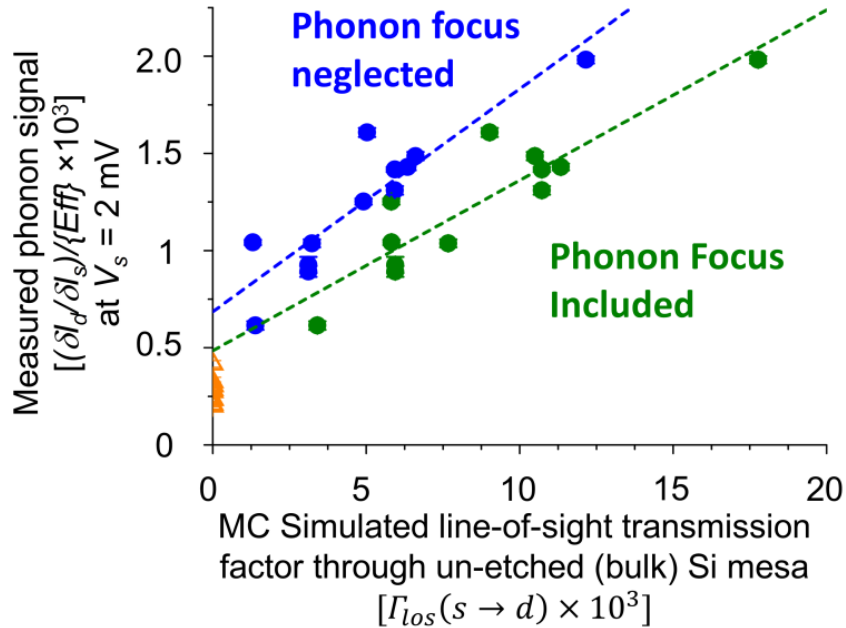


Figure 3.5: Measured Phonon Transmission Signals through Un-etched (bulk) Si Mesa and Comparison to Simulated Transmission Factors. Vertical axis is measured signal produced by phonon transmission at $V_s = 2.0$ mV through un-etched (bulk) Si mesa in ten different geometries. Horizontal axis is Monte Carlo (MC) calculated transmission factor for line-of-sight transmission. Closed circles: measured transmission, comprising

backscatter \dot{n}_{bs} plus line-of-sight $\dot{n}_{los}(s \rightarrow d)$ contributions. Open orange triangles: independent measurements of backscatter signal \dot{n}_{bs} on the same sample chips. Vertical error bar at each data point is standard error of average of measured signal value. Green circles: MC simulation includes phonon focusing effects in single crystalline Si. Blue circles: phonon focusing neglected. Dashed blue and green lines correspond to linear fits for blue and green circles. (Plot prepared by M. Aksit)

In Figure 3.5, each closed-circle data point represents a measurement of the differential transfer function $\delta I_d / \delta I_s$ of one device at a voltage of $V_s = 2.0$ mV (phonon peak frequency ~ 390 GHz). This value is plotted against the calculated transmission factor $\Gamma_{los}(s \rightarrow d)$ for that device. For comparison, we also plot the measured signals against an alternate calculation of transmission factors that neglects phonon focusing ($A_{foc}(\theta, \phi) = 1$ in equation (3.5)). The open-triangle symbols are measurements of $\delta I_d / \delta I_s$ made at $V_s = 2.0$ mV, on these same chips, for pairs of source and detector STJs that do not share a line-of-sight. These twelve values, which should offer an independent measurement of \dot{n}_{bs} at this V_s level, have an average value 2.7×10^{-4} and standard deviation 6.1×10^{-5} .

The $\Gamma_{los}(s \rightarrow d)$ transmission factors were calculated according to equation (3.5) using a Monte Carlo algorithm. This approach is based on ray-tracing of phonons within the region enclosed by the device dimensions.[133] The geometric boundaries are set by the mesa dimensions, and location and extent of STJ source and ‘finger’ detector. We assume the top surface and tilted sidewall surfaces of the mesa to be perfectly smooth. The bottom plane of the mesa is assumed to be an ‘open’ surface

through which phonons may escape. Each iteration of the algorithm traces the trajectory of a single phonon within the silicon, beginning at the STJ source located on the mesa (111) sidewall. The frequency of the phonon and its corresponding wavevector (k vector) magnitude in silicon are fixed. Within the area of the STJ source, a point is randomly chosen for the origin of the trajectory. To account for effects of ‘phonon focusing’ on the trajectory, we randomly select the k vector’s direction from a Lambertian distribution at the source position, and solve the 3-dimensional equations of motion (Christoffel equations) for the group velocity.[92-94, 132] Since the source plane is not a symmetry plane for the Si crystal, some of the randomly-selected k vector directions result in phonon group velocities pointing out of the mesa sidewall; in these cases we must reverse the direction of the calculated group velocity vector. After leaving the source, the phonon’s trajectory is traced in a straight line until it reaches a surface. A phonon striking a perfectly smooth surface reflects specularly and continues in a straight-line trajectory. If it strikes the detector sidewall within the boundaries of the detector, the trajectory is terminated and the phonon is added to the tally of detected phonons. If the phonon crosses the bottom plane of the mesa or displaces laterally more than 30 μm away from the source STJ, it is assumed to be out of the system and is counted as an undetected phonon. The MC simulation is repeated 4 million times to find with high accuracy the fraction reaching the detector. (See Supplementary Discussion A5 and Supplementary Figure A10 and A11 for verification that the MC algorithm matches the prediction of a more conventional geometric calculation.)

In Figure 3.5, the linear relationship between experimental signal values and the corresponding simulated phonon transmission factors indicates that we have accurately

calculated $\Gamma_{los}(s \rightarrow d)$ in these ten devices, properly accounted for differences in detector tunneling efficiency $\{Eff\}$, and held all other relevant parameters constant. A linear-regression fit of measured $\frac{\delta I_d/\delta I_s}{\{Eff\}}$ against calculated $\Gamma_{los}(s \rightarrow d)$ finds a slope of 0.088 ± 0.013 , with intercept $(4.9 \pm 1.2) \times 10^{-4}$ and an R-square goodness of fit of 0.81. The intercept and the independently-measured \dot{n}_{bs} levels are nearly in agreement, within uncertainties. This result demonstrates that we can model line-of-sight ballistic phonon transport in our system using $\dot{n}_{ph,d} = \dot{n}_{bs} + (2\delta I_s/e) \cdot \Gamma_{los}(s \rightarrow d)$ as predicted by equation (3.4), and implies that \dot{n}_{bs} may be independently measured and subtracted from phonon spectral data by using non-line-of-sight source/detector pairs (Figure A7). The small remaining discrepancy between the intercept and the independently-measured \dot{n}_{bs} may indicate additional phonon scattering processes occurring in the bulk substrate, for instance impurity scattering and/or scattering from crystal defects. We expect such processes to be independent of mesa and nanosheet geometry, so that at worst they would constitute a fixed offset in the estimate of \dot{n}_{bs} . We may take the uncertainties in the regression fit to represent the maximum systematic error to be expected in determining a phonon transmission factor Γ from a signal value $\delta I_d/\delta I_s$. From this error, we may place an upper limit on the spatial resolution achievable with this type of device: For signals traversing a 7 micron wide Si mesa, we can expect to resolve separations as small as 400 nm between adjacent detectors. This resolution could be readily improved by simple changes such as placing the entire source STJ onto the mesa side-wall. Figure 3.5 also verifies that phonon focus effects are necessary in order to accurately model the line-of-sight ballistic transport. Assuming

that phonons propagate isotropically ($A_{foc} = 1$) leads to a poorer match of the intercept to the independently-measured \dot{n}_{bs} values. Future studies of phonon transmission in finite sized structures should take account of such effects.[105]

The linear behavior appearing in Figure 3.5 indicates that the contribution of \dot{n}_{bs} may be readily subtracted from measured signals, and that our models of phonon propagation and of the source and detector STJ behavior predict accurately the relative signal sizes as the transmission factor is varied. In order to predict absolute signal sizes, we must express the differential transfer function ($\delta I_d / \delta I_s$) quantitatively in terms of phonon transmission factor. To achieve this we may first take the differential phonon emission rate in terms of differential emitter current ($\dot{n}_{ph,s} = 2\delta I_s / e$), and multiply it by the transmission factor Γ (equation (3.5)) to find $\dot{n}_{ph,d}$. We next must use this value of $\dot{n}_{ph,d}$ to calculate the detector response (equation (3.3)), integrating across the phonon spectrum (Figure 3.2c) to find detector quasiparticle production rate $\langle \dot{n}_{QP,ph} \rangle$. Next, to account for the relationship between quasiparticle production rate and differential detector current, we must scale $\langle \dot{n}_{QP,ph} \rangle$ by the detector tunneling efficiency $\{Eff\}$. Finally, we multiply by e to find δI_d . If we undertake this calculation for a phonon distribution peaked at ~ 390 GHz, we find that $\frac{\delta I_d}{\delta I_s} / \{Eff\}$ is equal to ~ 8 times the transmission factor (Figure A2). For comparison, the measured slope in Figure 3.5 is 0.088. Evidently our prediction of absolute phonon flux is missing a scaling factor, which remains constant across all of the devices in this data set because all device parameters were held fixed except for transmission factor $\Gamma_{los}(s \rightarrow d)$ and detector efficiency $\{Eff\}$. We note that nanosheet transmission data analyzed similarly in Figure

3.6 (as discussed below) has a slope of 0.139 — a remarkably similar number to the one found in Figure 3.5, despite the fact that bulk and nanosheet transmission factors were calculated using two models of very different complexity, and that the two sets of measurements were made months apart on different sets of devices resulting from very different microfabrication processes. (The higher slope in Figure 3.6 may reflect the fact that the detectors used in these measurements employed slightly thicker Al films, leading to higher absorption α_{abs} .) A likely explanation for the missing scaling factor is that we may be greatly overestimating detector efficiencies $\{Eff\}$. [124] Future resolution of this issue would permit accounting for absolute phonon flux.

Having verified for the case of bulk transmission that the experimental signal values $\delta I_d/\delta I_s$ scale linearly with transmission factor, we can now model the nanosheet transmission factors to shed light on whether the transmission is in the Casimir limit. If nanosheets are present, then we can use equation (3.4) to express the expected phonon arrival rate $\dot{n}_{ph,d}$ at the detector, defining additional transmission factors $\Gamma_{los}(s \rightarrow ns \rightarrow d)$ and $\Gamma_{sc}(s \rightarrow ns \rightarrow d)$.

$$\begin{aligned} \dot{n}_{ph,d}(\omega) &= \dot{n}_{los}(s \rightarrow ns \rightarrow d) + \dot{n}_{sc}(s \rightarrow ns \rightarrow d) + \dot{n}_{bs} + \dot{n}_{los}(s \rightarrow d) \quad (3.6) \\ &= \left(\frac{2\delta I_s}{e}\right) \Gamma_{los}(s \rightarrow ns \rightarrow d) + \left(\frac{2\delta I_s}{e}\right) \Gamma_{sc}(s \rightarrow ns \rightarrow d) + \\ &\quad \dot{n}_{bs} + \left(\frac{2\delta I_s}{e}\right) \Gamma_{los}(s \rightarrow d) \end{aligned}$$

The scattering transmission factor $\Gamma_{sc}(s \rightarrow ns \rightarrow d)$ will depend on the nanosheet geometry, surface roughness, and source and detector geometries. The last term $\dot{n}_{los}(s \rightarrow d)$ in equation (3.6) accounts for any regions where there may be a path

for bulk line-of-sight transport between source and detector, for instance, if the nanosheets are not etched to the full depth of the mesa (0.8 μm). Then phonons may move ballistically through the un-etched bulk silicon beneath them (Figure. A6).

To model the behavior $\Gamma_{sc}(s \rightarrow ns \rightarrow d)$ of phonons scattering and reflecting multiple times from nanosheet surfaces, we apply our Monte Carlo ray-tracing algorithm to the more complicated case of a mesa that includes an array of nanosheets. We define dimensions, spacing and position of the array based on SEM images, and include 35 nanosheets in the model. (In our devices, the array size varied from 30 to 40 sheets, but the 3-5 nanosheets at each end of the array contribute negligibly to the number of detected phonons.) A phonon of frequency ω leaving the source is traced in a straight line. Upon striking a nanosheet wall or other surface, its change of motion is modeled according to the specularity (p) of the surface. For a given ω , we find p according to the Ziman theory (see Eq. 1), taking 6 km/s as the mean phonon velocity in silicon. AFM measurements of nanosheet sidewalls (Figure 3.1e) indicate a roughness of $\eta = 1$ nm. We assume that the nanosheet sidewall surfaces and the gaps between the nanosheets have this roughness, and that all other surfaces are smooth and have $p = 1$. To determine the phonon's change of motion, a random real number (s) between 0 and 1 is selected. If $s < p$, the phonon reflects specularly at the intersection point. If $s > p$, the phonon scatters diffusively: it is re-emitted at the intersection point with a randomized direction that adheres to a Lambertian distribution. (Phonon focusing effects are not taken into account for this re-emission.[2, 108]) Upon leaving the surface, the phonon's trajectory is again traced in a straight line until it strikes another surface. This procedure is repeated, with the phonon interacting with as many surfaces

as necessary until it is either lost or detected (see Figure A12 and Table A4 for test cases for the Monte Carlo algorithm). For a given phonon frequency, the transmission factor is found as the fraction that strike the detector, out of 4 million trial phonons. Finally, the entire simulation is repeated at a 3 GHz interval across the phonon spectrum (90 to 400 GHz) and these transmission factors are combined in a weighted average based on the phonon power spectral density (Figure 3.2c), to find the predicted transmission factor $\Gamma_{los}(s \rightarrow ns \rightarrow d) + \Gamma_{sc}(s \rightarrow ns \rightarrow d) + \Gamma_{los}(s \rightarrow d)$. [124]

To compare our measured signal against scattering rates expected in Ziman theory, we measure the differential transfer function $\delta I_d / \delta I_s$ in ten different nanosheet arrays for a phonon distribution peaked at 400 GHz (Figure 3.3a and Figure A8). As in the bulk measurements, we attempted to fashion all devices identically except for their geometries – all spectrometers were fabricated simultaneously onto 7 μm wide Si mesas, and later patterned and etched to form the nanosheets. In this set of measurements, we estimated \dot{n}_{bs} on each sample chip by independent measurement at the same peak frequency (400 GHz), and subtracted this value from the nanosheet transmission signals. (Estimated uncertainties in this subtraction appear as error bars in our data.) We plot these signal values $\delta I_d / \delta I_s / \{Eff\}$ in Figure 3.6 (y-axis) against calculated values of $\Gamma_{los}(s \rightarrow ns \rightarrow d) + \Gamma_{sc}(s \rightarrow ns \rightarrow d) + \Gamma_{los}(s \rightarrow d)$.

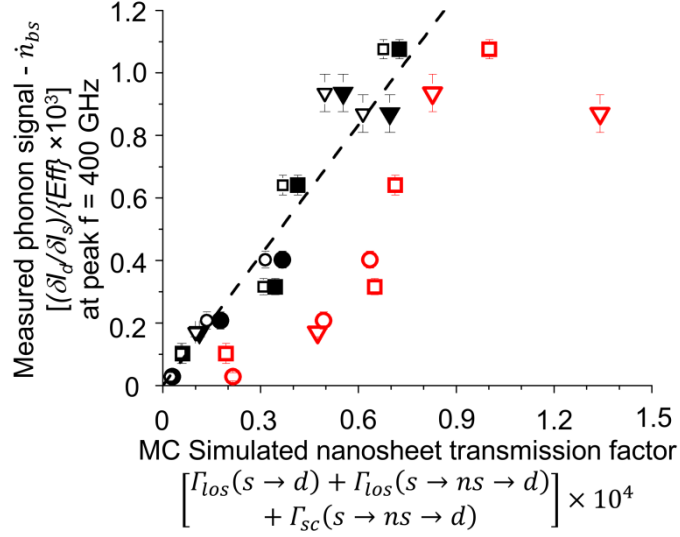


Figure 3.6: Measured Phonon Transmission Signals through Si Nanosheet Arrays: Comparison to Modeled Transmission Factors. Vertical axis is the measured signal for phonon transmission. Horizontal axis is the phonon transmission factor calculated using Monte Carlo (MC) algorithm. Circles: arrays A to C (widths $\sim 0.15 \mu\text{m}$). Squares: arrays D to G (widths $\sim 0.13 \mu\text{m}$). Triangles: arrays H to J (widths $\sim 0.35 \mu\text{m}$) (see Table 3.1). All measurements employ a phonon distribution peaked at 400 GHz. Vertical error bars derive from standard error of signal average in each measurement, and uncertainties in subtraction of \dot{n}_{bs} . The model includes phonon focusing effects in single crystalline Si. Phonon transmission factor comprises surface scattering term $\Gamma_{sc}(s \rightarrow ns \rightarrow d)$, and line-of-sight transmission terms $\Gamma_{los}(s \rightarrow ns \rightarrow d)$ and $\Gamma_{los}(s \rightarrow d)$, as described in Eq. (3.6). Red points: simulation employs Ziman expression, Eq. (3.1), to find nanosheet side-wall specularity, assuming roughness of $\eta = 1 \text{ nm}$ (as measured using AFM, see Figure 3.1e). Black closed points: simulation assumes specularity $p = 0$ at nanosheet side walls. Black open points: simulation completely neglects nanosheet surface-scattering ($\Gamma_{sc}(s \rightarrow ns \rightarrow d)$ set to zero). The fraction of phonons transmitted through

each nanosheet array is calculated for the estimated phonon frequency distribution (Figure 3.2c) of peak frequency 400 GHz, as described in the text. The zero specular prediction matches the measured signal with high confidence (dashed line: a linear fit to black closed points has $R^2 = 0.97$ and zero intercept). The prediction of the Ziman model, by contrast, exhibits a poor match to data. (Plot prepared by M. Aksit)

In simulating phonon transmission through nanosheets we try three possibilities. In the first case (Figure 3.6, black open symbols), we assume $\Gamma_{sc}(s \rightarrow ns \rightarrow d) = 0$, i.e., we neglect any phonons scattering from nanosheet surfaces and consider only phonons that either travel in direct ballistic line-of-sight from source to detector, or reflect specularly from the mesa top and strike the detector. In the second case (Figure 3.6, black closed symbols) we assume specularity $p = 0$ for the nanosheet sidewalls regardless of the phonon frequency. This condition corresponds to the Casimir-limit regime. In the third case (Figure 3.6, red open symbols) we use the Ziman theory of Eq. (3.1) to calculate the specularity $p(\lambda)$ for each phonon-surface interaction, as described above. The mesa-top surface comprises un-etched Si, which has a very low roughness (Figure. 3.1e) and therefore for all three cases this surface is assumed to be purely specular. In the third case, where the phonon transmission should be frequency-dependent, we weight the calculated transmission factors across the estimated STJ emission spectrum. As already shown for the bulk phonon transmission (Figure 3.5), a linear relationship between the experimental signal values and the corresponding simulated phonon transmission factors should indicate that the transmission factors are accurately calculated. Additionally, because the background scattering (\dot{n}_{bs}) has been

subtracted from the experimental signal values, the line should pass through the origin.

Examination of Figure 3.6 indicates that assuming purely-diffusive sidewalls ($p = 0$) predicts the relative magnitudes of the phonon transmission signal accurately, whereas calculating specularities based on the Ziman expressions and the measured sidewall roughness does not. For instance, consider nanosheets $\sim 0.12 \mu\text{m}$ wide and $0.6 \mu\text{m}$ long (Type E, Table 3.1). Ziman theory predicts that if the length is increased to $3 \mu\text{m}$ (type G), the transmitted flux should reduce by $3.7\times$, whereas if $p = 0$ is assumed then theory predicts a reduction of $6.8\times$. In fact, in the experiment the signal of type G is reduced by $6.3\times$, compared to type E. Or consider nanosheets $\sim 0.14 \mu\text{m}$ wide and $1 \mu\text{m}$ long (Type B). Increasing the length to $4 \mu\text{m}$ (type C) reduces the measured transmission by $7.4\times$, whereas Ziman theory predicts $2.3\times$, and the $p = 0$ assumption predicts $6.1\times$. If we take the plot of the zero-specularity prediction vs. measured data, and fit a straight line, we find a slope 0.139 ± 0.007 and a fit confidence (adjusted- R^2) of 97%, with an intercept consistent with zero, while the Ziman prediction offers a much poorer match and a negative intercept, which is physically incorrect (See Supplementary Figure A13 for the distribution of specularity values predicted by Ziman theory for the estimated STJ emission spectrum interacting with a 1 nm surface roughness). The zero-specularity predictions, moreover, match the data well for peak frequencies 400, 500 and 600 GHz (Figure A14). This frequency-independent behavior is consistent with ‘Casimir limit’ scattering.

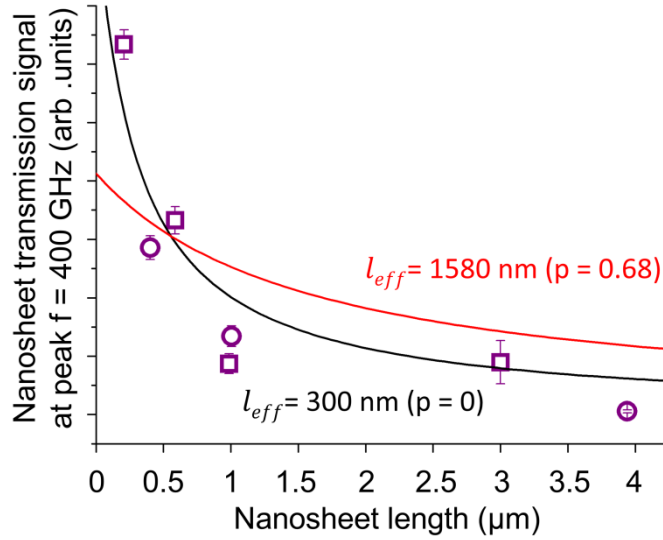


Figure 3.7: Estimated Transmission Through Si Nanosheet, as a Function of Nanosheet Length, for Phonon Distribution Peaked at 400 GHz. The signal values shown in Figure 3.6 for the nanosheet arrays are corrected here to find a best-estimate of the single-sheet transmission factor, as described in the text. Vertical error bars derive from those in Figure 3.6 by the same set of corrections. Circles: arrays A to C. Squares: arrays D to G. (See Table 1). Also plotted is the predicted transmission fraction $l_{eff}/(l_{eff} + L)$ for boundary-scattering mean-free paths $l_{eff} \approx 0.30 \mu\text{m}$ (black) and $l_{eff} \approx 1.58 \mu\text{m}$ (red), corresponding to specularities $p = 0$ and $p = 0.68$, respectively. (Plot prepared by M. Aksit and J.B. Hertzberg)

While Figure 3.6 demonstrates that measured signal levels are inconsistent with our model’s predictions employing the Ziman theory and the measured surface roughness, it offers little direct insight into the boundary-scattering mean-free path l_{eff} . Published expressions for the ‘Casimir limit’ mean free path l_0 of a rectangular

channel[114, 129] differ from our nanosheets in assuming that the channel is isolated and that all four walls have uniform specularity. Nonetheless, using these expressions to provide a rough estimate, the nanosheets in arrays A through G (Table 3.1) have Casimir-limit mean free path $l_0 = 0.26$ to $0.33 \mu\text{m}$. For $p = 0.68$, we find from Eq. (3.2) that $l_{eff} = 1.37$ to $1.73 \mu\text{m}$. As a prediction for transmission Γ in our nanosheets, we can use the expression $\Gamma = l_{eff}/(l_{eff} + L)$, which models the transport regime where there are both ballistic and diffusive contributions to transmission.[134-136] Whereas this model takes Γ to be the ratio of phonons exiting to those entering a nanosheet, the measured values $\delta I_d/\delta I_s/\{Eff\}$ in Figure 3.6 represent a ratio of phonon fluxes measured far from the entrance and exit of an array of nanosheets. Therefore, to compare the data of Figure 3.6 to the transmission model we must first extract from the data a value Γ_{sheet} for transmission through a single sheet. To account empirically for the demonstrated inefficiencies in the detection, we divide by the measured line slope ~ 0.09 shown in Figure 3.5. To account for un-etched portions of the mesa beneath the array, we subtract an estimate of line-of-sight ballistic transmission $\Gamma_{los}(s \rightarrow d)$ in each measurement. (See Eq. (3.6).) Finally, we correct for the line-of-sight ballistic propagation between the STJ source and the nanosheet entrance-faces, and between the nanosheet exit-faces and the detector. Using Eq. (3.5) and the dimensions listed in Table 3.1, a factor is computed for each nanosheet, and these are then summed to find a correction factor for the array. These combined corrections and scaling may be expressed as $\Gamma_{sheet} = \frac{[\delta I_d/\delta I_s/\{Eff\}]/0.09 - \Gamma_{los}(s \rightarrow d)}{\sum_i \Gamma_{los}(s \rightarrow ns) \cdot \Gamma_{los}(ns \rightarrow d)}$, with the sum ranging over all sheets in the array. This correction should accurately extract the relative values of Γ_{sheet} from

the measured transmission of different arrays. In principle, a measurement of the $L \ll l_{eff}$ case (for which the model predicts $\Gamma = 1$) could provide a further absolute scaling. Since this is not available, we adjust the height of model curves as a fit parameter. The result appears in Figure 3.7, along with model predictions of Γ for $l_{eff} = 0.30 \mu\text{m}$ ($p = 0$ case) and for $l_{eff} = 1.58 \mu\text{m}$ ($p = 0.68$ case). The model curve heights (4.4 and 2.0, respectively) are of order 1 as expected. The match for the $p = 0$ case is far better, having an adjusted R^2 value of 0.84, whereas the $p = 0.68$ prediction yields an adjusted R^2 value of 0.44.

3.5. Conclusions on Surface Scattering Studies

In combination with the observations of Figure 3.3 that show frequency independent spectral structure above ~ 300 GHz, the behavior in Figure 3.6 and Figure 3.7 strongly implies that our nanosheets exhibit Casimir-limit behavior at frequencies as low as 400 GHz. A purely line-of-sight prediction ($\Gamma_{sc}(s \rightarrow ns \rightarrow d) = 0$; Figure 3.6, black open symbols) offers yet another useful comparison. The data matches this prediction nearly as well as the diffusive sidewall ($p = 0$) prediction. Evidently, very few phonons that strike the nanosheet side-walls reach the detector, indicating a surface scattering rate far in excess of the Ziman prediction for 1 nm roughness. Geometric effects such as acoustic confinement within the sheets or scattering from impedance-mismatch at the ends of the sheets are unlikely to explain the observed behavior, since our nanosheets are all at least 120 nm wide, significantly larger than the phonon wavelengths.[26, 29, 97]

If we assume that phonon-surface interactions dominate the phonon trajectory,

this result raises the question whether the surface scattering rates could be better predicted by alternatives to the Ziman theory. One notable limitation of the Ziman theory is that the specular constant (equation (3.1)) is derived only for the case of normal phonon incidence. A more advanced model has been proposed to account for the incident angle of the phonons.[109, 137] However, this model predicts that phonons at normal incidence have the lowest specular constant, while at grazing angles, the specular constant will approach one. This more sophisticated model would therefore predict a transmission factor in even greater disagreement with our measurements. Other alternative theories go beyond the Casimir-Ziman model in considering more than just the height of the surface roughness. [96, 98] Waves scattering from a surface that exhibits lateral correlations in its roughness structure may exhibit more complicated effects of phase coherence that enhance the degree of scattering. Such theories may offer insight into our nanosheet measurements.

Another question arising from our result is whether additional surface scattering mechanisms may be at play besides the effects of surface roughness. Contamination, amorphization or excess oxidation of the silicon surface could all reduce its specular constant. For instance, recent molecular dynamics simulations predict that adding an amorphous layer to a Si nanowire surface can reduce the wire's thermal conductance more than 70%.[126] In our nanosheet fabrication process, we took precautions to limit damage or contamination of the etched surfaces (See Supplementary Methods A1). During the etch, a polymer coating protected the sidewall surfaces from direct ion bombardment. This coating was subsequently stripped in an oxygen plasma that likewise avoids direct ion bombardment of the sample. Surface oxidation in air remains a possibility, one that

would likely apply to many other studies of silicon nanostructures. While our fabrication procedures make it unlikely that phonons are scattering from defects within the bulk silicon, future studies should supplement the AFM roughness measurement with a careful elemental and atomic structural analysis of the nanosheet surfaces and sub-surfaces.

Our observations of excess phonon scattering rates suggest implications for thermal conductivity in nanostructures.[96, 125, 138] For instance, for a Si nanowire with ~ 1 nm surface roughness at $T \sim 5$ K, our result suggests that if surface-scattering dominates all other mechanisms, then the wire's thermal conductance should be 4 times lower than is typically assumed based on Casimir-Ziman theory and the dominant phonon frequency approximation. Even at room temperature, such enhanced surface scattering will strongly impact the thermal conductivity of nanostructures. Recent studies suggest that at 300 K, nearly half of the thermal energy in Si is carried by phonons whose mean free paths are longer than $1 \mu\text{m}$. [105, 121, 122] The microscale STJ phonon spectrometer thus offers a new tool to explore important surface-scattering phenomena.

CHAPTER 4

4 ENHANCEMENT OF PHONON BACKSCATTERING DUE TO CONFINEMENT OF BALLISTIC PHONON PATHWAYS IN SILICON AS PROBED WITH A MICROFABRICATED PHONON SPECTROMETER ♦

4.1. Abstract

In this work, the mechanism for enhanced phonon backscattering in silicon is investigated. An understanding of phonon propagation through substrates has implications for engineering heat flow at the nanoscale, for understanding sources of decoherence in quantum systems, and for realizing efficient phonon-mediated particle detectors. In these systems, phonons that backscatter from the bottom of substrates, within the crystal or from interfaces often contribute to the overall detector signal. We utilize a microscale phonon spectrometer, comprising superconducting tunnel junction emitters and detectors, to specifically probe phonon backscattering in silicon substrates ($\sim 500 \mu\text{m}$ thick). By etching phonon ‘enhancers’ or deep trenches ($\sim 90 \mu\text{m}$) around the detectors, we show that the backscattered signal level increases by a factor of ~ 2 for two enhancers versus one enhancer. Using a geometric analysis of the phonon pathways, we show that the mechanism of the backscattered phonon enhancement is due to confinement of the ballistic phonon pathways and increased scattering off the enhancer walls. Our result is applicable to the geometric design and patterning of different substrates that are employed in phonon-mediated detection.

♦ The content of this chapter was accepted for publication in Appl. Phys. Lett. on 10/07/2015.

4.2. Introduction

Understanding the dynamics of phonons in low-dimensional structures and systems has spurred interesting research efforts in recent years. The motivation for these phonon studies include the need for efficient thermal management and control at the nanoscale,[4, 24, 29, 139] the need for development of robust cryogenic particle detectors,[10-12] and the need to suppress decoherence of superconducting qubits in quantum information processing.[17, 140] In semiconductors and insulators, phonons are the dominant thermal energy carriers; hence, a thorough understanding of their propagation and scattering in nanoscale geometries will enable the development of efficient thermoelectric and microelectronic cooling devices.[6, 54] Although, the significant amount of nanoscale phonon literature have focused on reducing the phonon contribution to heat flow in order to enhance the thermoelectric figure of merit, enhancement of phonon conduction is needed in some applications. For instance to mitigate the effects of localized heat spots in microelectronic devices, increased thermal conductivity is needed.[141]

A crucial step for achieving better understanding of nanoscale phonon transport is the ability to spectrally resolve phonon transmission. To this end, several researchers have embarked on efforts to realize spectroscopic methods that provide frequency resolved information on phonon propagation. These techniques range from superconducting tunnel junction (STJ) spectroscopy,[33, 35, 124, 142] mean free path spectroscopy[105, 143, 144] and thermal conductivity spectroscopy.[121] In our previous work we have demonstrated the use of STJs as phonon transducers for the emission and detection of phonons in microscale geometries[124] and have utilized this

advancement to study frequency dependent surface scattering in silicon nanostructures.[142] In these experiments the measured phonon signal includes contributions from both a line-of-sight signal from emitter to detector, and a backscattered phonon signal from the substrate (phonons whose original trajectory do not intercept the detector solid angle, but due to reflections from an interface are redirected to the detector). We developed a geometric model to account for the line-of-sight signal, but the backscattered phonon contributions have not been studied in detail. While several studies have previously probed backscattered phonons,[61, 145, 146] the experiments were either performed with techniques that have no frequency selectivity or in cases where spectroscopic techniques were used; the experiments were focused on backscattering from metal/substrate interfaces. With a submicron spatial resolution,[124] our spectrometer allows for studying the effects of geometric structuring on backscattered phonons in substrates.

4.3. Phonon Backscattering and Phonon Enhancers

Phonon backscattering has important ramifications for the fidelity of experiments on nanoscale phonon transport, especially at low temperatures where the effective phonon mean free path is large compared to the substrate thickness. Phonons can backscatter from the bottom of the substrate, within the crystal, or from an interface.[142, 146] The control of backscattered phonon via their enhancement or reduction can have implications for nanoscale thermal management. Phonon backscattering in the substrates could also be important in the understanding of phonon-substrate interactions in applications such as quantum computing and microelectronic

cooling.[147, 148] Hence, an experimental investigation of the mechanism of phonon backscattering is needed.

In this work, we show how phonon ‘enhancers’ or deep trenches fabricated around phonon detectors of an STJ-based phonon spectrometer,[124, 142] can act as scattering interfaces, and lead to an enhancement of backscattered phonon signals. We describe a simple geometric analysis that shows that the origin of this enhancement is due to the confinement of the ballistic phonon pathways for non-line-of-sight signals. This geometric confinement would, in essence, lead to a reduction of phonon mean free path, cause the scattering of phonons within the confined volume, and enhance the number of phonons that reach the detector. Such enhancement mechanism could be either advantageous or detrimental depending on specific applications discussed above.

The experimental geometry utilized to study phonon backscattering is depicted in Figure 4.1. In our earlier work,[35, 124] we designed a microscale phonon spectrometer by isolating a raised mesa in silicon, fabricated aluminum STJs on the sidewalls of these mesas to act as phonon emitters and detectors, and used this mesa/STJ structure as a platform for investigating ballistic phonon studies in silicon. By etching a shallow trench in this mesa, the phonons that ordinarily should travel ballistically in line-of-sight from emitter to detector are impeded as shown in Figure 4.1a. Thus, phonon emission and detection with this mesa and trench geometry constitutes the backscattered phonon signal \dot{n}_{bs} . Phonons can backscatter from the bottom of the substrate or from scattering centers within the chip. The SEM image of the spectrometers is shown in Figure 4.1b,c. These spectrometers are fabricated using photolithographic patterning, anisotropic chemical etch, and double-angle electron-beam evaporation. (Complete spectrometer

fabrication details have been previously reported).[124] Phonons that strike the detector film break Cooper pairs[37] and the resulting quasiparticles diffuse until the tunnel through the junction and are measured as an increase in detector tunnel current. Since diffusion length in Al is $\sim 250 \mu\text{m}$, [65] phonons that strike the detector films within $250 \mu\text{m}$ of the tunnel junctions are considered as contributing to the measured signal; hence, we can assume that the overall length of the detector length relevant to phonon collection of backscattered phonon is $\sim 250 \mu\text{m}$. Using photolithography and deep reactive-ion etch, the phonon enhancers acting as additional phonon backscattering interfaces were patterned and etched on both or one side of the detector wiring traces as shown in Figure 4.1b,c. The enhancers are $\sim 10 \mu\text{m}$ wide, $\sim 10 \mu\text{m}$ offset from the detector film, and aligned along the detector film traces up to a radius approximately equal to the quasiparticle diffusion length.

From a strictly geometric standpoint, these phonon enhancers will reduce the solid angle subtended by the detector films with respect to the bottom of the substrate, and this reduction will depend on their depth. All the devices are batch fabricated; hence, only one enhancer depth is considered. To verify the depth of the enhancers ($\sim 90 \mu\text{m}$), the chips were cleaved along an enhancer with a diamond scribe and the sidewall of the enhancer is revealed as shown in Figure 4.1c. These enhancers are about two-orders of magnitude deeper than the mesa trenches. The mesas are $0.7 \mu\text{m}$ high, $7 \mu\text{m}$ wide and $\sim 250 \mu\text{m}$ long. Each mesa consist of two spectrometers (emitter and detector pair) spaced apart by $\sim 140 \mu\text{m}$. The substrate thickness is $\sim 500 \mu\text{m}$.

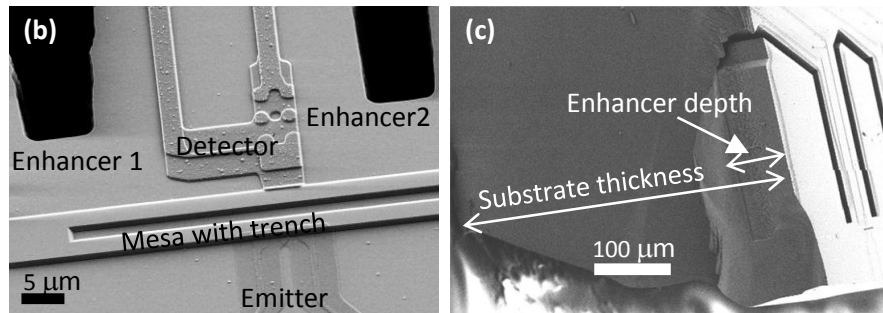
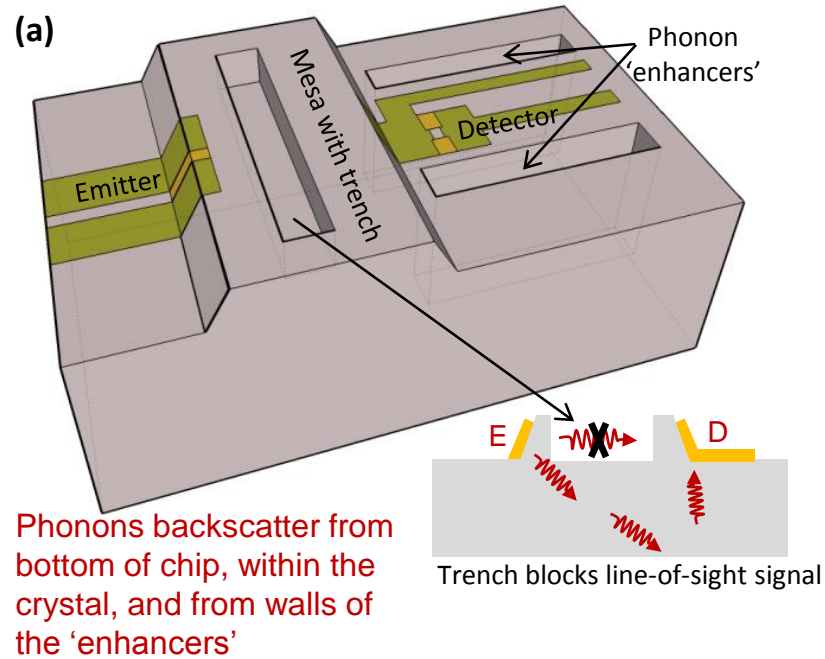


Figure 4.1: Experimental geometry for backscattering measurements. (a) Schematic of phonon backscattering measurement geometry showing mesa with trench, emitter, detector, and phonon 'enhancers' around the detector wiring trace. The trench in the mesa blocks the line-of-sight phonon between emitter (E) and detector (D); hence, only backscattered phonons are measured. (b) SEM image of a typical spectrometer, used for backscattered phonon studies. (c) SEM image of a wafer cleaved along a phonon enhancer and tilted to the side in order to reveal the full depth ($\sim 90 \mu\text{m}$) of phonon "enhancers."

4.4. Backscattered Phonon Enhancement Results

Phonon transport measurements were performed for spectrometers with and without phonon enhancers (or additional backscattering interfaces) around the detectors. By applying a stepped dc voltage $V_e > 2\Delta_e$ (2Δ is the superconducting gap) to the emitter STJ, paired electrons are broken and excited quasiparticles tunnel across the junction leading to the emission of phonons in to the adjoining silicon. In addition, an ac modulation voltage is applied to allow a thin slice of the entire phonon spectrum to be probed. Only phonons of energy $\hbar\omega > 2\Delta_d$ will break paired electrons in the detector films and register as an increase in tunnel current. A more rigorous description of the principle of phonon emission and detection are described elsewhere.[124] The measured phonon spectrum is a differential response of detector to the modulated portion of the incident phonon flux. The backscattered (line-of-sight between detector and emitter is blocked by a mesa trench) phonon spectra are scaled by detector efficiencies [36] and plotted against the peak phonon frequency $\left(\frac{eV_e - 2\Delta_e}{h}\right)$, as shown in Figure 4.2. The spectra with blue circle represents detectors with no additional backscattering interfaces or deep trenches; hence, this is the nominal backscattered signal \dot{n}_{bs} . The red and green circle spectra represent detectors with one and two additional backscattering interfaces respectively. In addition to backscattering measurements performed on each of the spectrometers in Figure 4.2, ‘cross’ measurements were taking for comparisons. A ‘cross’ measurement is configured so the emitter and detector do not directly face each other but are offset laterally by ~ 140 μm , creating a phonon pathway that falls outside of the phonon enhancer geometry. The ‘cross’ measurement is thus utilized as a control experiment to verify that the enhanced

backscattering observed in the detector of one spectrometer is due to a confined ballistic phonon path with respect to that spectrometer's emitter. The measured backscattering spectra shows a step increase in the measured phonon signal at the detector cut-off frequencies (~85 GHz), which shows the detection of relaxation phonons. Above this cut-off frequency, the backscattered phonon signal \dot{n}_{bs} shows a strong dependence on the number of phonon enhancers available. The \dot{n}_{bs} signal level is increased with the introduction of an enhancer along one side of the detector, and this increase is further enhanced with enhancers on both sides of the detector. This enhancement of phonon detection is observed throughout the range of frequencies measured. Although the solid angle subtended by the detector films with respect to the bottom of the substrate is reduced with the introduction of enhancers around the detector (**Figure B2** and **Table B2**) the phonons registering at the detector increases, suggesting that the phonons bouncing off the bottom of the chip play a little role in the observed phonon enhancement. The 'cross' spectra do not evince enhancement with or without introduction of enhancers around the detector, suggesting that the enhancement occurs in a region of the substrate very close to the detector films and not due to backscattering from scattering centers far away in the bulk.

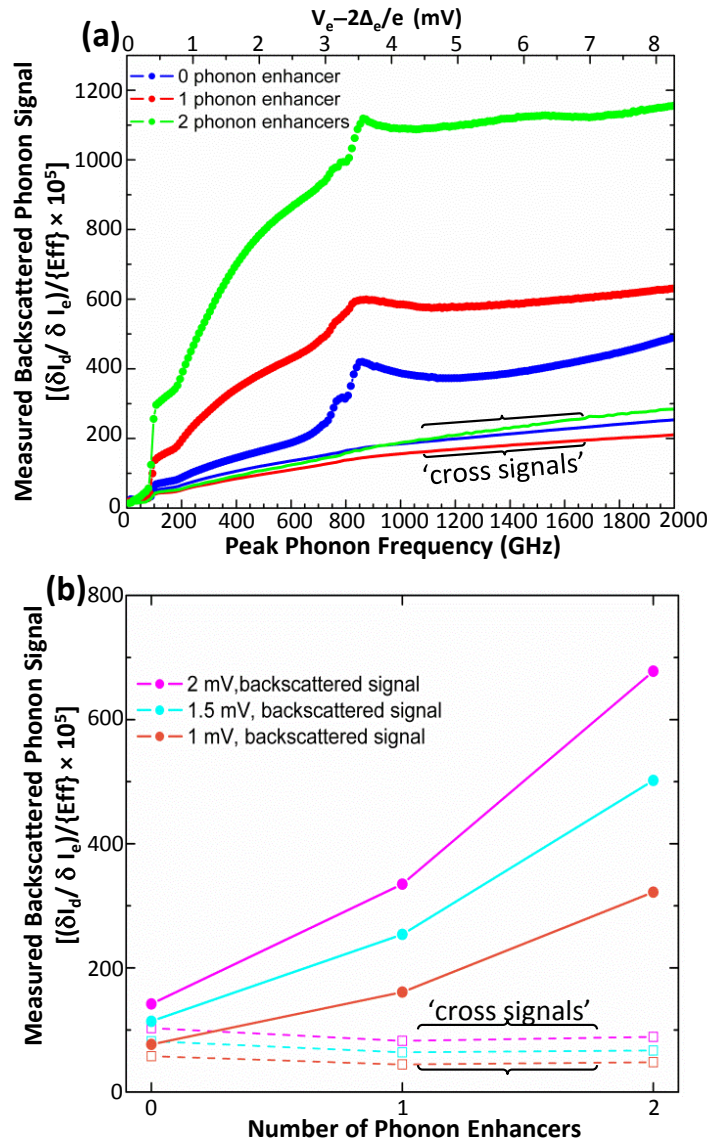


Figure 4.2: Measured phonon backscattering with and without enhancers. (a) Phonon backscattering spectra with no phonon enhancer, a single phonon enhancer, and double phonon enhancers. The cross signal represents measurements of phonon signal from one emitter to a detector located far away ($\sim 140 \mu\text{m}$) laterally from the emitter, thus providing a control signal. (b) Plots of backscattered phonon signal level versus number of enhancers at different emitter voltages (or phonon frequencies).

For clearer examination of the enhancement, Figure 4.2b shows the backscattered and cross signal level at selected emitter voltages ($V_e = 1$ mV, 1.5 mV, and 2 mV) with the number of phonon enhancers. (This voltage range is selected in order to remain within the maximum detector linearity regime for all the detectors.[124]) The ratio of backscattered signal level with and without the enhancers [$\dot{n}_{bs} : \dot{n}_{bs+1 \text{ enhancer}} : \dot{n}_{bs+2 \text{ enhancers}}$] is [1.00: 2.36: 4.78], [1.00: 2.22: 4.40], [1.00: 2.09: 4.20] for $V_e = 2$ mV, 1.5 mV and 1 mV respectively. The ratio of the enhanced backscattered signal for detectors with one versus two enhancers is ~ 2 for the selected emitter voltages. This enhancement factor, the suggestion that the backscattering enhancement occurs close to the detector, and the symmetrical placement of the enhancers with respect to the emitter indicate that phonons reflect off the walls of the enhancers with some redirected to the detector film. As a result, the ballistic phonon pathway through the substrate is confined. These results highlight the dramatic effect geometrical structuring could have on ballistic phonon propagation.[97, 149]

A closer examination of the oxygen resonance peaks in Figure 4.2a shows that backscattering from scattering centers within the substrate is an unlikely source of the enhancement. [142, 146] At peak phonon frequency just above ~ 800 GHz, we observe resonance peaks in the measured backscattered spectra, which have been previously attributed to resonance backscatter from oxygen impurities in silicon.[88, 124] This absorption band (with a bandwidth of ~ 12 GHz) is due to the bending motion of the Si—O—Si bond as discussed in previous work by Bosomworth et al.[150] This oxygen peak is visibly absent in the ‘cross’ spectra, suggesting that any resonance excitation within the substrate will only register at the detector if it occurs close to the detector.[88]

With the detector being $\sim 140 \mu\text{m}$ away from the emitters in cross measurements, we can assume that for any substrate backscattering to register at the detector, it must occur at least within a $140 \mu\text{m}$ radius. This assumption also allows the cross measurement to be used as a reasonable control measurement to the backscattering studies. In Figure 4.3, we plot the relative intensities of the oxygen backscatter peak between 600 to 1400 GHz. This plot assumes that the detector response is linear in this frequency window without any resonance scattering. The broadening of the peak is likely due to a convolution of the absorption band and the emitted phonon spectrum. The relative amplitude and width ($\sim 250 \text{ GHz}$) of the oxygen resonance peak detector shows negligible difference with or without enhancers, which evinces that the enhancement effect is not due to scattering centers in the substrate, but due to phonon scattering within the confined ballistic pathway created by the enhancers around the detector.

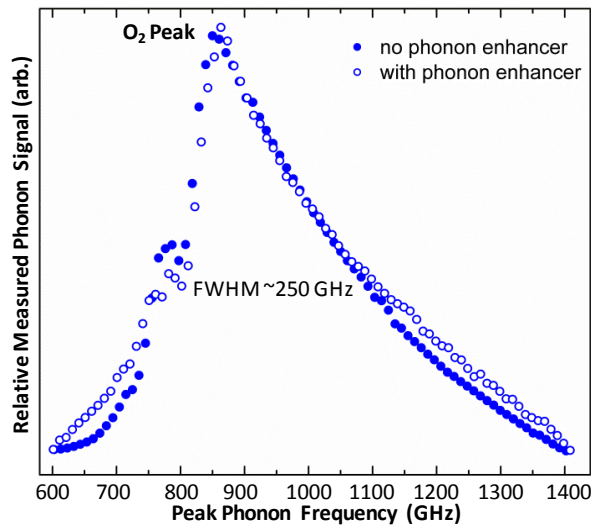


Figure 4.3: Plot of relative intensity of oxygen resonance peaks of backscattered signals with and without enhancers. The negligible differences seen in this plot suggests that

the enhancement of phonons registered at the detector is not due to resonant scattering within the substrate.

4.5. Geometric Analysis of Phonon Backscattering

To further quantify the enhancement factor of the backscattered phonons, a geometric analysis of the ballistic phonon trajectories is carried out upon simplifying the experimental geometry as illustrated in Figure 4.4a. This figure includes an isometric sketch of the simplified backscattering geometry in addition to an orthographic projection of the various planes and sections. This description allows an estimation of phonons that backscatter and are detectable based on the angular range of phonon emission. The emitter (Em) is assumed to be a point source of isotropic ballistic phonons.

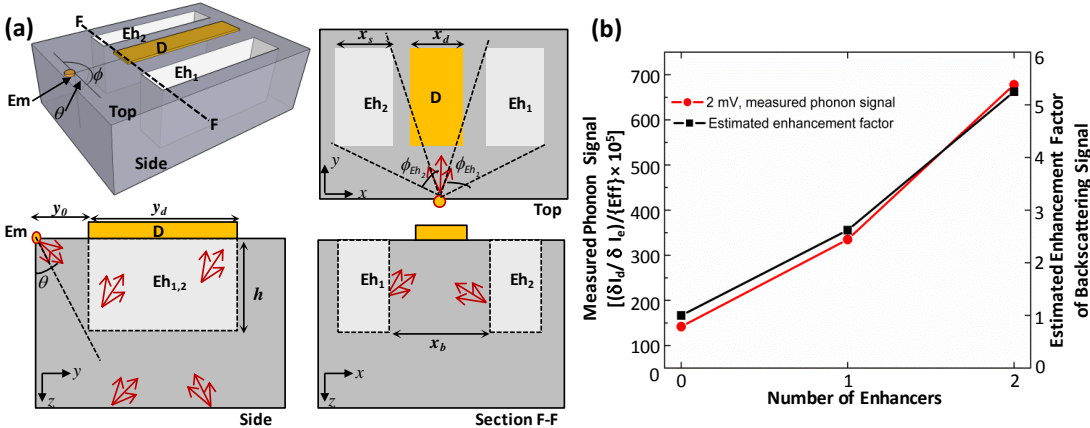


Figure 4.4: Analysis of enhanced phonon backscattering mechanism. (a) Simplified phonon backscattering measurement geometry. An orthographic projection of the simplified geometry is also shown. The widths of the detector film (x_d), enhancers (x_s) and confined silicon substrate between the enhancers (x_b) are $\sim 6 \mu\text{m}$, $\sim 10 \mu\text{m}$, and ~ 40

μm respectively. h is the height of the blockers ($\sim 90 \mu\text{m}$). y_0 ($\sim 20 \mu\text{m}$) and y_d ($\sim 250 \mu\text{m}$) are the distances between the emitter and detector and approximate length of the detector and the enhancers. (b) Plots of measured backscattered phonon signal level versus estimated enhancement factor of the backscattering signals obtained from geometrical analysis.

Each phonon is emitted within a quarter-sphere centered at the emitter in a direction $f(\varphi, \theta)$ dependent on the azimuthal and polar angles φ and θ respectively; such description of phonon trajectories have been previously employed in the past.[75, 151] The quarter-sphere coordinate was chosen because only phonons emitted towards the detector are considered; hence, the full range of isotropic emission without the presence of enhancers is $0 \leq \theta \leq \pi/2$ and $0 \leq \varphi \leq \pi$ and the full phonon interaction volume is $\int_0^\pi d\varphi \int_0^{\pi/2} \sin \theta d\theta \int_0^{r_m} r^2 dr$ (r_m is maximum radius corresponding to the phonon mean free path). The detector (D) geometry is also simplified to a single film with width proportional to the width of the actual detector traces. Since the backscattering geometry assumes that there is no line-of-sight between the emitter and detector, the detected phonon signals arise from backscattering from the bottom of the chip and walls of the enhancers (Eh_1 and Eh_2) (as shown with the red arrows in the Figure 4.4a). The widths of the detector film (x_d), enhancers (x_s) and confined silicon substrate between the enhancers (x_b) are $\sim 6 \mu\text{m}$, $\sim 10 \mu\text{m}$, and $\sim 40 \mu\text{m}$ respectively. h is the depth of the enhancers ($\sim 90 \mu\text{m}$). The length y_0 ($\sim 20 \mu\text{m}$) and y_d ($\sim 250 \mu\text{m}$) are the distances between the emitter and detector and approximate length of the detector and enhancers. By determining the various widths and lengths in our simplified model, we can then account

for the ballistic phonon paths—the phonons traveling in a straight line until reaching an interface—based solely on φ and θ . Due to the symmetry of the enhancers with respect to the emitter, and the batch fabrication process for etching them, it was not necessary to account for neither phonon focusing nor surface scattering in our simple estimation of enhanced backscattering.

The presence of the enhancers decreases the scattering volume of phonon interaction near the detector and thus, increases the number of phonons that can scatter from an interface and reach the detector. From the top projection in Figure 4.4a, the azimuthal range ($0 \leq \varphi \leq \pi$) of phonon emission is reduced as phonons emitted in the range φ_{Eh1} and φ_{Eh2} interact with the enhancer walls Eh₁ and Eh₂ respectively. Some of the phonons emitted in the polar angular range from 0 to $\pi/2$ (with $\pi/2$ emission angle collinear with the y-direction and the detector) will also interact with the enhancers. Considering the 500 μm thickness of the substrate and the listed dimensions in Figure 4.4a above, phonons with azimuthal emission angles φ_{Eh1} (34° to 86°), φ_{Eh2} (94° to 146°), and polar emission angles in the range $12.5^\circ \leq \theta \leq 90^\circ$ will interact with the enhancers. These angles are determined by trigonometric ratios (for example from side projection: $\tan^{-1} \frac{y_0}{h} = \tan^{-1} \frac{20}{90} = 12.5^\circ$); hence, the analysis could be adapted for any arbitrary widths or heights of enhancers, emitter-to-detector distance, or substrate thickness. This result implies that ~49.7% of all phonons emitted ballistically within the full angular range will interact with the walls of the enhancers. We note, however, that interaction with the enhancers does not necessarily imply that a phonon will backscatter to the detector. To account for phonons that actually reach the detector via backscattering, we have to estimate: (i) what fraction of the emitted phonons

backscattering from the bottom of the substrate reach the detector in the absence of enhancers, and (ii) what fraction of the 49.7% of enhancer-interacting phonons will be redirected to the detector? The former is the nominal \dot{n}_{bs} signal, while the latter represents the enhancement mechanism.

To estimate the nominal backscattering signal, we determine the polar and azimuthal phonon emission angle range as shown in supplementary Figure B3. In the simplest approximation, we assume that the bottom of the substrate is specular and that the phonon incidence angle equals the reflected angle. The polar emission range, θ_b , for which backscatter phonons can reach the detector is given by $\theta_b = [\tan^{-1} \frac{(y_0+y_d)/2}{d} - \tan^{-1} \frac{y_0/2}{d}]$, where d is the thickness of the substrate; hence, 13.96° is the polar emission range for our specific geometry corresponding to 15.5 % of the full polar angular range of phonon emission. Also from Figure B3, we can estimate the azimuthal fraction, $\phi_b = [2(\tan^{-1} \frac{x_d/2}{y_0})]$, reaching the detector to be ~ 9.5 % using similar analysis. Hence, the estimate fraction of total emitted phonons that backscatter and hit the detector is a minute fraction of ~ 1.47 % of the total phonon emission range.

Of the 49.7% of the phonon emission angles that are enhancer-interacting, only those phonons interacting with enhancer walls parallel to the detector length (along y -axis in Figure 4.4a) can be redirected to the detector film; hence, the total fraction of phonons interacting with enhancers and possibly reaching the detector reduces to ~ 39.2 % and 19.6 % for double and single enhancers respectively. From this reduced fraction, we then account for the actual fraction of phonons that can register at the detector film after backscattering. In Figure B4 (supplementary Information), the azimuthal

backscattering range from the walls, assuming specular reflection, can be estimated by $[\tan^{-1} \frac{x_b/2}{y_0}]$ to $[\tan^{-1} \frac{x_b/2}{y_0+y_d}]$, which is 45° to $\sim 81.57^\circ$ in our geometry. While the polar backscattering angle range from 12.5° to $\sim 56^\circ$ degrees. We can therefore conclude that from the total emitted phonons, 7.73 % interact with the walls of the two enhancers and are registered at the detector, and half of these interact with one enhancer and register at the detector. When scaled by the estimated nominal backscattered phonons \dot{n}_{bs} , the ratio of $[\dot{n}_{bs} : \dot{n}_{bs+1 \text{ enhancer}} : \dot{n}_{bs+2 \text{ enhancers}}]$ is [1:00: 2.63: 5.26] as shown in Figure 4.4b. It becomes evident that the enhancement mechanism of backscattered phonon is due to the confined volume and phonon mean free path reduction due to scattering from walls of the enhancers. While these analyses have been carried out for a specific experimental geometry, the geometry and dimensions are amenable to further modifications for specific applications. We note while this analysis does not take into accounts the exact nature of the surface or the anisotropy of silicon, the symmetry of the enhancers with respect to the emitter and the close agreement of the analysis result with experimental data, suggest their effects though may result in more phonons registering at the detector, the ratios of backscatter signal should not change. These results have implications for phonon transport in nanoscale geometrical structures, which tend to have multiple scattering interfaces. In addition, future studies could modify the experimental design by varying the surface roughness of the enhancers, or filling the enhancer trenches with materials with different elastic properties, in order to elucidate more on the effects of interface scattering.

4.6. Conclusion

In conclusion, we demonstrate phonon backscattering enhancement in silicon substrates. By etching phonon enhancers around the detector films, we show an enhancement in the detection of backscattered or non-line-of-sight phonons. This enhancement factor scales with the number of phonon enhancers. These results have implications for ballistic phonon transport, phonon-mediated detection, and thermal transport studies, and highlights the important effects of phonon scattering from interfaces in nanoscale geometrical designs.[61, 97, 152] This work could be further applied to the understanding backscattering phonons in substrates such as sapphire, doped-silicon, Si-C, and III-V materials.

CHAPTER 5

5 HIGHLY CONDUCTIVE Cu_{2-x}S NANOPARTICLE FILMS THROUGH ROOM TEMPERATURE PROCESSING AND AN ORDER OF MAGNITUDE ENHANCEMENT OF CONDUCTIVITY VIA ELECTROPHORETIC DEPOSITION[♦]

5.1. Abstract

A facile room-temperature method for assembling colloidal copper sulfide (Cu_{2-x}S) nanoparticles into highly electrically conducting films is presented. Ammonium sulfide is utilized for connecting the nanoparticles via ligand removal, which transforms the as-deposited insulating films into highly conducting films. Electronic properties of the treated films are characterized with a combination of Hall Effect measurements, field-effect transistor measurements, temperature-dependent conductivity measurements, and capacitance-voltage measurements, revealing their highly-doped p-type semiconducting nature. The spin-cast nanoparticle films have carrier concentration of $\sim 10^{19} \text{ cm}^{-3}$, Hall mobilities ~ 3 to $4 \text{ cm}^2\text{V}^{-1}\text{s}^{-1}$ and electrical conductivities ~ 5 to $6 \text{ S}\cdot\text{cm}^{-1}$. Our films have hole mobilities that are 1 to 4 orders of magnitude higher than hole mobilities previously reported for heat treated nanoparticle films of HgTe, InSb, PbS, PbTe and PbSe. We show that electrophoretic deposition (EPD) as a method for

[♦] The content of this chapter was adapted from an originally published article: O.O. Otelaja, D.-H. Ha, T. Ly, H. Zhang, and R.D. Robinson, "Highly Conductive Cu_{2-x}S Nanoparticle Films through Room Temperature Processing and An Order of Magnitude Enhancement of Conductivity via Electrophoretic Deposition," *ACS Appl. Mater. Interfaces*, vol. 6, p. 18911-18920, 2014. Reprinted with permission from the American Chemical Society.

nanoparticle film assembly leads to an order of magnitude enhancement in film conductivity ($\sim 75 \text{ S}\cdot\text{cm}^{-1}$) over conventional spin-casting, creating copper sulfide nanoparticle films with conductivities comparable to bulk films formed through physical deposition methods. X-ray diffraction pattern of the Cu_{2-x}S films, with and without ligand removal, matches the Djurleite phase ($\text{Cu}_{1.94}\text{S}$) of copper sulfide, and show the nanoparticles maintain finite size after the ammonium sulfide processing. The high conductivities reported are attributed to better interparticle coupling through the ammonium sulfide treatment. This approach presents a scalable room temperature route for fabricating highly conducting nanoparticle assemblies for large area electronic and optoelectronic applications.

5.2. Overview of Solution-Processed Electronic Fabrication

The need for solution-based processing of semiconductor electronics has spurred interesting research efforts in recent years. In addition to the lower cost for solution processing, it also allows for large area and flexible electronic applications compared to conventional semiconductor processing methods. Due to their exceptional size-dependent electronic properties and solution processability, semiconducting colloidal nanoparticles are becoming important building blocks for electronic and optoelectronic devices such as field-effect transistors, [153] photovoltaic devices, [154] and light-emitting diodes. [155] These nanoparticles have typically been assembled into thin films with short range ordering via drop-casting, spin casting, or inject printing. [46] Spin-casting is a widely known method for assembling nanoparticle films from colloidal solution, and the quality of the resulting films depends on appropriate solvent selection

and substrate preparation procedures. [46] For practical large area applications, the spin-casting process results in inefficient use of starting colloidal nanoparticles, because a significant portion of the nanoparticle solution is discarded during the process. In addition, obtaining uniform films over a large area is a challenge.

Electrophoretic deposition (EPD) is an alternate method for the fabrication of nanoparticle films that shows great promise for electronic applications.[156, 157] EPD has been widely used for the processing of thin films and coatings for a wide variety of novel applications. EPD is accomplished by applying a voltage between two conducting electrodes immersed in a solution containing nanoparticles. The resulting electric field drives the charged particles through the solution, onto electrodes of opposite polarity. The versatility of EPD for fabricating a wide variety of films of different materials, EPD's efficient use of the colloidal particles (most particles in solution are deposited), and the possibility of depositing films on substrates of arbitrary size and geometry, makes EPD an attractive method for depositing nanoparticle films for applications. EPD has been shown to result in closely packed nanoparticle assembly, often with mechanical robustness.[157-161] While the mechanical stability of EPD films over conventional film deposition has been previously demonstrated,[159] little is known about the electronic properties of the films deposited via EPD.

Copper sulfide is a p-type semiconductor material that has generated a great deal of interest due to its potential use in optoelectronic applications. While several methods such as physical deposition methods (evaporation and sputtering),[162] pulsed chemical vapor deposition,[163] and chemical bath deposition methods[164-166] have been used to deposit Cu_{2-x}S films, a facile method suitable for large scale applications is desirable.

Hence, a simple and robust method for solution-based processing of conducting Cu_{2-x}S films is important. In this work, we utilize electrophoretic deposition (EPD) as an alternate method for depositing conducting copper sulfide nanoparticle films, and we study the effect of deposition methods on electronic transport properties of EPD and spin-cast Cu_{2-x}S films. Our room-temperature method for realizing highly conductive Cu_{2-x}S nanoparticle films involves chemical treatment of as-deposited films with ammonium sulfide — a process that replaces the bulky surfactant ligands with metal-sulfide bonds — transforming the as-deposited insulating films into highly conducting films. When we compare the electronic properties of copper sulfide nanoparticle-based films deposited via electrophoretic deposition and spin-casting, we find that spin-casting can yield films with high conductivities ($5.7 \text{ S}\cdot\text{cm}^{-1}$) and mobilities ($4.3 \text{ cm}^2\text{V}^{-1}\text{s}^{-1}$), and that the EPD films consistently have an order of magnitude higher conductivity (up to $75 \text{ S}\cdot\text{cm}^{-1}$) than the spin-cast films. We believe this could pave the way for new methods of room temperature processing of nanoparticles for applications such as printable electronics.

5.3. Experimental Section

5.3.1. Overview of Experimental Procedures

Our experimental plan is summarized in the schematic of Figure 5.1a, showing colloidal Cu_{2-x}S nanoparticles utilized as building blocks for the fabrication of nanoparticle films via spin-casting and electrophoretic deposition. The copper sulfide nanoparticles shown in Figure 5.1b were synthesized in batch to ensure uniformity between multiple devices. [167] In preparation for film deposition the nanoparticles are

re-dispersed in hexanes, cleaned, and filtered through 0.2 μ m polyvinylidene fluoride (PVDF) membranes. The nanoparticles are then deposited by spin-casting or EPD onto the substrates and the electronic properties of the prepared films are studied by performing resistivity, Hall Effect, and field effect transistor (FET) measurements. Different substrates and substrate preparations are used for the Hall and FET measurements to match the experimental needs of each characterization method. For Hall measurements, an insulating substrate (e.g. glass) is ideal to prevent the Hall voltage from the measured film from being obscured by substrate. For the resistivity and Hall measurements, Cr/Au (5 nm/90 nm) electrodes are deposited on borofloat glass and doped-Si/SiO₂ substrates via electron beam evaporation such that after nanoparticle deposition, the films could be manually patterned into 5 mm squares with 200 μ m squares of gold contacts at the edges of the film. The FET devices consist of doped-Si/SiO₂/Cr/Au (500 μ m/300 nm/5 nm/100 nm) stacks to form a bottom-gate and bottom-contact transistor once the nanoparticle film is deposited. The substrates (both FET and Hall) used for spin-casting were cleaned in isopropanol, acetone, and methanol and vapor primed with hexamethyldisilazane (YES HMDS Oven for 16 minutes) prior to film deposition. For the spin-cast films ~50 μ l of 5 mg/ml of Cu_{2-x}S nanoparticles in hexanes are deposited for 30 seconds at 2000 rpm. This spin-casting condition is selected after characterizing the properties of films (conductivity and film homogeneity) obtained from varying spin parameters, primed and unprimed substrates, and varying solution concentration. This characterization, which should be done for different materials or different concentrations, is necessary because film property is very sensitive to process parameters (type of spinner, humidity, or closed versus open spinners) and

could vary with time. A selection of 10 silicon chips (5 primed and 5 unprimed) were utilized for spinning nanoparticle films at varying spin speeds (between 800 to 2500 rpm). After optical inspection and two-point conductivity check with a hand-held multimeter, the process parameter that leads to best film quality and conductivity was selected. The EPD of the copper sulfide films is carried out by applying a voltages (up to ~600 V) for up to 15 minutes between two conducting electrodes arranged in a parallel plate capacitor configuration and immersed in a colloidal solution of copper sulfide nanoparticle dispersed in hexanes, as shown in Figure 5.1a. Particles are attracted to the electrodes via Coulombic interaction. The spacing between the electrodes is ~3 mm, and with hexane having a dielectric constant of ~1.9, the effective electric field for film deposition is ~1050 V/cm. The particles are deposited onto the positive electrode, suggesting our particles are predominantly negatively charged. (See Supporting Information in Appendix C for further details on experimental methods used synthesis and film characterization.)

5.3.2. Optimal Nanoparticle Film Deposition Conditions

Film deposition conditions are optimized to obtain conducting films (>100 nm thickness) in a reproducible manner. The optimal EPD and spin cast conditions are characterized to ensure that the measured films are of identical thicknesses, as conductivity of the films often exhibit thickness dependent behavior. Ensuring that the film thickness obtained from EPD and spin-casting are identical often require multiple deposition cycles. Three EPD and ten spin-cast deposition cycles were usually carried out to obtain identical thicknesses of ~120 nm. The film thicknesses are determined

using an atomic force microscope (AFM) after cleaning a region of the films with a swab tip soaked in hexanes as shown in Figure 5.1c. Each deposition cycle consists of spin-casting/EPD of colloidal nanoparticles onto the substrates/devices, followed by an ammonium sulfide ($(\text{NH}_4)_2\text{S}$) ligand replacement step [168]: after each film layer is made by EPD or spin-casting, the substrate is immersed in a 4 mM of $(\text{NH}_4)_2\text{S}$ /methanol solution for 30 seconds, rinsed in methanol for 30 seconds, and dried in ambient temperature. The ammonium sulfide ligand replacement strips off the organic ligands and replaces them with sulfide anions, resulting in a metal-sulfur terminated nanoparticle surface [168]. With the removal of the bulky organic group the nanoparticle are also brought together in intimate contact. Both these effects (metal-sulfur surface and inorganic connections between nanoparticles) increases interparticle coupling and enhances charge transport. This step is critical for obtaining conductive films; without the ammonium sulfide treatment the films are insulating (See Supporting Information Figure C2 and C3 showing films without treatment are insulating).

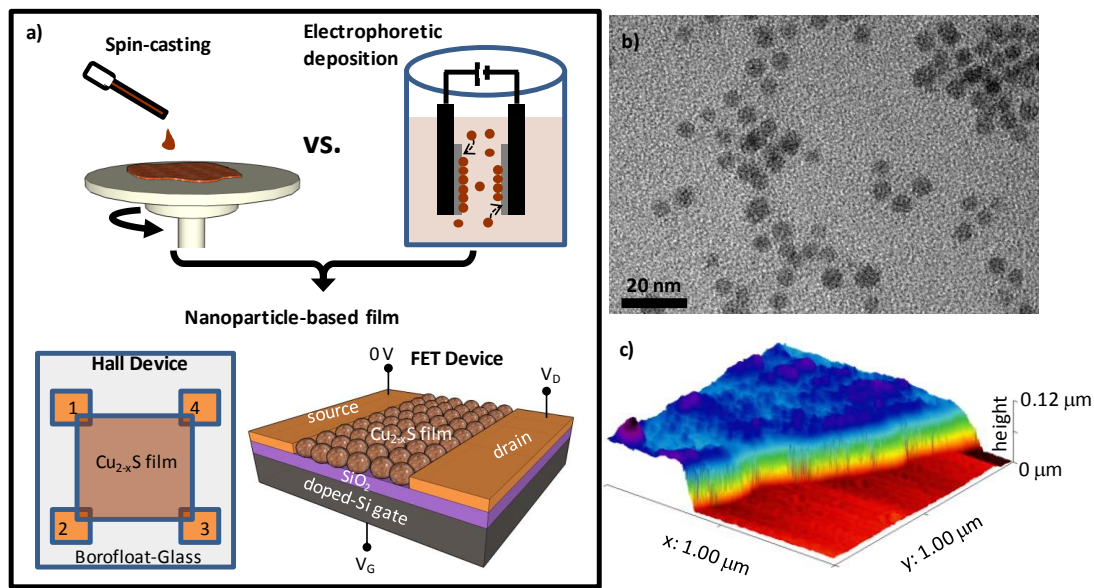


Figure 5.1: (a) Schematic depiction of experimental plan to study electronic transport in EPD and spin-cast copper sulfide films. (b) TEM of starting copper sulfide nanoparticles with average particle size of 5 nm. (c) AFM height image showing a step in height between the film and regions from which the films have been cleaned off, revealing film thickness.

5.4. Results and Discussion

5.4.1. Structural Characterization

Characterization of the colloidal nanoparticle building blocks by transmission electron microscopy (TEM) and the initial film by X-ray diffraction (XRD) show the nanoparticles having an average size of ~ 5 nm and matching the XRD pattern for copper sulfide (Figure 5.1b and 5.2a). The XRD pattern (Figure 5.2a) can be most closely compared to three different phases of copper sulfide Cu_{2-x}S : low Chalcocite $x \approx 0$, Djurleite $x = 0.06$, and Roxbyite $x = 0.19$. Cu_2S has been shown to be an intrinsic

semiconductor, [162, 169] whereas the $\text{Cu}_{1.94}\text{S}$ and $\text{Cu}_{1.81}\text{S}$ are p-type semiconductors due to the presence of copper vacancies. [170-174] The XRD pattern of our measured samples match the Djurleite phase most closely; hence, a p-type semiconducting behavior is expected. However, we note that the exact phase of Cu_{2-x}S has been known to be difficult to distinguish using XRD patterns alone, as mixed phases and transformation between phases is common. [23, 166, 171, 175] After the ammonium sulfide surface ligand treatment we observe no changes in the XRD patterns and Scherrer analysis of the XRD peaks indicates a crystal size of ~ 4.8 nm both before and after treatment (Figure 5.2a), indicating that the particles have not sintered into larger grains and that they have not disintegrated into smaller crystals. The ammonium sulfide treatment used in preparing these films has previously been shown to increase interparticle coupling. [168] TEM images of samples scraped off from the EPD films (Figure 5.2b and 5.2c) (See Supporting Information Figure C1 and C5 for post-ammonium sulfide treatment spin-cast films) suggest that the nanoparticles in the films have not sintered together from the ammonium sulfide treatment, but have formed a closely packed network of nanoparticles inorganically connected, as was seen in work by Zhang et al. [168] Preliminary analysis of film porosity also suggests that EPD films are better packed than spin-cast films (See Supporting Information Figures C2, C4, and C5). Hence, EPD films should have better interparticle coupling.

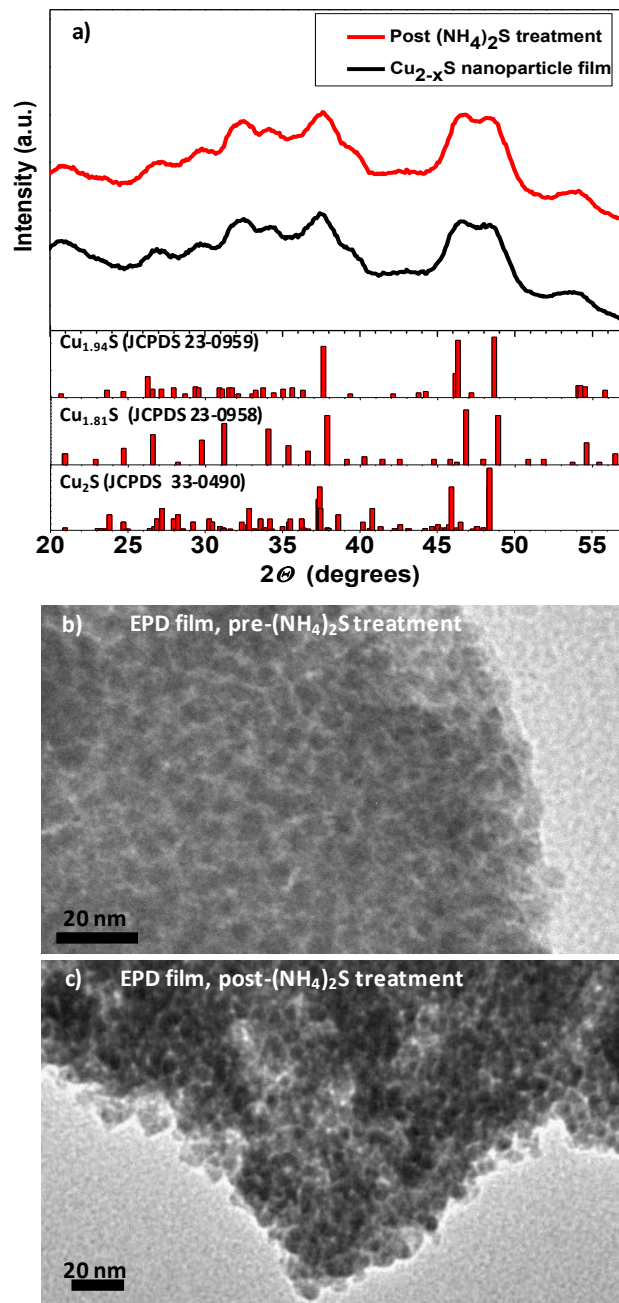


Figure 5.2: Structural characterization with XRD and TEM. (a) XRD pattern of the copper sulfide film before and after ammonium sulfide compared to the Djurleite $\text{Cu}_{1.94}\text{S}$ (JCPD 23-0959), Roxbyite $\text{Cu}_{1.81}\text{S}$ (JCPDS 23-0958), and low-chalcocite Cu_2S (JCPDS 33-0490) phases of copper sulfide. A close match to the Djurleite is observed,

indicating the presence of copper vacancies. (b) TEM of Cu_{2-x}S nanoparticles scraped off from EPD films without ammonium sulfide treatment. The films are insulating without ammonium sulfide treatment. (c) TEM of Cu_{2-x}S nanoparticles scraped off from EPD films treated with ammonium sulfide. These films have conductivities as high as 75 Scm^{-1} at room temperature. The particles are scraped off from films made by three EPD cycles.

5.4.2. Composition Studies with XPS

The stoichiometry and composition of the EPD and spin-cast films before and after the ammonium sulfide treatments are characterized with X-ray Photoelectron Spectroscopy (XPS). Supplementary Figures C6 and C7 show XPS survey scans of spin-cast and EPD-films before and after ammonium sulfide treatment. All XPS spectra are calibrated with the binding energy of the C 1s peak at 284.8 eV and the films were deposited on a doped-Si/SiO₂ substrate. The atomic percentages of the constituent elements are summarized in Supplementary Table C1. The Cu 2p, S 2p, O 1s, C 1s, N 1s, and Si 2 p peaks are used for calculating the atomic percentages. The ratio of Cu:S before the ammonium sulfide treatment for both spin cast and EPD films is close to 2:1 as expected for Cu_{2-x}S . However, due to the presence of a significant amount of C, O, and Si, the stoichiometry information obtained for Cu_{2-x}S from XPS data is not exact. The high resolution XPS spectra of C 1s in Supplementary Figures C8 and C9 indicate a reduction in carbon content after the ammonium sulfide treatment. After the ammonium sulfide treatment, the ratio of the atomic percentages of Cu:S films is ~1:1. This increase in sulfur content, in addition to the decrease in C and N peaks, is attributed

to the removal of organic ligands and replacement with sulfide anions. The absence of N peaks after treatment also indicates that no inorganic ligands (e.g., $(\text{NH}_4)_2\text{S}$ or $(\text{NH}_4)\text{S}^-$) or ammonium or ammonia moieties remain after treatment. These results – increase in sulfur, the lack of nitrogen signal, and the decrease in carbon – are all consistent with our previous work and extensive characterization of this ligand removal process.[168]

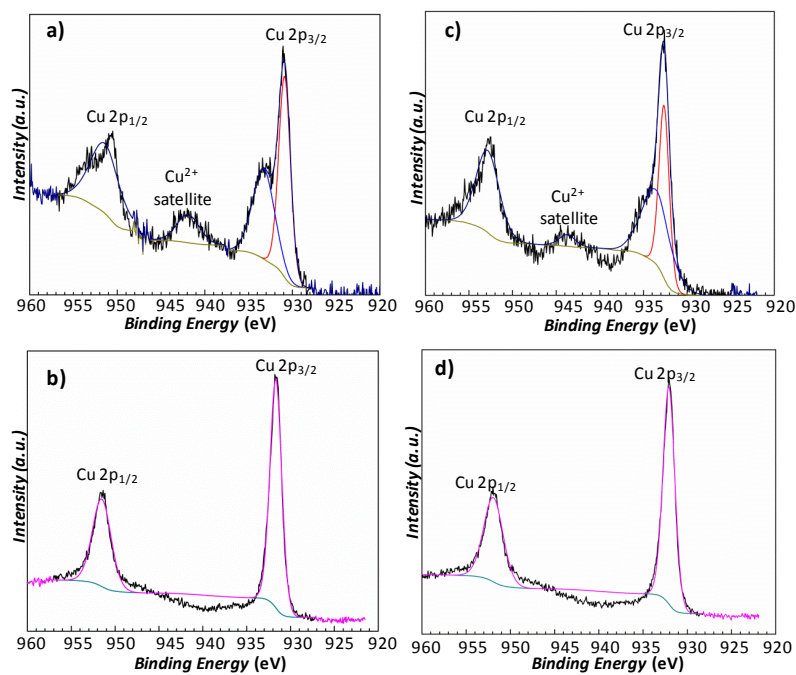


Figure 5.3: Compositional studies of copper sulfide nanoparticle films with XPS. High resolution XPS scan of the Cu 2p region for Spin-cast and EPD films (a) spin cast film before ammonium sulfide treatment. (b) Spin cast film after ammonium sulfide treatment.. (c) EPD film before ammonium sulfide treatment. (d) EPD film after ammonium sulfide treatment. The Cu 2p_{3/2} peak in (a) and (c) indicates a shift to higher binding energy, a consequence of oxidation. Satellite peaks (Cu²⁺) at ~943 eV observed in (a) and (c) is not observed in (b) and (d). See Figure C10 for corresponding high

resolution scans for the S 2p region.

From the high resolution scans of Cu 2p and S 2p in Figure 5.3, the chemical state of copper and sulfur in the films are further assessed. The binding energies of Cu $2p_{3/2}$ and Cu $2p_{1/2}$ are centered at 932.6 and 952.6 eV respectively, indicating a monovalent state of copper (Cu^+) as expected in Cu_2S . In addition, the presence of the Cu $L_3M_{4,5}M_{4,5}$ Auger transition with kinetic energy of 918.5 eV (showing up at binding energy ~ 568 eV on the survey scans) further suggest a Cu^+ state.[176] The satellite peaks which appear at 943.7 eV in the Cu 2p high resolution scans before ammonium sulfide treatment in Figure 5.3a and 5.3c are due to oxidation. The S 2p spectra in Supplementary Figure C10 shows a doublet species with binding energies of 162.7 and 163.9 eV corresponding to S $2p_{3/2}$ and S $2p_{1/2}$. These peaks are indicative of a Cu–S bond formation.[176] While the exact stoichiometry of the Cu_{2-x}S films is difficult to determine because excess S from the processing can produce misleading values, the XPS and XRD results infer that our films are Cu_{2-x}S .

5.4.3. Electronic Characterization

5.4.3.1. Hall Measurements

Hall Effect measurements of the carrier concentration, carrier type, and mobility reveal that the spin-cast copper sulfide films are highly conducting. Colloidal nanoparticles are spin-cast onto the devices for Hall measurements (Figure 5.1a). (The substrates for Hall measurements should be non-conducting – in our case, glass – on

which EPD cannot be performed.) All electrical measurements were done in a Physical Property Measurement System (PPMS Quantum Design). Sheet resistance was measured using the standard van der Pauw approach by determining resistance $R_{14,23}$, the resistance obtained by applying a DC current (I_{14}) through gold contacts 1 and 4 and measuring the voltage (V_{23}) that develops between gold contacts 2 and 3. By swapping the contact points for current injection and voltage measurements we observe identical resistance values and conclude that the films are of uniform thickness and suitable for Hall measurements. The sheet resistance is expressed as: $R_s = \pi R_{14,23} / \ln 2$. [177] For Hall Effect measurements we measure the voltage between contacts 2 and 4, while the current is applied between contact 1 and 3 in the presence of a magnetic field.

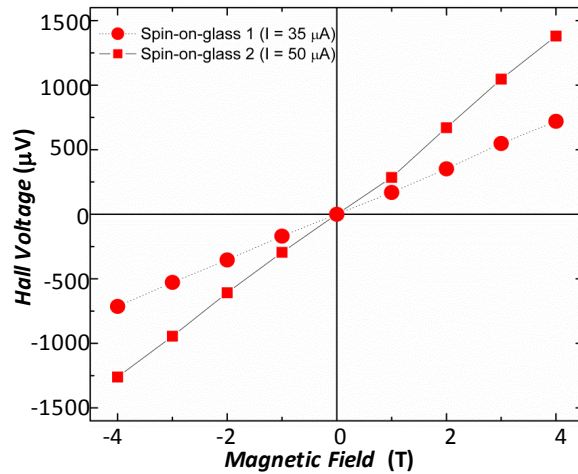


Figure 5.4: Hall Effect measurements for two spin-cast films on glass substrates. Films are treated with ammonium sulfide. The Hall voltage is determined for varying magnetic Field (-4 to 4 Tesla). Polarity of the Hall voltage indicates the Cu_{2-x}S are p-type semiconducting.

Table 5.1: Hall Effect measurements on spin-cast nanoparticle-based films.

Spin-on-glass films	Slope (V/T)	Film thickness (nm)	Conductivity ($S\text{cm}^{-1}$)	Carrier density (cm^{-3})	Hall mobility ($\text{cm}^2 \text{V}^{-1} \text{s}^{-1}$)
1	1.79×10^{-4}	112	5.74	1.09×10^{19}	3.28
2	3.28×10^{-4}	120	5.44	7.93×10^{18}	4.28

In Figure 5.4, the room temperature magnetic field-dependent Hall voltage V_H , measured for two spin-cast films (spin-on-glass **1** and **2**) is shown. These samples were prepared identically. The film thicknesses d measured from profilometry and AFM of the two samples **1** and **2** is determined to be 112 nm and 120 nm, respectively. The positive polarity at positive magnetic fields (0 to 4 T) of V_H is indicative of a p-type material, which is commonly reported for copper sulfide films with copper vacancies. [162, 164, 165, 171, 178] To ensure measurement accuracy, the polarity of the magnetic field is reversed. After magnetic field reversal, we observe that the polarity of V_H changes, but the magnitude remains approximately the same. This implies an accurate measurement of Hall voltage. We determine the conductivity ($\sigma = 1/R_s d$) of spin-on-glass samples **1** and **2** to be 5.74 and 5.44 $S \cdot \text{cm}^{-1}$, respectively. We determine the Hall carrier concentration n_H and Hall mobility μ_H using the expressions $\sigma = n_H \cdot e \cdot \mu_H$ and $V_H = \frac{IB}{n_H e d}$, where e is the elementary charge (1.602×10^{-19} C), I is the applied current, and B is the applied magnetic field. These results are summarized in Table 5.1. Compared to transistor-based measurements, Hall measurements have the

advantage of studying the intrinsic charge transport in nanoparticle-based films independent of charge trapping effects. [177, 179] Our Hall measurements result in Carrier concentrations of $\sim 10^{19} \text{ cm}^{-3}$ and Hall mobilities of ~ 3.3 and $4.3 \text{ cm}^2 \text{ V}^{-1} \text{ s}^{-1}$ for our spin-cast Cu_{2-x}S nanoparticle films **1** and **2**, respectively. Because our films are insulating before the ligand replacement step, we attribute these high conductivities to the post-deposition ammonium sulfide treatment, which increases interparticle coupling. Recent results have also shown conductivity enhancements in CuInSe_2 films with virtually bare nanoparticle surfaces after ligand exchange with 1-ethyl-5-thioerazole. [180]

The high conductivities and carrier concentrations of our films are comparable to values previously obtained from low-chalcocite ($\text{Cu}_{1.999}\text{S}$ and $\text{Cu}_{1.995}\text{S}$) copper sulfide films prepared by thermal evaporation ($\sim 1 \text{ }\mu\text{m}$ thick) and RF sputtering techniques ($0.1 - 0.5 \text{ }\mu\text{m}$ thick): $\text{Cu}_{1.999}\text{S}$ ($7 \text{ S}\cdot\text{cm}^{-1}$ and $1.5 \times 10^{19} \text{ cm}^{-3}$) and $\text{Cu}_{1.995}\text{S}$ ($35 \text{ S}\cdot\text{cm}^{-1}$ and 10^{20} cm^{-3}). [162] Even higher conductivities have been reported for anilite phase ($\text{Cu}_{1.75}\text{S}$) copper sulfide films,[178] although we note that: (i) copper sulfides are typically p-type from copper vacancies, with more copper vacancies generally leading to higher conductivity, (ii) XRD from Figure 5.2a suggests that our measured films are of the Djurleite phase ($\text{Cu}_{1.94}\text{S} - \text{Cu}_{1.96}\text{S}$), which has fewer copper vacancies than the anilite phase and more copper vacancies than the low-chalcocite phase, (iii) the anilite phase is expected to have higher conductivity than our Djurleite films as there are more copper vacancies in anilite, and (iv) our films are made from nano-size grains without thermal annealing and should not be expected to compete with bulk, however, our results show comparable values to thermally-processed bulk films. Thus, our measured

values of conductivities are remarkably high. When compared to copper sulfide films prepared by pulsed chemical vapor deposition of identical thickness (~120 nm) and stoichiometry (between $\text{Cu}_{1.9}\text{S}$ to Cu_2S) our nanoparticle based films show better or identical conductivities. [163] In Supplementary Table C2, we summarize the electrical conductivities of some copper sulfide films previously reported and we note their stoichiometry and method of determination, synthesis and deposition methods, and film thicknesses. Although the results are widely ranging, [162-166, 178, 181] we can infer that increasing copper vacancies suggest higher conductivities, that annealed films have higher conductivities than un-annealed films, and that our solution processed nanoparticle films perform on par with some of the physically deposited films, even though our nanoparticles have not been annealed.

It is interesting to note that a low cost solution-based process is able to realize highly conducting films comparable to bulk deposition methods without annealing. Our films have hole mobilities that are 1 to 4 orders of magnitude higher than hole mobilities previously reported for heat treated nanoparticle films of HgTe, InSb, PbS, PbTe and PbSe. [47] Our films also have 1 to 7 orders of magnitude higher conductivity than those of some previously reported metallic nanoparticles of Au, CoPt_3 , Ag, Pb, Co, and Pd.[48] Hence, our films are applicable as p-type conducting films, as well as conducting electrodes in an all-nanoparticle based device. However, we note that it is difficult to compare different material systems exactly. Such highly conductive nanoparticle-based films made without thermal annealing have also been recently reported for silver nanoparticles. [182] These silver films are metallic in nature while our Cu_{2-x}S films are p-type semiconducting; hence, our films are more suitable active

materials for electronic and optoelectronic applications. In addition, although silver nanoparticle based films could be used for device electrodes, Cu_{2-x}S films with high conductivities could also be used as electrodes with the added advantage of transparency, although the transparency will be dependent on film thickness. [178]

5.4.3.2. Temperature-Dependent Conductivity Measurements

The effect of film deposition methods on the electronic properties of these highly conducting Cu_{2-x}S are analyzed through temperature-dependent conductivity measurements on films (made via EPD and spin-casting) of identical thicknesses deposited on doped-Si/SiO₂ substrates with Au contact pads. The device geometry is similar to those used for the Hall measurements above, with the exception of a doped-Si/SiO₂ substrate in place of the glass substrate. EPD works for these substrates because the doped silicon is conductive. In addition, we measured the temperature dependence of the conductivity of spin-cast films (spin-on-glass **1** and **2**) that were used for Hall Effect measurements. All the electrical measurements are carried out in the PPMS and Ohmic contacts are ensured through wire-bonding. Conductivity is measured following the van der Pauw method described above, and film thicknesses are obtained from profilometry and AFM measurements. In Figure 5.5a, we show the temperature dependent conductivity of Cu_{2-x}S nanoparticle films formed by EPD (blue closed circles) and spin-casting (red symbols), between 25 K and 300 K. The plots with open red circles and open red diamonds are measurements of films spin-cast onto glass substrates, while the plot with solid red circles is from a film spin-cast onto doped-Si/SiO₂ substrates. Clearly, the effect of the substrate type on conductivity

measurements is not discernible. Slight variations in the properties of EPD films between runs are known to result from uncontrolled experimental conditions, such as humidity and temperature.[157, 158]

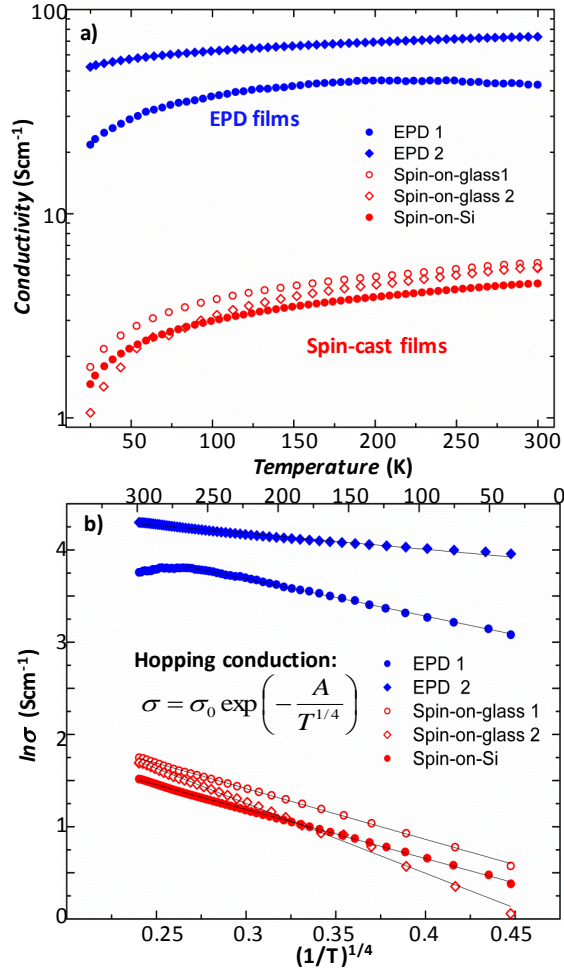


Figure 5.5: Temperature-dependent electrical conductivity measurements. (a) Conductivity measurements of EPD and spin-cast films from 25 to 300 K showing a decrease in conductivity with decreasing temperature. EPD films show an order of magnitude enhancement in conductivity. (b) Semi-log plot of conductivity ($\ln \sigma$) vs. $(1/T)^{1/4}$ shows variable-range hopping (VRH) conduction. The black solid lines are fits of the conductivity using Mott-VRH with $1/4$ power temperature dependence. The data

is best fit to a Mott-VRH (See Supporting Information Table C4 for different hopping fits).

From the results in Figure 5.5a, two points are worth noting: (i) EPD films have an order of magnitude higher conductivity than spin-cast films, and (ii) the conductivity of the films decreases with decreasing temperature. At room temperature, the highest conductivity of all the measured EPD films is $\sim 75 \text{ S}\cdot\text{cm}^{-1}$, while the highest conductivity from the spin-cast films is $5.7 \text{ S}\cdot\text{cm}^{-1}$. This corresponds to resistivities of $\sim 13.6 \text{ m}\Omega\cdot\text{cm}$ and $\sim 174 \text{ m}\Omega\cdot\text{cm}$ respectively. We attribute this order of magnitude enhancement in conductivity seen in EPD films to the close-packing of the nanoparticles as shown in Supplementary Figure C1. EPD is suggested to produce closely packed films in an energetically favored assembly, [183] whereas spin-cast films are prone to disorder. [157] These temperature dependent studies further confirm our earlier assertion that EPD films produce better conducting films than spin-cast films. We can infer from such conductivity trends that EPD films will likely have higher carrier mobilities than spin-cast films. We note that while the ammonium sulfide treatment may introduce some impurities that could potentially dope the films, the EPD and spin-cast films are subjected to identical ammonium sulfide treatment process.

5.4.3.3. Effect of Porosity on Conductivity

To clarify the conductivity effects, it is necessary to consider the pore volume of the films.[184] The improvement in conductivity of EPD over spin-casting can be a

result of higher packing order and/or better interlinking of the nanoparticles in the film. SEM images (Supplementary Figures C1 and C4) indicate that the EPD films are better packed than spin-cast films. To better assess the average porosity we measure the mass (before and after deposition) and height of the EPD and spin-cast films deposited on a 15 square mm silicon substrate, and calculate the film density. By assuming a bulk density of 5.6 g/cm^3 for Cu_2S , we estimate the percentage porosity and the solid fraction of the films (Supplementary Table C3). EPD films have ~38% film porosity and 0.62 solid fraction, while spin-cast films have ~57% film porosity and 0.43 solid fraction, indicating a higher packing fraction for the EPD films. These calculated values are in good agreement with the 2D solid fraction (“% area”) obtained from image-processed SEM images in Supplementary Figure C4 (solid fraction of 63% for EPD and 40% for spin-cast). The experimentally measured conductivity ($\sigma_{measured}$) should be related to the interlinking conductivity (σ_{IL}) of the nanoparticles and the solid fraction (S_f) of the films, by $\sigma_{measured} = \sigma_{IL}S_f$. To understand this effect the temperature-dependent conductivity of the films shown in Figure 5.5a is rescaled to express conductivity as the interlinking conductivity ($\sigma_{IL} = \sigma_{measured}/S_f$), as shown in Supplementary Figure C11. Despite normalizing for solid fraction, the EPD films still show an order of magnitude increase in conductivity compared to the spin-cast films. The results of this analysis implies that while the EPD films are less porous (denser) than spin-cast films, porosity alone does not account for the order of magnitude difference in conductivity. We can conclude from this study that the interlinking between particles is enhanced in EPD processing.

5.4.3.4. Hopping Conduction Mechanism

Analysis of the carrier transport mechanism from the temperature-dependence conductivities of the films reveals a hopping conduction mechanism for charge transport (Figure 5.5b). The trend shows a decrease in conductivity ($\ln\sigma$) with decreasing temperature, which is typical for semiconductors where thermally activated hopping — the process in which a charge carrier in a localized state moves to another state via energy it receives from a phonon— is prominent. [51] The hopping process extends beyond nearest neighbors with the further-distance hops resulting in smaller energy barriers. This process is counterbalanced by a decreasing tunneling probability over large distances, such that the conductivity is of the form $= \sigma_0 \exp(-\frac{A}{T^n})$, [49, 51, 185] where A is a constant proportional to the activation energy and hopping probability. The power law (n) dependence of the temperature in the conductivity equation is reported as 1 or 1/2 for nearest-neighbor hopping (also thermally-activated hopping) or Efros-Shklovskii variable-range hopping (VRH), respectively. [49, 50, 186] However, our data are best fit with a power of 1/4, suggesting Mott variable-range-hopping mechanism (Supplementary Information Table C4). [51, 186] The linear dependence of $\ln\sigma$ versus $T^{-1/4}$ from 25 to ~270 K in the spin-cast films and the EPD films in Figure 5.5b is therefore indicative of variable-range hopping conduction in both films. While previous work showed a transition temperature at which conduction changes from VRH to nearest-neighbor hopping, [187] our results do not exhibit any such transition in hopping mechanism, which is a similar conclusion found by Houtepen et al. for a $T^{-2/3}$ conductivity dependence in ZnO nanoparticles. [188] The parameters A

and σ_0 in the conductivity equation are extracted for Mott-VRH and shown in Table 5.2. The pre-exponential factor σ_0 , which is about an order of magnitude higher in the EPD films than in the spin-cast films, is inversely proportional to the lattice spacing, [51] further suggesting that better interparticle coupling is responsible for the enhanced conductivity in EPD films. Between 270 and 300 K, we observe that the conductivity in the EPD-1 film begins to deviate subtly from the expected hopping behavior, and, in fact, conductivity begins to decrease with increasing temperature. While the source of the deviation is not fully clear, such a trend of decreasing conductivity with increasing temperature has been observed in other studies on nanoparticle films where metal-like transport is suggested based on field-effect mobility measurements. [114, 177, 189]

Table 5.2: Linear fits of conductivity to Mott variable-range hopping equation.

	A (K ^{1/4})	σ_0 (S·cm ⁻¹)
EPD 1	4.04	134.04
EPD 2	1.74	110.04
Spin (glass) 1	5.51	21.45
Spin (glass) 2	7.57	33.94
Spin (Si)	5.32	16.19

5.4.3.5. Thermal Stability and Light Sensitivity

The temperature stability of the films is studied by extending the temperature range to 400 K (the maximum temperature of the PPMS). In Supplementary Figure C12 we show the resistivity data for two films made by EPD and spin-casting. We cycled the temperature from 300 to 25 K, and then from 25 K to 400 K. For both film types,

cycling from 25 to 300 K results in an increase in resistivity with a decrease in temperature; however, when cycling from 25 K to 400 K, a sharp and irreversible drop in resistivity (increased conductivity) is observed in the EPD and spin-cast film at ~350 K and ~380 K, respectively. The drop in resistivity suggests that the films are likely sintering at these higher temperatures. It is interesting to note that the EPD films sinter at lower temperatures than the spin-cast films. This is possibly due to the tighter packing of the EPD films over the spin-cast films. In addition, we note that a recent study demonstrated irreversible thermal doping in Cu₂S nanoparticle films above 350 K and this may provide an alternative explanation.[172]

We also assessed the light-sensitivity of the performance by measuring EPD and spin-cast films under 150 W illumination (Micro-Lite FL2000 High Intensity Fiber Optic Illuminator). For this study we varied the electrode spacing and measured the films with four-wire resistance. We find negligible light sensitivity in all cases. (See Supplementary Information Figure C13 for discussions on aging of the films in ambient conditions and Figures C14-C15 for data on light stability.)

5.4.3.6. Field-Effect Transistor (FET)-Geometry Measurements

In Figure 5.6 a and b, we show the output and transfer characteristics of FET devices. The transistor geometry is bottom-gate bottom-contact, with the nanoparticles being deposited onto the source and drain electrodes via EPD and spin-casting (schematic of construction shown in Figure 5.1a). The film thicknesses of the EPD and spin-cast films are ~350 nm and ~70 nm thick, respectively. The resulting transistor channel is 2.5 μm wide and 1 mm long. At gate voltage $V_{GS} = 0 V$, a substantial drain-

to-source current I_{DS} of ~ 0.96 mA is measured at a drain-to-source voltage $V_{DS} = 4$ V for EPD films, whereas at the same V_{DS} and V_{GS} , the drain current in the spin-cast films is ~ 4.2 μ A. Since conduction in FETs occur mostly via the surface channel, the difference in thickness cannot account for two orders of magnitude difference in current levels; hence, the higher current levels obtained from the EPD films further suggests that EPD films consistently form more conducting films than spin-cast films. The I_{DS} - V_{DS} graph is shown in logarithm-scale in order to display the differences between the EPD and spin-cast data on a single plot. Due to the two order of magnitude difference in I_{DS} between the EPD and spin-cast films, the features of the spin-cast data are suppressed when plotted on a traditional linear-scale (see Supplementary Figure C16). I_{DS} is slightly increased by changing the gate voltage from zero to negative values (-10 V and -20 V) for both EPD and spin-cast films, which is expected for a p-type semiconducting material, although the gate modulation is weak and no saturation occurs. Since the Cu_{2-x}S films obtained from EPD and spin-casting are conducting, utilizing them in a FET-geometry as channel material would imply a depletion-mode operation for such transistor. Transfer characteristics (I_{DS} - V_{GS} plots at $V_{DS} = 5$ V) of FETs made from both EPD and spin-cast films shown in Figure 5.6b, depict no rectification; however, qualitative assessment of the plots indicate that the gate modulation is minimal and that the drain-source current level decreases by using positive gate voltages. The change in slope observed in the I_{DS} - V_{GS} plot of the EPD film near $V_{GS} = 0$ V, which is not seen for the spin-cast films, is likely due to carrier depletion in the channel with positive gate voltages; however, the influence of charge trapping sites, which may be different for each film type might result in the disparity.

Further studies on charge trapping mechanisms might provide better clarifications. From the I_{DS} - V_{GS} plot, we calculated field-effect mobilities of $1.12 \text{ cm}^2\text{V}^{-1}\text{s}^{-1}$ and $0.0087 \text{ cm}^2\text{V}^{-1}\text{s}^{-1}$ for the EPD and spin-cast films respectively. We note that the field-effect mobility of the spin-cast sample is lower than that obtained from Hall effect mobilities in Table 5.1. Although, FET measurements have been typically used to characterize the electronic properties of nanoparticle films, the results are strongly affected by charge trapping. [177]

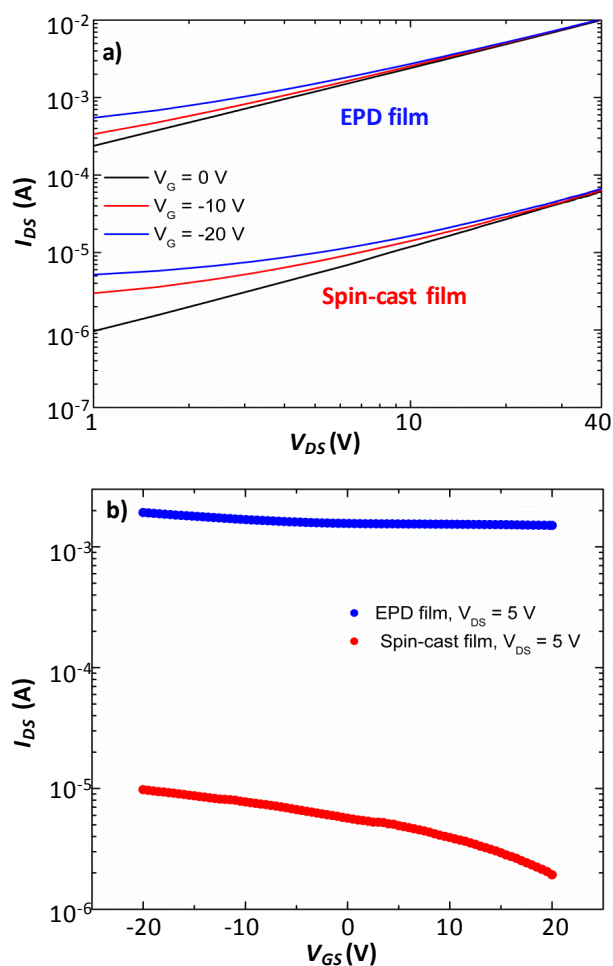


Figure 5.6: FET measurements of EPD and spin-cast films. (a) Log-log plot of drain-source current as function of drain-source voltage (FET output characteristics). The plot

shows minimal gate modulation and no saturation for both films. Channel width and length is 1 mm and 2.5 μm . Slight increase in drain current with negative gate voltages suggests a p-type channel. (b) Semi-log plots of drain-source current as a function of gate voltage (FET transfer characteristics) at a constant V_{DS} of 5 V. EPD films conduct higher drain currents than spin-cast films. FET mobilities extracted from plots in b) are $1.12 \text{ cm}^2\text{V}^{-1}\text{s}^{-1}$ and $0.0087 \text{ cm}^2\text{V}^{-1}\text{s}^{-1}$ for EPD and spin-cast films respectively.

5.4.3.7. Capacitance–Voltage Measurements

Capacitance-Voltage (C-V) measurements of EPD and spin-cast films reveal that the films are highly doped as their capacitance shows no voltage dependence. We fabricate metal (Au) – semiconductor (copper sulfide) – insulator (silicon oxide) – metal (doped-Si) (MSIM) capacitors (Figure 5.7a) and measured the equivalent capacitance C_{EQ} sweeping gate voltage from -45 to 45 V at 100 KHz with a precision LCR meter (Agilent 4284) as shown in Figure 5.7b. The equivalent capacitance of the MSIM structures — a series arrangement of oxide capacitance C_{OX} and nanoparticle film capacitance C_{NP} — is shown in Figure 5.7a. The measured equivalent capacitance $C_{EQ} = (1/C_{OX} + 1/C_{NP})^{-1}$. With increasing film capacitance, C_{EQ} tends towards C_{OX} . The estimated oxide capacitance C_{OX} is $\sim 0.552 \text{ nF}$ as depicted in Figure 5.7b (assuming a dielectric constant of 3.9 for silicon oxide, area of 4.88 mm^2 , and an oxide thickness of 300 nm.) Varying the gate voltage has negligible effect on the equivalent capacitance measured for both EPD (0.545 nF) and spin-cast films (0.4 nF), which further supports the minimal gate modulation seen in the output characteristics in

Figure 5.6a. These results, however, further support our assertion that more mobile charges are accumulated in EPD films than in spin-cast films; hence, the EPD films will have higher drain-to-source currents, as found in the FET measurements above. The constant capacitance with gate voltage, confirm that the Cu_{2-x}S films obtained from both EPD and spin-cast are highly doped. Although it is difficult to quantify the carrier concentration from C-V plots, [182] the Hall effect measurements shown in Figure 5.4 helps to assess the highly-doped nature of the films.

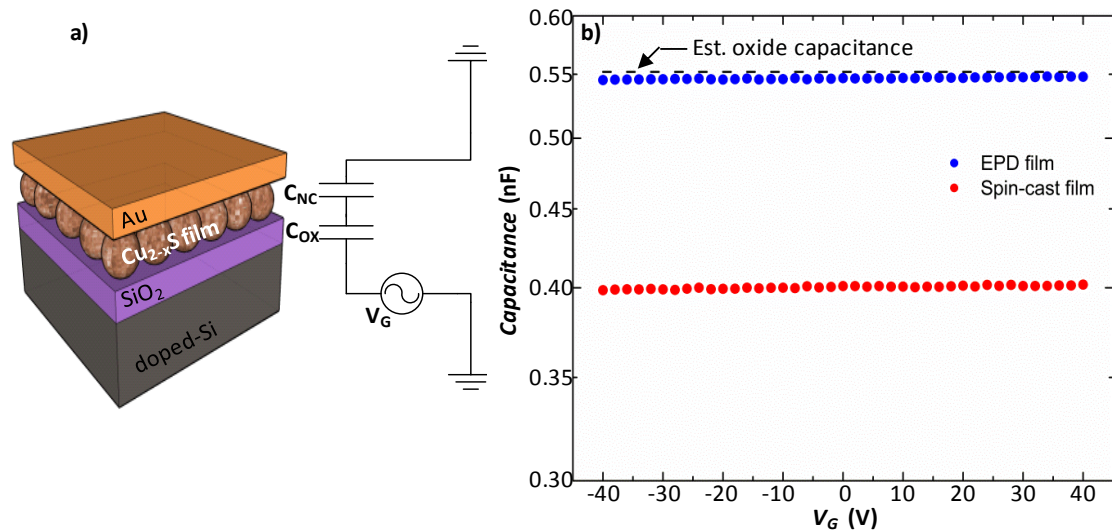


Figure 5.7: Capacitance-Voltage studies. (a) Schematic of the of Metal (Au)-Semiconductor (copper sulfide) - Insulator (silicon oxide)-Metal (doped-Si) (MSIM) capacitors fabricated with EPD and spin-cast films. Also shown is the equivalent capacitance of the MSIM structure, which is a series connection of oxide (C_{OX}) and nanoparticle film capacitance (C_{NP}). (b) High-frequency (100 KHz) Capacitance-Voltage (C-V) measurements of the MSIM capacitor in a). Estimated oxide capacitance assumes a dielectric constant of 3.9 and thickness of ~ 300 nm. Area is ~ 4.8 mm^2 .

5.5. Conclusion

While the high conductivity observed in these Cu_{2-x}S films does not make them ideal candidates for FET channel materials, they could potentially be utilized as source and drain electrode materials in an all-nanoparticle based transistor, as was recently demonstrated with Ag nanoparticles for the source and drain electrodes. [182] In addition, Cu_{2-x}S films could be employed as highly conducting p-type transparent conducting electrodes. [178] The order of magnitude enhancement in conductivity obtained for our EPD films could be applied to enhance the conductivities of films shown to have high electron mobilities ($> 10 \text{ cm}^2/\text{Vs}$) only after heat treatment or chemical doping. [111, 189]

In summary, we have shown that ammonium sulfide treatment of insulating Cu_{2-x}S nanoparticle-based films results in highly conducting films comparable to physically deposited thin films. Further, we show that EPD results in an order of magnitude enhancement in conductivity of these Cu_{2-x}S films than spin-casting. The increase in conductivity is attributed to better interparticle coupling in the EPD films. The result of this study presents a scalable route to producing highly electrically conductive solution-processed films for electronic and optoelectronic applications.

CHAPTER 6

6 CONCLUSION AND OUTLOOK

6.1. Summary of Thesis

In Chapter 1, a survey of the fundamentals relevant to understand subsequent sections of the thesis was presented. Starting with a motivation for the entire work, phonons were introduced as heat carriers, and phonon spectroscopy techniques were highlighted. The basic physics of the primary active device in this thesis — the superconducting tunnel junction (STJ) — was presented. In Chapter 2, the design, operation, and characterization of a microfabricated phonon spectrometer utilizing STJs as phonon transducers was presented. In Chapter 3, the microscale phonon spectrometer was utilized to directly measure surface scattering in silicon nanosheets and the experimental results and simulations were compared to decades' old Ziman theory. In Chapter 4, a mechanism for enhanced phonon backscattering in silicon due to confined ballistic phonon pathways was discussed. In Chapter 5, an assembly method for realizing highly conductive copper sulfide nanoparticle films was demonstrated, and the electronic transport mechanism in the films was characterized.

Altogether, the results described in this thesis have ramifications for understanding phonon transport in nanoscale systems and electron transport in solution-processed electronics. With the development of a phonon spectrometer, this thesis provides a much needed tool that allows the scientific community to probe unresolved questions about nanoscale heat flow as it relates to thermoelectrics, microelectronics, phonon-mediated particle detectors, or reliable quantum computing systems.

Specifically, the accomplishments in this thesis include the following:

Phonon Transport in Silicon Nanostructures

- Developing a microfabricated superconducting tunnel junction-based (STJ) phonon transducers for the emission and detection of tunable, non-thermal, and spectrally resolved acoustic phonons, with frequencies ranging from ~100 to ~870 GHz.
- Showing that phonon spectroscopy with STJs offers a spectral resolution of ~15-20 GHz, which is ~20 times better than thermal conductance measurements, for probing nanoscale phonon transport.
- Demonstration of ballistic phonon propagation through a silicon microstructure, with submicron spatial resolution.
- An energy resolution of ~60-80 μeV , corresponding to a frequency resolution of ~15-20 GHz, is about 20 times better than the energy resolution obtainable from conventional thermal transport measurements, which rely on a Planck distribution of phonons.
- Demonstration of a noise equivalent power, NEP, of $10^{-15} \text{ W}/\sqrt{\text{Hz}}$, the sensitivity of our STJ phonon detectors is comparable to similar low temperature thermal detectors.
- A novel silicon mesa platform (with STJs on the sidewall) is adaptable to studies of phonon transmission through nanostructures or nanomaterials by etching or depositing these into the ballistic path defined by the mesa.

- Demonstration of a method to fabricate high aspect ratio silicon nanosheets and measure their sidewall surface roughness (~1 nm) using atomic-force microscopy (AFM).
- Showing that the Ziman model underestimated the probability of totally diffusive surface scattering (the Casimir limit). Ziman model predicts 40% probability, while measurements and simulation indicate 100% probability for totally diffusive scattering at ~400 GHz for a 1 nm rough surface.
- Elucidating the mechanism of backscattered phonon enhancement in silicon substrates is due to confinement of the ballistic phonon pathways and increased scattering off the enhancer walls.

Electron Transport in Copper Sulfide Nanoparticle Films

- Room-temperature processing method for realizing highly conductive Cu_{2-x}S nanoparticle films.
- Order of magnitude enhancement in conductivity can be obtained when the films are assembled via electrophoretic deposition (EPD) ($\sim 75 \text{ S}\cdot\text{cm}^{-1}$) compared to films assembled by conventional spin-casting methods ($\sim 5.7 \text{ S}\cdot\text{cm}^{-1}$). Conductivity enhancement is due to better interparticle coupling and packing of the EPD films.
- Our temperature-dependent conductivity measurements, Hall effect measurements, Field effect transistor measurements, capacitance-voltage measurements, and detailed analysis of the charge conduction mechanism in copper sulfide nanoparticle films is most comprehensive electronic property studies on these materials till date and to our knowledge.

- The electronic behavior of Cu_{2-x}S is highly stoichiometry-dependent; hence, our full suite of electronic characterization helps to pin-point the electronic behavior of the Djurleite phase, and these techniques could be extended to other phases of Cu_{2-x}S nanoparticle films.

6.2. Additional Phonon Transport Studies

The microfabricated spectrometer described in this thesis is a versatile tool for spectrally resolving phonon transport in nanostructures. In this section, I will outline some stand-alone experiments that further characterize the spectrometer as well as demonstrate its applicability.

6.2.1. Phonon Transport in Silicon Oxide Films

In this experiment, phonon transmission via reflection was attempted to observe the effect of thin film phonon interference. Silicon oxide films ($\sim 2 \mu\text{m}$ thick) were thermally grown on a silicon wafer, and the emitter and detector STJs were fabricated on the silicon oxide as shown in Figure 6.1. Since silicon oxide is elastically isotropic, phonon focusing effects could be neglected. Emitted phonons can propagate to the detector only by reflecting off the silicon oxide/air and the silicon oxide/silicon interfaces.

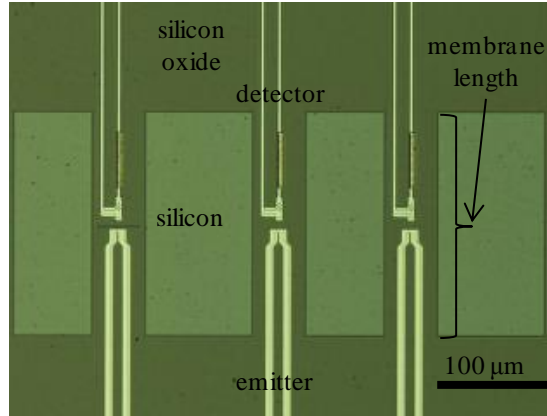


Figure 6.1: Optical microscope image of a phonon spectrometer fabricated on silicon oxide films for phonon transport experiments via reflection.

The transport geometry and preliminary experimental measurements of length dependent phonon transport are shown in Figure 6.2. This transport geometry differs from a line-of-sight or ballistic phonon transport geometry because the phonons are forced to interact with an interface from which they reflect as shown in Figure 6.2a. Since the phonon transducers are fabricated on the silicon oxide, even a backscattering experiment (when a trench is etched between the emitters and detectors) will likely include the effects of the interfacial scattering. In Figure 6.2b, the phonon reflection experiments was performed on a silicon oxide film between an emitter (E) and detectors (D1, D2, and D3) spaced $7\ \mu\text{m}$, $10\ \mu\text{m}$, and $15\ \mu\text{m}$ respectively. The measured signal shows a markedly different spectral signature from our previously reported phonon transport measurements in silicon. A resonance peak was observed at $\sim 110\ \text{GHz}$, and the oxygen resonance that typically occurs at emitter voltages around $\sim 4\ \text{mV}$ is now visibly absent. The fact the measured signal level decreases with increasing emitter-to-

detector distance is consistent with the reflection geometry depicted in Figure 6.2a, where scattering from the interface increases with length; hence, phonon signal decreases. In addition, when a trench is cut between the emitter and detector, the measured signal shows no resonance at 110 GHz, which helps to conclude that this spectral signature is due the silicon oxide.

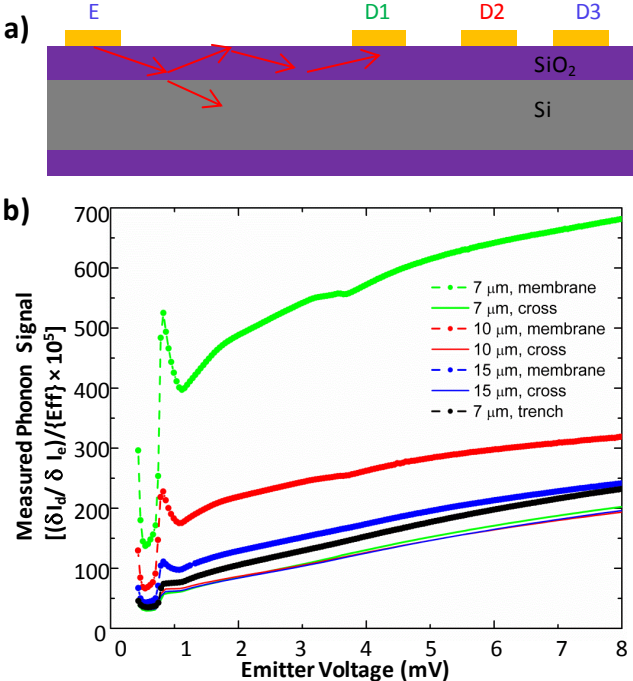


Figure 6.2: Phonon transport in silicon oxide membranes. (a) Schematic of phonon transport via reflection in a silicon oxide film with varying emitter-detector spacing. (b) Plots of measured phonon signal. The measured signal shows a resonance peak at 110 GHz, this resonance peak is indicative of Fabry-Perot type cavity arising from such interfacial backscattering. The black plot is the backscattered signal only, which shows no resonance peak, and is obtained when a trench is cut in the silicon oxide between the emitter and detector.

In this preliminary observation, the origin of the peak is thought to be due to phonon interference effects as the cavity behaves as a Fabry-Perot cavity (or etalon) for phonons. [190] While interference peak should result in multiple peaks, it is possible that the single peak observed in Figure 6.2b may be as a result of the near normal incidence of the phonons in this experimental design. This assumption needs to be investigated further by computational modeling of the experimental geometry.

To further investigate the effect of interface scattering in this reflection geometry, the silicon oxide film may be suspended to form a membrane. Hence, phonons will reflect off only silicon/air interfaces, and the effect of backscattering could be isolated. To this end, we explored utilizing xenon difluoride (XeF₂) (Xactix Inc.) as an isotropic etchant for silicon in order to fully or progressively suspend the silicon oxide membrane. The etch mechanism is:



The gas pressure, etch cycle, and etch times are the etch variables that need to be characterized to realize a fully suspended film. The current process parameters to fully suspend the membrane pattern in Figure 6.1 are: 9 etch cycles, 2.5 Torr, and 32 s etch time. A fully suspended silicon oxide membrane with STJ is shown in Figure 6.3.

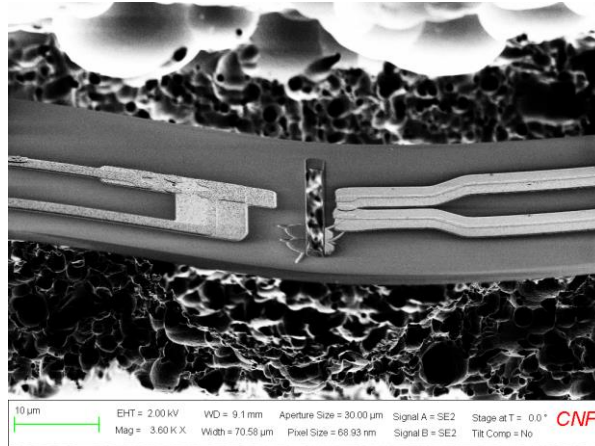


Figure 6.3: SEM of a fully suspended silicon oxide membrane with STJs and trench.

These results present an interesting application for the phonon spectrometer to be applied to study interfacial scattering, phonon crystal effects and phonon confinement effects. Beyond this thesis, the following studies are possible next steps:

- Obtain reliable and consistent phonon transport measurements in the suspended silicon oxide membranes and compare to supported silicon oxide films.
- Vary the silicon etch rates to create varying degrees of undercut/suspension to show if there is a progressive transition effect on phonon transport between fully suspended and fully supported films.
- Consider other membrane materials: Amorphous Si (PECVD deposited, etching with HF Vapor) or Silicon nitride (LPCVD deposition, nitride controlled XeF_2 etch). Note that a silicon-rich low stress silicon nitride film will not survive XeF_2 etch.
- Effect of varying membrane thickness: Membrane can be modeled as a doubly-clamped beam; hence, deflection and bending must be considered. In fact,

reducing the suspended area or membrane length by a factor of 2 or 4 will be helpful for higher yield for suspended STJs.

- In the region between the emitter and detector, a metal or polymeric film, or stack of films could be deposited to investigate 1D phononic crystal effects or anti-reflection.

6.2.2. Temperature Dependence of Phonon Transmission

In this experiment, the phonon transmission measurements were performed at base temperature of ~ 309 mK. Subsequently, heat was applied with the temperature controller (Quantum Design) in order to see what temperature the measured signal begins to degrade as shown in Figure 6.4. By modeling the temperature dependent behavior of the phonon detector, a quantitative estimation of recombination times as it relates to thermal quasiparticles may be possible.

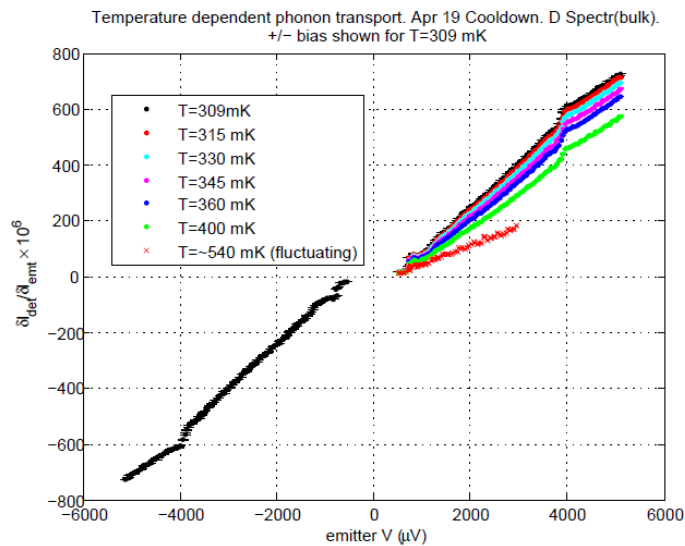


Figure 6.4: Temperature-dependent phonon transmission measurements.

6.2.3. Modulation Frequency Dependence of Phonon Transmission

In Chapter 2, the modulation technique for phonon transmission measurement was described and a modulation frequency between 7-11 Hz was described as ideal for low noise amplitudes. However, an important point to note is that in the case of variability in detector behavior (observed as high noise amplitude in this suggested frequency range), a modulation frequency that results in the lowest noise should be selected. The plot in Figure 6.5 shows a measurement of the modulated phonon signal versus frequency and serves as guide to know the frequency window in which varying modulation frequencies have negligible impact on detector signal.

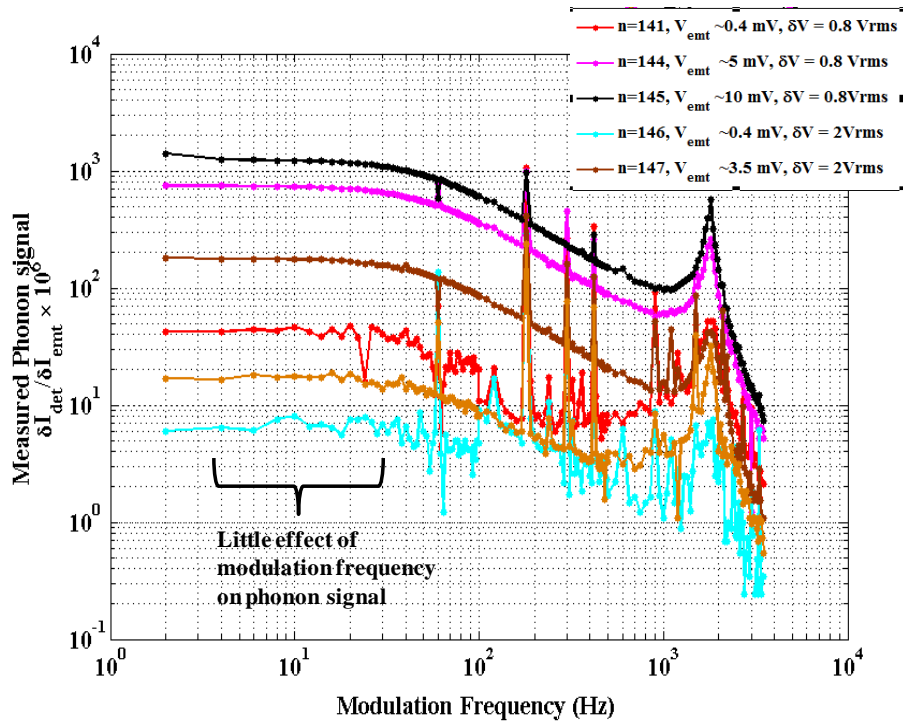


Figure 6.5: Effect of modulation frequency on detected phonon signal showing that modulation frequencies ~ 2 to 14 Hz do not lead to significant difference in detector signal. Measurements were taken by stepping the emitter voltage and sweeping the

modulation frequency. δV is the modulation amplitude. Resonance peaks due to line frequency (60 Hz) are also observed.

6.3. Future Work

Additional work that could advance this thesis include:

- Studying the effect of impurities on nanoscale phonon scattering: Initial experiments sought to utilize highly p-doped (boron) silicon wafers to fabricate the spectrometers. One major issue worth pointing out here is that dopants in silicon are effectively etch masks for KOH; hence, etch chemistry and parameters may need to be modified (e.g. by increasing temperature and concentration).
- Modification of the ballistic line-of-sight phonon path via geometric structuring. Fabrication of bends and cavities and their effect on phonon enhancement or reduction will be informative. In preliminary works, we showed that fabrication process for making the nanosheets in Chapter 3 could be applied to fabricating arbitrary geometries as shown in Figure 6.6. Experiments and complementary modeling of such structures could be pursued.

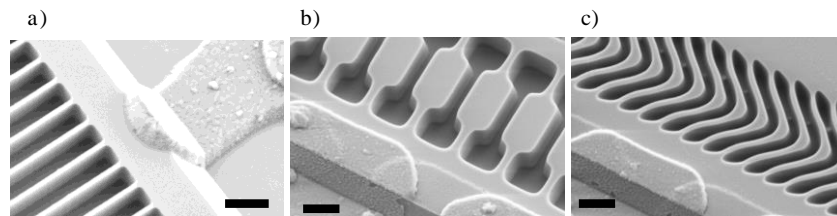


Figure 6.6: SEM images of (a) straight nanosheets, (b) nanosheets with cavities, and (c) bent nanosheets on silicon mesas.

- Modeling of phonon transmission with frequency information (Finite element, Finite Difference Time Domain (FDTD), plane wave expansion etc.) to guide phononic structure work is highly desirable.
- Study the effect of contact metallurgy for nanoparticle films for printed electronics and attempt to realize CMOS functionality with a single channel material.

APPENDIX A: SUPPLEMENTARY INFORMATION FOR CHAPTER 3

Supplementary Discussion A1: Casimir-Ziman Surface Scattering Regimes

From equations (3.1) and (3.2) of Chapter 3, we can see that a key characteristic of Casimir-limit scattering behavior (i.e. when $l_{eff} = l_0$) is that l_{eff} is independent of phonon frequency. For surface roughness of depth η , we can distinguish three distinct regimes of scattering behavior.

First, wavelengths much greater than η will reflect specularly, allowing the phonon to travel unimpeded down the nanosheet. Then l_{eff} is infinite, and transmission through the nanosheet should be 100%, independent of nanosheet length.

Secondly, in the opposite limit, wavelengths much smaller than η will scatter diffusively every time they strike the surface, emerging in a random direction, which reduces l_{eff} to equal l_0 (the so-called 'Casimir limit' value). For sheets of rectangular cross-section, analytic expressions for l_0 have been determined by McCurdy et al and have a value slightly larger than the width of the sheet.[129] In the 'Casimir limit', transmission through the nanosheet will be independent of wavelength, but will decrease for increasing sheet length.

Thirdly, in an intermediate regime, wavelengths $\lambda \approx \eta$ will be partially scattered diffusively and partially specularly reflected. In this regime, transmission will depend on both wavelength and channel length.

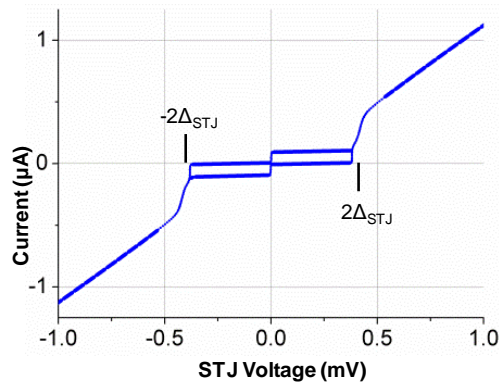
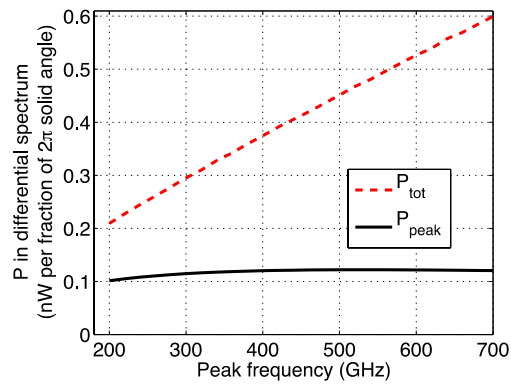
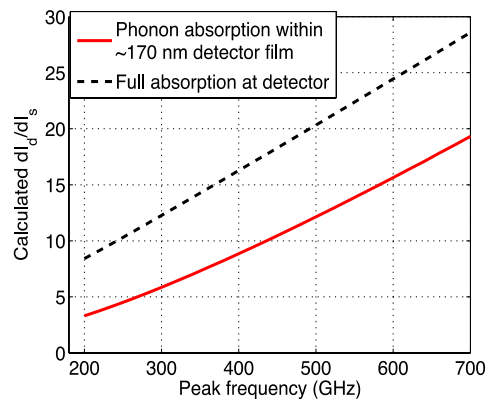


Figure A1: I-V curve of typical STJ phonon source. Reciprocal of the slope for the linear region above 0.5 mV gives the normal state resistance (R_n).



a)



b)

Figure A2: Calculations of phonon differential power emitted from source, and resulting current produced at detector, as function of phonon peak frequency. Calculations

assume that source STJ comprises lower Al film 20 nm thick, upper film 79 nm thick, and has $R_n = 1000\Omega$. Modulation width is fixed at ~ 20 GHz (modulation RMS voltage amplitude ~ 30 μ V, current ~ 30 nA).[124] a) Total emitted differential phonon power from STJ source is sum of direct emitted 1st and 2nd step QP relaxation, minus attenuation, plus reabsorbed/reemitted power. Emitted differential phonon power in spectral peak suffers from increasing attenuation as frequency increases. The plot shows that as the emitted STJ differential phonon spectral peak frequency is increased, the total power increases roughly linearly. Since the spectral peak frequency depends on the source STJ voltage V_s according to $f_{peak} = (eV_s - 2\Delta_s)/h$, this linear behavior is strictly dependent on change in source voltage. Changing the modulation amplitude changes the emitted phonon power proportionally. This calculation establishes that the total emitted phonon power is roughly proportional to the modulated source STJ current, thus enabling the differential transfer function $\delta I_d/\delta I_s$ to indicate the phonon transmission rate, as discussed in the text. b) Calculation of differential transfer function dI_d/dI_s for phonon emission spectra of part (a). In this calculation, both transmission factor Γ_{los} and detector efficiency $\{Eff\}$ are taken to be unity. Calculation assumes that differential phonon power spectrum of part (a) is incident on detector, integrates equation (3.3) across this spectrum to determine the rate of electrons produced in the detector film, and divides by approximate source differential current $dI_s = P_{tot}/2V_s$, to find the differential transfer function. Calculation is presented either assuming full phonon absorption ($\alpha_{abs} = 1$) or else taking $\alpha_{abs}(\omega)$ as a function of phonon frequency, for the aluminum film thickness (~ 170 nm) on detector sidewall in our devices.[62, 124]

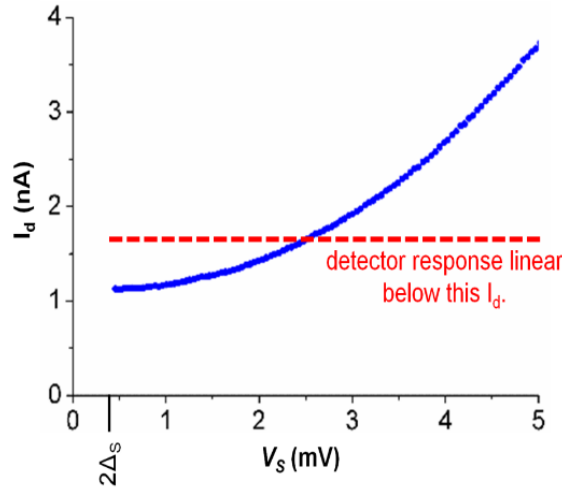


Figure A3: Typical total detector current I_d vs. emitter bias V_s at temperature of 0.3 kelvin. Maximum I_d for linear detector response is indicated by horizontal dashed red line.

Supplementary Methods A1: Fabrication and Characterization

Typical spectrometers with nanosheets appear in Figure 3.1b of the main text. To ensure that no phonons could travel ballistically from emitter to detector without passing through the nanosheets, we filled the region between emitter and detector with an array of identical nanosheets, extending the array more than $10 \mu\text{m}$ in each direction. We measured transmission through ten different arrays of nanosheets in three different array designs. (See Table 3.1).

The arrays of nanosheet were patterned on the silicon mesas using electron-beam lithography, after the STJs were fabricated. The developed pattern was etched into the mesa using an unpulsed Bosch process (SF_6 as etchant gas and C_4F_8 as the passivation layer) in a Unaxis 770 deep silicon etcher. A high etch resistant e-beam resist, such as

ZEP-520a (Zeon Corporation) is critical for this etch step. The continuous sidewall passivation during the etch step of the Bosch cycle prevents scalloping. The e-beam resist and passivation layer were subsequently stripped in a Gasonic Aura 1000 downstream asher, in which dissociated oxygen species chemically react with the polymers.

To reduce backscattering of phonons, we deposited a ~500 nm thick Ag film on the backside of each chip. Ag films have been reported to be excellent phonon absorbers.[61] We observed reduced phonon backscattering (\dot{n}_{bs} , equation (SE4)) in chips having Ag-coated backside, compared to chips with bare silicon backside. In addition to Ag-deposition, we found that proper thermal anchoring of the chip to the sample stage requires applying Apiezon N grease or silver paint (GC Electronics or SPI Supplies) between the chip and the Au-plated Cu sample stage, then clamping the chip to the stage using metal clips. We observe that grease led to the best reduction in phonon backscattering. For the ballistic measurements through bulk Si mesas, the grease was used; however, in mounting most of the chips for nanosheet measurements we used silver paint, as the grease was observed in some cases to creep onto the top surface of the chip and damage the nanosheets. In some of the detectors, a short strip of Au film ~150nm thick was deposited beneath the Al film near the STJ, on the side of the junction away from the finger, to act as a quasiparticle trap and prevent back-tunneling. However, we did not observe much difference in signal levels for detectors with and without Au quasiparticle traps.

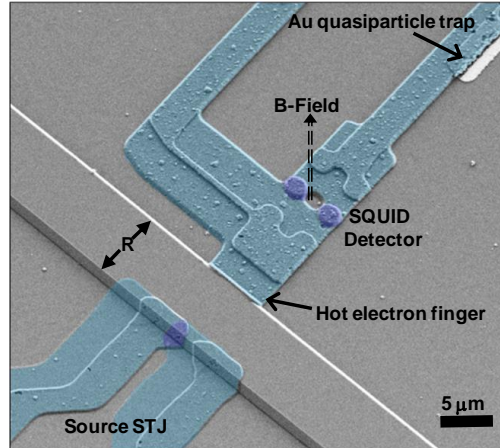


Figure A4: False-colored SEM image of a typical spectrometer used for characterizing purely ballistic phonon transmission. The widths R of the mesas in these measurements are 7, 10, or 15 microns.

To ascertain the sidewall surface roughness of the nanosheets, we fabricated on a separate n-type silicon (100) wafer, using the same electron-beam lithography and etch procedure as those used in the low-temperature measurements, a $0.8\ \mu\text{m}$ -pitch array of $\sim 0.12\ \mu\text{m}$ wide nanosheets. The nanosheets were aligned parallel to the $\langle 110 \rangle$ direction but were not embedded into a mesa. A $0.7\ \mu\text{m}$ tungsten probe tip in a micromanipulator stage was used to push the nanosheets over horizontally in order to access their sidewalls. SEM inspection of the broken nanosheets indicated that the probe tip did not damage their surfaces. The surface roughness of the nanosheets was determined using an atomic force microscope (Dimension Icon AFM with Scan Asyst) on selected nanosheets that were up to $3\ \mu\text{m}$ long. Imaging was done in tapping mode under ambient conditions with conical silicon tips (Nanoscience Instruments CT170, tip radius of 8 nm and resonant frequency of 170 KHz). The AFM images were analyzed with NanoScope Analysis (Bruker) and Gwyddion 2.24 software packages (Czech

Metrology Institute), leveled using 2nd order polynomial background subtraction. Roughness values were calculated for 0.52x0.52 μm^2 evaluation areas with pixel size of 1, 2 or 6 nm. In Figure A5, the amplitude probability density function of height was fitted to a Gaussian function and exhibited a typical RMS roughness value of ~ 1 nm. We further verified this measurement procedure by measuring the surface of an unetched region of the silicon wafer and found RMS roughness to be $\sim 0.17\text{nm}$, which is comparable to reported values for chemically polished silicon wafers.[191]

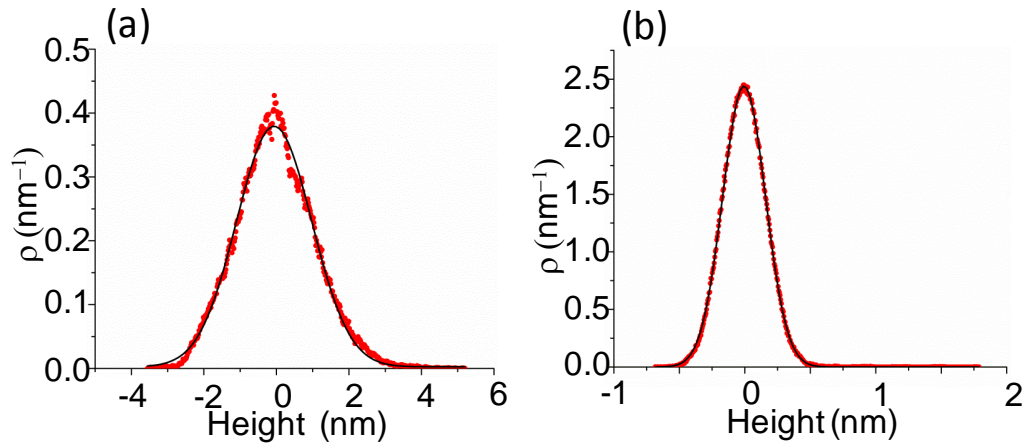


Figure A5: Roughness characterization of etched silicon nanosheet sidewalls. Distribution of surface amplitudes, measured with AFM. a) Representative distribution of nanosheets sidewall surface amplitude, fitted to a Gaussian function ($\sigma=1.04\text{E-}9$, adjusted- $R^2=0.99$). b) Height distribution for unetched region of silicon surface fitted to a Gaussian function ($\sigma=1.64\text{E-}10$, adjusted- $R^2=1.00$)

To assess the height of the measured nanosheets, we formed nanosheets on a separate silicon wafer and measured their etch depth. These nanosheet arrays were fabricated identically to those used in the phonon spectrometers, except that they were not embedded into a Si mesa. SEM inspection of the widths and lengths of the new array

of nanosheets show identical dimensions as those measured in our spectrometer experiments, allowing us to conclude that the depths should also be identical. Due to the small dimensions, with spacing between sheets as small as 170 nm (Figure A6) and inherent difficulty in assessing the full depth of etch of the nanosheets, accurate determination of the height is difficult in a standard SEM inspection. In order to better assess the height of the nanosheets, we cleaved the silicon wafer along the lengths of the nanosheets revealing the full sidewall of a few sheets close to the cleave plane. By orienting the substrate perpendicularly to the sample stage, we measure the accurate etch depth or nanosheet height for different nanosheet dimensions (See Table 3.1). We also checked that this procedure measured the thickness of the substrate accurately to be $\sim 525 \mu\text{m}$, as specified by the substrate manufacturer.

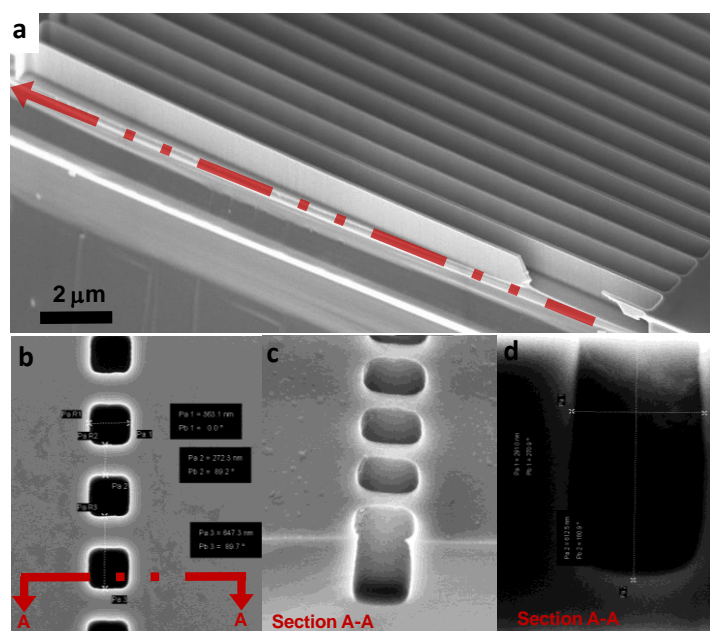


Figure A6: Technique for determining height of nanosheets a) Silicon wafer with arrays of nanosheets revealing sidewall of sheets after cleaving with a diamond scribe. The arrow indicates the cleave line is almost parallel to the nanosheets. b) SEM of the

shortest (0.2 μm long) nanosheets fabricated. The full height of the sheets is assessed by sectioning as shown. c) SEM image (45° tilt) of the full depth of the nanosheet. d) Accurate height was measured from SEM imaging done at 90° tilt angle. Due to the small etch area for these nanosheets, the measured height ($\sim 0.6 \mu\text{m}$) represents the shortest height of all nanosheets fabricated.

Supplementary Discussion A2: Detailed Explanation of Phonon Pathways

Here we reproduce equation (3.7) from the main text and describe its components in more detail. The rate $\dot{n}_{ph,d}$ of phonons striking the detector may comprise four possible components, where s (source), d (detector) and ns (nanosheets) indicate the phonon pathways (Figure 3.2e of main text):

$$\dot{n}_{los}(s \rightarrow d) \quad (\text{ballistic through bulk Si, frequency-independent}) \quad (\text{A.1})$$

$$\dot{n}_{bs} \quad (\text{scattering from substrate, possibly frequency-dependent})$$

$$\dot{n}_{los}(s \rightarrow ns \rightarrow d) \quad (\text{ballistic through nanosheets, frequency-independent})$$

$$\dot{n}_{sc}(s \rightarrow ns \rightarrow d) \quad (\text{scattering \& reflection through nanosheets, frequency-dependent})$$

First, in regions where nanosheets are absent, phonons travel ballistically in direct line-of-sight from source to detector, with phonon arrival rate $\dot{n}_{los}(s \rightarrow d)$. This rate will be independent of phonon frequency ω and will depend on the solid angle Ω_d defined by the detector relative to source STJ.

Second, a rate of phonons \dot{n}_{bs} may strike the detector and its attached wiring leads after back-scattering from the bottom surface of the chip or from resonant-

scattering impurities within the silicon.[75, 88] This rate may have some dependence on phonon frequency ω but should depend primarily on the scattering probability on the back-side of the Si chip; similar spectrometers on the same chip thus should register the same level of backscatter \dot{n}_{bs} , regardless of Ω_d or of whether nanosheets are present.

Third, if nanosheets occupy the line-of-sight path, then a reduced portion of ballistic line-of-sight flux $\dot{n}_{los}(s \rightarrow ns \rightarrow d)$ may transit to the detector after traversing the nanosheets without striking their walls. This rate is not expected to depend on ω .

Fourth, a rate of phonons $\dot{n}_{sc}(s \rightarrow ns \rightarrow d)$ reaches the detector after scattering or reflecting within the nanosheets. This will depend on the nanosheet geometry as well as the source and detector geometries, and is expected to be strongly frequency-dependent. This component is what allows us to probe Casimir-Ziman scattering behavior.

Supplementary Discussion A3: Measurement of Background Level \dot{n}_{bs}

As described in equation (3.9) of the main text, if nanosheets are present, we expect the phonon arrival rate at the detector to be

$$\dot{n}_{ph,d}(\omega) = \dot{n}_{los}(s \rightarrow ns \rightarrow d) + \dot{n}_{sc}(s \rightarrow ns \rightarrow d) + \dot{n}_{bs} + \dot{n}_{los}(s \rightarrow d) \quad (\text{A.2})$$

To assess the scattering transmission behavior, we must distinguish the backscatter signal \dot{n}_{bs} from the other components; this level may be comparable in size or even larger than the other two signal components (Figure A7). Since we expect that \dot{n}_{bs} is likely to be the same for all spectrometers on the same sample chip (see preceding discussion), a convenient way to measure \dot{n}_{bs} is through a spectrometer in which a trench is etched into the mesa to completely block the line-of-sight path for phonons,

but is otherwise identical to the other spectrometers on the chip.[35] Where this was not possible, we estimate $\dot{n}_{bs}(\omega)$ instead by measuring $\delta I_d/\delta I_s$ of a phonon source and detector that are separated by $\sim 100 \mu\text{m}$ on the same chip and do not share a line-of-sight. For such a source/detector pair, the trajectory for scattering from the bottom of the chip ($\sim 500 \mu\text{m}$ away) is much the same as for a more closely separated source/detector pair. The resulting signal level is slightly lower than that found in a ‘trench’ spectrometer. Comparing several such measurements of different pairs of sources and detectors on a single chip, we observe variations of ~ 10 to 20% in the backscatter signal level. These variations may be attributable to different scattering rates in different regions of the chip backside. We use these variations to estimate the systematic error in the subtraction of the level $\dot{n}_{bs}(\omega)$.

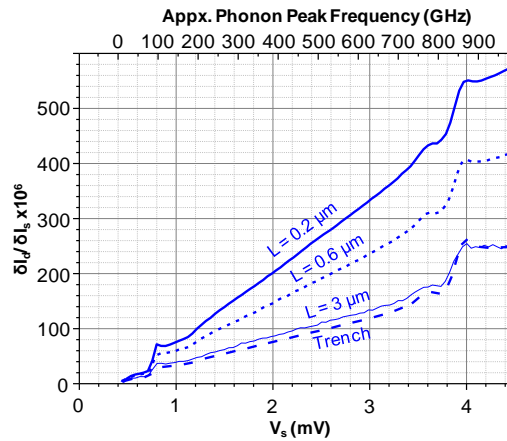


Figure A7: Phonon transmission measurement through three different types of nanosheet array on the same sample chip. For comparison, transmission through a spectrometer in which a trench blocks the line-of-sight path between source and detector is also shown. This ‘trench’ spectrometer is located on the same chip as the other measurements in this plot, and constitutes the measured \dot{n}_{bs} signal level on this chip. The spectrometers in this figure are samples D, E and G (see Table 3.1) The

transmission signal levels in this plot were subsequently corrected for detector efficiencies and had the ‘trench’ spectrum subtracted to remove \dot{n}_{bs} , and appear as part of Figure A8 below and as part of Figure 3.3 in the main text.

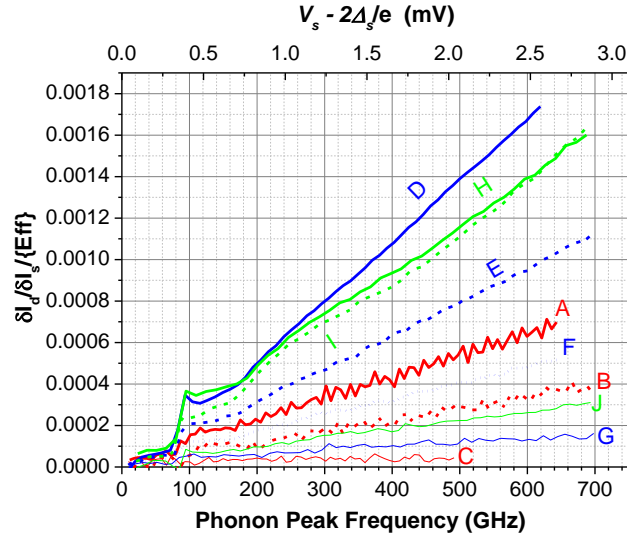


Figure A8: Phonon transmission measurement through ten different types of nanosheet array A through J. (See Table 3.1 and Table 3.2) Signals are corrected for estimated efficiency of each detector, and estimated background level \dot{n}_{bs} has been subtracted from each measurement trace. From this plot we select the signal values for phonon peak frequency of 400 GHz, and compare these values against calculated phonon transmission factors, as shown in figure A14 and in Figure 3.6.

Supplementary Discussion A4: Additional Details of Monte Carlo Calculations of Phonon Focus Behavior

The directional distribution of phonon group velocity vectors are significantly affected by the “phonon focusing” phenomenon.[93, 95] Incorporation of phonon focusing factors is thus essential for accurate modeling of phonon transmission in either the analytical or Monte Carlo models. Because of the elastic anisotropy of crystalline transport media, phonon energy concentrates along particular crystallographic directions and depletes them along other directions. We incorporate phonon focusing into the Monte Carlo model as follows. A phonon emerging from the source is assigned a random direction for its k vector. We then solve the non-dispersive Christoffel equation for a cubic crystal. The material parameters (elastic constants and density) required for this equation are listed in Supplementary Table A2. The resulting group velocity vector indicates the direction of travel of this phonon.[94, 192] The algorithm is repeated at least 10^6 times, a large enough number of times to cover all k vector directions and establish good statistics. We do an approximately equal number of repetitions for each of the three phonon polarizations: longitudinal (LA), slow transverse (ST) and fast transverse (FT). This calculation is undertaken only for phonons emerging from the source, and should accurately account for the phonon focusing effects on ballistic line-of-sight phonon propagation as well as specular reflection. If a phonon scatters diffusively from nanosheet sidewalls, we assume its subsequent propagation to be isotropic, as we assume that the randomization associated with diffusive scattering will wash out the phonon focus behavior. Incorporation of the phonon focusing factors in the analytical approach requires a 2D phonon focusing factor

map of the Si (110) plane, which can be generated by the Monte Carlo simulations. Figure 3.4 of the main text displays the angular 2D phonon focusing factor map on the (110) plane of Si.

Supplementary Methods A2: Generation of 2D phonon focusing factor map for angles relative to (110) direction, using the Monte Carlo Approach:

In the Monte Carlo simulations for generating the 2D phonon focusing factor map, a detector plane perpendicular to [110] (y axis) is positioned at a distance (Δy) from a point phonon source such that the detector plane is centered at $x = z = 0$. The detector plane is divided into 1000 by 1000 bins of equal area along x and z directions. The Monte Carlo model is run with and without the phonon focusing algorithm and the number of phonons collected by the bins are recorded. The ratio of the number of phonons collected by a bin with and without the phonon focusing effect gives the phonon focusing factor $A_{foc}(x_n, z_n)$ for that bin. The x and z coordinates of the bins are converted into angular coordinates $\varphi_n = \arctan(\frac{x_n}{\Delta y})$ and $\theta_n = \arctan(\frac{z_n}{\Delta y})$ where n is the index number for the bins.

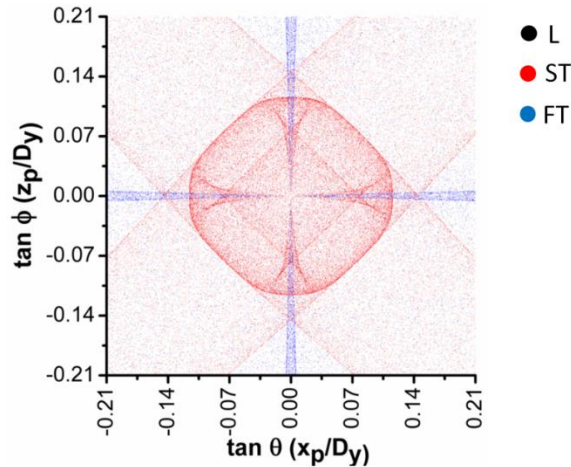


Figure A9: Phonon focusing image on (100) plane of Si, generated using Monte Carlo (MC) approach. The MC generated phonon focusing image matches with images previously reported by Tamura et. al. through experiment and simulations [92] and Jakata through simulations.[132, 192] (Plot prepared by M. Aksit)

Supplementary Discussion 5: Comparison of Monte Carlo and Analytic Calculations of Line-of-Sight Ballistic Phonon Transmission Factor

In Figures 3.5 and 3.6 of Chapter 3 and related discussions, we compare measured rates of phonon transmission to a Monte Carlo calculation of the transmission factor. In cases where phonon-surface scattering may be neglected, we compare these calculated transmission factors to values found using a simpler analytic expression. The ballistic line-of-sight transmission factor Γ_{los} is defined in equation (3.5) for the case of bulk line-of-sight transport, and may also be applied to find line-of-sight transport through nanosheets. The algorithm for the analytical model is derived by calculating the approximate fractional solid angle subtended by the detector from the generator. The generator and detector are divided into rectangular segments. Each generator segment is considered as a point source and all segments are considered to emit an equal rate of phonons. For the n^{th} generator-detector segment pair, the fractional solid angle subtended by the detector segment from the generator segment is approximated by $\Omega_n = \frac{A_{ds\perp}}{2\pi|\bar{R}_n|^2}$, where Ω_n is the fractional solid angle, \bar{R}_n is the position vector from the center point of the generator segment to the center point of the detector segment, $|\bar{R}_n|$ denotes the magnitude of \bar{R}_n and $A_{ds\perp}$ is the area of the detector segment projected onto a plane

perpendicular to \bar{R}_n .

For a given arrangement & geometry of source STJ, detector STJ and bulk crystal or nanosheet array, the fractional solid angles were calculated for all m possible generator-detector segment pairs, and summed together to find the total line-of-sight ballistic phonon transmission factor. $\Gamma_{los} = \sum_{n=1}^m 2\cos(\theta_n) \cdot A_{foc,n} \cdot \Omega_n$. The factor of $2\cos(\theta_n)$ introduces a Lambertian distribution to the emitted phonon flux, where θ_n is the angle between \bar{R}_n and the normal to the silicon surface at the STJ source. The effect of the mesa-top surface is included in this calculation of Γ_{los} , by assuming that this surface is specular. The sum then includes line-of-sight paths from the source to a mirror image of the detector with respect to the mesa top plane.

The phonon focusing factor $A_{foc,n}$ for the n th source-detector segment pair is found by using the 2D angular phonon focusing factor map generated for the (110) direction of Si. The ϕ and θ spherical-coordinate components of \bar{R}_n are calculated, and \bar{R}_n is assigned an angular width in ϕ and θ coordinates, based on the size of the detector segment. The angular width in ϕ and θ coordinates also corresponds to a rectangular window in the 2D phonon focusing factor map. The phonon focusing factors in the map are averaged within this angular window to find $A_{foc,n}$.

Since $A_{ds\perp}$ refers to a planar surface instead of a spherical surface, the exact value of the fractional angle can only be obtained for an infinitesimally small $A_{ds\perp}$ and for more accurate analytical calculations the detector needs to be divided into smaller segments. Similarly one needs to divide the generator area into smaller segments for a more accurate representation of the homogenous phonon emission from the entire generator area.

In Figures A10 and A11, we present the results of these calculations of $\Gamma_{los}(s \rightarrow d)$ and $\Gamma_{los}(s \rightarrow ns \rightarrow d)$. These figures reproduce from Figures 3.6 and 3.7 the measured signal levels and the ballistic line-of-sight transmission factors calculated using Monte Carlo simulations. The analytically calculated transmission factors are presented on the same axes. In both cases, these results show very good agreement between the analytical calculations and Monte Carlo simulations. The consistency between these two independent models confirms the validity of the Monte Carlo method to model ballistic phonon propagation. The trials presented in Fig. A12 and Supplementary Table A4 establish the further validity of the Monte Carlo algorithm to model partially-diffusive, partially-specular scattering from nanosheet surfaces. The Monte Carlo approach is well-suited for modeling phonon transport through nanostructures because it can handle stochastic phenomena such as phonon-surface diffusive scattering, (Eq. (3.1)) and it can readily handle interactions with multiple surfaces.

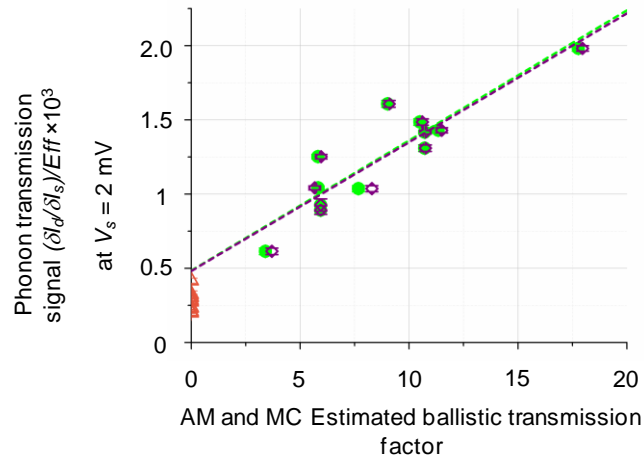


Figure A10. Measured signal produced by phonon transmission at $V_s = 2.0$ mV through un-etched (bulk) Si mesa. Signal values (vertical axis) are identical to those shown in

Figure 3.5 of Chapter 3: measured phonon transmission through mesa, presumed to be the sum of backscatter plus line-of-sight ballistic contributions, $\dot{n}_{bs} + \dot{n}_{los}(s \rightarrow d)$. Vertical error bars are standard error of signal average in each measurement. Horizontal axis is calculated transmission factor $\Gamma_{los}(s \rightarrow d) \times 10^3$ for line-of-sight ballistic transmission through silicon mesa. Calculated values for closed green circles were obtained using Monte Carlo approach and calculated values for open purple diamonds were obtained using Analytic model. Both approaches include phonon focusing (PF) effects in single crystalline Si. Dashed green and purple lines correspond respectively to linear fits for closed green circles and open purple diamonds. Open red triangles: independent measurements of backscatter signal \dot{n}_{bs} on the same sample chips. (Plot prepared by M. Aksit)

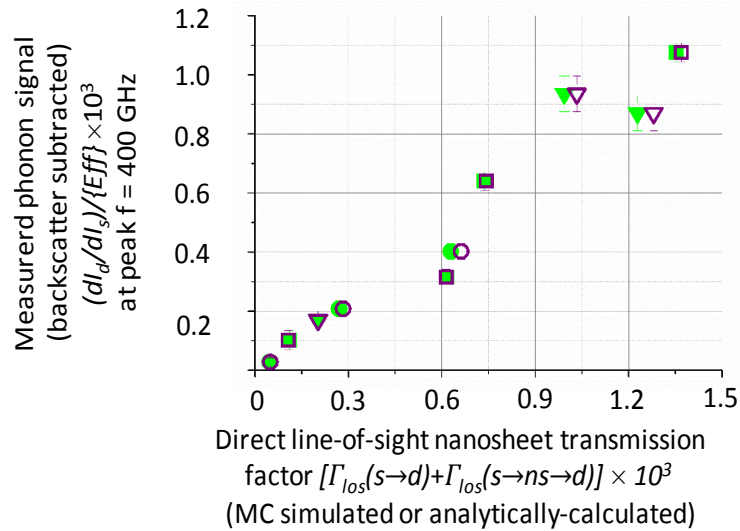


Figure A11. Measured signal produced by phonon transmission through ten different arrays of silicon nanosheets for phonon peak frequency of 400 GHz. Signal values (vertical axis) and error bars are identical to those shown in Figure 3.6: measured

phonon transmission through mesa, with estimated backscatter signal \hat{n}_{bs} subtracted. Circles, arrays A to C (widths $\sim 0.15 \mu\text{m}$). Squares, arrays D to G (widths $\sim 0.13 \mu\text{m}$). Triangles, arrays H to J (widths $\sim 0.35 \mu\text{m}$). Horizontal axis line-of-sight ballistic transmission factors $\Gamma_{los}(s \rightarrow d) + \Gamma_{los}(s \rightarrow ns \rightarrow d)$ are calculated using Monte Carlo approach (closed green symbols) or Analytic model (open purple symbols). Both approaches include phonon focusing effects in single crystalline Si.

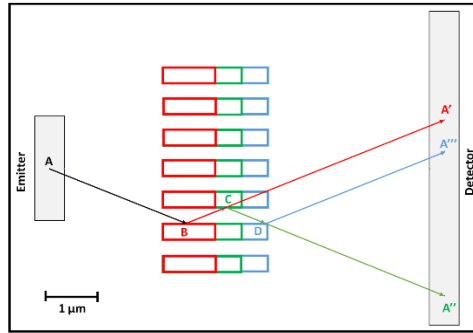


Figure A12: Test case performed to validate the Monte Carlo calculation of phonon surface interaction. Phonons are generated from a fixed point (A) source and the phonon vectors are also fixed to appropriate values to make all phonons hit point (B). Point (B) is located on the side wall of one of the $1 \mu\text{m}$ nanosheets (marked by red color). If the nanosheets are made to be $1.5 \mu\text{m}$ long (marked by green color) phonons specularly reflecting from point (B) hit point (C). If the nanosheets are made to be $2 \mu\text{m}$ long (marked by blue color) phonons specularly reflecting from point (C) hit point (D). Based on geometric calculations the phonons specularly reflecting from nanosheet sidewalls and hitting the detector are expected to land on points (A'), (A'') and (A''') for 1 , 1.5 and $2 \mu\text{m}$ long nanosheets respectively. The number of phonons that land on these three

points can be analytically calculated by $m \times p^n$ where m is number of generated phonons, p is specularity of the nanosheet sidewalls and n is number of phonon surface interactions between emission and detection. In Monte Carlo simulations, the number of phonons hitting points (A'), (A'') and (A''') are counted and compared with analytical calculations. See Supplementary Table A4 for this comparison and error analysis. (Plot prepared by M. Aksit)

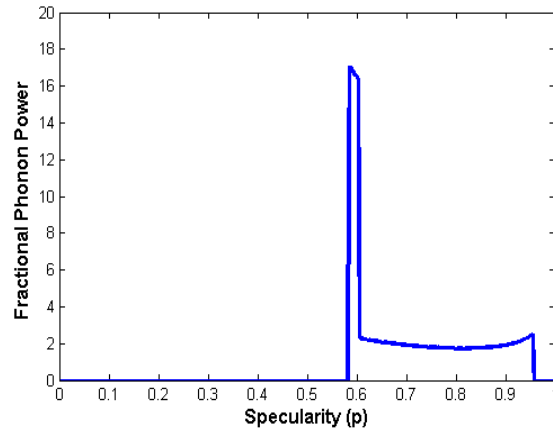


Figure A13: Distribution of specularity values predicted by Ziman expression for a 1 nm rough surfaces interacting with STJ emitted phonons at peak frequency of 400 GHz. The specularity distribution is plotted against fractional phonon power. Vertical axis units are fraction of total phonon power per unit specularity. (Plot prepared by M. Aksit and J. Hertzberg)

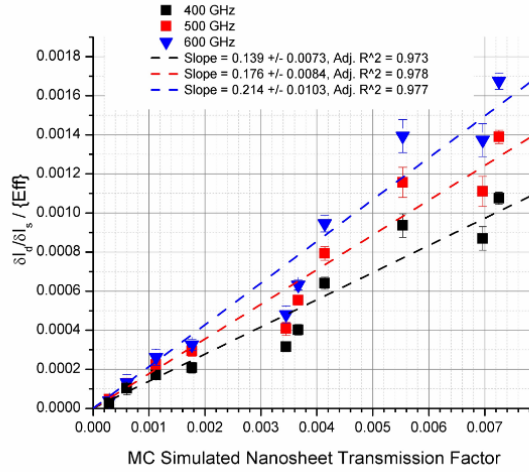


Figure A14: Zero-specularity model of transmission through nanosheet arrays, plotted against transmission measurements for peak frequencies 400, 500, 600 GHz. The horizontal axis values are phonon transmission factors $[\Gamma_{los}(s \rightarrow ns \rightarrow d) + \Gamma_{sc}(s \rightarrow ns \rightarrow d) + \Gamma_{los}(s \rightarrow d)] \times 10^3$, calculated using the Monte Carlo method assuming specularity $p = 0$ for phonon scattering at the nanosheet sidewalls, and are identical to those of the solid-symbol points in Figure 3.6 of the main text. Vertical values are taken from the data in figure A8 at the corresponding phonon spectral peak frequency. Estimated backscatter contribution \dot{n}_{bs} has been subtracted from all signal values. The 400 GHz datapoints in this plot are identical to the solid-symbol points in Figure 3.6 of the main text. Linear fit parameters are indicated in the legend at top of the figure. (Plot prepared by M. Aksit)

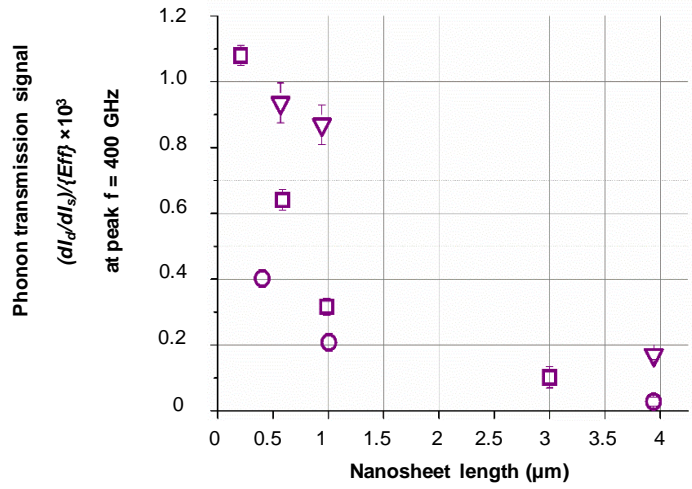


Figure A15: Measurements of phonon transmission through arrays of silicon nanosheets, using phonons of peak frequency 400 GHz. Signal values and error bars are identical to those in Figure 3.6. Horizontal axis is length of nanosheets in each array. Circles: arrays A to C. Squares: arrays D to G. Triangles: arrays H to J. (See Table 3.1).

(Plot prepared by M. Aksit)

Supplementary Table A1: Linear Fits of Phonon Transmission Signal

Line Fit Range (160-300 GHz) / Line Fit Range(\geq 300 GHz)			
Transport (through)	Slope	Intercept	Adjusted- R ²
Bulk	3.71E-6/3.71E-6	-2.09E-4/-2.16E-4	0.9991/0.9994
0.2 μm long Nanosheets (type D)	3.0E-6/2.88E-6	-1.26E-4/-1.01E-4	0.9976/0.9996
0.6 μm long nanosheets (type E)	1.64E-6/1.58E-6	-2.63E-5/-2.29E-5	0.9917/0.9989
1 μm long nanosheets (type F)	9.13E-7/7.50E-7	-1.81E-5/1.82E-5	0.9810/0.9918
3 μm long nanosheets (type G)	2.47E-7/1.77E-7	2.50E-5/6.32E-5	0.5996/0.7570

Supplementary Table A2: Elastic constants and density of Si

C_{11}	$1.7750 \times 10^{11} \text{ (kg m}^{-1} \text{ s}^{-2}\text{)}$
C_{12}	$0.745 \times 10^{11} \text{ (kg m}^{-1} \text{ s}^{-2}\text{)}$
C_{44}	$0.807 \times 10^{11} \text{ (kg m}^{-1} \text{ s}^{-2}\text{)}$
Density	$2.33 \times 10^3 \text{ (kg m}^{-3}\text{)}$

Supplementary Table A3: Ballistic Phonon Transport

Measured Spectrometer #	Mesa Width (μm)	Source STJ Width (μm)	Source STJ Fraction on Mesa Sidewall	Det. Width (μm)	Mid-line of Emitter-to-Detector Line-of-sight. Angle Relative to Si [110] (Deg.)	Source STJ R_N (Ω)	Det. STJ R_N (Ω)	Calculated Ballistic Transmission Factor
1	6.84	0.90	0.32	3.13	3	2531	182	0.0050
2	6.81	0.97	0.34	2.97	24	2351	185	0.0029
3	6.84	0.80	0.31	2.85	48	2400	186	0.0018
4^a	9.81	0.64	0.29	3.00	2	3915	197	0.0023
5^b	9.81	0.65	0.28	6.00	3	4057	202	0.0042
6	15.16	0.66	0.28	3.00	1	4139	200	0.0011
7	15.20	0.86	0.33	5.93	1	4056	207	0.0023
8	6.81	0.81	0.33	5.85	4	3590	207	0.0085
9^b	9.81	0.65	0.28	6.00	3	4051	204	0.0042
10^a	9.81	0.64	0.29	3.00	2	3913	198	0.0023
11	9.88	0.65	0.31	6.00	7	4094	194	0.0045
12	9.84	0.54	0.25	5.89	7	3631	187	0.0036

Table A3: Geometric configurations of phonon sources and detectors in bulk transmission measurements, with corresponding normal state resistance values. The phonon spectrometers marked with α and β indicate repeated measurements of the same two spectrometers during two separate cooldowns of our cryostat.

Supplementary Table A4: Trial of Monte Carlo Diffusive Scattering Algorithm

Nanosheet Length	# Emitted Phonons	# Phonon Surface Interactions	Points Where Phonons are Expected to Land on the Detector	Specularity of Nanosheet Sidewalls	#Phonons that are expected to land on point A, A' and A''	# Phonons that land on point A, A' and A'' in MC Simulations	% Error for MC simulations
1 μm	1000000	1	A'	0.5	$0.5^1 * 1000000 = 500000$	499963	-0.0074
				1	$1^1 * 1000000 = 1000000$	1000000	0
1.5 μm	1000000	2	A''	0.5	$0.5^2 * 1000000 = 250000$	249511	-0.1956
				1	$1^2 * 1000000 = 1000000$	1000000	0
2 μm	1000000	3	A'''	0.5	$0.5^3 * 1000000 = 125000$	125491	0.3928
				1	$1^3 * 1000000 = 1000000$	1000000	0

Supplementary Table A4: Number of phonons hitting points (A'), (A'') and (A''') in Monte Carlo simulations of 3 different test cases described in Figure S12 and their comparison with analytical calculations (See captions of Figure A12). Error values for Monte Carlo simulations are reported in the last column. (MC simulation performed by M. Aksit)

APPENDIX B: SUPPLEMENTARY INFORMATION FOR CHAPTER 4

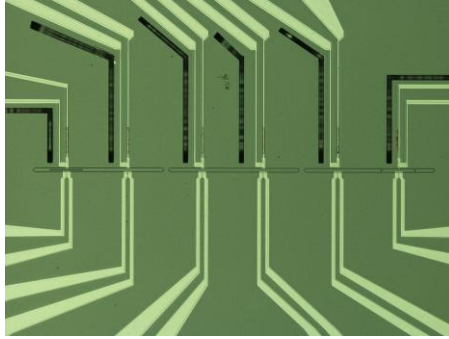


Figure B1. Optical microscope image of spectrometers with single blockers.

Table B1. Electronic Characterization of Phonon Spectrometers for Backscattering Studies

Experiment type	Emitter STJ $R_n (\Omega)$	Detector STJ $R_n (\Omega)$	$2\Delta_e$ (μeV)	$2\Delta_d$ (μeV)	Maximum detector linearity (GHz)	Emitter IV step width (μeV)	Mod. Amp δV_e ($\mu\text{V rms}$)	Estimated detector efficiency {Eff}
0 Enhancer, Backscattering	519	88	388	332	694	44	13.80	0.45
0 Enhancer, Cross	515	88	388	332	856	45	23.60	0.45
1 Enhancer, Backscattering	451	60	405	341	446	50	15.70	0.66
1 Enhancer, Cross	451	64	405	343	1345	50	24.50	0.82
2 Enhancers, Backscattering	949	326	415	369	284	73	7.38	0.12
2 Enhancers, Cross	2269	326	426	369	1362	74	5.40	0.12

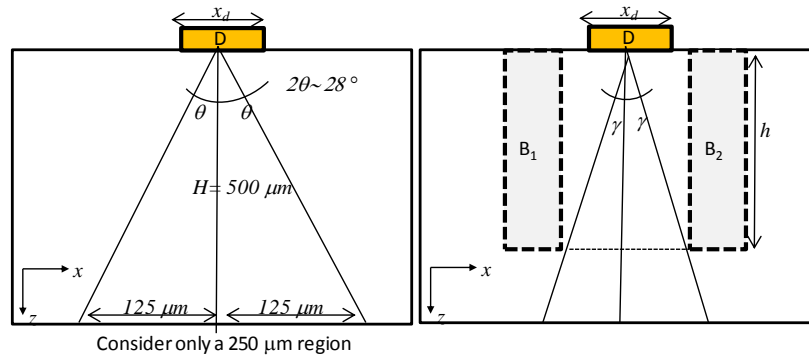


Figure B2. Schematic illustrating mechanism by which deep trenches around the detector wiring trace should lead to a reduction of collected phonons, as solid angle subtended by the detector with respect to the bottom of the substrate is reduced with the presence of the enhancers.

Table B2. Estimated Reduction in background signal based on subtended angle with bottom of substrate.

h	2γ	$2\theta/2\gamma$
$50 \mu\text{m}$	22.6	1.24
$100 \mu\text{m}$	11.4	2.45

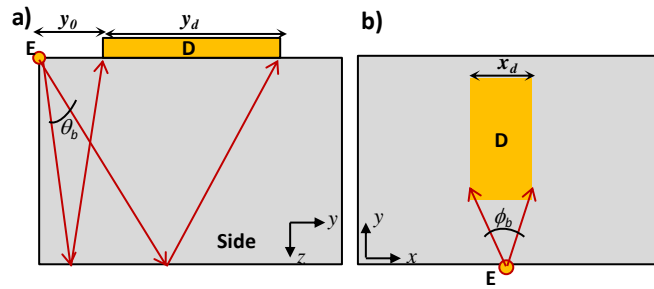


Figure B3. Schematic illustrating the estimation of backscattering of phonons based on (a) polar and (b) azimuthal phonon emission angle range. We note that this analysis assumes a specular bottom substrate; hence, incidence angle is the same as the reflected angle.

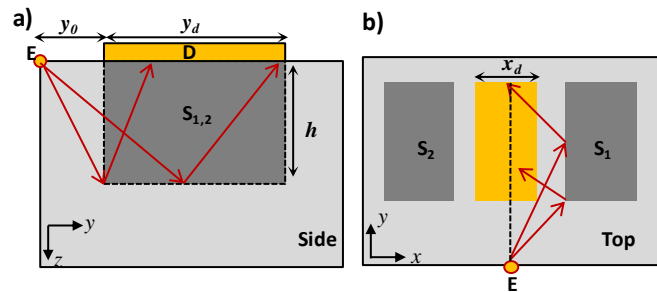


Figure B4. Schematic illustrating backscattering of phonons from enhancer walls based on (a) polar and (b) azimuthal angle range for phonon emission. We note that this analysis assumes a specular reflection. Due to symmetry only one blocker wall interaction is shown. Polar range from 12.5° to 56° and azimuthal range from 45° to 81.6° .

APPENDIX C: SUPPLEMENTARY INFORMATION FOR CHAPTER 5

Further Details on Experimental Methods

Chemicals: Hexanes ($\geq 98.5\%$), ethanol ($\geq 99.5\%$), ammonium sulfide (40-48 wt% solution in water), oleylamine (70%), copper(I) chloride (99.995%) were purchased from Aldrich. Molecular sieves (UOP type 3 Å) were also purchased from Aldrich and activated at 300 °C under dynamic vacuum for 3 hours before use.

Synthesis: A large-scale synthesis of Cu_{2-x}S nanoparticles followed standard procedures. [167] The synthesis was carried out in a dry, oxygen-free, dinitrogen atmosphere by employing standard Schlenk line and glove box techniques. A mixture of 1 g copper (I) chloride and 10 mL oleylamine was heated at 80 °C until the solution became clear. Temperature was then lowered to ~50 °C and 10 mL molecular sieve-dried $(\text{NH}_4)_2\text{S}$ oleylamine solution (0.5 mmol/mL) was added. The reaction was kept for 5 mins and the reaction flask was then immersed into an oil bath which has been pre-heated to 180 °C. The reaction was allowed to proceed for 40 mins and cooled down by removing oil bath. Ethanol was added to the solution to precipitate out nanoparticles, which were separated by centrifugation and washed one more time with hexanes/ethanol. The purified NCs were dissolved in hexanes. The prepared nanoparticles were stored in ambient conditions prior to utilization for transport studies. Although the particles have likely aged, all comparisons of EPD and spin-casting are for films made from the same stock of re-dispersed nanoparticles.

Transmission Electron Microscopy: TEM images of the nanoparticle samples were obtained using a FEI Tecnai F12 microscope operating at 120 keV. At least 100 particles were analyzed per sample to obtain a representative size distribution.

X-ray Diffraction: XRD (X-ray diffraction) spectra were collected using a Bruker General Area Detector Diffraction System (GADDS). Average grain sizes within the nanoparticle samples were determined from the XRD spectra using the Scherrer equation. The correction for instrumental broadening was conducted using the standard Al₂O₃ sample.

Atomic Force Microscopy: AFM imaging was conducted with an Asylum MFP-3D. Imaging was done in tapping mode with an Olympus AC1160TS probe and at a scan rate of 1 Hz.

Device Fabrication: Silicon-based devices were fabricated from p-doped silicon wafers (resistivity <0.005 W-cm ,with ~300 nm thick thermal oxide) purchased from Addison Engineering Inc. Metal layers for all devices (with the exception of the MSIM capacitors) were deposited using lift-off techniques. For the MSIM capacitors, a shadow mask was utilized to deposit the gold films onto the nanoparticles. Electron-beam evaporation was used throughout for metal deposition.

FET Measurements: All FET measurements were taken with a Karl Suss PM6 probe station equipped with Keithley 237 source measurement units.

Capacitance-Voltage Measurements: C-V data were taken with an Agilent 4284 Precision LCR meter equipped with an Agilent 16047A Test Fixture. The H_{pot} and H_{cur} leads are connected to the gate (doped-Si), and the L_{pot} and L_{cur} leads are connected to the reference (Au).

X-ray Photoelectron Spectroscopy (XPS): XPS data were collected on a Surface Science Instruments SSX-100 operating a pressure < 2×10⁻⁹ Torr and with monochromatic Al K α X-rays at 1486.6 eV.

Supplementary Information on Characterization of Nanoparticles and Nanoparticle Films

Scanning electron micrographs and AFM images of films prepared by EPD and spin-casting suggests that EPD films are more compacted. Figure C1a-d shows scanning electron micrographs (SEM) of typical Cu_{2-x}S films deposited by EPD and spin-casting, treated with ammonium sulfide, that was measured in our studies. The SEM images were processed with ImageJ software (National Institute of Health) in order to assess the packing of the film. By first applying high contrast to the SEM images and thresholding the resulting image, the pores and particles in the image are counted and sized. [193] Upon analyzing images of the EPD and spin cast films in Figure C1b and d, the percentage area of the nanoparticles is found to be 63% and 40%, respectively, suggesting that the EPD films are more compacted than spin-cast films for all the films observed in the SEM. This basic particle count analysis, which focuses mostly on the topmost layer of the films, could be improved by carrying more rigorous pore sorption measurements in the future. Tapping mode height and phase AFM images of EPD and spin cast films are taken to further understand the film compaction as shown in Figure C1e-h. The root mean square (rms) roughness of the $1\ \mu\text{m} \times 1\ \mu\text{m}$ scan area of the EPD and spin-cast film is 6 nm and 14 nm, respectively. (We note that the AFM images were taken using a tip of radius of ~ 8 nm; hence, the images do not laterally resolve individual particles ~ 5 nm in diameter.) The phase images (Figure C1g and h), which monitor the phase lag between the drive signal of the cantilever and the actual cantilever oscillation, reveal the homogeneity of the deposited films of the films as tip interaction with different materials result in different phase offsets. In addition, the phase images show

that the porous region of the films have a larger phase offset than regions with nanoparticles, providing better visualization of the packing of the films. These results suggest that EPD forms more closely packed nanoparticle films than spin-cast films and are thus likely to have better interparticle coupling, corroborating the observation from the SEM images.

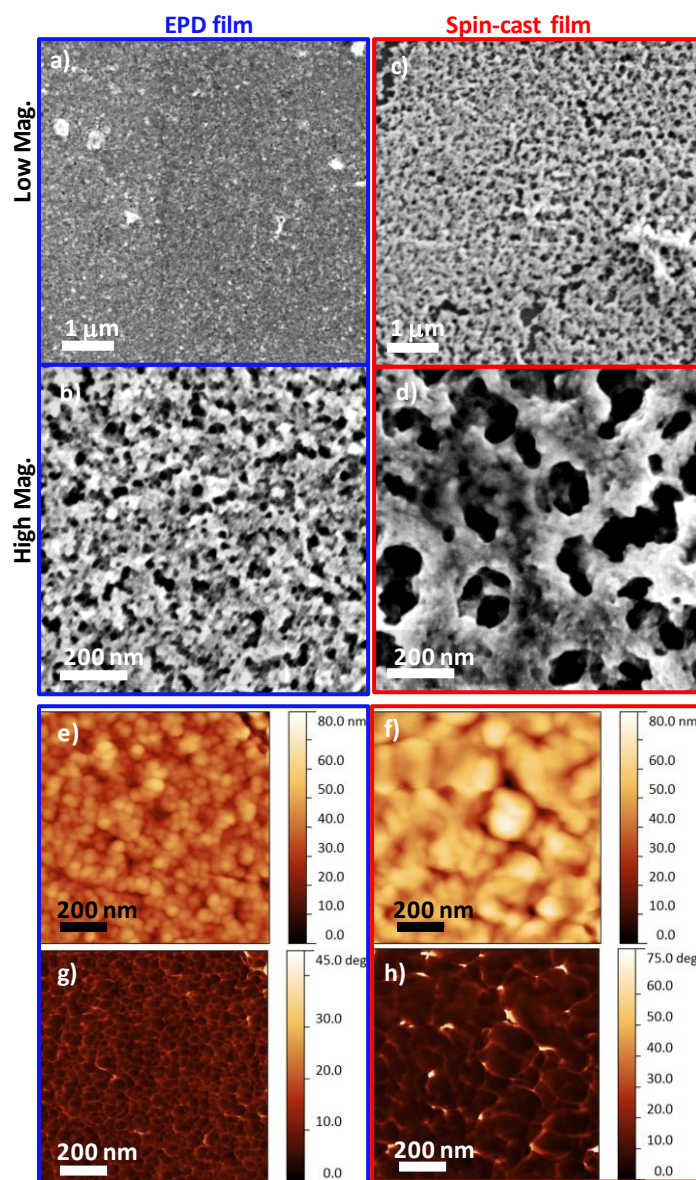


Figure C1: SEM and AFM images of EPD (blue outlines) and spin-cast (red outlines)

films treated with ammonium sulfide. a-d) Low and high magnification SEM micrographs of typical EPD (a,b) and spin-cast films (c,d) after ammonium sulfide treatment. EPD is shown to form more tightly packed films than spin-cast films. e) AFM height image of typical EPD film. f) AFM height image of typical spin-cast film. g) AFM phase image of typical EPD film. h) AFM phase image of typical spin-cast film.

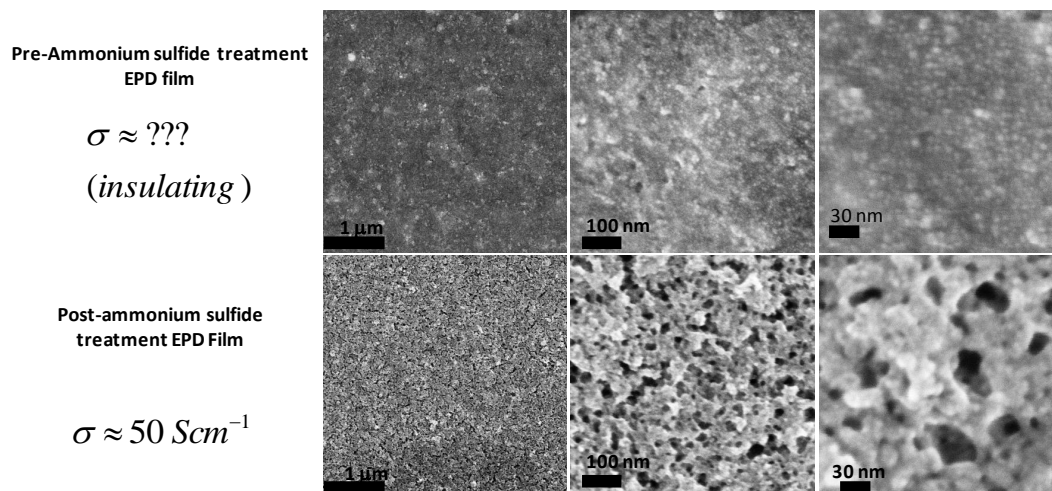


Figure C2: SEM of EPD films with and without ammonium sulfide treatment. Magnification increases from left to right. Without the ammonium sulfide treatment that links the particle together, the EPD films are insulating.

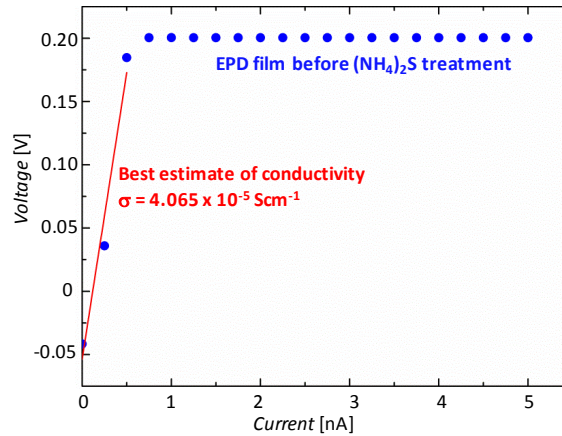


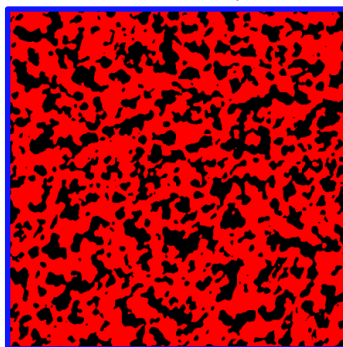
Figure C3: Four-wire resistance measurement of EPD pre-ammonium sulfide treatment. Measurement instrument (Keithley 237) reaches compliance voltage of 0.2 V at 1 nA of source current. This implies that the sheet resistance will be in the order of $G\Omega$; hence, we can conclude the films are insulating before ammonium sulfide treatment.

Supplementary discussion: Percentage Area Estimation with ImageJ

From the SEM images of the nanoparticle films in Figure C1, we observed that the EPD films appear to have smaller pore sizes than spin-cast films. However, in order to obtain a more quantitative estimate of the percentage area of the images that consist of nanoparticles, the SEM images were processed with ImageJ. We note that since the films are made from multiple deposition cycles, this analysis method is mostly providing information about the topmost layer of the films. First we enhance the contrast of the images by 100% to better distinguish the nanoparticle regions and the pores—leading to a binary image with higher pixel intensity for the nanoparticle regions, and low intensity for the pore regions, since the original SEM images are grayscale. With ImageJ, we made sure a threshold value of 129 is obtained for the enhanced contrast

images, which implies converting the original grayscale images into binary images with only two pixel values, 0 and 255, corresponding to pore regions and nanoparticle regions respectively. The percentage of pixels with 255 value then represent the area occupied by the nanoparticles. The results are shown in Figure C4.

Processed Image of EPD Film
(% Area of NP film (red pixels) = 63)



Processed Image of Spin-casted Film
(% Area of NP film (red pixels) = 40)

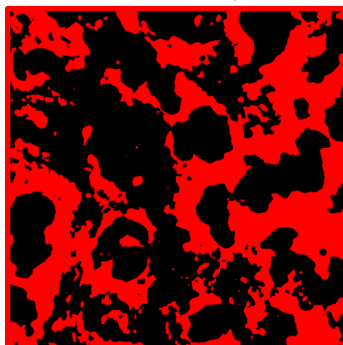


Figure C4: ImageJ-processed images of SEM micrographs of EPD and spin-cast films (Figures C1b and C1d). Images are processed following standard procedures [193]. EPD films has large percentage area of nanoparticles (63%) than spin-cast films (40%) suggesting better film better compaction, which likely enhances interparticle coupling.

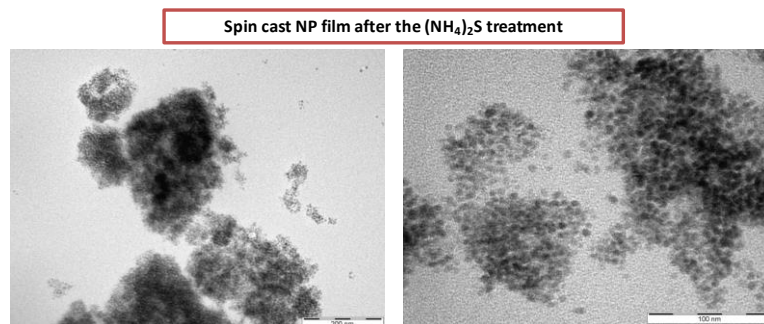


Figure C5: Low and high magnification TEM images of nanoparticles scrapped off from spin-cast films treated with ammonium sulfide. Nanoparticles do not appear to be sintered, but are tightly connected.

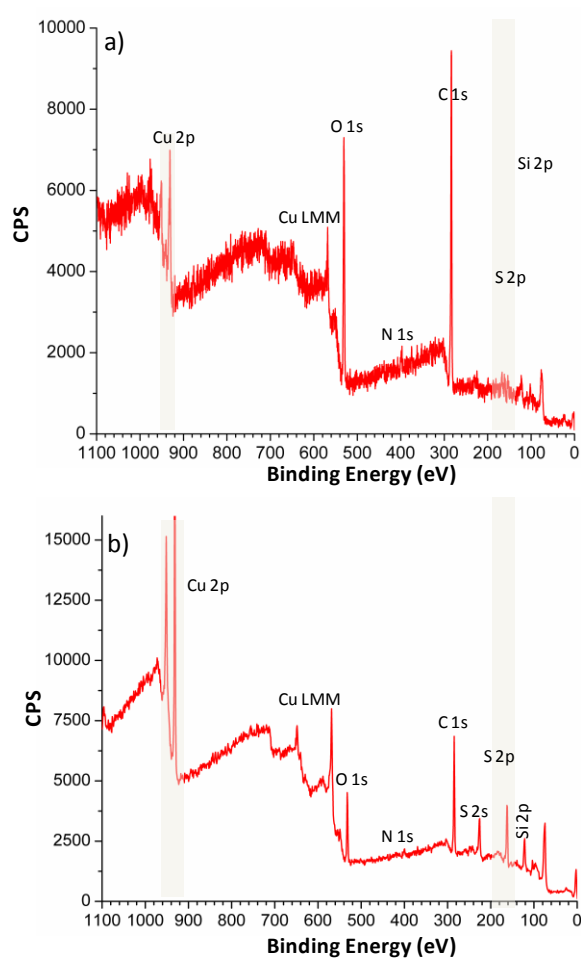


Figure C6: XPS survey scan of spin-cast film. a) pre-ammonium sulfide treatment. b)

post-ammonium sulfide treatment.

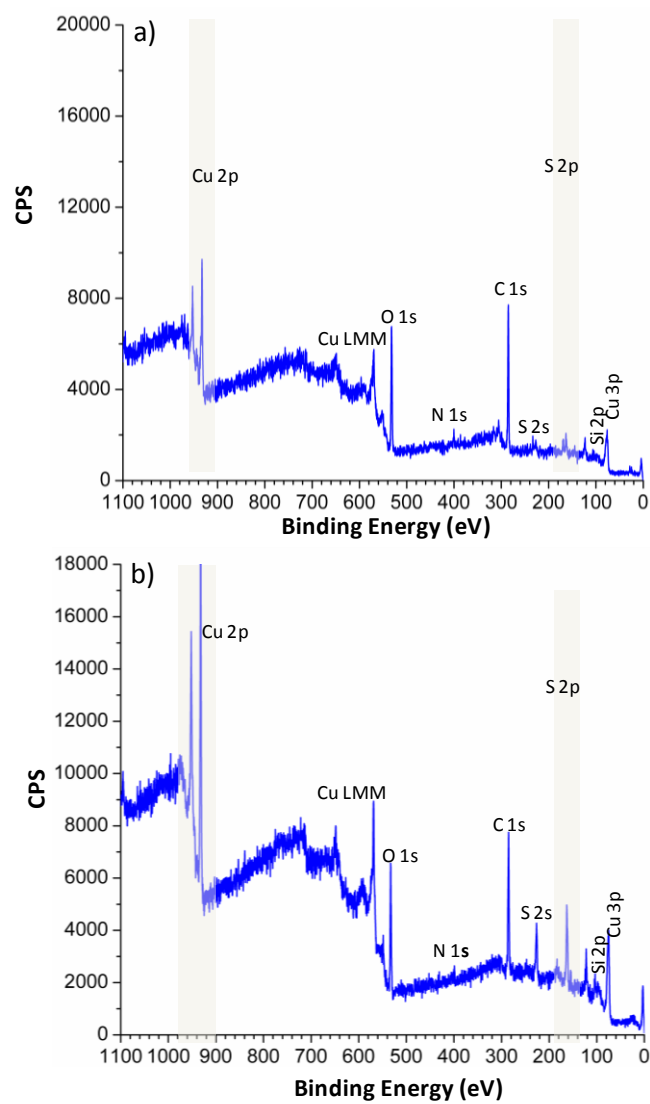


Figure C7: XPS survey scan of EPD film. a) pre-ammonium sulfide. b) post-ammonium sulfide treatment.

Table C1: Summary of atomic percentages of elements analyzed in XPS spectra of spin-cast and EPD films before and after ammonium sulfide treatment. Films for XPS studies were deposited on doped-Si/SiO₂ substrates.

Element	Spin-cast before (NH ₄) ₂ S	Spin-cast after (NH ₄) ₂ S	EPD before (NH ₄) ₂ S	EPD after (NH ₄) ₂ S
C	70.49	32.48	65.07	49.4
O	21.08	17.25	24.02	14.64
N	2.15	2.87	2.1	0.45
Cu	4.12	22.03	5.96	14.72
S	1.99	22.19	2.81	17.55
Si	0.16	2.78	0	3.24

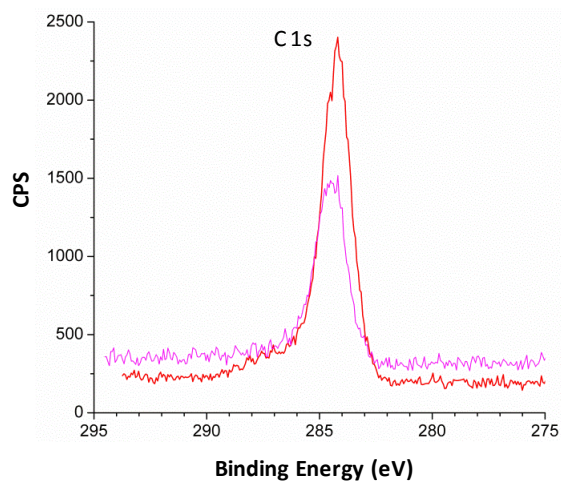


Figure C8: High resolution XPS scan of the C 1s region for spin-cast before (red) and after (magenta) ammonium sulfide treatment.

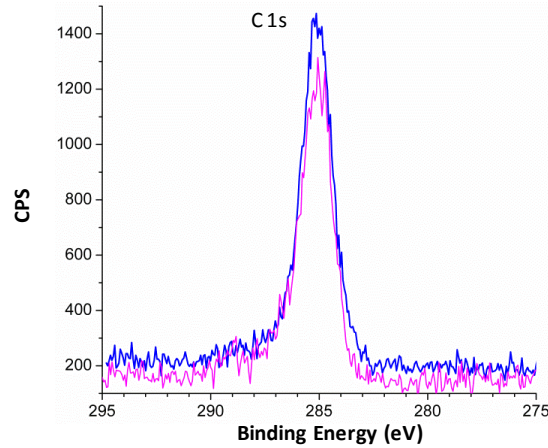


Figure C9: High resolution XPS scan of the C 1s region for EPD film before (blue) and after (magenta) ammonium sulfide treatment.

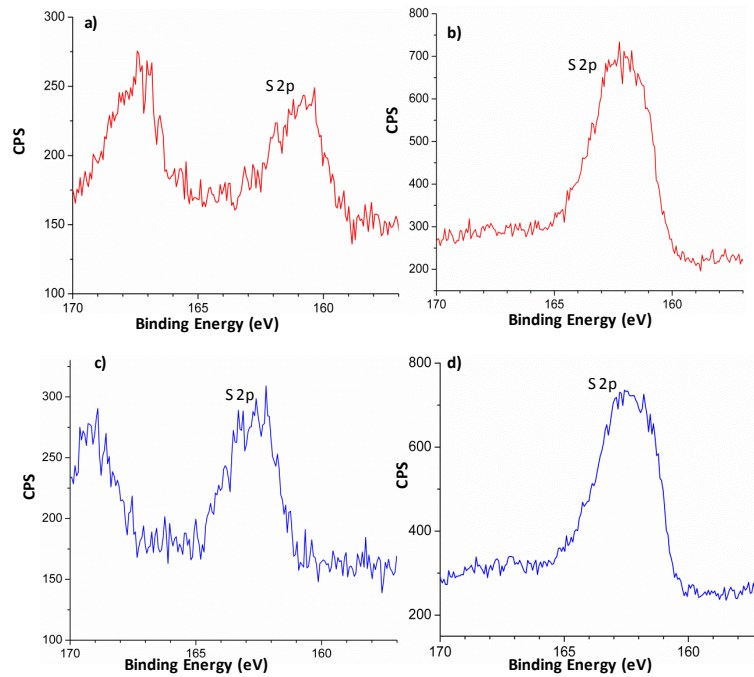


Figure C10: High resolution XPS scan of the S 2p region for spin cast films (a) Spin-cast film before ammonium sulfide treatment. (b) Spin-cast film after ammonium sulfide treatment. (c) EPD films before ammonium sulfide treatment. (d) EPD films after ammonium sulfide treatment.

Table C2: Comparison of our nanoparticle-based Cu_{2-x}S films to previous work.

Synthesis	Deposition method	Stoichiometry (x in Cu_xS)	Stoichiometry determination	Film thickness	Conductivity [Scm^{-1}]	Reference
Copper target in Ar- H_2S - H_2 atmosphere/ Cu1.8S source	RF sputtering/ Evaporation	1.995 and 1.999	Electrochemical methods	0.1-0.5 μm / 1 μm	35 and 7	Wagner et al. [162]
Copper in $\text{H}_2\text{S}/\text{Ar}$ atmosphere	RF sputtering	Not specified	None	1 μm	17.6	Leong et al. [181]
K15 (based on Cu(hfac)(tmvs))	Pulsed CVD	1.9-2.0	EXAFS	120 nm	18.5	Carbone et al. [163]
Aqueous Cu thiosulfate	Chemically deposited	1.8 and 2.0	Rutherford backscattering analysis, and film color	120 nm and 80 nm	277 and 69	Grozdanov et al. [164]
Bath of Copper chloride, triethanolamine, ammonia, sodium hydroxide, thiourea, and DI water	Chemically deposited	1.8	X-ray diffraction	100 nm	2000-10000 (after annealing)	Cardoso et al. [165]
Bath of Copper chloride, triethanolamine, ammonia, sodium hydroxide, thiourea, and DI water	Chemical bath deposition	Not specified	Comparison with reported stoichiometry-dependent sheet resistance	150 – 350 nm	1 -250 (annealed and dependent on deposition time)	Nair et al. [166]
Dissolution of copper chloride in a mixed solution of water ammonium hydroxide, TEA, and thiourea	Surface induced nucleation and in-situ assembly	1.75	Electron diffraction	~100 nm	~2000	Liufu et al. [178]
Heat-up colloidal synthesis (Copper chloride and oleylamine) [167]	Spin-casting + ammonium sulfide treatment / EPD + ammonium sulfide treatment	1.94-1.96	X-ray Diffraction	~120 nm	5.7 / ~75	This work

Table C3: Determination of percentage porosity in EPD and spin-cast films.

Deposition Method	Mass (mg)	Height (nm)	Volume (cm ³)	Density (g/cm ³)	Porosity %	Solid Fraction
Spin	0.08	149	3.35×10^{-5}	2.39	57	0.43
EPD	0.12	154	3.47×10^{-5}	3.46	38	0.62

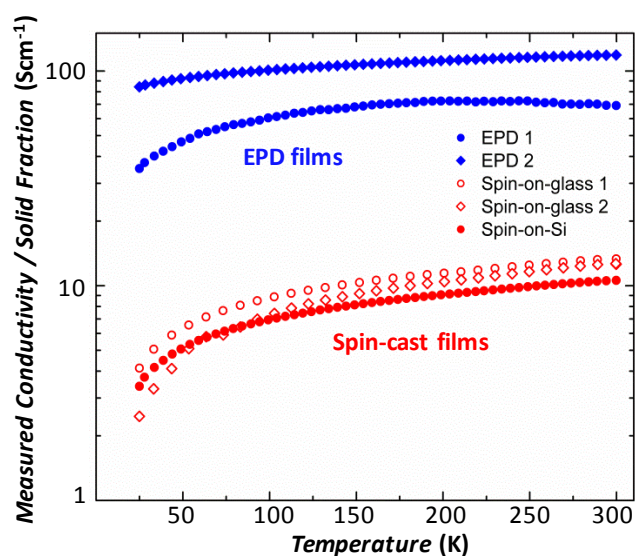


Figure C11: Temperature-dependent conductivity scaled by the solid fraction of copper sulfide to express the interlinking nanoparticle conductivities of EPD and spin-cast films. EPD and spin-cast films have ~38% and 57% porosity, respectively.

Table C4: Adjusted- R^2 of linear fits of the temperature-dependence of conductivity to nearest-neighbor hopping, Efros-Shklovskii variable-range hopping, and Mott variable-range hopping.

Sample	Adjusted $-R^2$ values of linear fits of conductivity with different powers of temperature (T)		
	$1/T$	$1/T^{0.5}$	$1/T^{0.25}$
EPD1	0.962	0.970	0.950
EPD2	0.852	0.951	0.982
Spin-on-Si	0.928	0.989	0.999
Spin-on-glass 1	0.936	0.993	0.999
Spin-on-glass 2	0.949	0.996	0.996

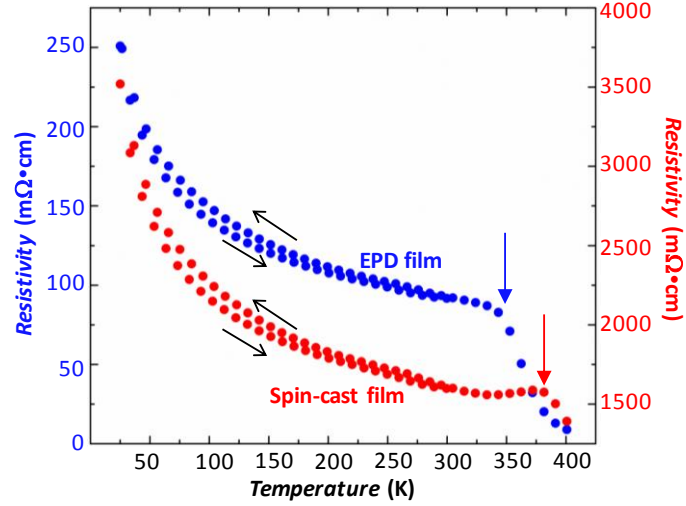


Figure C12: Plot of temperature-dependent resistivity of EPD and spin-cast films that have been thermally cycled from 300 K to 25 K, and then from 25 K to 400 K. 400 K is the maximum temperature obtainable in our measurement apparatus (PPMS). The blue and red arrows indicate the onset of a sharp drop in resistivity for EPD and spin-cast films, respectively.

Supplementary Discussion: Film performance over time

The conductivity of one of the spin-cast films measured in ambient over time suggest a degradation in film performance with time as shown in Figure C13: After ~50 days, room temperature conductivity remains the same order of magnitude, but after ~140 days, room temperature conductivity drops by an order of magnitude. Such studies will be important considerations needed for practical applications. Perhaps, the films should not be stored in ambient conditions for a lengthy study.

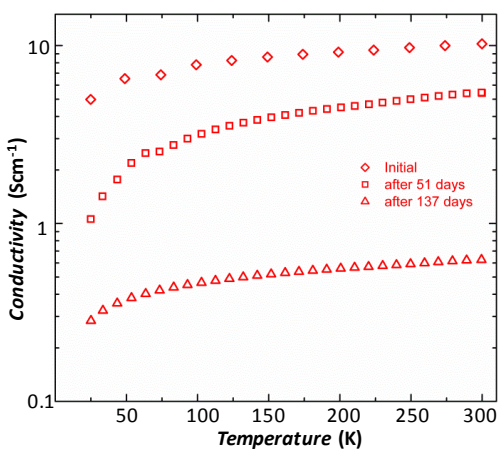


Figure C13: Plots of conductivity of a spin-cast film over time. After ~50 days in ambient condition, the spin-cast film has about the same order of magnitude room-temperature conductivity, but drops about $\frac{1}{2}$ in value. Film conductivity degrades over time when left in ambient conditions.

Supplementary Discussion: Light Stability

In order to assess the sensitivity of the films to light, four-wire resistance measurements of the films deposited on two gold electrodes of varying spacing (50 to 400 μm) were performed in dark (in an enclosed probe station) and in light (with Microlite FL2000

150 W Fiber Optic Illuminator). We observed negligible changes in film resistance in the films as shown in Figures C14 and C15. In addition, the resistance of the EPD films increases with increasing electrode spacing suggesting a more uniform film, while the spin-cast films appear to have an inhomogeneous coverage.

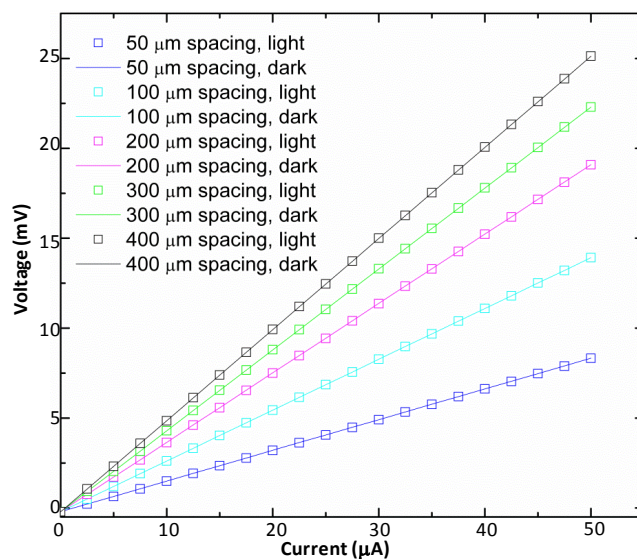


Figure C14: Current-Voltage (I-V) measurements of EPD films in the dark (lines) and under illumination (squares) with a 150 W illuminator showing negligible light sensitivity. 4-wire resistance measurements were performed with films deposited on Au electrodes with varying spacing (50 to 400 μm).

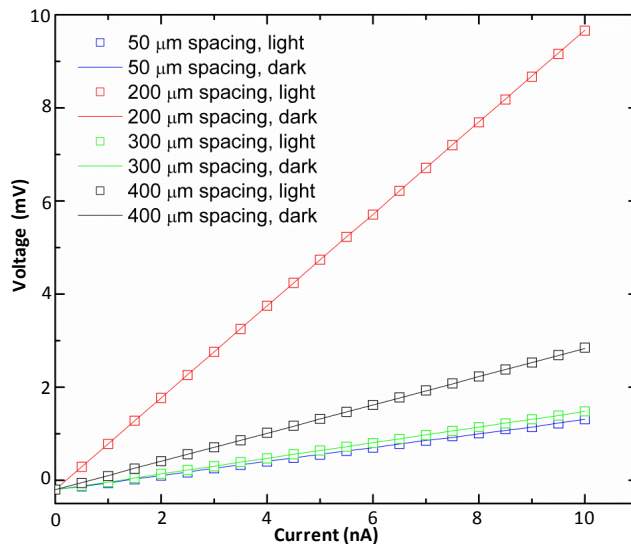


Figure C15: Current-Voltage (I-V) measurements of spin-cast films in the dark (lines) and under illumination (squares) with a 150 W illuminator showing negligible light sensitivity. 4-wire resistance measurements were performed with films deposited on Au electrodes with varying spacing (50 to 400 μm).

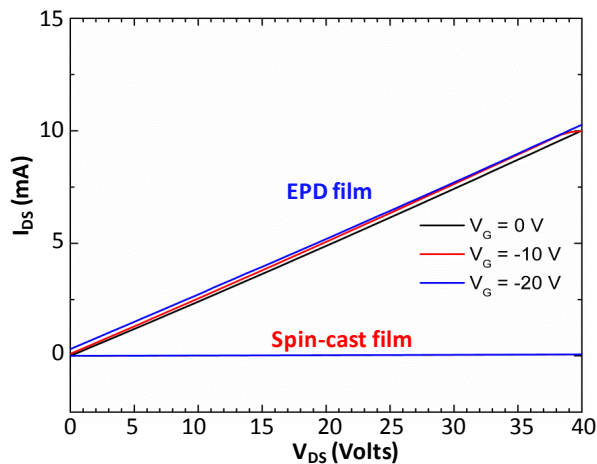


Figure C16: Linear scale plot of drain-source current as a function of drain source voltage (FET output characteristics). Minimal gate modulation is observed. The higher conductivity of the EPD films suppresses the features of the spin-cast film plot when

shown in a linear scale. Hence, a log-log plot is shown in Figure 5.6a.

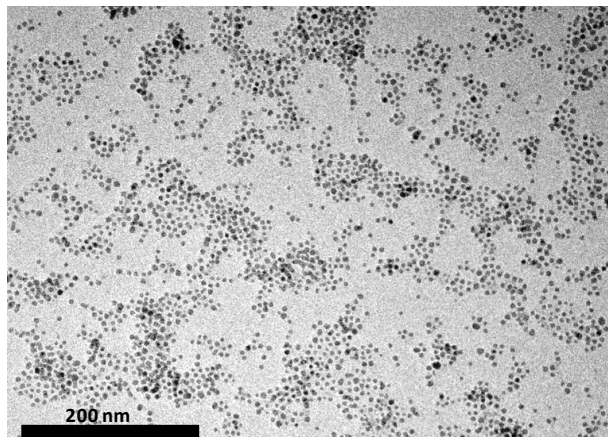


Figure C17: TEM of the starting copper sulfide nanoparticles

APPENDIX D: ADDITIONAL EXPERIMENTAL DETAILS AND TECHNIQUES

Fabrication Process Flow

In this section, an overview of the experimental flow and customized techniques is discussed. All the tools in the CNF have detailed training and instructions; however, some details that pertain to the work in this thesis will be highlighted. The process flow for a complete device fabrication (STJ fabrication for phonon project) or metal depositions for (nanoparticle project) is depicted in Figure D1. The following are peculiar details regarding each process step that may not have been listed in chapter 2:



Figure D1: Schematic showing the overview of fabrication steps for STJ or typical metal film deposition.

- CAD Design: AutoCAD (from AutoDesk, licensed yearly from Cornell IT) is used to design all devices, and the file formats are .DWG and .DXF. The DXF file is needed for subsequent conversions to file formats acceptable for CNF tools. All the device files are stored in the Robinson Group office computer (*Phonon Spectroscopy Desktop > Phonon Spectroscopy > Designs > Devices*) and clean room data are stored in (*Phonon Spectroscopy Desktop > Phonon Spectroscopy > Clean Room Data.*) Avoid sharp corners as much as possible. Note that the scale is mm.
- CAD conversion: LINKCAD , a proprietary software available to CNF users, is needed to convert .DXF files to .GDS (the format required for mask making tools). Ensure that the drawing scale is set appropriately. GDS files are also needed for file processing for other specialized tools like the E-beam Lithography tools (JEOL 6300).
- Photolithography : All masks were fabricated at CNF with the Heidelberg DW2000 mask writer. It accepts .GDS files. All the written masks (are scaled to be 5x the actual size of the pattern to be fabricated on wafers; hence, a 5X stepper (Autostep i-line or 5X G-line stepper) is needed. Note that some photoresists are optimized for either g-line (435 nm) or i-line (365 nm). Shipley S1818 and S1813 were used when thick and thin resist layers were desired respectively.
- Lift off: For lift off metal deposition a bilayer of LOR20B/S1818 was utilized. LOR 20B is a special formulation (Microchem Inc.) which is a more viscous resist with faster dissolution rate than typical LOR resists. This lift-off resist is spun 3 times to get a desired thickness of $\sim 2.6 \mu\text{m}$ ($\sim 10000 \text{ rpm}$, 1000 rpm/s ,

60 s.) Then S1818 is spun (4000 rpm, 90 secs) to complete the bilayer. Following exposure (with the G-line 5X tool) and post exposure bake (115 °C for 60 s), hand development is performed in metal-ion free MIF726 or MIF 300 solution until desired undercut (~ 3-4 μm) is obtained. LOR 5A/S1813 bilayer is sufficient for metal deposition for making nanoparticle devices.

- Descum: Before any metal deposition step, it is necessary to descum the pattern with light oxygen plasma exposure (Oxygen clean recipe in Oxford 80 etchers) to prevent deposited film from delaminating.
- Evaporation: Evaporation of metal films such as gold or silver require adhesion layer (~5-10 nm of Ti or Cr) to prevent films from delaminating (follow listed CNF deposition criteria which changes from time to time). Au deposition is mostly used for nanoparticle electrodes, e-beam alignment marks, and quasiparticle traps. For STJ Al deposition, the Baker Lab evaporator, equipped with our custom built tilt stage is used for evaporation. Graphite crucibles do not work for Al deposition, instead a FABMATE® crucible (TLI Inc.) is needed. Our home built tilt stage for shadow evaporation is shown in Figure D2

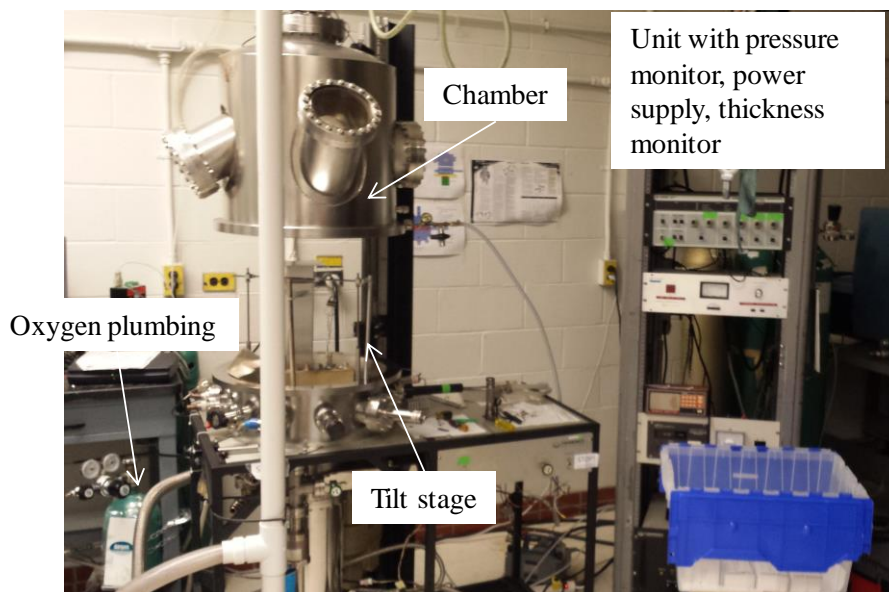


Figure D2: STJ Evaporation chamber in Bard Hall (Baker Lab.) modified to include sample tilting capability and oxygen plumbing.

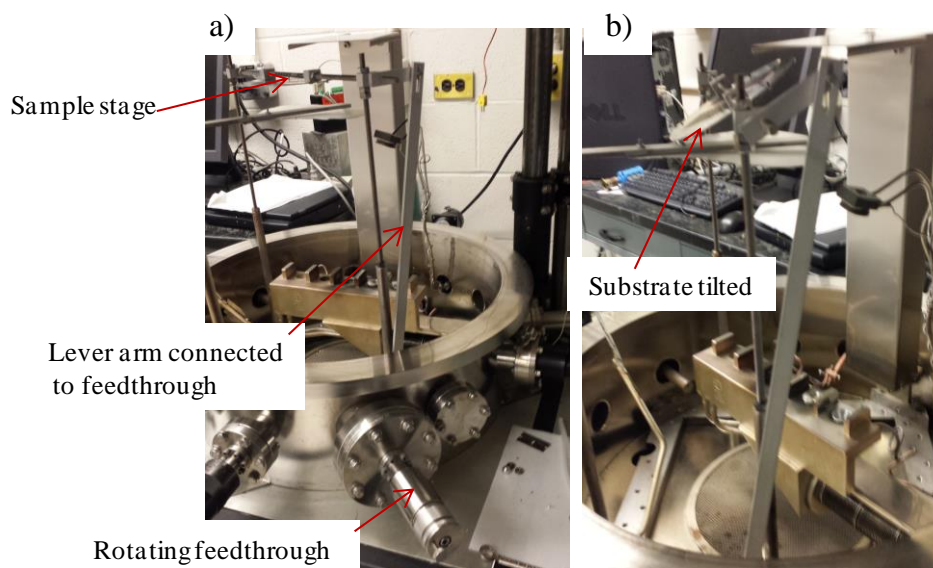


Figure D3: Tilt stage and lever-arm operation showing (a) rotating feedthrough set for (a) normal evaporation and (b) shadow evaporation with tilted sample stage.

- Inspection: It is important to utilize an optical microscope to inspect the fabrication process throughout to ensure resist are formed well, wafer surface is smooth, Dolan bridges are intact, appropriate junction overlap is obtained etc. SEM inspection of a wafer with STJs should be done with caution, as the electron beams sometimes damage the devices. Also proper grounding is needed. Film heights and etch depths must be checked with profilometer (Alpha Tencor P10).
- Probe Station Testing: A room temperature resistance measurement with the probe station is needed to check if the fabricated STJs are functioning appropriately. A very low resistance ($< 20 \Omega$) is likely a short, while $G\Omega$ resistances indicate an open loop (likely be due to film scratch or junctions not overlapping.) Desired overlap area and resistance could be pre-determined as discussed in Chapter 2 of this thesis.
- Packaging: Wafers are diced into 4.5 sq. mm chips with the dicing saw and mounted on a custom built sample stage (depicted in Chapter 2). Al wire bonds are used for electrical connections in the CNF, and the devices are brought to the lab in Bard Hall for measurements.

Procedure for Shallow-depth Anisotropic Etching of Mesas on Silicon using KOH as Etchant

1. Obtain new silicon wafers and RCA clean the wafers in the MOS Clean hood (10 mins in acid and base tanks, and 10 seconds in HF tank).
2. Deposit about 100nm LS Nitride in the furnace B4

3. Measure actual nitride thickness deposited with the Filmetrics film mapper 50
4. Prime wafer with nitride in YES vapor prime oven (optional)
5. Spin Photoresist S1813 on wafer: 5500 rpm, 1000 rpm/s, 60 sec. bake at 115 C for 60 sec.
6. Expose GCA alignment mark on wafer using the GCA 5x-stepper. Standard or Non-Standard alignment as required. For Non-standard alignment, press 'A' to move from right alignment mark to left. Exposure: 0.5secs, Focus offset:-10.
7. Develop by hand in MIF 300, while gently agitating, for 90 sec and rinse thoroughly in de-ionized (DI) water.
8. Inspect alignment marks under optical microscope to ensure pattern is scum free and fully developed.
9. Etch the nitride off the Alignment keys in Oxford plasma Etcher 81/82 based on thickness measured in step 3 and recent etch parameter in tool log book. (For 82, 4 minutes CF_4 etch would suffice). CF_4 is thought to be better than CHF_3/O_2 for nitride etch.
10. Resist hot strip the wafers to remove all of resist (or oxygen plasma clean the wafer for 10mins after CF_4 etch)
11. Additional cleaning in Aura resist stripper (recipe 9) if hot strip was used.
12. Prime wafers as in step 4. (Not optional this time or else mesa patterns would disperse during development).
13. Repeat step 5.
14. Expose mesa pattern on the 5x stepper; expo: 0.45, focus offset:-10 (may vary).
15. Repeat step 7

16. Inspect patterns optically to ensure no scum on wafers. additional development may be necessary
17. Etch the nitride as in step 9. Only mesa tops would have nitride in chip area.
18. Strip resist in hot strip, use Aura clean (recipe 9), and then MOS Clean the wafers [etching should begin not more than 5 hours after MOS clean].
19. Etch setup: Place the Branson Ultrasonicator in the Base hood and fill with warm water. Change temperature set-point to 50 Celsius and begin heating. Place magnetic stirrer/stand set-up in the ultrasonicator.
20. Place magnetic stirrer and ~5 in round teflon tripod stand in crystallizing dish.
21. Add 1.2 L of 50% KOH to dish, cover and place on the stirrer /stand.
22. Get another dish with DI water heated to about 50-60 Celsius in preparation for rinsing immediately after etch.
23. In Acid hood, prepare two dishes of dilute HCl (HCl:H₂O 1:6) and DI water for rinsing after etch.
24. Place thermocouple in the KOH solution to monitor solution temperature different from temperature of surrounding water.
25. Stir at about 300-350 rpm, or as deemed necessary.
26. When the KOH is close to 50 Celsius, turn on the sonicator (temperature would increase fast, but don't let it rise above 50 Celsius as etch rate is rapidly increased with minor temperature increase between 50 and 60 Celsius).
27. With ultrasonicator 'ON' and KOH temperatures at 50 C, place wafer to be etched on the tripod stand and begin timing.
28. From Seidel et al, [194] Etch rate is 7.5 $\mu\text{m/hr}$ at 50 C/50% KOH (shouldn't be

more than 11 minutes for $\leq 2 \mu\text{m}$ mesa height)

29. Once etching is complete, rinse thoroughly in warm DI water, but don't dry.
30. Safely transport wafer to acid hood and rinse in dilute HCl, then rinse in DI water. Spin rinse dry in Verateq spin dryer.
31. Inspect etch under the microscope
32. Profilometry: to determine etch depth, mesa angle, and roughness estimate.
33. SEM to determine surface roughness of (100) and (111) planes, and exact etch angles.
34. Etch nitride in 49% HF for about 30 -45 mins. Rinse in DI water. Blow dry.

Procedure for Fabricating High Aspect Ratio Nanostructures

1. Nanostructure are patterned with Electron-Beam Lithography (JEOL 6300) using ZEP 520A (Zeon Chemical Inc.) as the e-beam resist. This is a high resolution resist with good etch mask capabilities.
2. Develop pattern in ZED N50 (Zeon Chemicals) for 40 secs
3. Rinse in Methyl Isobutly Ketone:Isopropyl alcohol (MIBK:IPA) for 30 seconds
4. Rinse in IPA for 30 seconds
5. Etch for 5 mins in UNAXIS (OOO24.BCH Batch file), and check etch depth with profilometer (usually ~ 7 mins of etch is required for a $1 \mu\text{m}$ depth, but etch rate is very pattern and wafer size dependent and must be characterized for each new pattern). Small chips must be mounted on a carrier wafers with thermal grease.
6. Etch further as needed based on etch rate determined from step 5.

7. Etch Process (OOO24.BCH in the UNAXIS etcher): Main Etch step setting (C₄F₈ = 60 sccm, SF₆ = 30 sccm, Ar = 40 sccm, O₂ = 10 sccm. RF1 = 10 W, RF2 = 700 W)
8. Strip Resist (do as last step before preparing for cooldown and after dicing etc.) in Gasonic Aura etcher (Recipe 9). Slight decrease in STJ resistances may occur.

Cooldown and Measurements

In this section, all the steps that ensue after a completed chip is ready for measurement are highlighted. The physical basis for understanding the STJ spectrometer and specific instrumentation for operating the spectrometer have been discussed fully in Chapter 2 of this thesis. In this section, some useful practical insights and measurement details will be highlighted. While these details describe specific experimental details, it is worth pointing out that these details are more of a guide for successful implementation of all the experimental details discussed in Chapter 2.

- ***Helium for Measurements:*** Liquid helium could be obtained from LASSP Cornell or from Praxair. As at July 2015, Airgas is now the LHe supplier. In case of the need to transfer LHe from Dewar to Dewar, see procedures below.
- ***Sample Mounting and Demounting:*** Once the chips to be measured have been wire-bonded on the sample stage, they must be carefully mounted on the fridge, while ensuring proper grounding with wrist straps on the fridge. A video for the sample mounting and demounting was created by J.B Hertzberg, and is found on the office computer (*Phonon Spectroscopy*> *Phonon Spectroscopy*

Project>Video for mounting /Video for demounting). The goal here is to thermally anchor the chip/sample stage onto the fridge, and to make sure all the electrical connections and devices are intact by measuring the room temperature resistance with a multimeter. In Figure D4, the size of the (4.5 x 4.5 mm) chips and an illustration of a properly and completely mounted chip are shown as a reference. The steps for chip mounting are reversed for chip demounting.

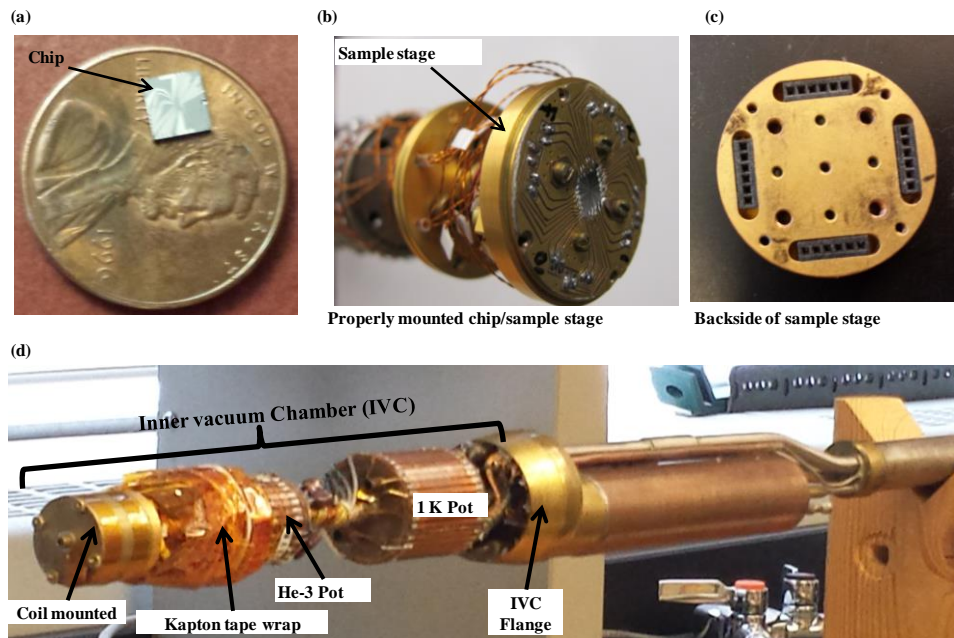


Figure D4: (a) Typical chip containing six spectrometers on a penny. (b) Image of chip wire-bonded to sample stage and mounted properly on the He-3 fridge. (c) Backside of sample stage showing slots for mini-dc connections used for electrical connections to STJs. (d) Top of fridge after completion of sample mounting, electrical connection, coil mounting, and wrapping of wiring with kapton tape.

- ***Cool, measure, and warm:*** A cool down from room temperature to experimental temperature of ~0.3 K, involves a step by step process adopted by the Robinson group. One overarching idea is to minimize LHe boil off throughout the process. The cool down process commences after the final sample mounting step shown in Figure D4 (c). The steps are listed as follows:
 - (i) Clean tapers around IVC flange and add vacuum grease with beta wipe
 - (ii) Place the IVC can on.
 - (iii) Pump out the IVC with a rough pump
 - (iv) Perform a leak check of the IVC with Alcatel Leak detector (no leaks should be detected on the 10×10^{-8} atm.cc/s scale).
 - (v) Add ~10 cc of air to IVC for exchange gas. Typically done by blanking the IVC flange, opening the IVC valve, and closing the valve immediately.
 - (vi) Preload ~ 5cc of helium gas to be used later for exchange gas to IVC
 - (vii) Pump and purged the 1 K pot about 3 times. Purging is done by adding 5 psig of helium. Pump out to about 75 mT. Monitor pressure with DV-23 pressure gauge
 - (viii) While still purging, bubble test the 1 K pot to ensure there is no blockage. This is implemented by connecting one side a tiny tubing to the 1K pot orifice and placing the other side in a little beaker of water. Gas bubbles in the water indicate no blockage.

- (ix) Immerse fridge in Liquid Nitrogen. Temperature monitoring with Labview commences in this step (*C:\users\Richard Robinson\My documents\LabVIEW data\John\Interactive Temperature Controller with Cernox and Fluke*).
- (x) After ~30 minutes immersion in LN₂, when the temperature of cold stage ($T_{\text{cold}} \sim 175$ K, and 1 K pot ($T_{1\text{K}} \sim 125$ K, add the He exchange gas. A sharp drop in temperature will now occur
- (xi) After ~2 hours immersion in LN₂, $T_{\text{cold}} = T_{1\text{K}} = 77$ K
- (xii) Check resistance of all devices and coil at 77 K (note that there is no reason to progress if devices are faulty or something needs to be fixed)
- (xiii) While still purging, immerse the cryostat in Liquid helium in gradual steps.
- (xiv) After ~40 minutes after immersion in LHe, $T_{\text{cold}} = 4.2$ K and $R_{1\text{K}} = 163$ K Ω
- (xv) Stop Purging the 1 K pot.
- (xvi) Pump out the IVC using the Turbo pump (Edwards). Desired vacuum level is $\sim 10^{-7}$ Torr, and this step could take 5 – 8 hours.
- (xvii) Check resistance of all devices and coil at 4.2 K (note that there is no reason to progress if devices are faulty or something needs to be fixed)
- (xviii) Perform vibration isolation and grounding: place rubber pads underneath the Dewar tires, and ensure that the fridge, Dewar and equipment rack are properly grounded.

- (xix) Fridge is now at 4.2 K in LHe; however, to perform measurements at 0.3 K, He-3 needs to be condensed to the He-3 Pot.
- (xx) Turn on the 1 K Pot by pumping with the big rough pump (Leybold).
Instantly, $R_{1K} = 170 \text{ K}\Omega$ and $T_{1K} \sim 1.3 \text{ K}$
- (xxi) Apply 10 mA current to charcoal pump heat of the fridge
- (xxii) After 20 minutes, increase current to 20 mA
- (xxiii) After 20 minutes, increase current to 25 mA. T_{cold} rises to $\sim 1.36 \text{ K}$ and then starts to drop
- (xxiv) After 20 minutes, shut off heater. Fridge cools down naturally until $T_{\text{cold}} \sim 0.3 \text{ K}$.
- (xxv) The summary of the cool down procedure are illustrated in Figure D5 and D6

Typical Cooling Procedure

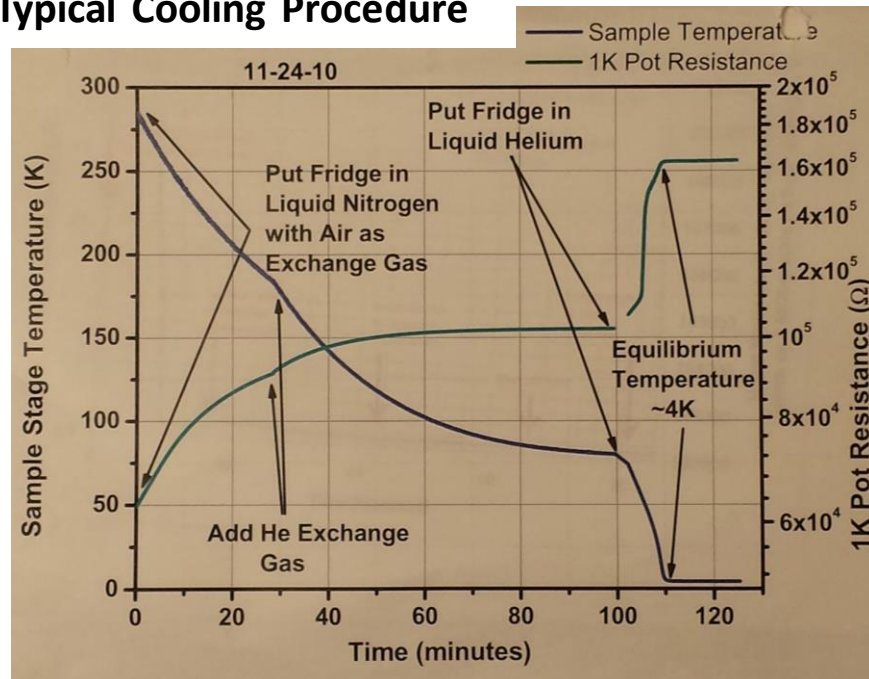


Figure D5: Typical plot of cool down procedure

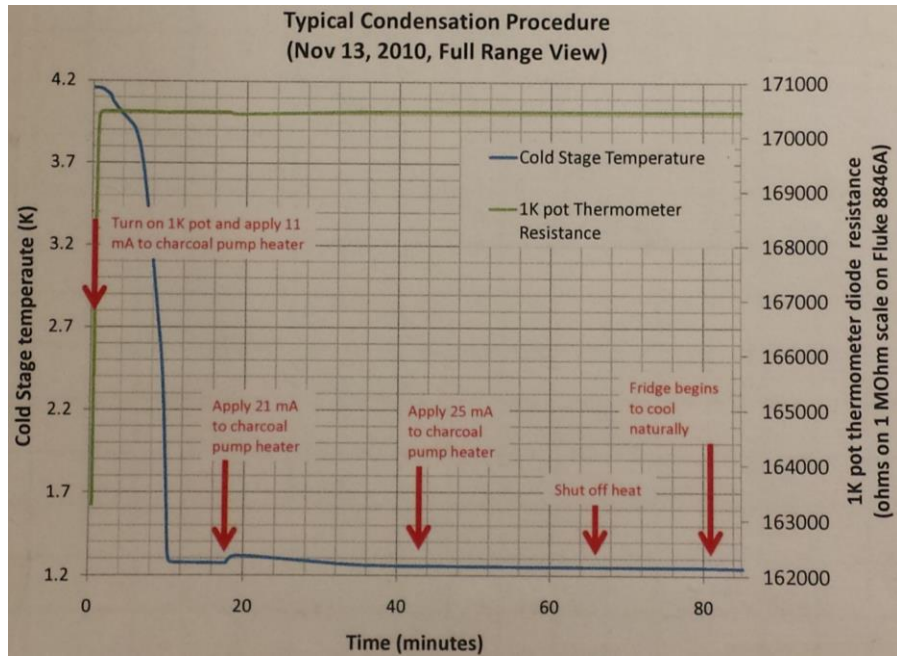


Figure D6: Typical plot of condensation procedure.

(xxvi) Measurements: Measurements include I-V measurements of STJ, Josephson current suppression and transport measurements, and the details have been described fully in chapter 2. Measurement is performed via virtual instrumentation with Matlab (Mathworks Inc.) and LabView (National Instruments). LabView routines, mostly written by N.J. Yoshida, are used for mostly for temperature monitoring and heater control. The files are located in the Phonon Lab computer: *C:\users\Richard Robinson\My documents\LabVIEW data\John\Interactive Temperature Controller with Cernox and Fluke*. The data taking process itself (IV curve measurements, Josephson

current suppression, and modulated transport data) as described in chapter 2 are performed using Matlab scripts, mostly written by J.B. Hertzberg. The files can be found on the office PC (*Phonon Spectroscopy Desktop > Phonon Spectroscopy > Matlab Routines.*) Below is a picture of the experimental set up during a measurement run, and note that the actual circuitry may be found in chapter 2 or in Lab note books.

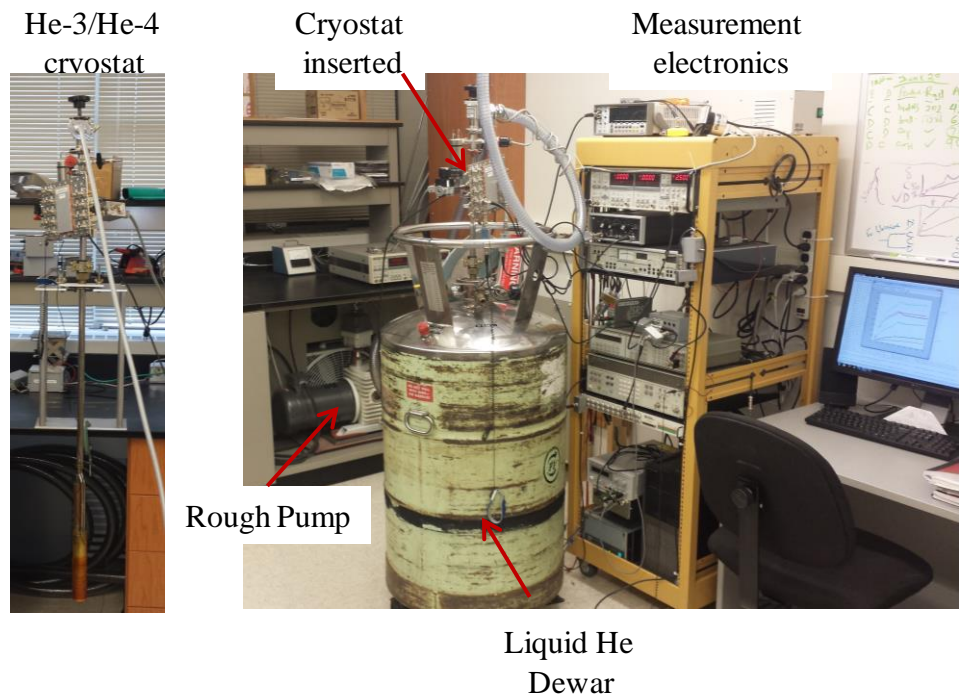


Figure D7: Experimental setup for phonon transport measurements showing cryostat, Dewar, pump, and measurement electronics.

(xxvii) Warm up procedure: After all measurements have been performed, careful steps must be taken to pull out the fridge from the Dewar as shown in Figure D8.

- (xxviii) Disconnect all wiring to fridge, except temperature and pressure monitor
- (xxix) Attach blow off valve to IVC and open the IVC valve
- (xxx) Pump out 1 K pot
- (xxxii) Raise fridge gradually over an hour
- (xxxiii) When $T_{\text{cold}} \sim 49 \text{ K}$ and $T_{1\text{K}} = 80 \text{ K}$, and $P_{1\text{K}} = 1 \text{ Torr}$, lift out fridge from liquid helium Dewar
- (xxxiv) Continue pumping 1K pot and monitor temperature while fridge warms up

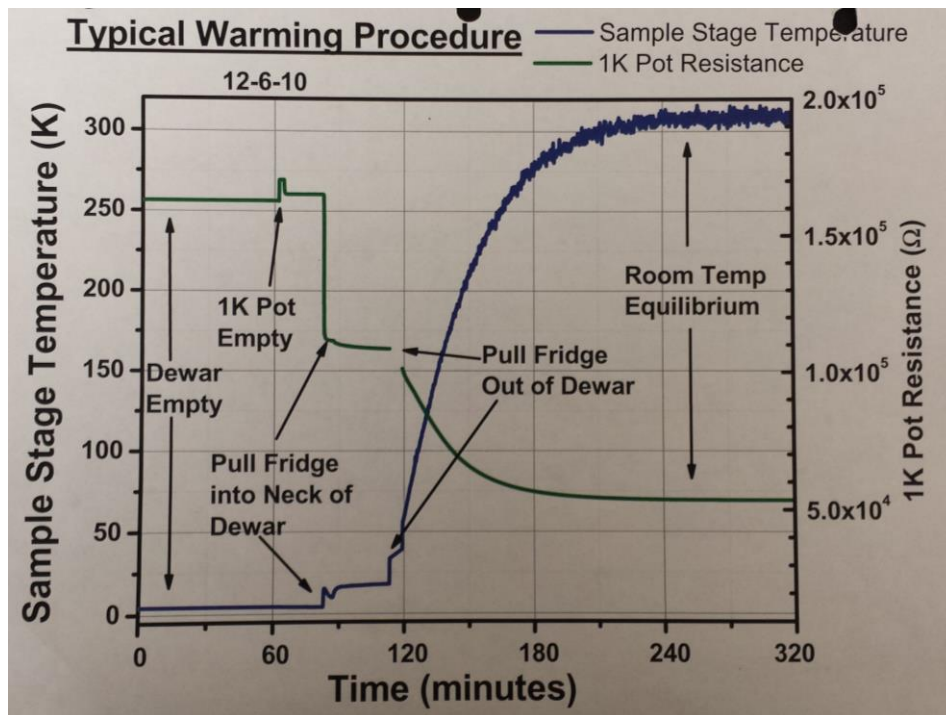


Figure D8: Typical warming procedure before pulling out fridge.

Procedure for Transferring Liquid Helium from Dewar to Dewar

1. Check and record the levels of each Dewar.
2. (In the event the level meter is malfunctioning, use the heat gun to melt any potential ice buildup)
3. Attach the Helium gas to the intake valve of the source Dewar. Do not open the valves.
4. Slowly insert the transfer tube (long side) into the source Dewar and wait until cold gas comes out the end.
5. Make sure the relief valve is closed on the source Dewar and that the receiving Dewar has the level meter in place and the correct fitting for the transfer tube attached.
6. Quickly open the exhaust and neck valves of the receiving Dewar and insert the transfer tube. If done too slowly, moisture may enter and freeze in the Dewar or the transfer tube may freeze to the fitting.
7. Once the transfer tube is inserted all the way in both source and receiving Dewars, allow the Helium flow to slow on its own.
8. Apply pressurized Helium gas (about 5psi) to the source Dewar. Double check that the relief valve is still closed. Watch the pressure gauges on source and receiving Dewars - if they are working properly, you should see a couple PSI pressure rise in the source Dewar but none or very little in the receiving Dewar.
9. Continue to monitor the level in the receiving Dewar. Turn off the pressure when the level reads about 60L and allow Helium flow to stop naturally. Or if the

source Dewar runs empty, the level in the receiving Dewar will stop rising and the pressure in the source Dewar will drop.

10. Once Helium flow has stopped, depressurize the source Dewar by shutting off the He gas inlet valve, opening the exhaust and the relief valve, then remove the transfer tube and level meter.
11. Close up both Dewars leaving only the relief valves open.
12. Put away the level meter and transfer tube, and be sure that you have all the fittings.

BIBLIOGRAPHY

- [1] M. Maldovan, *Nature*, vol. 503, pp. 209-17, 2013.
- [2] G. Chen, *Nanoscale Energy Transport and Conversion : A Parallel Treatment of Electrons, Molecules, Phonons, and Photons*. Oxford; New York: Oxford University Press, 2005.
- [3] A. A. Balandin, *Journal of Nanoscience and Nanotechnology*, vol. 5, pp. 1015-22, 2005.
- [4] D. G. Cahill, W. K. Ford, K. E. Goodson, G. D. Mahan, A. Majumdar, H. J. Maris, *et al.*, *Journal of Applied Physics*, vol. 93, pp. 793-818, 2003.
- [5] E. Pop, *Nano Research*, vol. 3, pp. 147-169, 2010.
- [6] A. Shakouri, *Proceedings of the IEEE*, vol. 94, pp. 1613-1638, 2006.
- [7] L. Lindsay, D. A. Broido, and T. L. Reinecke, *Physical Review Letters*, vol. 111, p. 025901, 2013.
- [8] N. E. Booth and D. J. Goldie, *Superconductor Science and Technology*, vol. 9, p. 493, 1996.
- [9] T. Saab, R. M. Clarke, B. Cabrera, R. A. Abusaidi, and R. Gaitskell, *Nuclear Instruments and Methods in Physics Research Section A: Accelerators, Spectrometers, Detectors and Associated Equipment*, vol. 444, pp. 300-303, 2000.
- [10] B. Cornell, D. C. Moore, S. R. Golwala, B. Bumble, P. K. Day, H. G. LeDuc, *et al.*, *Journal of Low Temperature Physics*, vol. 176, pp. 891-897, 2014.
- [11] B. S. Karasik, S. V. Pereverzev, A. Soibel, D. F. Santavicca, D. E. Prober, D. Olaya, *et al.*, *Applied Physics Letters*, vol. 101, p. 052601, 2012.
- [12] K. D. Irwin, S. W. Nam, B. Cabrera, B. Chugg, and B. A. Young, *Review of Scientific Instruments*, vol. 66, pp. 5322-5326, 1995.
- [13] G. Wang, *Journal of Applied Physics*, vol. 107, p. 094504, 2010.
- [14] R. M. Clarke, P. L. Brink, B. Cabrera, P. Colling, M. B. Crisler, A. K. Davies, *et al.*, *Applied Physics Letters*, vol. 76, pp. 2958-2960, 2000.
- [15] J. Clarke and F. K. Wilhelm, *Nature*, vol. 453, pp. 1031-1042, 2008.
- [16] C. H. Bennett and D. P. DiVincenzo, *Nature*, vol. 404, pp. 247-255, 2000.
- [17] L. B. Ioffe, V. B. Geshkenbein, C. Helm, and G. Blatter, *Physical Review Letters*, vol. 93, p. 057001, 2004.
- [18] D. Mozysky, S. Kogan, V. N. Gorshkov, and G. P. Berman, *Physical Review B*, vol. 65, p. 245213, 2002.
- [19] S. Chu and A. Majumdar, *Nature*, vol. 488, pp. 294-303, 2012.
- [20] L. D. Hicks and M. S. Dresselhaus, *Physical Review B*, vol. 47, pp. 12727-12731, 1993.
- [21] A. Khitun, A. Balandin, K. L. Wang, and G. Chen, *Physica E: Low-dimensional Systems and Nanostructures*, vol. 8, pp. 13-18, 2000.
- [22] P. Kim, L. Shi, A. Majumdar, and P. L. McEuen, *Physical Review Letters*, vol. 87, p. 215502, 2001.
- [23] A. I. Boukai, Y. Bunimovich, J. Tahir-Kheli, J.-K. Yu, W. A. Goddard III, and J. R. Heath, *Nature*, vol. 451, pp. 168-171, 2008.
- [24] A. I. Hochbaum, R. Chen, R. D. Delgado, W. Liang, E. C. Garnett, M. Najarian,

- et al.*, *Nature*, vol. 451, pp. 163-168, 2008.
- [25] J. P. Heremans, M. S. Dresselhaus, L. E. Bell, and D. T. Morelli, *Nature Nanotechnology*, vol. 8, pp. 471-473, 2013.
- [26] K. Schwab, E. A. Henriksen, J. M. Worlock, and M. L. Roukes, *Nature*, vol. 404, pp. 974-977, 2000.
- [27] J. K. Yu, S. Mitrovic, D. Tham, J. Varghese, and J. R. Heath, *Nature Nanotechnology*, vol. 5, pp. 718-21, 2010.
- [28] P. E. Hopkins, C. M. Reinke, M. F. Su, R. H. Olsson, E. A. Shaner, Z. C. Leseman, *et al.*, *Nano Letters*, vol. 11, pp. 107-112, 2011.
- [29] J. S. Heron, T. Fournier, N. Mingo, and O. Bourgeois, *Nano Letters*, vol. 9, pp. 1861-1865, 2009.
- [30] J. H. Seol, I. Jo, A. L. Moore, L. Lindsay, Z. H. Aitken, M. T. Pettes, *et al.*, *Science*, vol. 328, pp. 213-216, 2010.
- [31] C. Kittel, *Introduction to Solid State Physics*, 8th ed. Hoboken, NJ: Wiley, 2005.
- [32] W. Eisenmenger and A. H. Dayem, *Phys. Rev. Lett.*, vol. 18, pp. 125-127, 1967.
- [33] H. Kinder, *Physical Review Letters*, vol. 28, pp. 1564 - 7, 1972.
- [34] H. Kinder, Ed., *Monochromatic Phonon Generation by Superconducting Tunnel Junctions* (Nonequilibrium Phonon Dynamics. New York: Plenum Press, 1985.
- [35] J. B. Hertzberg, O. O. Otelaja, N. J. Yoshida, and R. D. Robinson, *Review of Scientific Instruments*, vol. 82, pp. 104905-6, 2011.
- [36] J. Bardeen, L. N. Cooper, and J. R. Schrieffer, *Physical Review*, vol. 108, pp. 1175-1204, 1957.
- [37] L. N. Cooper, *Physical Review*, vol. 104, pp. 1189-1190, 1956.
- [38] T. VanDuzer and C. W. Turner, *Principles of Superconductive Devices and Circuits*. Upper Saddle River, N.J. : Prentice Hall, 1999.
- [39] M. Tinkham, *Introduction to Superconductivity*. Mineola, N.Y.: Dover Publications, 2004.
- [40] B. D. Josephson, *Physics Letters*, vol. 1, pp. 251-253, 1962.
- [41] V. Ambegaokar and A. Baratoff, *Physical Review Letters*, vol. 10, pp. 486, 1963.
- [42] D. G. Cahill, P. V. Braun, G. Chen, D. R. Clarke, S. Fan, K. E. Goodson, *et al.*, *Applied Physics Reviews*, vol. 1, p. 011305, 2014.
- [43] M. N. Wybourne and J. K. Wigmore, *Reports on Progress in Physics*, vol. 51, p. 923, 1988.
- [44] M. D. Losego and D. G. Cahill, *Nature Materials*, vol. 12, pp. 382-384, 2013.
- [45] W.-L. Ong, S. M. Rupich, D. V. Talapin, A. J. H. McGaughey, and J. A. Malen, *Nature Materials*, vol. 12, pp. 410-415, 2013.
- [46] D. V. Talapin, J. S. Lee, M. V. Kovalenko, and E. V. Shevchenko, *Chemical Reviews*, vol. 110, p. 389, 2009.
- [47] F. Hetsch, N. Zhao, S. V. Kershaw, and A. L. Rogach, *Materials Today*, vol. 16, p. 312, 2013.
- [48] A. Zabet-Khosousi and A. A. Dhirani, *Chemical Reviews*, vol. 108, p. 4072, 2008.
- [49] P. Guyot-Sionnest, *Journal of Physical Chemistry. Letters*, vol. 3, p. 1169, 2012.
- [50] A. L. Efros and B. I. Shklovskii, *Journa of Physics C: Solid State Physics*, vol.

- 8, p. L49, 1975.
- [51] N. F. Mott, *Conduction in Non-Crystalline Materials*, 1993.
- [52] NSF/WTEC. (2010). *Nanotechnology Research Directions for Societal Needs in 2020*.
- [53] A. P. Alivisatos, P. Cummings, J. D. Yoreo, K. Fichthorn, B. Gates, R. Hwang, *et al.*, "Nanoscience Research for Energy Needs: Report of the National Nanotechnology Initiative Grand Challenge Workshop, March 16-18, 2004," in *Basic Energy Sciences and the National Science and Technology Council*, ed: National Nanotechnology Coordination Office, 2004, p. 69.
- [54] J. Zou and A. Balandin, *Journal of Applied Physics*, vol. 89, pp. 2932-2938, 2001.
- [55] N. Gomopoulos, D. Maschke, C. Y. Koh, E. L. Thomas, W. Tremel, H. J. Butt, *et al.*, *Nano Letters*, vol. 10, pp. 980-984, 2010.
- [56] A. Balandin and K. L. Wang, *Physical Review B*, vol. 58, pp. 1544-1549, 1998.
- [57] J. Tang, H.-T. Wang, D. H. Lee, M. Fardy, Z. Huo, T. P. Russell, *et al.*, *Nano Letters*, vol. 10, pp. 4279-4283, 2010.
- [58] W. E. Bron, *Reports on Progress in Physics*, vol. 43, p. 301, 1980.
- [59] L. G. C. Rego and G. Kirczenow, *Physical Review Letters*, vol. 81, pp. 232-235, 1998.
- [60] J. M. Ziman, *Electrons and Phonons; the Theory of Transport Phenomena in Solids*. Oxford: Clarendon Press, 1960.
- [61] T. Klitsner and R. O. Pohl, *Physical Review B*, vol. 36, pp. 6551-6565, 1987.
- [62] S. B. Kaplan, C. C. Chi, D. N. Langenberg, J. J. Chang, S. Jafarey, and D. J. Scalapino, *Physical Review B*, vol. 14, pp. 4854-4873, 1976.
- [63] M. Welte and W. Eisenmenger, *Zeitschrift für Physik B Condensed Matter*, vol. 41, pp. 301-313, 1981.
- [64] J. D. Teufel, "Superconducting Tunnel Junctions as Direct Detectors for Submillimeter Astronomy," Yale University, 2008.
- [65] S. Y. Hsieh and J. L. Levine, *Physical Review Letters*, vol. 20, pp. 1502-1504, 1968.
- [66] W. Eisenmenger, "Physical Acoustics - Principles and Methods." vol. XII, W. P. Mason and R. N. Thurston, Eds., ed: Academic Press, 1976, pp. 79-153.
- [67] A. R. Long, *Journal of Physics F: Metal Physics*, vol. 3, p. 2023, 1973.
- [68] S. B. Kaplan, *Journal of Low Temperature Physics*, vol. 37, pp. 343-365, 1979.
- [69] H. Kinder, *Zeitschrift für Physik*, vol. 262, pp. 295-314, 1973.
- [70] M. Welte, K. Lassmann, and W. Eisenmenger, *Journal of Physics. Colloques*, vol. 33, pp. C4-25-C4-27, 1972.
- [71] A. R. Long, *Journal of Physics F: Metal Physics*, vol. 3, p. 2040, 1973.
- [72] V. M. Bobetic, *Physical Review*, vol. 136, pp. A1535-A1538, 1964.
- [73] A. Mrzyglod and O. Weis, *Journal of Low Temperature Physics*, vol. 97, pp. 275-286, 1994.
- [74] W. Burger and K. Lassmann, *Physical Review B*, vol. 33, pp. 5868-5870, 1986.
- [75] H. J. Trumpp and W. Eisenmenger, *Zeitschrift für Physik B Condensed Matter*, vol. 28, pp. 159-171, 1977.
- [76] V. Savu, L. Frunzio, and D. E. Prober, *Applied Superconductivity, IEEE*

- Transactions on*, vol. 17, pp. 324-327, 2007.
- [77] A. F. G. Wyatt, *Journal of Physics C: Solid State Physics*, vol. 9, p. 2541, 1976.
 - [78] L. Solymar, *Superconductive Tunnelling and Applications*. London: Chapman and Hall, 1972.
 - [79] C. M. Wilson and D. E. Prober, *Physical Review B*, vol. 69, p. 094524, 2004.
 - [80] A. Rothwarf and B. N. Taylor, *Physical Review Letters*, vol. 19, pp. 27-30, 1967.
 - [81] G. J. Dolan, *Applied Physics Letters*, vol. 31, pp. 337-339, 1977.
 - [82] P. J. Koppinen, L. M. Vaisto, and I. J. Maasilta, *Applied Physics Letters*, vol. 90, p. 053503, 2007.
 - [83] I. M. Pop, T. Fournier, T. Crozes, F. Lecocq, I. Matei, B. Pannetier, *et al.*, *Journal of Vacuum Science & Technology B: Microelectronics and Nanometer Structures*, vol. 30, p. 010607, 2012.
 - [84] A. W. Kleinsasser, R. E. Miller, and W. H. Mallison, *Applied Superconductivity, IEEE Transactions on*, vol. 5, pp. 26-30, 1995.
 - [85] R. C. Dynes and J. P. Garno, *Physical Review Letters*, vol. 46, pp. 137-140, 1981.
 - [86] R. W. Cohen and B. Abeles, *Physical Review*, vol. 168, pp. 444-450, 1968.
 - [87] H. Greenhouse, *Parts, Hybrids, and Packaging, IEEE Transactions on*, vol. 10, pp. 101-109, 1974.
 - [88] O. Koblinger, J. Mebert, E. Dittrich, S. Dottinger, W. Eisenmenger, P. V. Santos, *et al.*, *Physical Review B*, vol. 35, pp. 9372-9375, 1987.
 - [89] O. Naaman and J. Aumentado, *Physical Review Letters*, vol. 98, p. 227001, 2007.
 - [90] W. Forkel, M. Welte, and W. Eisenmenger, *Physical Review Letters*, vol. 31, pp. 215-216, 1973.
 - [91] F. Giazotto, T. T. Heikkilä, A. Luukanen, A. M. Savin, and J. P. Pekola, *Reviews of Modern Physics*, vol. 78, pp. 217-274, 2006.
 - [92] S. Tamura, J. A. Shields, and J. P. Wolfe, *Physical Review B*, vol. 44, pp. 3001-3011, 1991.
 - [93] B. Taylor, H. J. Maris, and C. Elbaum, *Physical Review Letters*, vol. 23, pp. 416-419, 1969.
 - [94] J. P. Wolfe, *Imaging Phonons : Acoustic Wave Propagation in Solids*. Cambridge, U.K.; New York: Cambridge University Press, 1998.
 - [95] H. J. Maris, *Journal of the Acoustical Society of America*, vol. 50, pp. 812 - 818, 1971.
 - [96] R. Chen, A. I. Hochbaum, P. Murphy, J. Moore, P. D. Yang, and A. Majumdar, *Physical Review Letters*, vol. 101, p. 105501, 2008.
 - [97] J. S. Heron, C. Bera, T. Fournier, N. Mingo, and O. Bourgeois, *Physical Review B*, vol. 82, p. 155458, 2010.
 - [98] K. Hippalgaonkar, B. L. Huang, R. K. Chen, K. Sawyer, P. Ercius, and A. Majumdar, *Nano Letters*, vol. 10, p. 4341, 2010.
 - [99] J. W. Lim, K. Hippalgaonkar, S. C. Andrews, A. Majumdar, and P. D. Yang, *Nano Letters*, vol. 12, p. 2475, 2012.
 - [100] D. A. Broido, M. Malorny, G. Birner, N. Mingo, and D. A. Stewart, *Applied Physics Letters* vol. 91, p. 231922, 2007.

- [101] A. Ward, D. A. Broido, D. A. Stewart, and G. Deinzer, *Physical Review B*, vol. 80, p. 125203, 2009.
- [102] K. Esfarjani, G. Chen, and H. T. Stokes, *Physical Review B*, vol. 84, p. 085204, 2011.
- [103] H. J. Maris and S. Tamura, *Physical Review B*, vol. 85, p. 054304, 2012.
- [104] A. J. H. McGaughey and A. Jain, *Applied Physics Letters*, vol. 100, p. 061911, 2012.
- [105] J. A. Johnson, A. A. Maznev, J. Cuffe, J. K. Eliason, A. J. Minnich, T. Kehoe, *et al.*, *Physical Review Letters*, vol. 110, p. 025901, 2013.
- [106] H. B. G. Casimir, *Physica*, vol. 5, p. 495, 1938.
- [107] K. Fuchs, *Mathematical Proceedings of the Cambridge Philosophical Society*, vol. 34, p. 100, 1938.
- [108] T. Klitsner, J. E. VanCleve, H. E. Fischer, and R. O. Pohl, *Physical Review B*, vol. 38, p. 7576, 1988.
- [109] S. B. Soffer, *Journal of Applied Physics*, vol. 38, p. 1710, 1967.
- [110] Z. M. Zhang, *Nano/Microscale Heat Transfer*, 2007.
- [111] D. S. Chung, J. S. Lee, J. Huang, A. Nag, S. Ithurria, and D. V. Talapin, *Nano Letters*, vol. 12, p. 1813, 2012.
- [112] J. Cuffe, O. Ristow, E. Chavez, A. Shchepetov, P. O. Chapuis, F. Alzina, *et al.*, *Physical Review Letters*, vol. 110, p. 095503, 2013.
- [113] W. Fon, K. C. Schwab, J. M. Worlock, and M. L. Roukes, *Physical Review B*, vol. 66, p. 045302, 2002.
- [114] J. N. Coleman, M. Lotya, A. O'Neill, S. D. Bergin, P. J. King, U. Khan, *et al.*, *Science*, vol. 331, p. 568, 2011.
- [115] H. F. C. Hoevers, M. L. Ridder, A. Germeau, M. P. Bruijn, P. A. J. de Korte, and R. J. Wiergerink, *Applied Physics Letters*, vol. 86, p. 251903, 2005.
- [116] V. Yefremenko, G. S. Wang, V. Novosad, A. M. Datesman, J. E. Pearson, R. Divan, *et al.*, *Applied Superconductivity, IEEE Transactions on*, vol. 19, p. 489, 2009.
- [117] N. Mingo, *Physical Review B*, vol. 68, p. 113308, 2003.
- [118] M. Kazan, G. Guisbiers, S. Pereira, M. R. Correia, P. Masri, A. Bruyant, *et al.*, *Journal of Applied Physics*, vol. 107, p. 083503, 2010.
- [119] D. Lacroix, K. Joulain, D. Terris, and D. Lemonnier, *Applied Physics Letters*, vol. 89, p. 103104, 2006.
- [120] L. Shi, *Nanoscale Microscale Thermophysical Engineering*, vol. 16, p. 79, 2012.
- [121] A. J. Minnich, J. A. Johnson, A. J. Schmidt, K. Esfarjani, M. S. Dresselhaus, K. A. Nelson, *et al.*, *Physical Review Letters*, vol. 107, p. 095901, 2011.
- [122] K. T. Regner, D. P. Sellan, Z. H. Su, C. H. Amon, A. J. H. McGaughey, and J. A. Malen, *Nature Communications*, vol. 4, p. 1640, 2013.
- [123] A. J. Kent, N. M. Stanton, L. J. Challis, and M. Henini, *Applied Physics Letters*, vol. 81, p. 3497, 2002.
- [124] O. O. Otelaja, J. B. Hertzberg, M. Aksit, and R. D. Robinson, *New Journal of Physics*, vol. 15, p. 43018, 2013.
- [125] A. I. Boukai, Y. Bunimovich, J. Tahir-Kheli, J. K. Yu, W. A. Goddard, and J. R. Heath, *Nature*, vol. 451, p. 168, 2008.

- [126] M. Aksit, D. P. Toledo, and R. D. Robinson, *Journal of Materials Chemistry*, vol. 22, p. 5936, 2012.
- [127] M. Aksit, B. C. Hoselton, H. J. Kim, D. H. Ha, and R. D. Robinson, *ACS Applied Materials and Interfaces*, vol. 5, p. 8998, 2013.
- [128] Y. S. Ju and K. E. Goodson, *Applied Physics Letters*, vol. 74, p. 3005, 1999.
- [129] A. K. McCurdy, H. J. Maris, and C. Elbaum, *Physical Review B*, vol. 2, p. 4077, 1970.
- [130] S. Tamura, *Physical Review B*, vol. 31, p. 2574, 1985.
- [131] P. E. Hopkins, L. M. Phinney, J. R. Serrano, and T. E. Beechem, *Physical Review B*, vol. 82, p. 085307, 2010.
- [132] K. Jakata and A. G. Every, *Phys. Rev. B*, vol. 77, p. 174301, 2008.
- [133] C. Blanc, A. Rajabpour, S. Volz, T. Fournier, and O. Bourgeois, *Appl. Phys. Lett.*, vol. 103, p. 043109, 2013.
- [134] S. Datta, *Quantum Transport*, 2005.
- [135] M. J. M. Dejong, *Physical Review B*, vol. 49, p. 7778, 1994.
- [136] J. A. Wang and J. S. Wang, *Applied Physics Letters*, vol. 88, p. 111909, 2006.
- [137] Z. Aksamija and I. Knezevic, *Physical Review B*, vol. 82, p. 045319, 2010.
- [138] J. Carrete, L. J. Gallego, L. M. Varela, and N. Mingo, *Physical Review B*, vol. 84, p. 075403, 2011.
- [139] L. N. Maurer, Z. Aksamija, E. B. Ramayya, A. H. Davoody, and I. Knezevic, *Applied Physics Letters*, vol. 106, p. 133108, 2015.
- [140] L. Fedichkin and A. Fedorov, *Physical Review A*, vol. 69, p. 032311, 2004.
- [141] E. Pop, S. Sinha, and K. E. Goodson, *Proceedings of the IEEE*, vol. 94, pp. 1587-1601, 2006.
- [142] J. B. Hertzberg, M. Aksit, O. O. Otelaja, D. A. Stewart, and R. D. Robinson, *Nano Letters*, vol. 14, pp. 403-415, 2014.
- [143] H. Zhang, C. Hua, D. Ding, and A. J. Minnich, *Scientific Reports*, vol. 5, p. 9121, 2015.
- [144] M. E. Siemens, Q. Li, R. Yang, K. A. Nelson, E. H. Anderson, M. M. Murnane, *et al.*, *Nature Materials*, vol. 9, pp. 26-30, 2010.
- [145] D. Marx and W. Eisenmenger, *Zeitschrift für Physik B Condensed Matter*, vol. 48, pp. 277-291, 1982.
- [146] W. Eisenmenger, "Phonon Scattering at Surfaces and Interfaces," in *Phonon Scattering in Condensed Matter V*. vol. 68, A. Anderson and J. Wolfe, Eds., ed: Springer Berlin Heidelberg, 1986, pp. 204-211.
- [147] A. M. Savin, J. P. Pekola, D. V. Averin, and V. K. Semenov, *Journal of Applied Physics*, vol. 99, p. 084501, 2006.
- [148] J. M. Martinis, M. Ansmann, and J. Aumentado, *Physical Review Letters*, vol. 103, p. 097002, 2009.
- [149] W.-Q. Huang, G.-F. Huang, L.-L. Wang, and B.-Y. Huang, *Physical Review B*, vol. 75, p. 233415, 2007.
- [150] D. R. Bosomworth, W. Hayes, A. R. L. Spray, and G. D. Watkins, *Proceedings of the Royal Society of London A*, vol. 317, pp. 133, 1970.
- [151] G. A. Northrop and J. P. Wolfe, *Physical Review B*, vol. 22, pp. 6196-6212, 1980.

- [152] S. M. Meenehan, J. D. Cohen, S. Gröblacher, J. T. Hill, A. H. Safavi-Naeini, M. Aspelmeyer, *et al.*, *Physical Review A*, vol. 90, p. 011803, 2014.
- [153] D. V. Talapin and C. B. Murray, *Science*, vol. 310, p. 86, 2005.
- [154] I. Gur, N. A. Fromer, M. L. Geier, and A. P. Alivisatos, *Science*, vol. 310, p. 462, 2005.
- [155] S. Coe, W. K. Woo, M. Bawendi, and V. Bulovic, *Nature*, vol. 420, p. 800, 2002.
- [156] L. Besra and M. Liu, *Progress in Materials Science*, vol. 52, p. 1, 2007.
- [157] K. W. Song, R. Costi, and V. Bulović, *Advanced Materials*, vol. 25, p. 1420, 2013.
- [158] M. A. Islam, Y. Xia, D. A. Telesca, M. L. Steigerwald, and I. P. Herman, *Chemistry of Materials.*, vol. 16, p. 49, 2003.
- [159] D. H. Ha, M. A. Islam, and R. D. Robinson, *Nano Letters*, vol. 12, p. 5122, 2012.
- [160] S. A. Hasan, D. W. Kavich, and J. H. Dickerson, *Chemical Communications*, p. 3723, 2009.
- [161] M. A. Islam and I. P. Herman, *Applied Physics Letters*, vol. 80, p. 3823, 2002.
- [162] R. Wagner and H. D. Wiemhöfer, *J of Physics and Chemistry of Solids*, vol. 44, p. 801, 1983.
- [163] I. Carbone, Q. Zhou, B. Vollbrecht, L. Yang, S. Medling, A. Bezryadina, *et al.*, *Journal of Vacuum Science & Technology A*, vol. 29, p. 051505, 2011.
- [164] I. Grozdanov and M. Najdoski, *Journal of Solid State Chemistry*, vol. 114, p. 469, 1995.
- [165] J. Cardoso, O. GomezDaza, L. Ixtlilco, M. T. S. Nair, and P. K. Nair, *Semiconductor Science and Technology*, vol. 16, p. 123, 2001.
- [166] M. T. S. Nair and P. K. Nair, *Semiconductor Science and Technology*, vol. 4, p. 191, 1989.
- [167] H. Zhang, B. R. Hyun, F. W. Wise, and R. D. Robinson, *Nano Letters*, vol. 12, p. 5856, 2012.
- [168] H. Zhang, B. Hu, L. F. Sun, R. Hovden, F. W. Wise, D. A. Muller, *et al.*, *Nano Letters*, vol. 11, p. 5356, 2011.
- [169] X. Liu, X. Wang, B. Zhou, W. C. Law, A. N. Cartwright, and M. T. Swihart, *Advance Functional Materials*, vol. 23, p. 1256, 2013.
- [170] T. D. Sands, J. Washburn, and R. Gronsky, *Physica Status Solidi A*, vol. 72, p. 551, 1982.
- [171] Y. Zhao, H. Pan, Y. Lou, X. Qiu, J. Zhu, and C. Burda, *Journal of the American Chemical Society*, vol. 131, p. 4253, 2009.
- [172] Y. Bekenstein, K. Vinokurov, S. Keren-Zur, I. Hadar, Y. Schilt, U. Raviv, *et al.*, *Nano Letters*, vol. 14, p. 1349, 2014.
- [173] Y. Xie, A. Riedinger, M. Prato, A. Casu, A. Genovese, P. Guardia, *et al.*, *Journal of the American Chemical Society*, vol. 135, p. 17630, 2013.
- [174] J. M. Luther, P. K. Jain, T. Ewers, and A. P. Alivisatos, *Nature Materials*, vol. 10, p. 361, 2011.
- [175] P. L. Saldanha, R. Brescia, M. Prato, H. Li, M. Povia, L. Manna, *et al.*, *Chemistry of Materials*, vol. 26, p. 1442, 2014.
- [176] J. Shan, P. Pulkkinen, U. Vainio, J. Maijala, J. Merta, H. Jiang, *et al.*, *Journal of Materials Chemistry*, vol. 18, p. 3200, 2008.

- [177] J. Jang, W. Liu, J. S. Son, and D. V. Talapin, *Nano Letters*, vol. 14, p. 653, 2014.
- [178] S. C. Liufu, L. D. Chen, Q. Yao, and F. Q. Huang, *Journal of Physical Chemistry C*, vol. 112, p. 12085, 2008.
- [179] V. Podzorov, E. Menard, J. A. Rogers, and M. E. Gershenson, *Physical Review Letters*, vol. 95, p. 226601, 2005.
- [180] J. Lauth, J. Marbach, A. Meyer, S. Dogan, C. Klinke, A. Kornowski, *et al.*, *Advanced Functional Materials*, vol. 24, p. 1081, 2014.
- [181] J. Y. Leong and J. H. Yee, *Applied Physics Letters*, vol. 35, p. 601, 1979.
- [182] A. T. Fafarman, S. H. Hong, S. J. Oh, H. Caglayan, X. Ye, B. T. Diroll, *et al.*, *ACS Nano*, vol. 8, p. 2746, 2014.
- [183] A. Singh, N. J. English, and K. M. Ryan, *Journal of Physical Chemistry B*, vol. 117, p. 1608, 2012.
- [184] P. E. Lyons, S. De, F. Blighe, V. Nicolosi, L. F. C. Pereira, M. S. Ferreira, *et al.*, *Journal of Applied Physics*, vol. 104, p. 044302, 2008.
- [185] D. Yu, C. Wang, B. L. Wehrenberg, and P. Guyot-Sionnest, *Physical Review Letters*, vol. 92, p. 216802, 2004.
- [186] M. S. Kang, A. Sahu, D. J. Norris, and C. D. Frisbie, *Nano Letters*, vol. 11, p. 3887, 2011.
- [187] H. Liu, A. Pourret, and P. Guyot-Sionnest, *ACS Nano*, vol. 4, p. 5211, 2010.
- [188] A. J. Houtepen, D. Kockmann, and D. Vanmaekelbergh, *Nano Letters*, vol. 8, p. 3516, 2008.
- [189] J. H. Choi, A. T. Fafarman, S. J. Oh, D. K. Ko, D. K. Kim, B. T. Diroll, *et al.*, *Nano Letters*, vol. 12, p. 2631, 2012.
- [190] M. Rothenfusser, W. Dietsche, and H. Kinder, *Physical Review B*, vol. 27, pp. 5196-5198, 1983.
- [191] L. W. Shive and B. L. Gilmore, *ECS Transactions*, vol. 16, pp. 401-405, October 3, 2008.
- [192] K. Jakata, "Spatial Dispersion in Phonon Focusing," MS, University of Witwatersrand, Johannesburg, 2007.
- [193] D. S. Bright. (2004). *Digital Image Processing with NIH Image (Mac) and ImageJ*. Available: <http://www.nist.gov/lispix/imlab/labs.html>
- [194] H. Seidel, L. Csepregi, A. Heuberger, and H. Baumgärtel, *Journal of The Electrochemical Society*, vol. 137, pp. 3612-3626, 1990.